LEABHARLANN CHOLÁISTE NA TRÍONÓIDE, BAILE ÁTHA CLIATH | TRINITY COLLEGE LIBRARY DUBLIN
Ollscoil Átha Cliath | The University of Dublin

Terms and Conditions of Use of Digitised Theses from Trinity College Library Dublin

Copyright statement

All material supplied by Trinity College Library is protected by copyright (under the Copyright and Related Rights Act, 2000 as amended) and other relevant Intellectual Property Rights. By accessing and using a Digitised Thesis from Trinity College Library you acknowledge that all Intellectual Property Rights in any Works supplied are the sole and exclusive property of the copyright and/or other IPR holder. Specific copyright holders may not be explicitly identified. Use of materials from other sources within a thesis should not be construed as a claim over them.

A non-exclusive, non-transferable licence is hereby granted to those using or reproducing, in whole or in part, the material for valid purposes, providing the copyright owners are acknowledged using the normal conventions. Where specific permission to use material is required, this is identified and such permission must be sought from the copyright holder or agency cited.

Liability statement

By using a Digitised Thesis, I accept that Trinity College Dublin bears no legal responsibility for the accuracy, legality or comprehensiveness of materials contained within the thesis, and that Trinity College Dublin accepts no liability for indirect, consequential, or incidental, damages or losses arising from use of the thesis for whatever reason. Information located in a thesis may be subject to specific use constraints, details of which may not be explicitly described. It is the responsibility of potential and actual users to be aware of such constraints and to abide by them. By making use of material from a digitised thesis, you accept these copyright and disclaimer provisions. Where it is brought to the attention of Trinity College Library that there may be a breach of copyright or other restraint, it is the policy to withdraw or take down access to a thesis while the issue is being resolved.

Access Agreement

By using a Digitised Thesis from Trinity College Library you are bound by the following Terms & Conditions. Please read them carefully.

I have read and I understand the following statement: All material supplied via a Digitised Thesis from Trinity College Library is protected by copyright and other intellectual property rights, and duplication or sale of all or part of any of a thesis is not permitted, except that material may be duplicated by you for your research use or for educational purposes in electronic or print form providing the copyright owners are acknowledged using the normal conventions. You must obtain permission for any other use. Electronic or print copies may not be offered, whether for sale or otherwise to anyone. This copy has been supplied on the understanding that it is copyright material and that no quotation from the thesis may be published without proper acknowledgement.

EXPERIMENTAL AND THEORETICAL INVESTIGATIONS OF PILE AND PENETROMETER INSTALLATION IN CLAY

BY

DAVID R. GILL

OCTOBER 1999

DISSERTATION SUBMITTED TO THE UNIVERSITY OF DUBLIN IN PARTIAL FULFILMENT OF THE REQUIREMENTS FOR THE DEGREE OF DOCTOR OF PHILOSOPHY

Department of Civil, Structural and Environmental Engineering

Trinity College, Dublin

TRINITY COLLEGE
- 7 FEB 2000
LIBRARY DUBLIN
Thesis
5322

DECLARATION

I, the undersigned, declare that this Thesis has not been submitted as an exercise for a degree at this or any other University. I further declare that, except where reference is made in the text, it is entirely my own work. I agree the library may lend or copy this thesis upon request.

David Gill

David R. Gill

October 29, 1999.

SUMMARY

This Thesis advances our understanding of the type of ground movements and strains that take place during installation of closed-ended piles and penetrometers in clay, with particular reference to penetrometers with flat and 60° conical tips. This was to be achieved by; (a) conducting model experiments to measure the displacements around penetrating penetrometers and (b) the development of a numerical/theoretical model.

(a) *Experimental measurement*

A new laboratory test was developed for the measurement of soil displacements around model penetrometers. The development of a transparent 'clay' and the use of a video camera system, capable of a very high resolution of measurement, have allowed the radial and vertical soil movements to be recorded in a 3-D model penetrometer test. A unique and comprehensive account is provided of the relatively complex deformational behaviour of soil surrounding penetrating penetrometers. Some conclusions drawn from the experimental results are:

- The total radial displacement of the soil is relatively insensitive to the tip geometry, while the vertical displacements show a significantly influence. Displacement paths measured for soil elements during penetrometer installation displayed a greater complexity of behaviour than previously indicated.
- A wedge of soil forms ahead of the tip of a flat penetrometer and close to the shaft, shear planes are formed in the soil which separate regions of relatively high vertical displacement from regions of low vertical displacement a short distance away.

(b) *Numerical modelling*

The approach adopted in this research builds on a previous advance of the Strain Path Method. A standard finite element (FE) fluid dynamics package is used to produce velocity fields around penetrometers of different geometry and SPM theory is used to calculate the inferred strains and displacements. The FE package allows two addition factors to be included in the flow solution to refine the strain and deformation predictions; (i) the relative velocity specified on the penetrometer boundary and (ii) the introduction of fluid viscosity. These flow parameters allow the down drag of soil close to a penetrometer shaft and upward ground heave in the far field to be replicated. The main conclusions drawn from the theoretical approach are:

- An improved prediction of soil deformation around penetrometers has been achieved with the modified SPM approach, although not all the features of real soil behaviour can be replicated.
- A comparison of the computed strains and displacements with experimental values show that a good prediction of far field behaviour was made but near field prediction, close to the penetrometer was more approximate.

ACKNOWLEDGMENTS

In the course of researching and writing this Thesis I received a lot of help in different ways from many people and I take this opportunity to thank them.

Barry Lehane has provided invaluable guidance and expertise in his supervision of my research, and much of credit for the unconventional side to this Thesis falls to him.

The technical staff of the TCD Civil Engineering Department have assisted me in the experimental work despite doubting the sanity of my project. In particular Martin Carney in the soil laboratory, and 'Chief' Chris O'Donovan, who was a believer, are due many thanks.

I also wish to acknowledge the financial assistance of the Geotechnical Society of Ireland who blessed me with two years of the Geotechnical Award.

There have been many non-academic contributions to this Thesis, all of them inspirational, provided in turn by; the postgraduate 'old boys' Ian 'Ernie' Byrne, Peter Mitchell, Robert Leslie, Steve Power, Pat Treacy, and Sea-moose O'Brien who gave research a bad name; David Flynn and Peter Fitzgerald who proved work is an unnecessary evil; thanks to Ken Gavin, Andrea Faulkner, Samir Hebib and Bryan McCabe who are the friendly side of geotechnics; most recently Shane Murray, Ian 'DJ' Maher and Steve 'Cheese' Bredin who have ably distracted me from my work, if help was needed; the Civ-Eng football team (RIP) also deserves special mention, boys, we could have been great.

The last word goes to my parents, who have supported, if not carried me this far and not least provided food, water and shelter, all at a very reasonable rate.

TABLE OF CONTENTS

TABLE OF CONTENTS

Chapter 1

INTRODUCTION

1.1 THESIS AIM 2
1.2 PENETROMETERS 2
1.3 BACKGROUND TO THEORETICAL INTERPRETATION OF PENETROMETER INSTALLATION 4
1.4 RESEARCH OBJECTIVES AND APPROACH TAKEN 4
1.5 CONTENTS OF THE THESIS 5

Chapter 2

LITERATURE REVIEW: GROUND DEFORMATION DUE TO PENETROMETER INSTALLATION

2.1 INTRODUCTION 9
2.2 A REVIEW OF PREDICTIVE METHODS 9
2.2.1 General *9*
2.2.2 Cavity Expansion Theory *10*
2.2.2.1 Outline 10
2.2.2.2 Solutions to cavity expansion 11
2.2.2.3 Summation of cavity expansion theory 13
2.2.2.4 Application of cylindrical cavity expansion in this research 14
2.2.3 The Strain Path Method *15*
2.2.3.1 Outline 15
2.2.3.2 Application of the Strain Path Method (SPM) 16
2.2.3.3 Simple pile solution 18
2.2.3.4 Problems identified with the SPM 20
2.2.3.5 Alternative solutions using SPM theory 21
2.2.4 Finite Element Methods *28*
2.2.4.1 General 28
2.2.4.2 The Lagrangian approach 30
2.2.4.3 The Eulerian approach 37
2.2.4.4 The Arbitrary Lagrangian Eulerian approach 39
2.3 A REVIEW OF EXPERIMENTAL MEASUREMENTS 41
2.3.1 Outline *41*
2.3.2 Laboratory Tests *42*
2.3.2.1 Radiographic techniques 42
2.3.2.2 Visual techniques 44
2.3.3 Field Measurements *50*
2.3.4 Formation of Slip Planes During Penetrometer Installation *52*
2.4 SUMMARY AND OUTLINE OF ADOPTED APPROACH 52

Chapter 3

MODIFICATIONS TO THE STRAIN PATH METHOD APPROACH

3.1 INTRODUCTION 58
3.2 APPLICATION OF SPM 58
3.2.1 Outline *58*
3.2.2 Simple Pile Formulation *59*
3.2.3 Modelling Different Shaped Penetrometers Using Potential Flow Theory *67*

3.3 APPLICATION OF FINITE ELEMENT FLOW MODELLING TO SPM 68
3.3.1 General Description Of FE Model *68*
3.3.2 Modelling Flow Around A Fixed Penetrometer *69*
3.3.3 Interpolating Flow Paths *71*
3.3.4. Calculation Of Strains And Displacements *73*

Chapter 4

SOLUTIONS FROM MODIFIED STRAIN PATH METHOD APPROACH

4.1 INTRODUCTION 78
4.1.1 Introduction of Two Flow Parameters *78*
4.2 STRAIN PATH PREDICTIONS 79
4.2.1 Solutions for 60° Cone *79*
4.2.1.1 Comparison with SPM 80
4.2.1.2 The effects of fluid viscosity (μ) 81
4.2.1.3 Relative velocity on penetrometer boundary 82
4.2.1.4 The effects of initial radial distance (r_0/R) 84
4.2.2 Solutions For Flat-Ended Penetrometer *85*
4.2.2.1 The effect of viscosity (μ) 85
4.2.2.2 Penetrometer boundary effects 86
4.2.3 Comparison Of 60° Cone and Flat-Ended Penetrometers *88*
4.3 DISPLACEMENT PREDICTIONS 89
4.3.1 Outline *89*
4.3.2 Displacements around 60° Cone *90*
4.3.2.1 Effect of viscosity (μ) 90
4.3.2.2 Effect of slip condition 91
4.3.2.3 Effect of z/R on displacements 92
4.3.2.4 Displacement paths for 60° cone 93
4.3.3 Displacements Around Flat-Ended Penetrometer *95*
4.3.3.1 Effect of viscosity (μ) 95
4.3.3.2 Effect of slip condition 96
4.3.3.3 Displacement paths for flat tip 97
4.4 SUMMARY OF FLOW EFFECTS 98

Chapter 5

DEVELOPMENT OF A TRANSPARENT SOIL

5.1 INTRODUCTION 102
5.2 REVIEW OF TRANSPARENT SOILS 102
5.2.1 Transparent Granular Soil *102*
5.2.2 Transparent Clays *103*
5.1.2.1 Initial investigations by Mannheimer and Oswald (1993) 103
5.1.2.2 Further study by Iskander *et al.* (1994) 105
5.3 TCD TRANSPARENT CLAY 107
5.3.1 Objective *107*
5.3.2. The Silica *107*
5.3.2.1 Precipitated Silica 108
5.3.2.2 Fumed Silica 108
5.3.3. Properties Of The Pore Fluid *111*
5.3.3.1 Determining the optimum refractive index for the pore fluid 111
5.3.3.2 Viscous effects of silica concentration 113
5.3.4 Geotechnical Characteristics of the TCD Transparent Clay *114*
5.3.4.1 Phase relationships for slurry and soil 114
5.3.4.2 Consolidation tests on TCD transparent clay 115

5.3.4.3 Effective porosity and interaggregate void ratio 120
5.3.4.4 Aggregate-pore fluid relationship in TCD transparent clay 121
5.3.4.5 Consolidation of the TCD transparent clay within the test chamber 124
5.3.4.6. Dissipation analysis 126
5.3.4.7 The behaviour of TCD transparent clay in direct shear 127
5.3.4.8. Undrained strength from triaxial and hand vane tests 130
5.4 SUMMARY 131

Chapter 6

MEASUREMENT OF SOIL DISPLACEMENTS DURING PENETROMETER INSTALLATION

6.1 INTRODUCTION 134
6.2 DESIGN OF A MODEL PENETROMETER EXPERIMENT 134
6.2.1 Outline Of Design Process *134*
6.2.2 The Test Chamber *135*
6.2.2.1 Glass inner chamber 136
6.2.2.2 Steel outer casing 138
6.2.2.3 Loading the soil 142
6.2.2.4 Drainage 143
6.3 THE MODEL PENETROMETER TEST 145
6.3.1 Outline *145*
6.3.2 Preparation Of A Soil Sample *145*
6.3.3 Penetrometer Installation *148*

Chapter 7

EXPERIMENTAL RESULTS - MODEL PENETROMETER TEST

7.1 INTRODUCTION 153
7.2 CORRECTIONS APPLIED TO CAMERA MEASUREMENTS 153
7.2.1 General *153*
7.2.2 Data Averaging *155*
7.2.3 Camera-Test Chamber Relative Movement *155*
7.2.4 Rotation of the Camera Reference Frame *157*
7.2.5 Eccentricity of Soil Markers *158*
7.2.6 Calculating Soil Marker Position Relative to Penetrometer (z/R) *159*
7.3 SOIL DISPLACEMENTS 161
7.3.1 Displacement Fields *161*
7.3.1.1 Results from Tests 1 & 2 161
7.3.1.2 Displacement trends 162
7.3.2 Displacement Paths *168*
7.4 SOIL STRAIN 170
7.4.1 Strain Paths *170*
7.4.2 Strain Contours *178*
7.5 DISCUSSION ON DATA QUALITY 185

Chapter 8

COMPARISON OF THEORETICAL AND EXPERIMENTAL RESULTS

8.1 INTRODUCTION 188
8.2 BEST FIT SOLUTION FOR FLAT-ENDED PENETROMETER 188
8.2.1 General *188*
8.2.1.1 Physical Significance of the Fluid Flow Parameters 189

8.2.2 Displacements *190*
8.2.2.1 Comparison of theoretical and experimental displacement paths 194
8.2.3 Strains And Strain Paths *198*
8.2.3.1 Comparison of theoretical and strain paths derived from experimental data 200
8.3 BEST FIT SOLUTION FOR 60° CONE 203
8.3.1 General Flow Description *203*
8.3.2 Displacements *204*
8.3.3 Strains *208*
8.4 DISCUSSION OF THE MODIFIED SPM APPROACH 211
8.4.1 General *211*
8.4.2 Flat-ended Penetrometer *211*
8.4.3 The 60° Cone *213*
8.4.4 Comparison Of 60° Cone and Flat tip Solutions *214*
8.4.5 Summary *215*
8.4.6 Improving The SPM Predictive Method *215*

Chapter 9

CONCLUSIONS

9.1 OUTLINE 219
9.2 EXPERIMENTAL MEASUREMENTS 219
9.2.1 TCD Model Penetrometer Tests *219*
9.2.2 Observations from Experimental Data *220*
9.2.3 Transparent Soil *220*
9.3 PREDICTIVE CAPABILITIES OF THE MODIFIED SPM APPROACH 221
9.3.1 Choice Of Predictive Approach For Penetrometer Installation *221*
9.3.2 Influence Of Flow Properties On SPM Solutions *222*
9.3.3 Best-fit Predictions for the Modified SPM *223*
9.4 FUTURE RESEARCH 225
9.4.1 Experimental Work *225*
9.4.2 Improving SPM Prediction *226*

Appendix A

APPLICATION OF THE CAVITY EXPANSION METHOD

A1 GENERAL 229
A2 CYLINDRICAL CAVITY EXPANSION THEORY 229
A2.1 Derivation Of Expressions For Cylindrical Cavity Expansion *230*
A2.2 Cylindrical Cavity Expansion in Purely Elastic Soil *234*
A2.3 Cylindrical Cavity Expansion In Elastic-Perfectly Plastic Soil *234*
A3 THE MODIFIED CAM-CLAY MODEL 236
A3.1 General *236*
A3.2 Model Parameters and Stress-Strain Relationships *237*
A4 APPLICATION OF THE MODIFIED CAM-CLAY MODEL TO STRESS PATH PROBLEMS 241
A4.1 Outline *241*
A4.2 Conventional Drained Triaxial Compression *242*
A4.3 Conventional Undrained Triaxial Compression *246*
A5 APPLICATION OF THE MODIFIED CAM-CLAY MODEL TO PLANE STRAIN CONDITIONS 249
A5.1 Outline *249*
A5.2 Expressions For Radial and Circumferential Stress And Strain *249*
A5.4 Converting Strains To Stresses *250*
A5.5 Application Of MCC To A Specific Cavity Expansion Problem *253*

Appendix B

APPLICATION OF SPM TO ANSYS FLOW RESULTS

B1 INTRODUCTION 258
B2 CONVERSION OF ANSYS RESULTS FILES 258
B3 FINDING INTERPOLATION CONSTANTS 262
B4 INTERPOLATING STREAMLINES THROUGH THE GRID 264
B5 DETERMINING STRAINS AND DISPLACEMENTS 265
B6 ANSYS STREAM FUNCTION ERROR 267

Appendix C

THE VIDEOEXTENSOMETER DOT MEASURING SYSTEM

C1. GENERAL 271
C2. SYSTEM COMPONENTS 271
C3. GENERAL CAMERA OPERATION PROCEDURES 271
C4. ASSESSING VIDEOEXTENSOMETER DOT MEASURING ACCURACY 274
C5. DETERMINING CAMERA ACCURACY IN PRACTICE 275

REFERENCES 281

LIST OF FIGURES

Chapter 2

Figure 2.1. Effective stresses at the end of pile installation for (a) OCR = 1 and (b) OCR = 8 (Randolph et al., 1979) 12

Figure 2.2. Effective stresses for cylindrical cavity expansion at OCR = 1 & 8 (Collins & Yu, 1996) 13

Figure 2.3. Deformation patterns in steady-state testing of wedges in modelling clay: apex angle 2θ = (a) 20°; (b) 60°; (c) 90° (Baligh & Scott, 1975) 16

Figure 2.4. Predicted deformation and streamline patterns around a 'simple pile' (Baligh 1985) 17

Figure 2.5. Strain Paths followed during penetration of a 'simple pile' (Baligh 1985) 20

Figure 2.6. Flow fields around cones (Tumay *et al.*, 1985) 21

Figure 2.7. Octahedral strain rates around cones (Tumay *et al.*, 1985) 22

Figure 2.8. Strain paths due to penetrometers with different apex angles (Teh 1987) 23

Figure 2.9. Stress and strain contours around a 60° cone penetrometer (Teh 1987) 24

Figure 2.10. Comparison of axial strain history obtained from numerical and analytical analysis of the simple sampler (Clayton *et al.* 1998) 27

Figure 2.11. Detail of boundary conditions change of nodal points at the upper and lower ends of the cone (Kiousis 1988) 31

Figure 2.12. (a) Separation of the soil-penetrometer interface: (b) Displacement field around the penetrometer (Kiousis 1988) 32

Figure 2.13. Octahedral shear strain contours around the penetrometer (Kiousis 1988) 33

Figure 2.14. Finite Element scheme adopted by Cividini & Gioda (1989) in simulation of the advancing process 34

Figure 2.15. Stress distribution due to penetration assuming (a) a smooth pile (b) a soil-pile interface with adhesion equal to the cohesion of the soil (after Cividini & Gioda, 1989) 35

Figure 2.16. Incremental penetration of a cone penetrometer (Abu-Farsakh *et al.* 1998) 36

Figure 2.17. Schematic view of an Eulerian approach to the cone penetration problem (Van Den Berg *et al.*, 1996) 38

Figure 2.18. Influence of the boundary condition at the shoulder of the cone (Van Den Berg *et al.*, 1996) 39

Figure 2.19. Incremental displacements at different stages of 'spudcan' penetration (Hu & Randolph, 1998) 41

Figure 2.20. Ground movements caused by penetrometer installation: (a) Vertical soil movements; (b) Radial soil movements (after Bond 1989) 43

Figure 2.21. Photograph after driving a closed-ended pile (Gue, 1984) 45

Figure 2.22. Radial soil movements from semi-cylindrical model pile tests (Gue 1984) 46

Figure 2.23. Vertical soil movements from semi-cylindrical model pile tests (Gue, 1984) 47

Figure 2.24. 2-D model penetrometer test in crushed glass (Allersma 1988): (a) Test set-up; (b) stress distribution during penetration 48

Figure 2.25. Semi-cylindrical 60° cone tests in sand: (a) Probe penetrated into sand; (b) Displacement vectors for dense sand (Davidson & Boghrat, 1983) 49

Figure 2.26. Strain fields for a 60° cone test in dense sand: (a) Volumetric strains; (b) shear strains (Davidson & Boghrat, 1983) 50

Figure 2.27. Vertical ground displacements from field tests (Cooke *et al.* 1979): (a) 0.5 m below the surface; (b) 2.2 m below the surface 51

Figure 2.28. Experimental displacements measured in model pile tests; (a) radial movements, (b) vertical movements 56

Chapter 3

Figure 3.1 Spherical and cylindrical co-ordinate systems 60
Figure 3.2. Prediction of grid deformation and streamlines due to simple pile penetration 62
Figure 3.3. Geometry of the simple pile problem (Teh 1987) 64
Figure 3.4 Octahedral strain rate contours during simple pile penetration 65
Figure 3.5. Spreadsheet prediction of strain paths during simple pile penetration 66
Figure 3.6. Flow pattern around a 'cone' shaped penetrometer using potential theory 68
Figure 3.7. Flow Model: (a) boundary conditions; (b) nodal grid 70
Figure 3.8. Velocities for the 60° cone at z/R = 20 for two FE meshes 71
Figure 3.9. Interpolated streamline in the nodal grid 72
Figure 3.10. Streamline interpolation through the nine-node local mesh 73

Chapter 4

Figure 4.1. Teh's (1987) solution for SPM: strain path at $r_0/R = 1$ for 60° cone 80
Figure 4.2. Deviatoric strain paths at $r_0/R = 1$ during penetration of a 60° cone for 'full slip' flow 82
Figure 4.3. Deviatoric strain paths at $r_0/R = 1$ during penetration of a 60° cone for different boundary conditions with constant viscosity 83
Figure 4.4. Deviatoric strain paths at $r_0/R = 0.5$, 1 & 2 for 'full slip' flow conditions ($v_{pent}/U = 1$) and viscosity, $\mu = 1$ Nsm^{-2} (Re = 2000) 84
Figure 4.5. Deviatoric strain paths at $r_0/R = 1$ during penetration of a flat ended penetrometer for 'full slip' flow 86
Figure 4.6. Deviatoric strain paths at $r_0/R = 1$ during penetration of a flat ended penetrometer for different boundary conditions with constant velocity 87
Figure 4.7. Comparison of deviatoric strain paths at $r_0/R = 1$ for penetrometers with 60° cone and flat tips with 'full slip' flow ($v_{pent}/U = 1$) 89
Figure 4.8. Displacements at z/R = 20 around a 60° cone for 'full slip' flow 90
Figure 4.9. Displacements at z/R = 20 around a 60° cone for constant viscosity 92
Figure 4.10. Comparison of displacements at z/R = 5 & 20 for 'partial slip' flow ($v_{pent}/U = 0.975$) around a 60° cone 93
Figure 4.11. Displacement paths at r0/R = 0.5, 1, 2 & 4 for a 60° cone with 'full slip' flow conditions (Flow C) and $\mu = 1.2$ 94
Figure 4.12. Displacements at z/R = 20 around a flat-ended penetrometer for 'full slip' flow 96
Figure 4.13. Displacements at z/R = 20 around a flat-ended penetrometer for constant viscosity 97
Figure 4.14 Displacement paths at $r_0/R = 0.5$, 1, 2 & 4 for a flat tip with 'full slip' flow conditions (Flow J) and $\mu = 1$ 98

Chapter 5

Figure 5.1. Measured and theoretical time settlement curves (Iskander *et al.*, 1994) 105
Figure 5.2. The relationship between the co-ordination number (number of particle contacts) and the pore volume (Iler, 1979) 109
Figure 5.3. Electron microscope image of TCD transparent clay magnified 30,000 times (after consolidation to 225 kPa). 111
Figure 5.4. Electron microscope image of undisturbed Boston Blue clay (Mesri & Ali, 1999) 111
Figure 5.5. Density versus refractive index for various forms of silica (Iler, 1979) 112

Figure 5.7. Settlement-log time consolidation plot for transparent clay; increment 25 → 50 kPa 117
Figure 5.8. Settlement-log time consolidation plot for transparent clay; increment 50 → 100 kPa 117
Figure 5.9. Settlement-log time consolidation plot for transparent clay; increment 100 → 200 kPa 117
Figure 5.10. Effect of consolidation pressure and particle size on permeability of transparent soil 119
Figure 5.11. Schematic diagram showing three states for pore fluid within silica 122
Figure 5.12. 1-D consolidation for 'free' pore fluid 123
Figure 5.13. Test chamber *e*-log σ' curve (for 100% primary consolidation) 126
Figure 5.14. Dissipation of pore pressures at various points along penetrometer shaft (after Teh, 1987) 127
Figure 5.15 (a) & (b). Direct drained shear tests on normally consolidated transparent soil 128
Figure 5.16. Mohr diagram for normally consolidated transparent clay 129
Figure 5.17. Direct undrained shear tests on overconsolidated transparent soil at σ'_v = 25 kPa (OCR = 8) 130
Figure 5.18. Unconsolidated undrained triaxial test on transparent clay (cell pressure = 200kPa). 131

Chapter 6

Figure 6.1. The test chamber in plan and elevation. 137
Figure 6.2. Load versus deflection for three-point test with laminated and plate glass 138
Figure 6.3. The forces on the sides of the test chamber during consolidation. 142
Figure 6.4. Consolidation of a soil sample within the test chamber using the vertical loading system of the large shear box apparatus 144
Figure 6.5. Two rows of soil markers (beads) at mid-depth in the test chamber prior to penetrometer installation (as seen by the video camera, field of view = 192×144 mm) 146
Figure 6.6. Settlement-log time consolidation plot for transparent soil within the test chamber for load increment 100→150 kPa 147
Figure 6.7. The penetrometer after installation into the glass chamber has been completed 149
Figure 6.8. Camera images of penetrometer installation at: (1) z/R = -20; (2) z/R = - 10; (3) z/R = - 4; (4) z/R = -2; (5) z/R = 2; (6) z/R = 20 151

Chapter 7

Figure 7.1. Distance effect of using reference markers on front of chamber 156
Figure 7.2. Image taken from Test 2, which illustrates the very slight inclination of the penetrometer to the X-Y plane 157
Figure 7.3. Rotation of the X-Y co-ordinate plane to allow for any misalignment of the penetrometer 158
Figure 7.4. Schematic diagram of eccentric effect of soil markers on camera displacement measurements 159
Figure 7.5. Determining z/R for soil markers during penetration 160
Figure 7.6. Radial displacements for Tests 1 & 2 at z/R = 5. 163
Figure 7.7. Vertical displacements for Test 1 & 2 at z/R = 5 with: (a) negative values not shown; (b) negative values shown 163
Figure 7.8. Radial displacements for Test 1 & 2 at z/R = 20. 164
Figure 7.9. Vertical displacements for Test 1 & 2 at z/R = 20: (a) negative values not shown; (b) with negative values shown 164
Figure 7.10. Comparison of radial displacements at z/R=5 & z/R=20 with other experimental data 165
Figure 7.11. Comparison of vertical displacements at z/R=5 & z/R=20 with other experimental data: (a) negative values not shown; (b) with negative values shown 167

Figure 7.12. Displacement paths during penetrometer installation: (a) $r_0/R < 1.6$; (b) $1.6 < r_0/R < 5$; (c) $r_0/R > 5$ 169
Figure 7.13. Curves fitted to displacement data using MATLAB ($r_0/R < 3$) 172
Figure 7.14. Curves fitted to displacement data using MATLAB ($r_0/R > 3$) 173
Figure 7.15. Schematic diagram showing differentiation in the radial direction with points along 'flow paths' 174
Figure 7.16. Strain paths followed by soil elements during penetrometer installation ($r_0/R < 1.5$) 175
Figure 7.17. Strain paths followed by soil elements during penetrometer installation ($1.5 < r_0/R < 2$) 175
Figure 7.18. Strain paths followed by soil elements during penetrometer installation ($2 < r_0/R < 5$) 176
Figure 7.19. Strain paths followed by soil elements during penetrometer installation ($r_0/R > 5$) 176
Figure 7.20. Strain contours around a flat ended penetrometer 179
Figure 7.21 Radial strain contours around a flat ended penetrometer 180
Figure 7.22 Circumferential strain contours around a flat ended penetrometer 181
Figure 7.23 Vertical strain contours around a flat ended penetrometer 182
Figure 7.24 Shear strain contours around a flat ended penetrometer 183
Figure 7.25. Radial distribution of strain at $z/R = 1, 5$ & 20 184

Chapter 8

Figure 8.1. Radial and vertical displacement fields at $z/R = 20$ during penetration of a flat-ended penetrometer for 'best-fit' flow and experimental measurements 191
Figure 8.2. Log plot of the radial and vertical displacements at $z/R = 20$ during penetration of a flat-ended penetrometer for 'best-fit' flow and experimental measurements 192
Figure 8.3. Log plot of the radial and vertical displacements at $z/R = 5$ during penetration of a flat-ended penetrometer for 'best-fit' flow and experimental measurements 193
Figure 8.4. Displacement paths during penetration of a flat ended penetrometer for the 'best-fit' flow solution (Flow N): (a) in the near field $r_0/R \leq 1$; and (b) in the far field $r_0/R > 1$ 194
Figure 8.5. Experimental displacement paths during penetrometer installation: (a) $r_0/R < 1.6$; (b) $1.6 < r_0/R < 5$; (c) $r_0/R > 5$ 196
Figure 8.6. Predicted near field deviatoric strain paths at $r_0/R = 0.5$, 1 & 2 during penetration of a flat ended penetrometer for 'best fit' flow 199
Figure 8.7. Predicted far field deviatoric strain paths at $r_0/R = 2$, 4 & 6 during penetration of a flat ended penetrometer for 'best fit' flow 200
Figure 8.8. Experimental strain paths followed by soil elements during penetrometer installation 202
Figure 8.9. Radial and vertical displacement fields at $z/R = 20$ during penetration of a 60° cone for 'best-fit' and 'full-slip' flows 205
Figure 8.10. Log plot of the radial and vertical displacements at $z/R = 20$ during penetration of a 60° cone for 'best-fit' and 'full-slip' flows 206
Figure 8.11. Displacement paths during penetration of a 60° cone for the 'best-fit' solution (Flow M) 208
Figure 8.12. Predicted deviatoric strain paths in the near field ($r_0/R \leq 2$) during penetration of a 60° cone for the 'best-fit' solution (Flow M) 209
Figure 8.13. Predicted deviatoric strain paths in the far field ($r_0/R \geq 2$) during penetration of a 60° cone for the 'best-fit' solution (Flow M) 210
Figure 8.14. Stress-strain rate relationships for different types of fluid (after Massey, 1991) 217
Figure 8.15. Stress vs. strain relationship for: (a) an 'ideal' Bingham model; (b) a 'bi-viscosity' Bingham model (after ANSYS Users Manual, 1997) 218

Appendix A

Figure A1. Finite cylindrical cavity expansion as a model for pile installation. 230
FigureA2. Radial and circumferential stress equilibrium on a soil element (after Benham & Warnock, 1976) 233
Figure A3. Relationship between shear stress and strain for elastic-perfectly plastic material 234
Figure A4. Radial and circumferential stresses around an expanding cylinder (cavity expansion = 2 % R) in an elastic-perfectly plastic soil 236
Figure A5. (a) Elliptical yield locus and critical state line (csl) in p':q plane; (b), (c) normal compression line (ncl), unloading-reloading line (url) and csl in compression plane (after Muir Wood (1990). 239
Figure A6. Stress increment expanding current yield locus; (b) stress increment inside current yield locus (after Muir Wood (1990) 241
Figure A7. Stress increment in conventional drained triaxial compression test; $\delta q = 3\delta p'$ (after Muir Wood, 1990) 242
Figure A8. Sequence of stress increments in drained triaxial compression test; (a) p':q effective stress plane; (b) v:p' compression plane; (c) q:ε_q stress:strain plot; (d) v:ε_q volume:strain plot 243
Figure A9. Modified Cam-clay spreadsheet model results for a conventional drained triaxial compression test on a lightly overconsolidated clay (OCR = 1.5) 245
Figure A10. Modified Cam-clay spreadsheet model results for a conventional drained triaxial compression test on a heavily overconsolidated clay (OCR = 5) 246
Figure A11. Modified Cam-clay spreadsheet model results for a conventional undrained triaxial compression test on a lightly overconsolidated clay (OCR = 1.2) 248
Figure A12. Modified Cam-clay spreadsheet model results for a conventional undrained triaxial compression test on a heavily overconsolidated clay (OCR = 5) 249
Figure A13. Stress distributions in the soil around a cylindrical cavity expansion, for OCR = 1 255
Figure A14. Stress distributions in the soil around a cylindrical cavity expansion, for OCR = 8 255
Figure A15. Stress distributions in the soil around the model pile at z/R = 5, for OCR = 8 256

Appendix B

Figure B1 Interpolated streamline through the nodal mesh showing a 'kink' behind cone shoulder 268
Figure B2. Comparison of radial and vertical velocities; (i) found directly from ANSYS and (ii) derived from the nodal stream function values 269
Figure B3. Mesh areas for 60° cone; the 'correct' order of meshing is shown 269

Appendix C

Figure C1. Deviation of camera measurements for different set-ups 276
Figure C2. Camera view of 'screw-adjusted' plates painted with dots 277
Figure C3. Typical displacement error for camera plotted against test time 279

LIST OF TABLES

Chapter 4

Table 4.1. ANSYS flow solution for 60° cone.....79
Table 4.2. ANSYS flow Solutions for flat-ended penetrometer.....85

Chapter 5

Table 5.1. TCD Transparent soil: material properties.....110
Table 5.2. Soil properties measured during consolidation tests.....115
Table 5.3. Distribution changes of the pore fluid within the soil during consolidation.....123
Table 5.4. A comparison total and interaggregate pore fluid.....124
Table 5.5. Phase relationships for transparent clay before and after 1-D consolidation to 225 kPa.....125
Table 5.6. Undrained shear strengths from hand vane tests for soil in test chamber.....130

Chapter 8

Table 8.1. Flow properties of the 'best-fit' solution for a flat-ended penetrometer (Flow N).....189
Table 8.2. Experimental measurements of displacements around penetrometers.....204

Appendix C

Table C1. Minimum resolution for different fields of view.....275
Table C2. Comparison of different videoextensometer set-ups.....276
Table C3. Comparison of camera and micrometer displacement measurement.....278

CHAPTER 1
INTRODUCTION

Chapter 1

1.0 INTRODUCTION

1.1 THESIS AIM

This Thesis represents an attempt to advance our understanding of the type of ground movements and strains that take place during installation of a penetrometer in soil. Both experimental and theoretical techniques are employed to achieve this objective.

1.2 PENETROMETERS

In geotechnical engineering, a *penetrometer* is a generic term which includes displacement piles, cone penetrometers and dilatometers. The function of penetrometers may be wide ranging but all are relatively long and slender members which are driven or jacked into the ground. Penetration problems, by their nature, are complex and difficult to interpret due to the relatively high range and level of deformation imposed to the soil surrounding a penetrometer during its installation. The function and state of knowledge of the main types of penetrometer are briefly described here.

(i) *Piles*

Piles are used to transmit foundation loads through soil strata of lower bearing capacity to deeper, more competent strata. They are also used in normal ground conditions to resist heavy uplift forces or in poor soil conditions to resist horizontal loads. Although the basic function of piling is easily understood, predicting the axial capacity of driven piles remains an area of considerable uncertainty in foundation design.

Most design methods for piles are based on the correlation of pile capacities measured in controlled load tests to the undrained strength of a clay or the resistance measured during penetration of a device smaller than a full scale pile (e.g., in a Cone Penetration Test or a Standard Penetration Test). Historically, most displacement piles were driven until the base reached a competent stratum. In these situations, a large component of the total capacity was derived from base resistance and the pile design was often controlled by the ability of

the pile itself to carry the load. However, the demand for larger structures, on less suitable ground and for offshore structures meant that longer and larger piles were required. These longer piles relied on shaft friction (e.g., for piles supporting offshore structures in clay this can be up to 90% of their total capacity) and it became clear that more soundly based design methods were required.

Most offshore piles are designed according to American Petroleum Institute (API) recommendations which have been developed from simple empirical methods based on small onshore pile tests. These empirical design rules, however, are inconsistent with the physical processes involved during pile installation and have subsequently come under strong criticism. The poor physical basis of the approach prompted a lot of research in recent years, much of which has centred around field measurements of radial effective stresses developed on pile shafts. This research has reaped many benefits and has led to new empirical design methods such as those summarised in Jardine and Chow (1996). There is, however, considerable room for improvement, given that existing theoretical approaches cannot match *in situ* radial effective stress measurements with an acceptable degree of reliability.

(ii) *Cone Penetration Test*

The cone penetration test (CPT) has been established as the most versatile *in situ* soil exploration test currently available and is consequently fast becoming the most widely used world-wide. The use of a penetrometer with pore pressure measurement for soil profiling is unsurpassed by any other modern instrument, as it is capable of providing continuous measurement over the whole depth of penetration.

The advance in equipment design, however, is not matched by the progress in interpretation techniques. At present, a rigorous quantitative interpretation of CPT data is still not available. Correlation between test data and soil properties still rely very heavily on empirical relationships. This difficulty in providing an analytical solution (as is also the case for piles) lies in the complexity of soil behaviour and boundary conditions in the cone penetration problem.

(iii) *Dilatometer*

The flat-type dilatometer (Marchettii dilatometer) is a spade-shaped probe with an expandable metal-faced pressure cell on one face of the probe. The device is pushed or

hammered into the soil and has some similarities to the CPT equipment but causes less disturbance of the soil than the standard cone.

1.3 BACKGROUND TO THEORETICAL INTERPRETATION OF PENETROMETER INSTALLATION

Early attempts to model pile and penetrometer installation theoretically used bearing capacity and cavity expansion techniques. Later, a more complex approach referred to as the Strain Path Method (SPM), based on work by Levadoux and Baligh (1980), gave a two dimensional representation to the soil straining processes around penetrometers during their undrained installation in clay. The key conceptual assumption of the SPM is that the deformation and strain fields caused during the penetration processes are strongly constrained kinematically and can be estimated independently from the actual constitutive properties of the surrounding soil. Baligh (1985) estimated the strain fields for a variety of penetrometer geometries using the velocity fields of ideal inviscid fluids calculated from potential theory. This approach was developed further by Teh (1987) who adopted an alternative numerical procedure to the potential theory approach and used a finite difference method to predict the velocity field of an inviscid fluid flowing around a penetrometer with a 60° conical tip.

1.4 RESEARCH OBJECTIVES AND APPROACH TAKEN

The work described in this Thesis is aimed primarily at improving the present understanding of *closed-ended* piles and penetrometers in clay, with particular reference to penetrometers with flat and 60° conical tips. This was to be achieved by; (a) the development of a numerical/theoretical model and (b) conducting model experiments to measure the displacements around penetrating penetrometers.

(a) *Numerical modelling*

The approach adopted in this research builds on the analytical approach of the SPM and numerical developments of Teh (1987). A standard finite element (FE) fluid dynamics package is used to produce velocity fields around penetrometers of different geometry and a numerical application of the SPM is used to calculate the inferred strains and displacements. The FE package allows two addition factors to be included in the flow

solution to refine the strain and deformation predictions; (i) the relative velocity specified on the penetrometer boundary and (ii) the introduction of fluid viscosity. These flow parameters allow the down drag of soil close to a penetrometer shaft and upward ground heave in the far field to be replicated.

(b) *Experimental measurement*

Experimental data are required to test and develop any theoretical approach. There is, however, a dearth of reliable measurements of soil displacements around penetrometers in clay (and other soil types) and a key objective of this research was to extend the existing database. Previous experimental approaches that could be considered to be truly three-dimensional tests have involved either large-scale field tests or laboratory tests using radiographic techniques.

A new laboratory test for the measurement of soil displacements around model penetrometers was developed within the budget constraints of this research project. A transparent material was developed with geotechnical properties similar to clay. This allowed the radial and vertical soil movements, in a three-dimensional model test, to be recorded using a (specially acquired) video camera system capable of very high resolution measurement of displacement and strain.

1.5 CONTENTS OF THE THESIS

This Thesis is divided into nine chapters. A brief description of each chapter is outlined here.

Chapter 2: reviews the recent approaches that have been taken to improve the understanding and interpretation of pile and penetrometer installation. This includes theoretical approaches for the prediction of stress and strain around penetrometers and experimental work conducted to measure the soil deformations induced during installation.

Chapter 3: describes essential features of the original Strain Path Method (SPM) formulation and the modifications which have been subsequently introduced in this research to allow improved solutions. The Finite Element (FE) approach used here to model fluid flow fields and procedures for calculating strains and displacement are described in detail.

Chapter 4: presents solutions to the modified Strain Path Method for different flow conditions. The effect of different fluid viscosity and penetrometer boundary conditions on the inferred strains and displacements is investigated. A comparison is also made between the 60° cone tip and the flat-ended penetrometer to determine the influence of the tip geometry on the inferred deformation.

Chapter 5: outlines the development of a transparent soil used in the model penetrometer tests of this Thesis and a gives a description of its measured geotechnical properties.

Chapter 6: describes the laboratory experiment conducted to measure the soil movements around a model penetrometer during its installation into a test chamber. A visual measuring technique using a video camera system was employed to record the displacement of markers within a transparent soil. This chapter describes the test chamber, the visual measuring system, and the experimental procedure undertaken.

Chapter 7: presents the results from the model penetrometer tests and outlines the procedures taken to minimise inaccuracies and remove the effects of external factors from the results. The experimental results are presented as radial and vertical soil movements, displacement paths, strain paths and strain contours.

Chapter 8: compares the prediction of soil strain and displacement from the modified Strain Path Method (SPM) approach with experimental measurements. Solutions presented provide the 'best' or closest fit to the experimental data. The 'best-fit' solution for a flat ended penetrometer has been fitted to the soil displacements measured in model penetrometer tests conducted in this Thesis. The 'best-fit' flow properties found for the flat tip have also been applied to a solution for the 60° cone tip and this is compared with existing experimental displacement results in the literature and the standard SPM predictions.

Chapter 9: is a summary of the major conclusions from each individual chapter. In particular the major tends observed from the experimental and theoretical prediction of strain and displacements are summarised. Recommendations for future research into the prediction of soil behaviour around piles and penetrometers are also made.

Supplementary information is provided in the appendices:

Appendix A: presents the theory and solutions for the application of cylindrical cavity expansion to elastic perfectly plastic and Modified Cam-clay stress-strain models. This represents a preliminary investigation into the application of stress models to simple strain fields and their influence on the stresses developed on the shaft of penetrometers and driven piles. Future research efforts will focus more closely on this aspect of the problem.

Appendix B: describes the complete procedure for finding a SPM solution from the ANSYS flow results.

Appendix C: gives a detailed description of the video camera system used in the model penetrometer experiments including system components, operation procedures and accuracy capabilities.

CHAPTER 2
LITERATURE REVIEW: GROUND DEFORMATION DUE TO PENETROMETER INSTALLATION

Chapter 2

2.0 LITERATURE REVIEW: GROUND DEFORMATION DUE TO PENETROMETER INSTALLATION

2.1 INTRODUCTION

This chapter presents a literature review of both the theoretical and experimental approaches that have been taken to improve the understanding of the soil deformation that takes place during penetrometer installation (penetrometers include piles, cone penetrometers and dilatometers). Section 2.2 discusses existing theoretical approaches for the solution of ground penetration problems while Section 2.3 describes experimental work that has been conducted to measure the soil displacements and strains around model piles. A summary of the work relevant to this Thesis and how it has influenced my research topic is given in Section 2.4.

2.2 A REVIEW OF PREDICTIVE METHODS

2.2.1 General

In recent years, there have been three main approaches used to model deep penetrometer installation: Cavity Expansion Methods (CEM), the Strain Path Method (SPM) and Finite Element Methods (FEM). The important aspects of these techniques are outlined in this chapter. Bearing capacity theory, which provided the initial, if inadequate, attempt at solving deep penetrometer problems, is also discussed briefly.

Theoretical analysis of penetrometer installation is a very difficult task since it involves moving boundary conditions, large deformations and a non-linear material behaviour. Nevertheless an accurate analysis is essential if a correct interpretation of this type of problem is to be obtained. Initially, the penetration problem was approached using bearing capacity theory by a number of investigators such as Meyerhof (1961) and Begemann (1965). This was followed by later work such as that reported by Durgunoglu and Mitchell (1973) and more recently by Koumoto and Kaku (1982). The main objective of this work

has been to find a relationship between the undrained strength of the soil and the tip resistance in the Cone Penetration Test, i.e. to determine a relationship for the cone factor, N_k.

Despite its success as a predictive technique for shallow foundations, bearing capacity theory is not, however, adequate for use in analysing deep penetration problems. One of the major difficulties with this approach stems from the rigid-plastic soil assumed in the theory. In addition, most of the analyses are based on assumed failure mechanisms which are incompatible with the boundary conditions of penetration problems.

2.2.2 Cavity Expansion Theory

2.2.2.1 Outline

Cavity Expansion Methods (CEM) have been used widely in geotechnical engineering to model *in situ* soil testing (e.g. pressuremeters and cone penetrometers), pile driving and tunnelling. For penetrometers, the penetration of the tip has been compared to the expansion of a spherical cavity, while the installation of the penetrometer shaft, away from the influence of the tip or ground surface, has been considered analogous to an expanding cylindrical cavity (Butterfield & Bannerjee, 1970).

While cavity expansion techniques are still genuinely applicable to some geotechnical problems (such as interpretation for the pressuremeter), cavity expansion has been superseded by other techniques as a tool for understanding pile/penetrometer installation. The complex straining that the soil around a penetrometer experiences is poorly represented by the one dimensional monotonic straining of cavity expansion and therefore provides a poor analogy to real penetrometer installation.

The theoretical curves for radial movements predicted by cylindrical cavity expansion theory are shown in Figure 2.20, and are discussed later;

$$\xi/R = \left[(r/R)^2 + \rho^2\right]^{1/2} - r/R \tag{2.1}$$

where ξ is the radial movement of a point at distance r from the pile axis; R is the pile radius; and ρ is an 'area ratio', i.e., $\rho = 1$ for closed ended piles.

2.2.2.2 Solutions to cavity expansion

Cavity expansion theory was first applied to metal indentation problems by Bishop *et al.* (1945) and Hill (1950), who assumed frictionless material properties. The problem was treated as an expansion into an elastic-ideally plastic infinite medium. The first attempts to apply cavity expansion techniques to geotechnical problems were those of Meyerhof (1951) and Skempton (1951) who attempted to solve deep bearing capacity problems using spherical expansion theory. Ladanyi (1963) continued to use spherical cavity expansion in bearing capacity problems, and showed that the strain field around an expanding cavity is independent of soil properties but is uniquely determined by the geometry of the problem. A more general solution of the cavity expansion problem in a Mohr-Coulomb material was presented by Vesic (1972), who calculated the ultimate cavity pressure and excess pore water pressures for spherical and cylindrical cavities.

More advanced soil models were subsequently applied to cavity problems to give better estimates of the stress conditions surrounding penetrometers. Carter *et al.* (1979) and Randolph *et al.* (1979) conducted similar analyses to determine the stress and pore pressure changes in saturated clay due to a cylindrical cavity expansion, and suggested that the solutions were relevant to the problem of pile installation. Carter *et al.* (1979) used two soil models, an ideal elastic-plastic one, and the Modified Cam-clay which is a work-hardening model. It was concluded that the dissipation of pore pressure with time is relatively unaffected by the choice of soil model, although the predicted total stress changes were found to be highly dependent on the soil model.

Randolph *et al.* (1979) restricted their study to just one soil model, the Modified Cam-clay soil model, to estimate the effective and total stress changes during both expansion and subsequent consolidation of the soil around the pile. The effect of past history (OCR) on the soil behaviour during these processes was also investigated. The results indicated that the shaft capacity of a driven pile in a soil of given undrained strength is independent of OCR (although this has been contradicted in later studies). The effective stress distributions around a cylindrical cavity expansion found by Randolph *et al.* (1979) are

shown in Figure 2.1 for OCR values of 1 & 8. Appendix A provides a more detailed analysis of this research, where cylindrical cavity expansion solutions are presented with results for radial stresses around the shaft of a penetrometer predicted as part of this research.

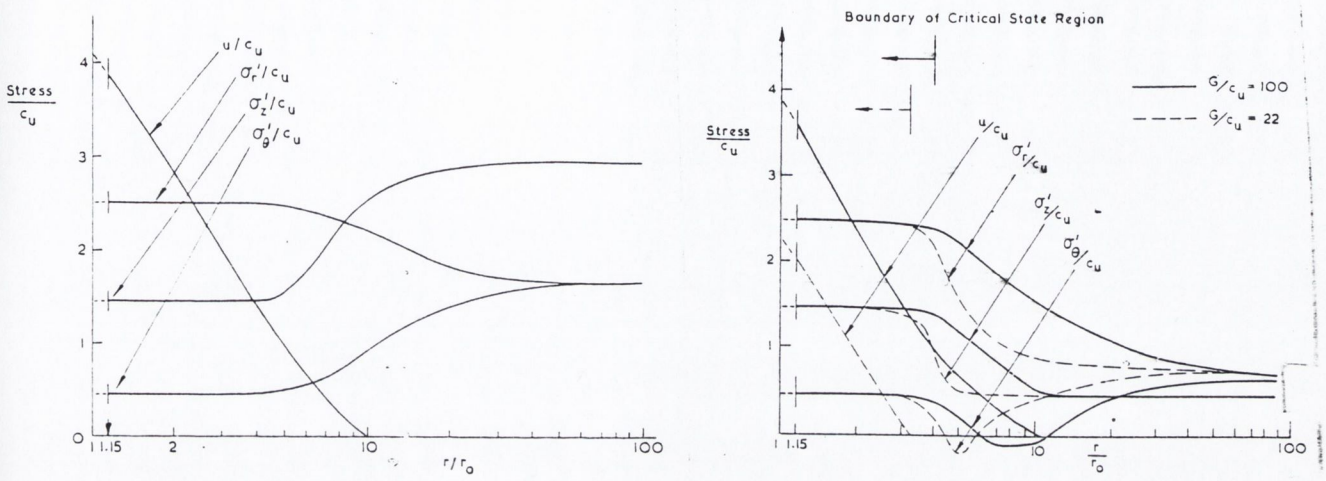

(a) (b)

Figure 2.1. Effective stresses at the end of pile installation for (a) OCR = 1 and (b) OCR = 8 (Randolph et al., 1979)

Collins & Stimpson (1994) described a cavity expansion procedure for hardening/softening soils, using the Modified Cam clay in both drained and undrained conditions, with the aim of providing a realistic and theoretically sound model on which to base analyses of the action of penetrometers and piles. The creation of a spherical cavity from a zero initial radius was considered by them to be the same as the deformation at the tip of a cone penetrometer. The solutions were obtained by numerical integration of systems of ordinary differential equations, thus avoiding the necessity for finite element procedures. The general equations were formulated in rate form so there are no small strain approximations (i.e., a large strain analysis was conducted). Some of the problems associated with modelling both normally consolidated and overconsolidated clays were highlighted. Collins & Yu (1996) extended this work for undrained cavity expansion with the original Cam-clay and the Modified Cam-clay critical state models. Stress distributions were found for the plastic zone around a penetrometer shaft using cylindrical cavity expansion, these are shown in Figure 2.2 for OCR = 1 & 8. The effective stress values at the cavity boundary were found to differ for the two OCRs contrary to the findings of Randolph *et al.*

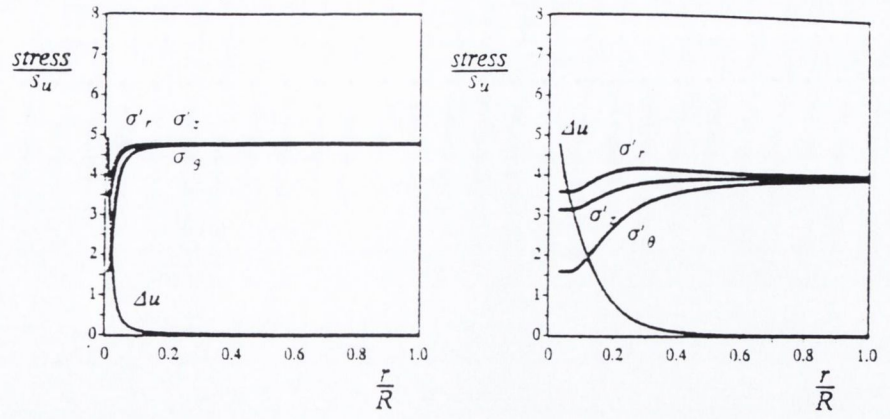

(a) Cylindrical Cavity in Original Cam-Clay (b) Cylindrical Cavity in Modified Cam-Clay

Stress distributions in the plastic region for OCR = 1.001

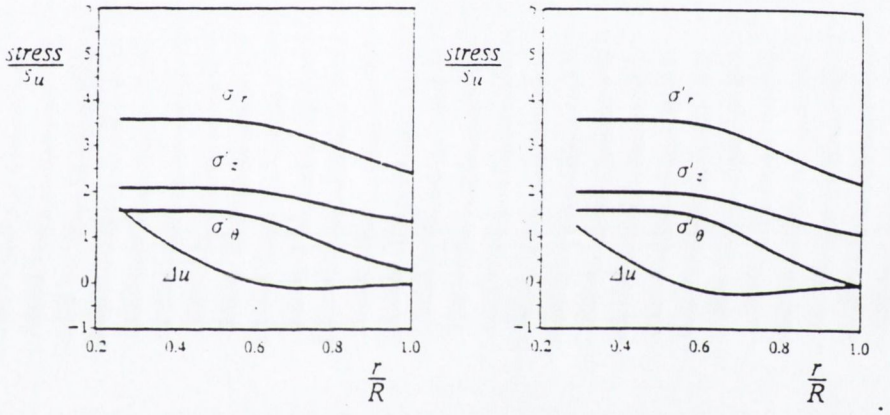

(a) Cylindrical Cavity in Original Cam-Clay (b) Cylindrical Cavity in Modified Cam-Clay

Stress distributions in the plastic region for OCR = 8

Figure 2.2. Effective stresses for cylindrical cavity expansion at OCR = 1 & 8 (Collins & Yu, 1996).

(1979) in Figure 2.1. Further sophistication has been added by the application of anisotropic soil models such as MIT-E3.

2.2.2.3 Summation of cavity expansion theory

The main developments in thirty years of cavity expansion theory use in soil mechanics has been the application of progressively more sophisticated soil models and, most recently, the application of large strain theory to overcome the problem of infinite straining at the

penetrometer boundary. Although the most recent of these studies still claims to have a role in improving the understanding of the mechanisms of pile driving and penetrometer testing, the limitations of the theory in this respect are widely recognised. These limitations are rooted in the physical modelling of the penetration process and the actual shape of penetrometer or pile. Cylindrical or spherical CEMs restrict the dependence of field variables (i.e., displacements, strains, stresses and pore pressures) to the radial co-ordinate only and cannot, therefore, incorporate the dependence of soil deformations on the vertical co-ordinate during vertical penetration. This over-simplification of the penetration problem to a one-dimensional analysis means that the complicated strain paths followed by soil elements close to a penetrometer during installation cannot be reproduced by cavity expansion. Therefore, no matter how refined the soil models applied to cavity expansion become, an accurate description of the stress states around piles or penetrometers will not be obtained.

Baligh (1986) stated that spherical cavity solutions are nowhere applicable during pile penetration and should therefore be abandoned as a tool for estimating penetration effects. In regard to the use of cylindrical cavity expansion solutions to analyse soil conditions around penetrometer shafts, Baligh considered this be ill advised and unnecessary in view of the availability of simple pile solutions (see Section 2.2.3.3).

These observations on cavity expansion solutions have been confirmed by the findings of Silvestri *et al.* (1997) who conducted cone penetration and indentation tests in clay to determine a relationship between the point resistance, the apex angle of the cone, and the undrained shear strength. For all cone angles the results for cone factors N_k were found to agree with Baligh's (1975) penetration theory. The experimental value of N_k was 16 for the 60° cone and spherical cavity expansion predictions of N_k were found to be approximately 3 times lower ($5.8 \leq N_k \geq 8.6$). Spherical cavity expansion was therefore considered by Silvestri *et al.* (1997) not to adequately represent cone penetration phenomena in any way.

2.2.2.4 Application of cylindrical cavity expansion in this research

Despite the limitations of Cavity Expansion Methods, the technique has been used in this Thesis to help give an insight into the major influences on stresses in the soil around the shafts of penetrometers. The application of cylindrical cavity expansion theory is presented

in Appendix A. The material properties used in the analysis conducted were an elastic-perfectly plastic material and the Modified Cam-clay model. Stress results calculated from cylindrical cavity expansion are presented in Appendix A and these represent a preliminary investigation into the application of stress models to simple strain fields. The cylindrical cavity expansion model thus provides a bench mark for comparison with the stress findings from other methods, along penetrometer shafts. Its main advantages are its simplicity in application, and the availability of published solutions to the problem which allows verification of the calculated results.

2.2.3 The Strain Path Method

2.2.3.1 Outline

Typically in geotechnical problems the stresses in the ground can be related directly to the depth of overburden and the applied loads; (such as those involving retaining walls, slopes or shallow foundations). However, experimental observations of deep penetration problems (Vesic, 1963; Szechy, 1968) indicate that soil deformations due to the penetration of piles and penetrometers are similar even though the properties of the soils may be very different. Baligh & Scott (1975) conducted undrained penetration tests with different shaped wedges in a saturated modelling clay (see Figure 2.3), and also observed the soil deformation patterns to be insensitive to material properties. This led Baligh & Scott (1975) to hypothesise that, due to the severe kinematic restraints associated with pile installation, soil deformations and strains are essentially independent of the shearing resistance of the soil and can be estimated with reasonable accuracy without the need to consider the soil's constitutive relations. This in turn led to the development of a new approximate method of analysis which was called the Strain Path Method (SPM).

The Strain Path Method, developed by Baligh (1985) at MIT, was designed to achieve a better understanding of the mechanisms governing the installation of rigid objects at depth and hence to predict the behaviour of "deep" foundations. This includes the deep penetration of axisymmetric rigid bodies such as piles, cone penetrometers and samplers in saturated clays. The SPM assumes that, during undrained penetration, the relative position of soil particles to a penetrometer are the same as the streamlines followed by an inviscid incompressible fluid as it flows around a fixed penetrometer. By representing the soil as an

ideal inviscid fluid any soil deformation is assumed independent of its shearing characteristics, and therefore the problem is essentially strain controlled.

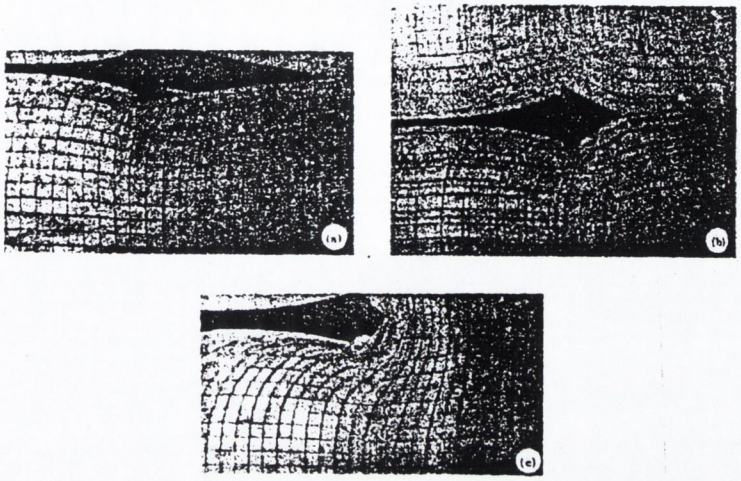

Figure 2.3. Deformation patterns in steady-state testing of wedges in modelling clay: apex angle 2θ = (a) 20°; (b) 60°; (c) 90° (Baligh & Scott, 1975)

2.2.3.2 Application of the Strain Path Method (SPM)

The steady state nature of penetrometer installation is central to the problem being modelled as one involving steady flow, i.e., for an observer moving with the penetrometer in a homogeneous soil, the deformation pattern in the soil does not vary with time. Accordingly, by changing the reference co-ordinate system, the penetration process can be modelled by a steady flow of soil past a stationary penetrometer. With respect to this reference system, the paths of the soil particles can then be defined by the streamlines followed by the fluid. Baligh (1985) predicted the paths of such streamlines using potential fluid flow theory and modelled penetrometer geometries through a combination of sources and sinks in a uniform flow.

The simplest case, and the first penetrometer shape analysed using the SPM, was referred to by Baligh (1985) as the 'simple pile', and is discussed in detail in Section 2.2.3.3. The configuration of this pile and its associated deformation (shown in Figure 2.4) pattern was generated by introducing a single spherical source which discharges an incompressible material at a steady rate into a field of uniform velocity in the vertical (z) direction. This solution elucidated the strong two-dimensional nature of undrained penetrometer installation

in a succinct manner and succeeded in changing the course of research on driven piles and on the interpretation of Cone Penetration Test (CPT) data, e.g., see Whittle and Baligh (1988). More complicated pile geometries have been analysed (e.g., 18° & 60° cones and sampling tubes) by adding further sources and sinks at the appropriate locations.

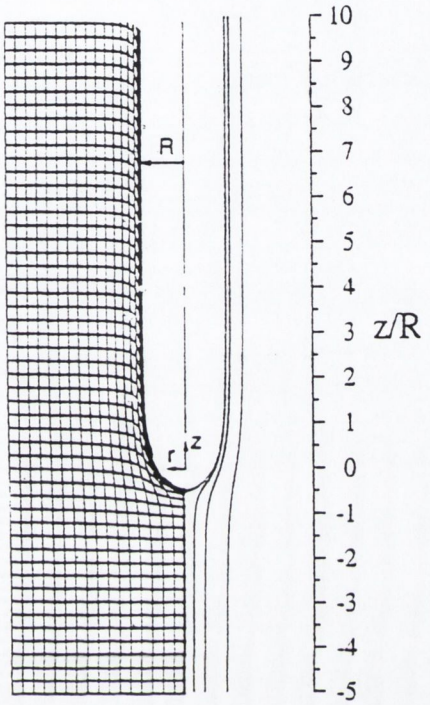

Figure 2.4. Predicted deformation and streamline patterns around a 'simple pile' (Baligh 1985)

A complete solution to the deep penetration problem consists of the determination of the states of stress and strain in the soil. The principal steps followed in the SPM procedure for undrained total stress analysis are as follows:

1. Estimate the initial total stresses and, if necessary, the hydrostatic pore pressures.
2. Generate the streamline pattern and calculate the soil velocities.
3. Differentiate the soil velocities with respect to the spatial co-ordinates to obtain strain rates and integrate the velocities with respect to time to obtain soil deformations.
4. Integrate the strain rates *along* streamlines to determine the strain histories for individual soil elements around the pile.
5. Estimate the effective stress fields from the strain histories (paths) using a generalised effective stress model to characterise the constitutive behaviour of the soil.

6. Calculate the pore pressures from either the vertical or radial equilibrium equation. It is generally found that when one equation is satisfied, the stresses do not obey the other precisely. This discrepancy reflects the errors in the initial flow field, which was derived from potential theory.

This Thesis focuses on steps 2-4, which involve the calculation of the strains and displacements around the penetrometer (presented in detail in Chapter 3). The stress calculations in steps 4-5 are largely ignored since the difficulties in achieving equilibrium of the stress field is beyond the scope of this Thesis, which is limited to measuring and predicting more realistic deformation and strain fields.

The flow of an incompressible, inviscid fluid around a regular body of revolution is a well established procedure in potential theory, with extensive applications in fluid mechanics. Such problems are usually solved by superimposing a suitable distribution of sources and sinks in a uniform flow. The stream function formulation has proved to be particularly convenient since many complicated flow patterns can be obtained by superimposing the stream functions of the individual sources and sinks. In steady flow, this formulation has the added advantage that lines of constant stream function also represent particle paths.

Later work at MIT by Whittle & Baligh (1988) and Whittle (1991) focused on the application of stress models (such as MIT-E3) to the SPM solution and the subsequent correction of strains to satisfy equilibrium. This approach has also been adopted by Teh (1987) and is described in Section 2.2.3.5. Recent correspondence with Whittle (1999) has revealed that no further research into the SPM has been conducted since 1991 at MIT but that the current focus is the prediction of shallow displacements, stresses and pore pressures.

2.2.3.3 Simple pile solution

A clear picture of the process of pile installation, as predicted by the SPM is shown in Figure 2.5. This figure plots the variations of the vertical strain (E_1), the cavity expansion strain (E_2) and the simple shear strain (E_3) experienced by three soil elements (A, F, G) as each passes the pile tip during installation. The three 'E' strain invariants proposed by Baligh (1985) are defined by;

$$E_1 = \varepsilon_{zz} \qquad E_2 = \left(\varepsilon_{rr} - \varepsilon_{\theta\theta}\right)/\sqrt{3} \qquad E_3 = 2\,\varepsilon_{rz}/\sqrt{3} \tag{2.2}$$

where ε_{zz}, ε_{rr} & $\varepsilon_{\theta\theta}$ are the direct vertical, radial & circumferential strains and ε_{rz} is the complimentary shear strain in the *r-z* plane..

Several interesting features are apparent from the strain paths plotted in Figure 2.5:

(i) Each component of strain has a maximum when the soil element is at a different location relative to the pile tip; vertical strains are a maximum below the pile tip, whilst cavity strains reach a maximum near the shoulder of the pile tip.

(ii) The soil elements are not strained monotonically. Simple shear and vertical strains increase monotonically until the soil elements are at or close to the pile tip but with continued penetration, as the pile tip advances to deeper levels, the sign of the incremental strains reverse and can even reverse again after further penetration. Cavity expansion strains may also show strain reversal for piles with different tip geometries (e.g. 60° cone, Levadoux and Baligh 1980).

These predictions suggest that any method that does not incorporate the correct strain history of soil elements (e.g., the CEM which assumes that the soil elements experience a monotonic increase in cavity expansion strain only) will not evaluate non-linear effects adequately. It should be noted, however that the geometry of the 'simple pile' is one of the limitations of this solution as a model for penetrometer installation and is discussed in later in this and other chapters. A consequence of the flow analogy is that scale effects can be removed by normalising distances with respect to the pile radius (R). The stresses or displacements, for example, at a given normalised radial distance from the centreline (r/R) and height above the tip (z/R) are independent of pile radius.

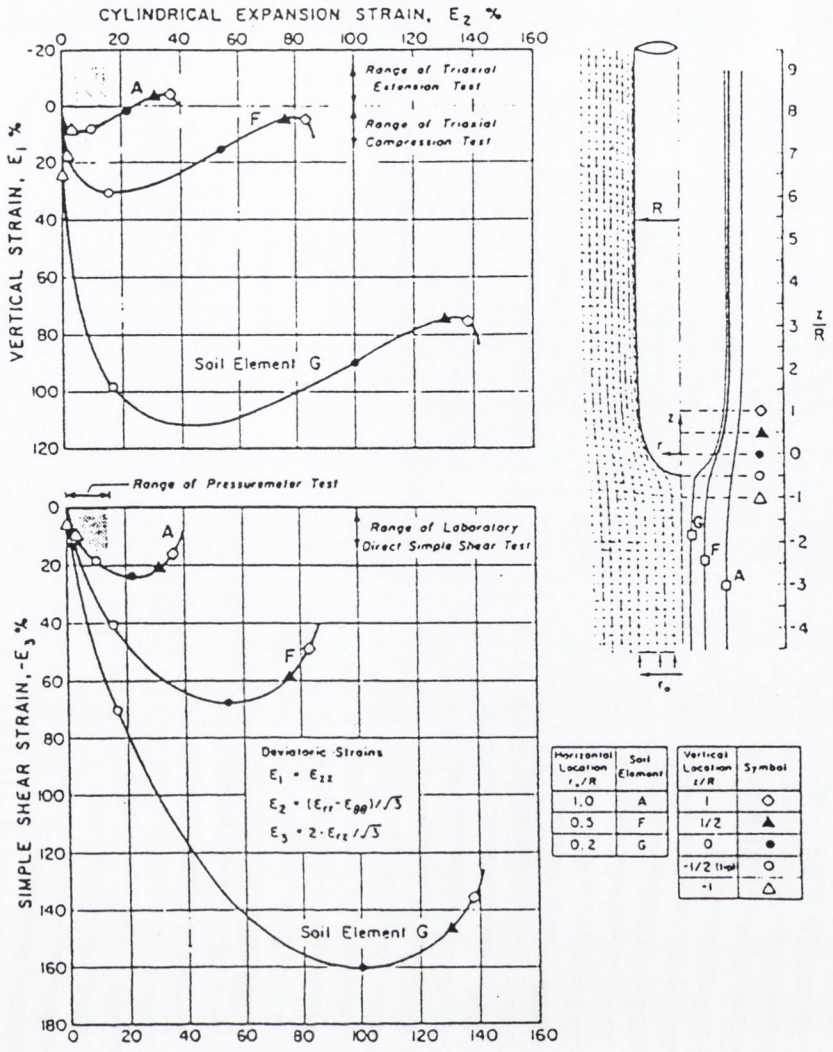

Figure 2.5. Strain Paths followed during penetration of a 'simple pile' (Baligh 1985)

2.2.3.4 Problems identified with the SPM

In the Strain Path Method the resistance of the soil to distortion is ignored in the calculations of the velocity field. Soil shear strength is, however, introduced in the calculation of stresses and this creates incompatibilities in the stress solution, particularly with regard to the shear stresses developed at the penetrometer shaft. This failure is reflected in the dependence of the stresses on the integration path; different stress fields are calculated from the radial and axial directions respectively. Another important drawback in these analyses (according to Kiousis *et al.*, 1988) is the incorrect use of small strain theory. For example, Baligh calculates the deformation field and finds strains in the order of 100 per cent by assuming linear geometric relations (small strains).

2.2.3.5 Alternative solutions using SPM theory

(i) Tumay *et al.* (1985)

Tumay *et al.* (1985) presented an alternative analytical solution for the calculation of flow fields around cones penetrating an inviscid and incompressible fluid. The approach allowed the true shape of cones to be modelled using an analytical technique, rather than the curved approximations using the Baligh (1985) method. In the solution by Tumay *et al.* (1985), stream function values, velocities and strain rates were evaluated and used to produce the velocity field and octahedral strain rates around 18° and 60° cones. The stream function and selected velocity vectors for 18° and 60° cones within an inviscid, incompressible flow are shown in Figure 2.6, and the corresponding octahedral stain rate values are shown in Figure 2.7. It is assumed by Tumay *et al.* (1985) that these strain fields give a first approximation to the *in situ* strains during penetration of very soft cohesive soils.

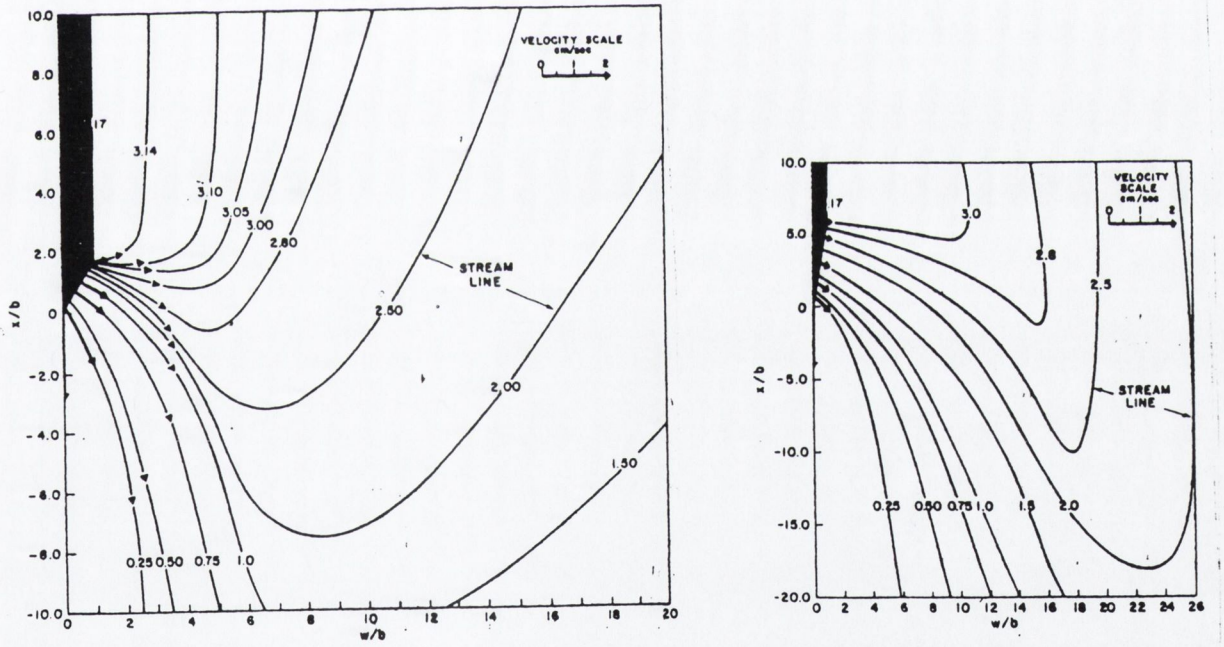

(a) 60° cone

(b) 18° cone

Figure 2.6. Flow fields around cones (Tumay *et al.*, 1985)

The solution to the problem was achieved using a complicated technique involving the conformal mapping of boundaries and transformation of the governing flow equations. It involves the use of mathematical techniques that are far from straight forward. In addition, strains are not readily derived from the strain rates as the specific paths of individual

streamlines are not followed. The difficulty in obtaining solutions readily explains why there have been no further approaches to the problem using this technique.

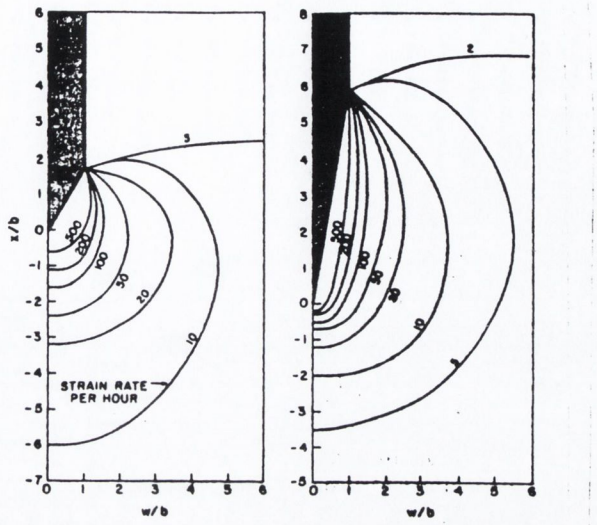

(a) 60° cone (b) 18° cone

Figure 2.7. Octahedral strain rates around cones (Tumay *et al.*, 1985)

(ii) Teh (1987)

Teh (1987) adopted an alternative numerical procedure to the potential theory approach of the original SPM and used a finite difference method to predict the velocity field of an inviscid fluid flowing around a penetrometer with a 60° conical tip. This approach allowed the actual shape of a cone penetrometer to be incorporated rather than the curved approximation initially produced by Baligh's (1985) potential theory approach. The procedures employed by both Baligh (1985) and Teh (1987) do not involve specification of a constraint to the flow tangential to the penetrometer boundary and their solutions approximate those of a smooth or lubricated boundary. The choice of an inviscid flow field was arbitrary since the computation method used by Teh (1987) is also capable of modelling viscous flows. Inviscid flow conditions were adopted to avoid further complications introduced by viscous flow modelling, the principal complication for a viscous flow solution was that it would require special treatment of the boundary layer and it was not clear how this should be interpreted for soil. Furthermore the viscous flow field is dependent on the Reynolds number, which introduces an additional arbitrary factor.

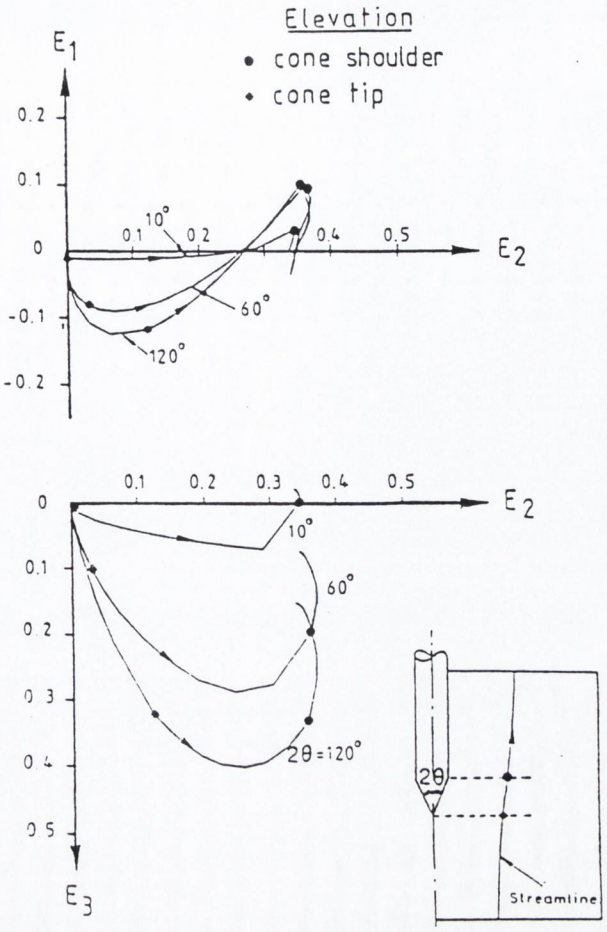

Figure 2.8. Strain paths due to penetrometers with different apex angles (Teh 1987)

The strain components were computed by integrating the strain rates along the line of flow (i.e., the streamlines) from a point sufficiently far 'upstream' of the cone tip. Strain paths produced by Teh (1987) for penetrometers with different angles within inviscid flow are shown in Figure 2.8 (the calculation procedure is presented in Chapter 3). These strain paths are for a soil element with an initial location of one radius ($r_0/R = 1$) from the penetrometer axis. A comparison of Teh's strain paths for three different cone types with Baligh's 'simple pile' solution in Figure 2.5 (path 'A' at $r_0/R = 1$) shows the large influence the penetrometer geometry can have on the soil straining. It also serves to highlight the limitations of the 'simple pile' as a general solution for all penetrometer types.

The strains calculated from the inviscid flow solution are used as an initial estimate for calculating the stresses during penetration (the initial estimate of strain contours for a 60° cone are shown in Figure 2.9, with compressive strains taken as negative). The soil was modelled as an elastic-perfectly plastic material obeying the von Mises yield criterion. The

initial estimate of stresses obtained from the Strain Path Method was found to give an inexact solution due to the idealisation of the soil behaviour. The approximate nature of the computation is revealed by the failure of the deviatoric stresses to satisfy the equilibrium equations. Teh (1987), therefore, attempted to modify the velocity field the in the regions of high uncertainty to find an improved solution. Three different numerical algorithms (the Newton-Raphson, pseudo-dynamic and finite element correction methods) were applied by Teh (1987) to derive an improved velocity estimate, although none of these was successful in completely eliminating the errors. The stress contours for a 60° cone shown in Figure 2.9 have been partially corrected for equilibrium imbalance by the iterative pseudo-dynamic scheme.

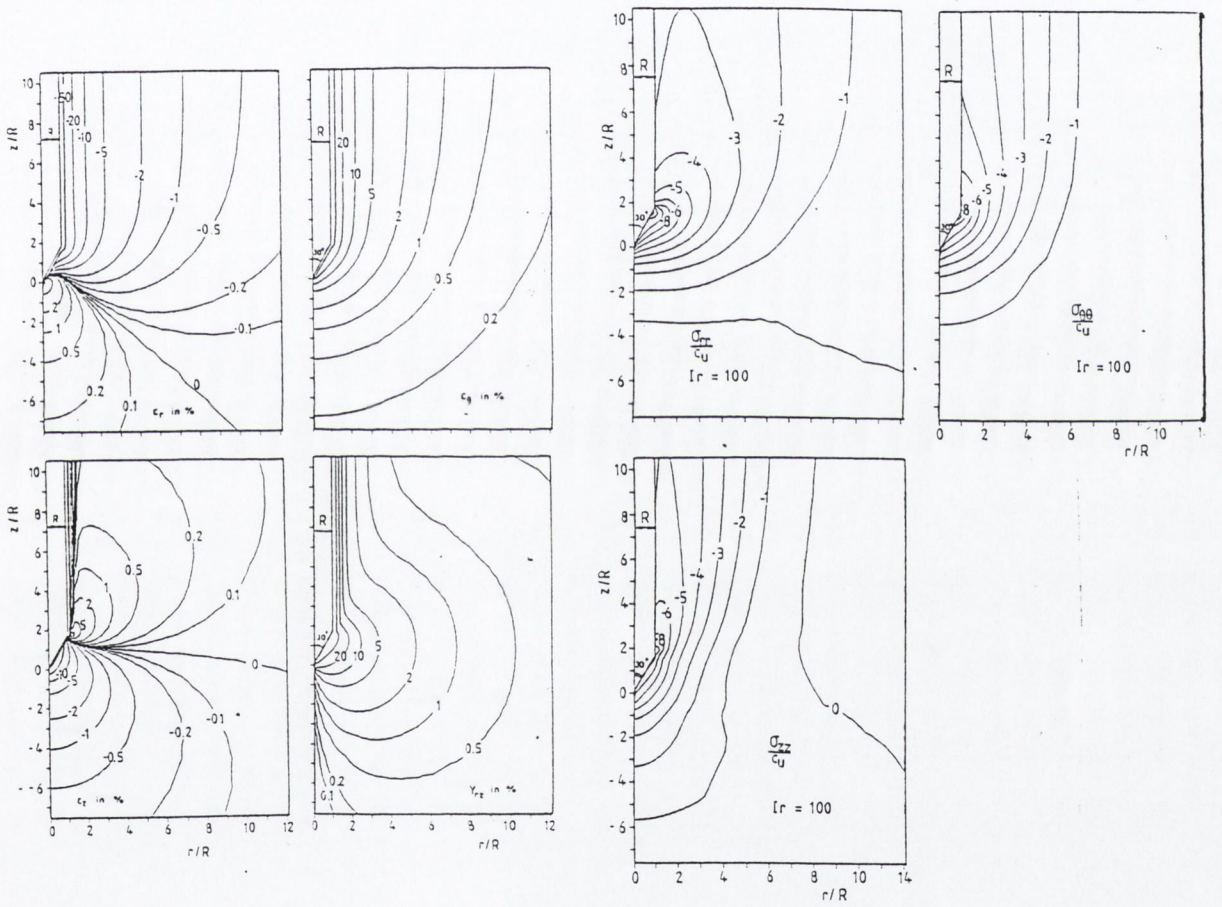

Figure 2.9. Stress and strain contours around a 60° cone penetrometer (Teh 1987)

One of the numerical approaches used by Teh (1987) to solve the inequilibrium problem was a large strain, Lagrangian finite element analysis. The method involves combining the merits of the SPM (which correctly accounts for steady state flow but results in an error in equilibrium) with the finite element method which satisfies equilibrium correctly. The

solution from the SPM is used as the initial stress condition, and the inequilibrium of this initial state is represented as a set of out of balance body forces which are eliminated by applying incrementally equal and opposite forces to give a new set of adjusted streamline paths which are in equilibrium. This correction procedure is carried out with the cone fixed. After the inequilibrium has been eliminated the cone is penetrated further until a steady load is reached. This is achieved by imposing vertical increments of displacement to the cone. It is because of the substantial displacement involved in this operation that a large strain formulation of the finite element method is required. According to Teh (1987) the finite element correction scheme did not in fact work. This was considered to be due, in the most part, to difficulties in the interpolation of stresses between the rectangular mesh used for the strain path analysis to the Gauss points in the triangular mesh used in finite element analysis.

The finite element method used is compared by Teh & Houlsby (1991) with the methods used by de Borst & Vemeer (1984) and Kiousis *et al.* (1988). In these other approaches the penetrometer is effectively inserted in a pre-bored hole, with the surrounding soil still in its *in situ* stress state, before an incremental plastic collapse calculation is carried out. Teh & Houlsby (1991) consider this interpretation not to be entirely correct since during the real penetration of a penetrometer, very high lateral and vertical stresses develop adjacent to the shaft, which are underestimated if the analysis simulates penetration into a pre-bored hole. Therefore, a careful distinction is necessary between a plastic collapse solution and steady state penetration. The steady state penetration technique was used to find theoretical values of the cone factor N_k for the 60° cone. The material properties applied to the soil were elastic-perfectly plastic, and the cone factor was found to depend on; the rigidity index, the horizontal stress and the roughness of the penetrometer.

(iii) Clayton *et al.* (1998)

Clayton *et al.* (1998) examined the use of the SPM for the assessment of tube sampling disturbance. The method was implemented via a finite-element approach to determine the influence of area ratio, cutting edge angles and inside clearance on sample disturbance which was assessed on the basis of strains imposed on the centre-line of a soil sample. The validity of the finite element technique was established by bench-marking its results

against those reported by Baligh (1985) and additional analytical solutions by Clayton *et al.* (1998) based on Bessel function solutions to the strain path problem of a sampler.

The numerical analyses for predicting flow velocities were performed using a general-purpose engineering package (LUSAS) which incorporates steady and transient analysis. Axisymmetric solutions for different sampler end conditions were conducted with an inviscid fluid. Friction on the impermeable sample boundary was neglected. Clayton *et al.* (1998), therefore maintained the assumptions the SPM that the soil shear strength can be ignored and that no tangential stresses develop on the sampler boundary. The output from the finite-element program consisted of a value of flow velocity at each node in the mesh. The stream function and strain values were then calculated from the nodal velocities.

The stream function values were found by calculating the flow between adjacent nodes and adding this to the value of stream function (ψ) of the previous node (the value of ψ at all the nodes on the centreline of the sampler was assumed to be zero). Streamlines could then be interpolated from the nodal values. The radial strains along each streamline were estimated from its radial position relative to that on the bottom boundary, which was assumed to have zero radial (and vertical) strain. Axial strain (ε_a) was calculated assuming no volumetric strain, implying $\varepsilon_a = -2\varepsilon_r$. This is only valid at the centreline, although its effects appeared small at other points within the central half of the sampler (according to Clayton *et al.*, 1998).

An irrotational fluid flow can be characterised by its streamlines, which are tangential to the direction of flow at every point, and are normal to the equipotential lines. In the special case of continuous incompressible irrotational flow the Laplace equations apply, and a solution can be obtained in terms of either the stream function ψ in (2.2) or the potential function ϕ in (2.3):

$$\frac{\partial^2 \psi}{\partial x^2} + \frac{\partial^2 \psi}{\partial y^2} = 0 \tag{2.2}$$

and

$$\frac{\partial^2 \phi}{\partial x^2} + \frac{\partial^2 \phi}{\partial y^2} = 0 \tag{2.3}$$

The finite element method approximates the differential equation in (2.2) and can therefore be presumed to produce approximations to the correct solution for a given problem. The adequacy of a finite element solution was seen as a function of, amongst other things, the type and number of elements used. The relative merits of various meshes was judged in respect to the separation of the streamline touching the tip of the sample tube from the inside of the tube wall, and the severity of this error. It was found the error could be reduced to an acceptable value by;

a) increasing the number of elements used (to at least 2000),
b) using high-order nine-noded axisymmetric elements, with a quadratic variation of the potential function, Φ, within the element, that is capable of modelling curved boundaries,
c) refining the mesh in areas near the edges and bottom of the sampler,
d) fixing the far field boundary sufficiently far from the sampler so as not to interfere with the inside of the sampler tube.

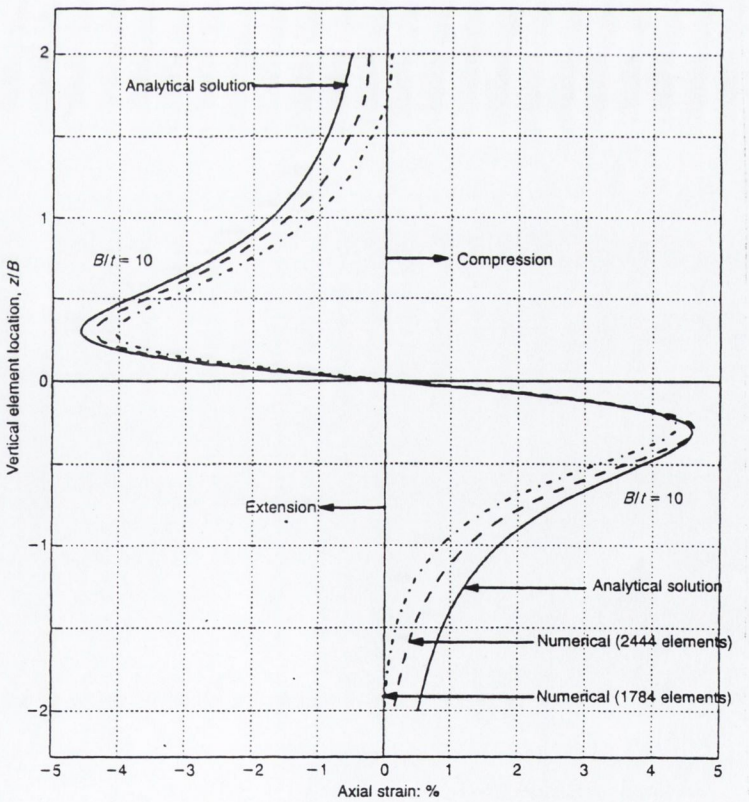

Figure 2.10. Comparison of axial strain history obtained from numerical and analytical analysis of the simple sampler (Clayton *et al.* 1998)

Further compensation was carried out by correcting the calculated velocities on the inside of the sampler tube to ensure that the streamline touching the tip of the sample tube then followed the inside edge.

The ability of the finite element method to give satisfactory results was established by comparisons with the analytical results predicted by Baligh (1985) and Baligh *et al.* (1987). This is illustrated in Figure 2.10 by the comparison of analytical with the FE results for different mesh densities. Examination of different sampler end conditions such as flat-ended and more realistic geometries showed considerable differences in the strain experienced by samples. According to Clayton *et al.* (1998) these results reinforce the view that penetrometer geometry has a large influence on the straining in the soil that occurs during installation, contrary to the conclusions of Baligh (1985) who stated there was 'no significant effect'.

2.2.4 Finite Element Methods

2.2.4.1 General

In the past two decades there have been a variety of numerical techniques employed to solve problems involving large deformation or large strain and one of these has been finite elements. In principle, numerical techniques, such as the Finite Element Method (FEM) can be adapted to modelling penetrometer installation. Computation procedures are not however so developed that a solution can be provided that is directly useful in geotechnical practice (van Den Berg *et al.*, 1996). In finite element analysis, there have been four main approaches to deal with this type of problem, namely the Total Lagrangian (TL), Updated Lagrangian (UL), Eulerian (E) and Arbitrary Lagrangian-Eulerian (ALE) formulations.

The first attempts to solve this type of penetration problem were small-strain finite element analyses which started to emerge in the early 1980's (de Borst, 1982, and de Borst & Vermeer, 1984). These solutions used the Total Lagrangian formulation which is suitable for large rotations but only for small strains. The penetrometer was inserted in a pre-bored hole and a small-strain analysis was carried out for an undisturbed soil mass using a simple linear elastic-perfectly plastic material model. However, the large strains and deformations that are produced in the soil during penetrometer installation mean that the problem cannot

be solved by conventional small strain finite element techniques, for which the limit is typically 10% strain. Solving problems involving strains larger than this with finite elements requires the use of large strain theory.

Analysis of large strains is considerably more difficult than small strain analysis (Wroth & Houlsby, 1985). The first problem lies in the choice of the appropriate definition for stresses and strains. The Lagrangian approach is often preferred in the literature, mainly because it is well suited to problems of large strain elasticity. The Lagrangian approach considers a reference volume of material and describes its displacements and the changes in stresses and strains. In solid mechanics it is the Total Lagrangian (TL) and Updated Lagrangian (UL) descriptions that are more commonly used to deal with large displacements, rotations and strains (Hu & Randolph, 1998). The difference between the two approaches lies in the reference state for the body, which is taken at time zero (initial conditions) in the TL approach, while the current (updated) geometry is used in the UL approach. The UL formulation is more common, with the spatial position of the body updated with each deformation increment. A serious limitation of both Lagrangian approaches is the gross distortion of individual finite elements that accompanies large strain within the body. Also, additional terms such as second order corrections to the strain relationships to allow for rotation need to be added to the conventional small strain finite element equations.

Wroth & Houlsby (1985) suggested the Eulerian approach may be more convenient for soil since it does not require the definition of a natural reference state. This simplifies the equilibrium equations but it poses other difficulties with moving boundaries and stress history. In the Eulerian or spatial approach, attention is focused on the response within a fixed region of space as time passes and it describes the behaviour of the material moving through it. The method is well suited to the study of fluids and other homogeneous materials, particularly where there is no free boundary. However in solid mechanics it is more natural to adopt a Lagrangian approach, considering a given region of material, rather than a region of space which the material occupies momentarily. The Lagrangian approach allows simpler application of the governing equations of statics and dynamics, which refer directly to the solid matter, than the Eulerian approach, which must include complex material and stress derivatives. This can render the finite element equations highly non-linear (Hu & Randolph, 1998) and for this reason there has been less effort devoted to the

Eulerian formulations for solid mechanics. However, van den Berg *et al.* (1996) successfully demonstrated the potential of the approach in deep penetration problems.

In an attempt to overcome the limitations of the pure Lagrangian and Eulerian approaches an approach called the Arbitrary Lagrangian-Eulerian (ALE) has been developed. This has been applied by Hu & Randolph (1998) to large deformation problems in soil. The problem of element distortion can be avoided with this method by uncoupling the nodal point displacements and material displacements. The extent to which stress and material properties flow through the finite element mesh (Eulerian) or the mesh moves with the material (Lagrangian) may be varied arbitrarily.

2.2.4.2 The Lagrangian approach

As has been mentioned, there are two Lagrangian finite element techniques commonly used to deal with large displacements, rotations and strains; these are the Total Lagrangian (TL) and Updated Lagrangian (UL) techniques. The TL approach is suitable for large rotations and small strains, or where a complex stress-strain law for large strains is to be followed. In this system, the stress and strain are related to the initial configuration. The UL formulation, which is more common (Hu & Randolph, 1998), is a TL technique in which the reference configuration is the current configuration, but is held fixed while the equilibrium iterations are performed. It is also necessary to include second derivatives in the description of strains in order to account for finite rotations of the body.

Three applications of the updated Lagrangian approach to finite element modelling of the cone penetration probelem are presented here, that of Kiousis *et al.* (1988), Cividini & Gioda (1989) and Abu-Farsakh *et al.* (1998). These three studies bear similarities in their application of the Updated Lagrangian method to the cone penetrometer test, but each apply different soil models which greatly influences the predicted deformation behaviour. Importantly, in recognition of the complexity of the problem, none of the studies claim to have found a completely realistic solution.

(i) Kiousis *et al.* (1988)

The computational method developed by Kiousis *et al.* (1988) was based on an elasto-plastic large strain formulation. Material and geometric non-linearities were introduced

into the study to examine the deformation behaviour of the soil during cone penetration. The soil is modelled as an elasto-plastic material. The plasticity model used was the 'cap model', which consists of a fixed yield surface and a hardening yield cap. The soil is assumed to undergo undrained loading if it is strained with a rate greater than 2 per cent per hour. The strain rates are calculated assuming a penetration velocity of 2 cm/sec.

The analysis is based on the assumption that the penetrometer is infinitely stiff, and the interface friction between the soil and penetrometer is negligible. The latter assumption is one of the drawbacks in this analysis. The major 'flaw' in the analysis is that the penetrometer is assumed to start at a certain depth and penetration continues until a complete failure is achieved.

A uniform vertical movement of the boundary line of the cone tip simulates the penetration of the cone (heavy line in Figure 2.11a). During this movement the nodes are allowed to move freely along the penetrometer boundary as the rollers in Figure 2.11 indicate. During this process, the nodes close to the upper and lower ends of the cone tip eventually have to change boundary conditions. These are shown in the encircled regions 1 and 2 in Figure 2.11a, and the changes in boundary conditions at these points are examined here separately:

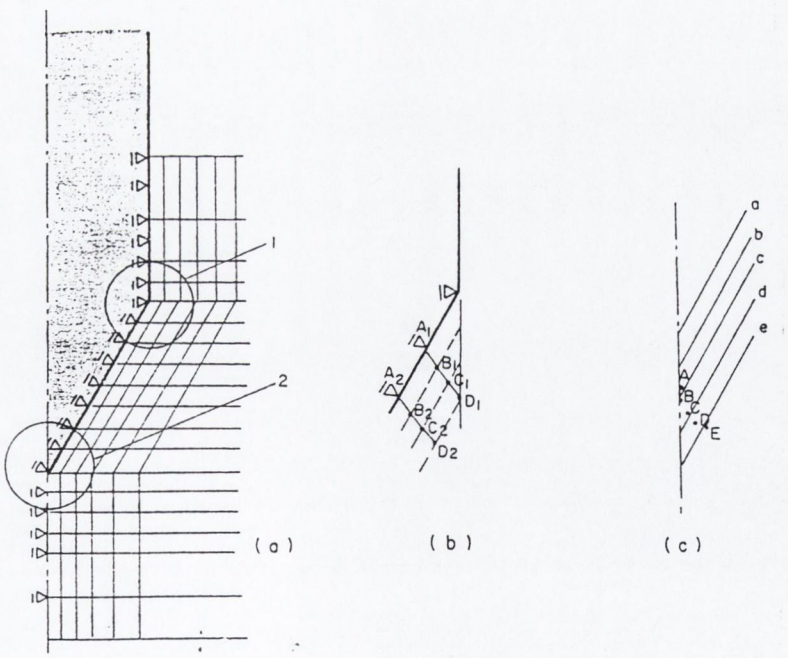

Figure 2.11. Detail of boundary conditions change of nodal points at the upper and lower ends of the cone (Kiousis 1988)

Cone shoulder: In Figure 2.11b the movement is traced of a node, A_1, initially positioned on the cone face of the moving penetrometer boundary as it moves to B_1-C_1-D_1. When in positions A_1, B_1 and C_1 the node is within the radius of the penetrometer shaft and is restricted to move along the cone tip boundary. At position D_1, the nodal point has reached the physical boundaries of the cone shaft. If the nodal point tends to move outwards all restrictions are removed and it is free to do so; a void in this region can therefore be formed. If it shows a tendency to move inwards, its movement is restricted along the cone shaft with the use of a vertical roller. The procedure is repeated for the next point.

Cone tip: In Figure 2.11c an analogous procedure is followed for nodes immediately below the lower end of the cone tip. Node A is originally restricted to move on the axis of symmetry. When the tensile forces cause fracture of the soil, the restriction is removed (positions A-D Figure 2.11c). Again, this can result in a void forming, this time ahead of the tip. As penetration continues, the node comes into contact with the cone surface and the node is restricted to slide along the surface of the cone.

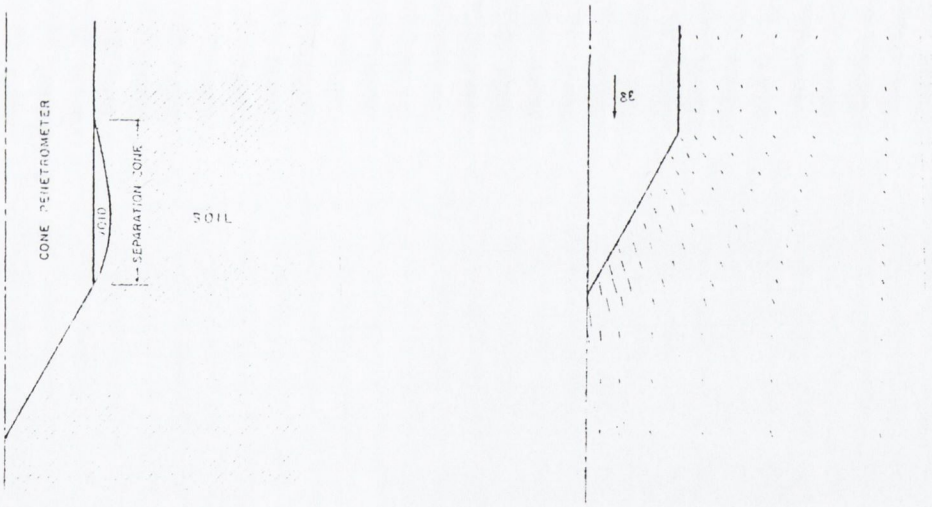

(a) (b)

Figure 2.12. (a) Separation of the soil-penetrometer interface: (b) Displacement field around the penetrometer (Kiousis 1988)

The displacement results from the analysis were clearly dominated by these imposed boundary conditions. In advance of the tip there was always a small void created by the ruptured material since in the analysis the axis of symmetry does not have to be occupied by soil material at all times. A second interesting point that is observed in the displacement

field is the separation of soil and the cone shaft interface for approximately 35 mm in the region just above the cone shoulder (Figure 2.12a). Kiousis *et al.* (1988) used this finding to explain the sharp decrease in pore pressures measured by pore pressure transducers located in this region. Voids of this nature have not, however, been observed experimentally. Displacements (shown in Figure 2.12b) are essentially vertical underneath the cone tip, and acquire more oblique angles at increased radial distance from the cone. At large radial distances from the cone surface, slight upward motion is observed.

Kiousis *et al.* (1988) also calculated the changes in octahedral shear strain around the penetrometer (see Figure 2.13) and found them to be very large in the region of the tip. Straining due to penetration was seen to extend to a considerable distance from the penetrometer, although failure was confined to a region 2-3 radii from the penetrometer shaft.

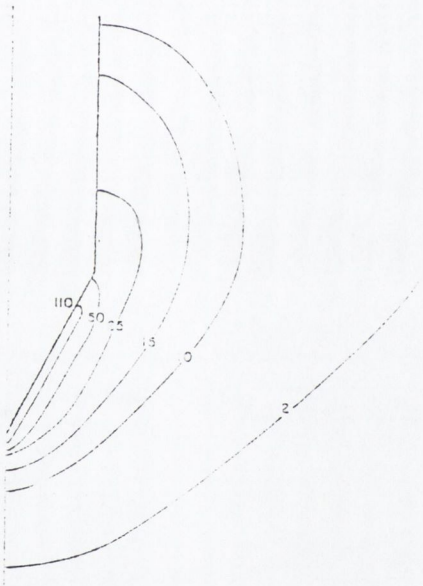

Figure 2.13. Octahedral shear strain contours around the penetrometer (Kiousis 1988)

(ii) Cividini & Gioda (1989)

Cividini & Gioda (1989) conducted a large strain finite element procedure to evaluate the stress and strain states induced in a soil deposit by pile installation. The main complexity of the problem was seen to lie in the non-linear mechanical behaviour of soils and in the changes to the geometry of the problem during the advancing process. An updated

Lagrangian approach was adopted and in the calculations an attempt was made to account for the non-linear behaviour of the soil and the pile soil interface.

The main difference between this and the other updated Lagrangian analyses is that the penetrometer is not introduced into a pre-bored hole, i.e., the ground/finite element mesh is initially in an undisturbed state. The penetrometer was represented by means of a rough, rigid "rail" consisting of a series of straight segments to which the soil is constrained by a means of rollers (Figure 2.14). Two cases for the penetrometer were modelled. In one the penetrometer is assumed to be perfectly smooth, and in the other the pile-soil adhesion was set to equal the soil cohesion. Shear interaction was taken into account between soil and penetrometer by applying tangential forces to each roller (T_{LIM} in Figure 2.14). A comparison between the mean normal stresses calculated using the finite element method and a cavity expansion approach was made. The cavity expansion approach was shown to overestimate the volumetric stress at the end of penetration.

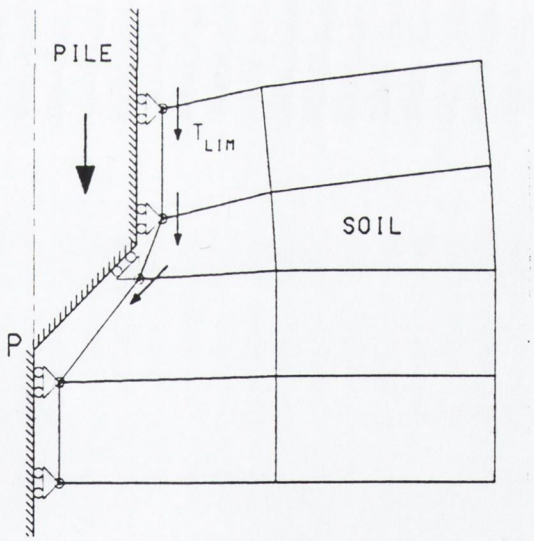

Figure 2.14. Finite Element scheme adopted by Cividini & Gioda (1989) in simulation of the advancing process

Results from the study by Cividini and Gioda (1989) are shown in Figure 2.15 for the limit cases of a perfectly smooth pile (Figure 2.15a) and for pile-soil interface cohesion equal to the cohesion of the soil (Figure 2.15b). They show the radial variation of the mean component of the normal stresses, σ_m and the second invariant of the deviatoric stresses J_2,

and both normalised by the soil cohesion, c. The curves a, b & c represent the stress distributions for the depths of penetration of $3r_p$, $6.5r_p$ & $10\ r_p$ respectively, where r_p is the pile radius. In general, the effect of introducing shear traction on the pile boundary is to increase the stresses calculated in the soil. However, Cividini and Gioda (1989) gave no description of the type of soil stress model used.

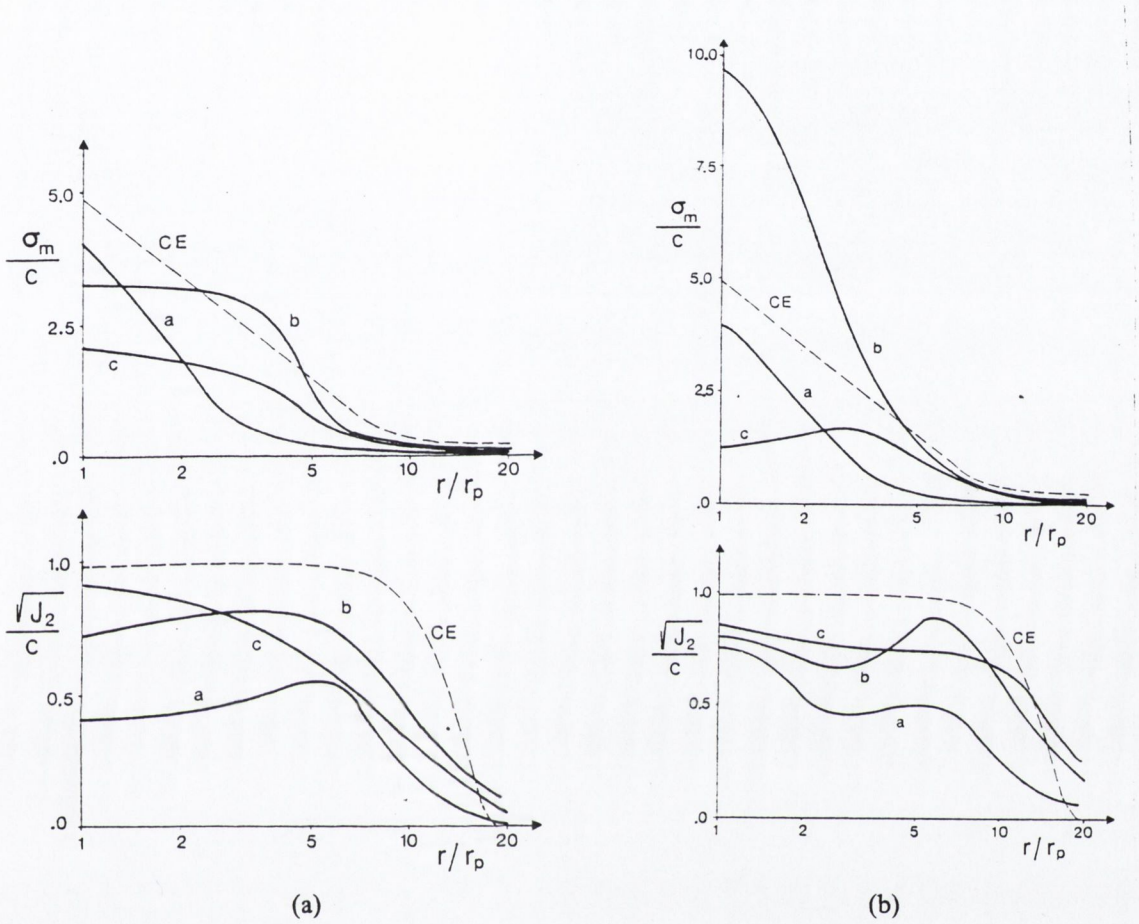

Figure 2.15. Stress distribution due to penetration assuming (a) a smooth pile (b) a soil-pile interface with adhesion equal to the cohesion of the soil (after Cividini & Gioda, 1989)

(iii) Abu-Farsakh *et al.* (1998)

Abu-Farsakh *et al.* (1998) used a finite element program to simulate the penetration of a piezocone in cohesive soils. The results from the numerical simulations were compared with miniature piezocone penetration tests conducted on cohesive soil specimens in a calibration chamber.

An Updated Lagrangian formulation was used with the Modified Cam-clay model adopted to describe the plastic behaviour of the clayey soil. The continuous penetration of the

piezocone was simulated by imposing an incremental vertical displacement to the cone tip boundaries. A Mohr-Coulomb approach was used to model the soil-piezocone interface friction. Two types of analyses were conducted, one with the soil-penetrometer interface friction taken into account, and one without. In these simulations the penetrometer is assumed to be initially pre-bored to a certain depth, which causes an error in the initial stresses, but avoids the computational difficulties that arise from large rotations of the elements when the penetration is process started from the top surface of the soil. The boundary conditions imposed on the element nodes as they slide past the cone allow voids to occur below the tip and past the cone shoulder (as shown in Figure 2.16). The formation of voids around the cone tip and shoulder is common to the updated Lagrangian analyses reported by Kiousis *et al.* (1988) and Cividini & Gioda (1989).

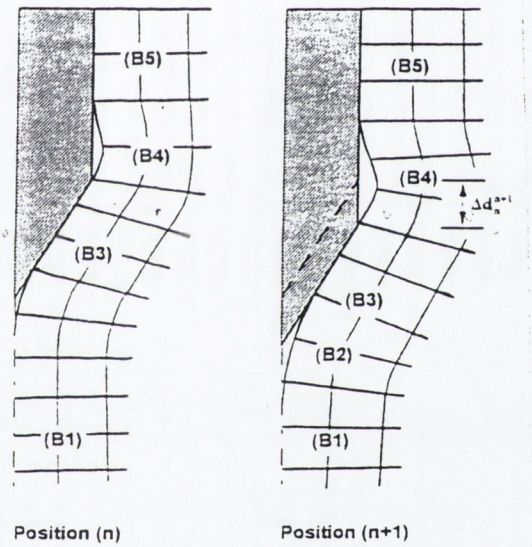

Figure 2.16. Incremental penetration of a cone penetrometer (Abu-Farsakh *et al.* 1998)

The cone tip resistance and excess pore pressures obtained numerically were found to reach a steady state condition at much smaller penetrations than was observed experimentally by Abu-Farsakh *et al.* (1998). The final values of excess pore water pressure obtained from the numerical model after the steady state condition is reached are about 10-15 per cent higher than those obtained experimentally. It was also found the dissipation predictions were quite close to the experimental values and to those obtained using the Strain Path Method by Levadoux & Baligh (1986).

2.2.4.3 The Eulerian approach

There has been only one application of the Eulerian finite element approach to solving penetrometer problems and this was by Van Den Berg *et al.* (1996). This approach was an extension of the updated Lagrangian approach, taking into account convection of deformation history dependent properties as well as material properties. The Eulerian framework avoids the problem of the conventional updated Lagrangian method which produces highly distorted elements by de-coupling the movement of the element nodes and the material points. This implies that the material can flow through the elements. This is achieved by the decoupling of nodal displacements and velocities and material displacements using what is termed the Arbitrary Lagrangian-Eulerian (ALE) formulation.

Modelling the penetration process

In the Eulerian approach to the penetration process the cone is modelled as a fixed boundary and the interface friction is taken into account between this boundary and the soil. The effect of the far field is incorporated by the insertion of spring elements at the outer boundary of the finite element model. The radial spring stiffness is determined using a cavity expansion approach. At the start of the analysis, the initial state of stress is defined by the soil weight and the lateral pressure ratio at rest. The cone is introduced into a pre-bored hole and the penetrative process is initiated by applying incremental material displacements at the lower boundary of the mesh. Material streams upwards through the mesh (as shown in Fig. 2.17) and the corresponding stress and strain fields around the cone are calculated. The calculation is stopped when a steady state is reached with respect to the strain and strain distribution in the complete finite element mesh. This type of analysis has no free surface and is therefore valid for deep penetration only.

Finite elements and the mesh

The application of the conventional eight noded quadrilateral elements with full (nine point) and reduced (four point) integration were found to give poor results and therefore simple four-noded elements were used. To account for the contact-frictional interface behaviour between the penetrometer and the soil, four noded interface elements are incorporated in the model. To obtain a smooth stress state around the corner point it was necessary for the shape of the cone to be rounded.

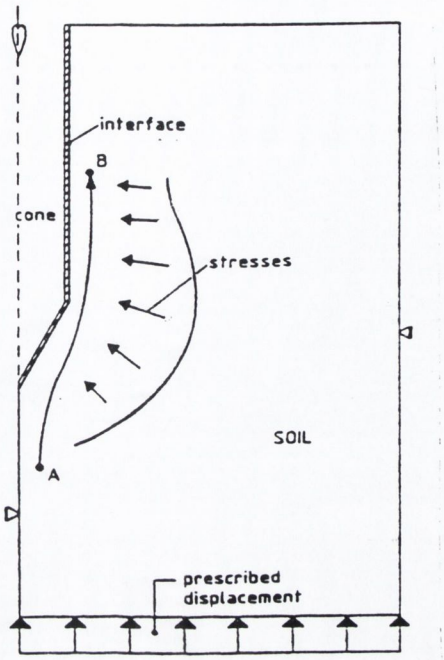

Figure 2.17. Schematic view of an Eulerian approach to the cone penetration problem (Van Den Berg *et al.*, 1996)

Modelling the shoulder of the cone

The cone shoulder dominates in the total reaction force of the penetrometer and this was demonstrated using the three different boundary conditions applied at cone shoulder (A, B & C). In these cases the soil is forced to move; A, in a vertical direction, C, in a direct line with the slope of the cone tip, and B, in an intermediate direction (Figure 2.18). Mesh refinement was shown to reduce the influence of the boundary condition, and this is evident in Figure 2.18 which shows the tip reaction force for different mesh refinements. These three boundary conditions have an influence on the effective radius of the cone, with case A effectively reducing the radius (by half an element width) and case C enlarging the radius (by half an element width).

Cone penetration was simulated in a layered soil by applying two sets of material properties, one to represent clay and the other with properties of sand. The strength of the sand was characterised by a non-associative Drucker-Prager criterion, and the undrained clay behaviour was modelled using a Von Mises criterion. The results suggest that a cone coming out of a sand layer senses a soft clay layer ahead, at a distance of about three times

the diameter of the cone. Simulation of cone penetration from a soft clay into sand showed that a penetrating distance into the sand layer of at least four times the cone diameter is needed to reach the new steady state resistance corresponding to that layer. The main purpose of the analysis by Van Den Berg *et al.* (1996) was the development of a finite element algorithm for layered soils and the demonstration of its applicability to soil models, and not the simulation of cone penetration or other *in situ* soil tests.

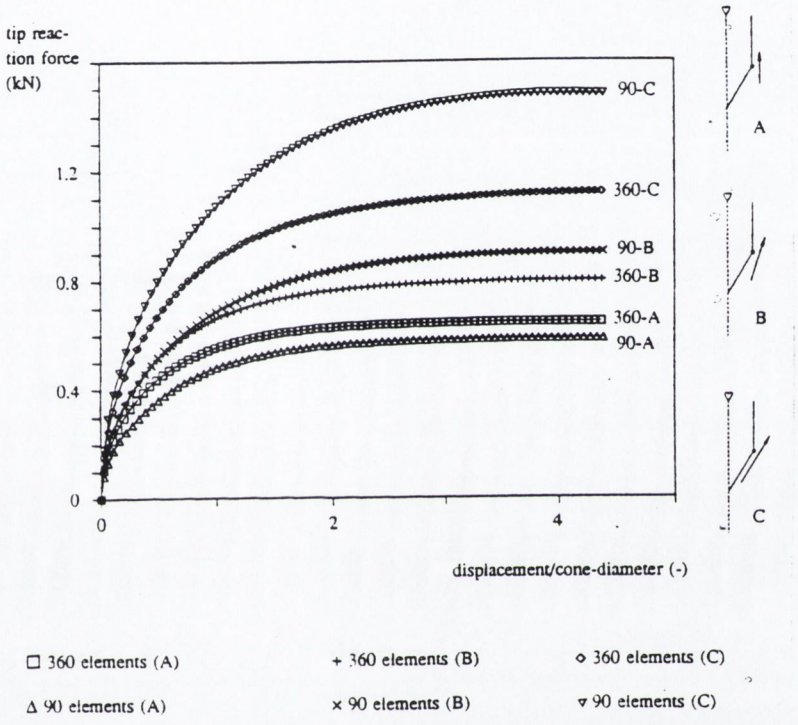

Figure 2.18. Influence of the boundary condition at the shoulder of the cone (Van Den Berg *et al.*, 1996)

2.2.4.4 The Arbitrary Lagrangian Eulerian approach

Hu & Randolph (1998) present an alternative approach to the Lagrangian or Eulerian methods for the numerical analysis of problems in solid mechanics which involve large strains or deformations, and is referred to as Arbitrary Lagrangian-Eulerian (ALE). The method comprises simple infinitesimal strain analysis (in increments) combined with regular updating of co-ordinates, remeshing of the domain and interpolation of material and stress parameters. The approach attempts to overcome the limitations of the pure Lagrangian and Eulerian formulations. The problem of element distortion is avoided by uncoupling of nodal point displacements and material displacements. The extent to which

stress and material properties 'stream' through the finite element mesh (Eulerian) or the mesh moves with the material (Lagrangian) may be varied arbitrarily.

The mesh generation and interpolation algorithms were implemented with the AFENA finite element package, which was developed at the Geotechnical Research Centre, University of Sydney. The solution procedure comprises;

a) mesh generation,
b) analysis of incremental displacements for a small number of steps,
c) mesh regeneration,
d) stress interpolation,
e) and analysis of the next set of incremental displacements.

The cycle (c)-(e) is repeated until the desired settlement (or penetration) is reached.

Application of the technique focused on the penetration of surface foundations into soft soil, which is modelled as a simple Tresca or Von Mises material. The method was illustrated with three surface penetration problems involving; a strip footing on the soil surface, a cavity expansion and a spudcan foundation penetrating significantly into the soil. The computed load-penetration responses were compared with calculations of bearing capacity based on plasticity approaches, and were shown to be within 10 percent for the strip footing problem and 20 percent for the spudcan solution.

This approach has the advantage of using well-established small strain finite element codes to solve soil mechanics problems that involve large strains and deformations (although the solutions presented by Hu & Randolph 1998 have been achieved by rather simple soil models). The application of the approach to a surface penetration problem is illustrated by Figure 2.19 which shows the penetration of a 'spudcan' at incremental stages. It is not, however, immediately apparent from the free surface solutions presented if the technique is directly applicable to deep penetration problems with their associated kinematic restraints. As has been discussed, the soil deformation in deep penetration problems tends to be dominated more by the imposed boundary conditions than the soil characteristics, which dominate in 'surface' problems.

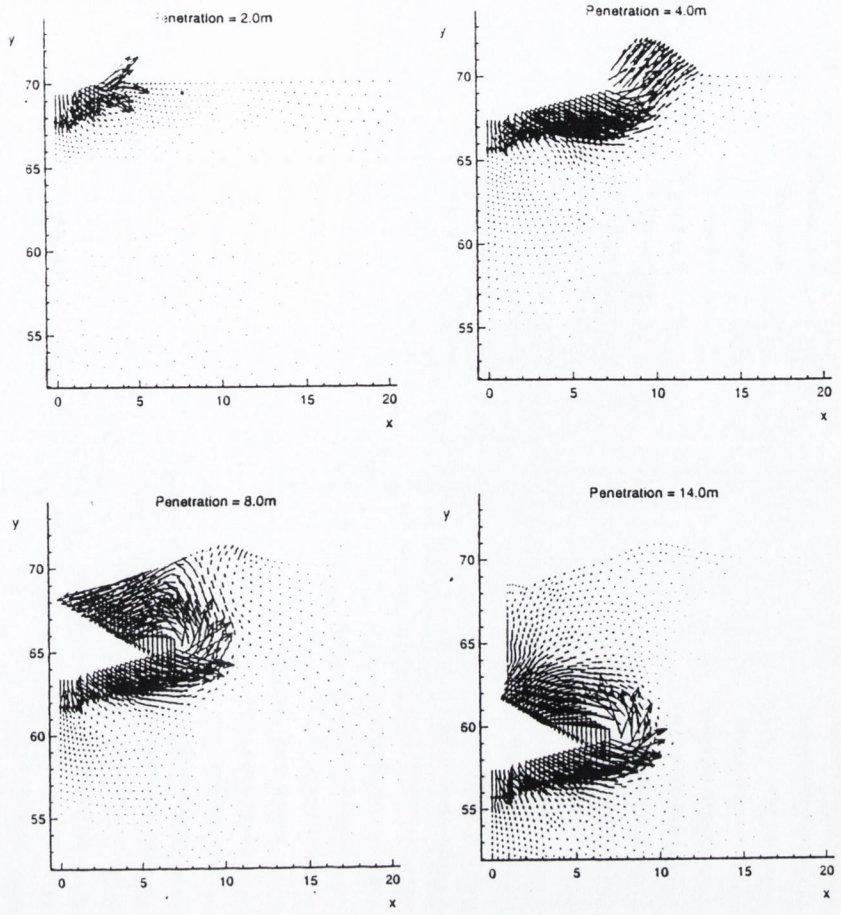

Figure 2.19. Incremental displacements at different stages of 'spudcan' penetration (Hu & Randolph, 1998)

2.3 A REVIEW OF EXPERIMENTAL MEASUREMENTS

2.3.1 Outline

The understanding of soil behaviour during penetrometer installation can be enhanced significantly by good quality experimental data. The accurate measurement of deformations within a soil mass has many difficulties not least of which is the need to ensure results have not been unduly affected by the recording methods. The ground movements due to penetrometer installation which are of relevance to this thesis are those measured for 'deep' penetration (typically for depths > 10 pile radii). Experimental observations of the displacement fields around penetrometers have been made in small scale model tests by Randolph *et al.* (1979), Francescon (1983) and Gue (1984), while a limited set of data from the field have been presented by Cooke & Price (1973) and Cooke *et al* (1979).

These measurement techniques fall into two main categories; those that are intrusive into the soil mass, and those that use external observation. The first category are typically field tests where instruments such as inclinometers and settlement plates have been inserted into the ground to record movements. Laboratory experiments typically adopt the second category where it is possible to create a soil sample with markers positioned within the mass which can be tracked by an external device, such as X-ray equipment or visual/photographic techniques.

2.3.2 Laboratory Tests

2.3.2.1 Radiographic techniques

A technique that has been used by a number of authors in laboratory tests to measure the deformations around model piles involves the use of X-rays, e.g., Levadoux and Baligh (1980), Steenfelt *et al.* (1981) and Francescon (1983). Difficulties associated with X-ray measurement of displacements within a soil mass have been identified by Levadoux and Baligh (1980) and include;

- the high resolution needed,
- the limited size of the clay sample that can be penetrated by regular X-ray machines for reasonable exposure time and sufficient image sharpness (~20 cm),
- the limitation in penetrometer size so as to avoid boundary effects,
- and the limited acceptable density of lead shot within the soil mass in order to avoid interference with clay deformations.

The method was shown by Levadoux and Baligh (1980) to be imprecise, even under ideal conditions involving uniform strain fields. In penetration experiments in clays, the use of X-rays is further complicated by the high deformation gradients encountered. Therefore, although available experimental measurements of soil deformations during penetration are valuable in evaluating predictions, Levadoux and Baligh (1980) they should not be used to estimate strain fields.

Francescon (1983) conducted laboratory tests on 18.9 mm diameter model penetrometers jacked into re-consolidated kaolin clay. A calibration chamber 250 mm in diameter and

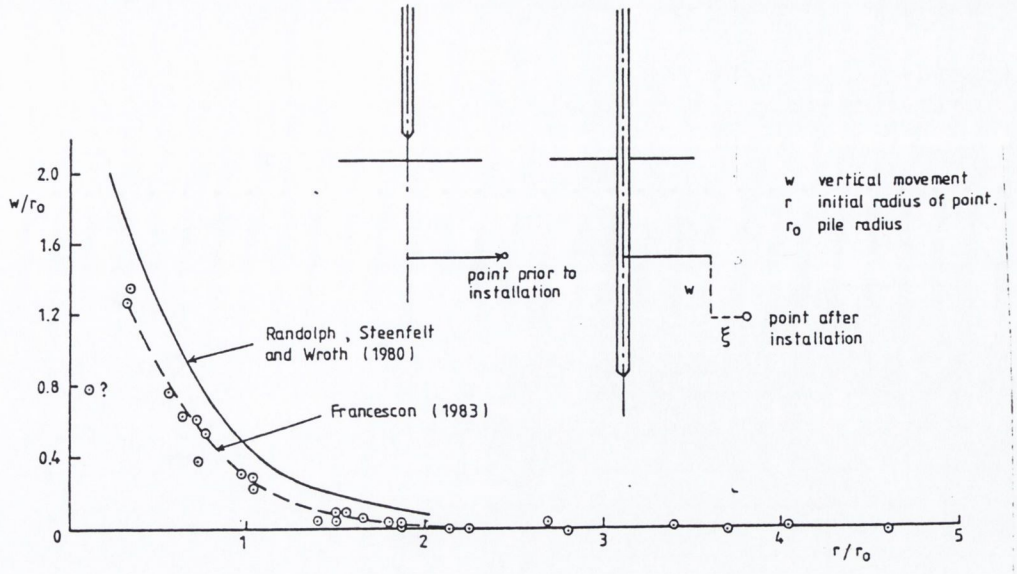

(a)

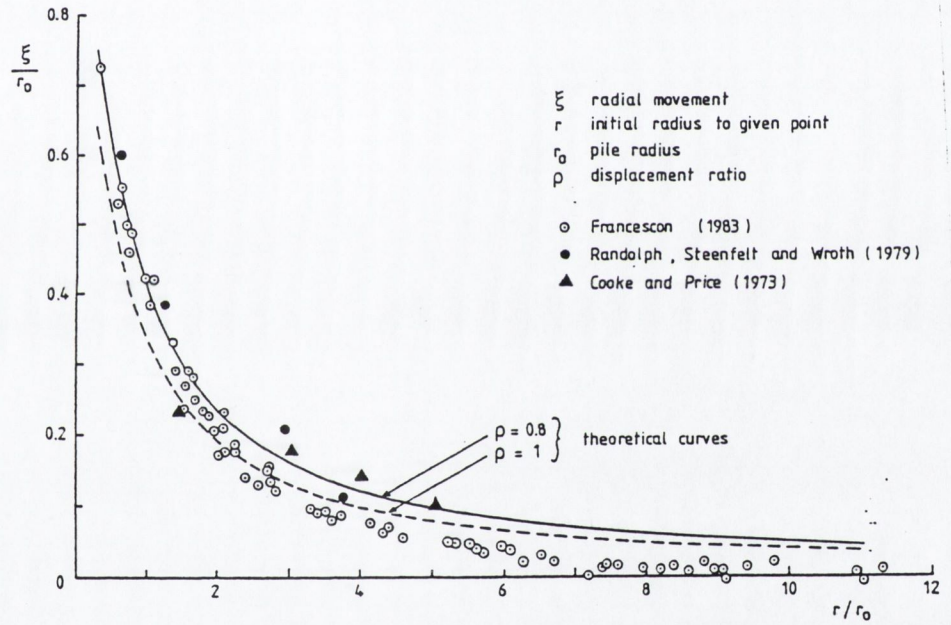

(b)

Figure 2.20. Ground movements caused by penetrometer installation: (a) Vertical soil movements; (b) Radial soil movements (after Bond 1989)

600 mm deep was used to contain the clay, i.e. 13 times larger than the penetrometer itself. The end geometry of the penetrometer consisted of a 45° cone cut off close to the apex to form a flat tip. The soil displacements in both vertical and radial directions were reported (Figure 2.20). These movements were determined using a radiographic (X-ray) technique, which tracked the movement of lead shot within the clay during penetrometer installation. The lead shot was positioned by means of thread strung across the test chamber prior to

introduction of the clay in a slurry form. The thread could then be removed at an early stage in the consolidation process. The lead shot had a diameter of 2 mm and was placed in four horizontal planes, each 50 mm apart in the vertical direction. The accuracy of displacement measurement was reported to be ±50 μm, i.e. a resolution of 0.005R. The maximum distance above the tip (z/R) at which the displacement measurements were made is not recorded but is considered to be greater than 10 radii.

2.3.2.2 Visual techniques

The use of visual techniques to monitor soil displacements have, until now, been restricted to measuring the movement of soil in direct contact with a transparent media (such as glass or perspex). Tests using photographic techniques are described in this section; these have been conducted in clay, sand and crushed glass.

(i) Model penetrometer tests in clay

Randolph, Steenfelt and Wroth (1979) presented the results of laboratory model tests in clay which observed the soil deformation patterns around closed ended piles during jacking. The studies were performed using a semi-cylindrical samples of clay prepared from Speswhite kaolin. The samples were one one-dimensionally consolidated in a cylinder before being cut in two. The flat vertical (cut) face of each specimen was marked with grid lines and placed against a lubricated perspex sheet. A semi-cylindrical pile was rapidly jacked into the clay flush with the perspex plate. Photographs were taken during pile installation and the radial movements of soil determined; these radial movements are shown on Figure 2.20.

Gue (1984) conducted a similar series of laboratory tests to that of Randolph, Steenfelt and Wroth (1979). In Gue's studies, model piles were jacked into a semi-cylindrical specimen of reconstituted kaolin clay with a perspex front face (Figure 2.21). The semi-cylindrical flat ended model pile, had a radius (R) of 8 mm, and the calibration chamber was 225 mm in radius (over 28 R). Lead shot, positioned on the face of the sample against the perspex, were used as soil markers and photographs taken before and after penetration allowed the vertical and radial movements of these markers to be measured. The marker movements were measured to a resolution of 0.1 mm, i.e., 0.0012 R. Radial movements (Figure 2.22) were

measured to a distance of 11 pile radii from the pile axis. The vertical movements (shown in Figure 2.23) were only measured to a radial distance of 5R from the pile centreline.

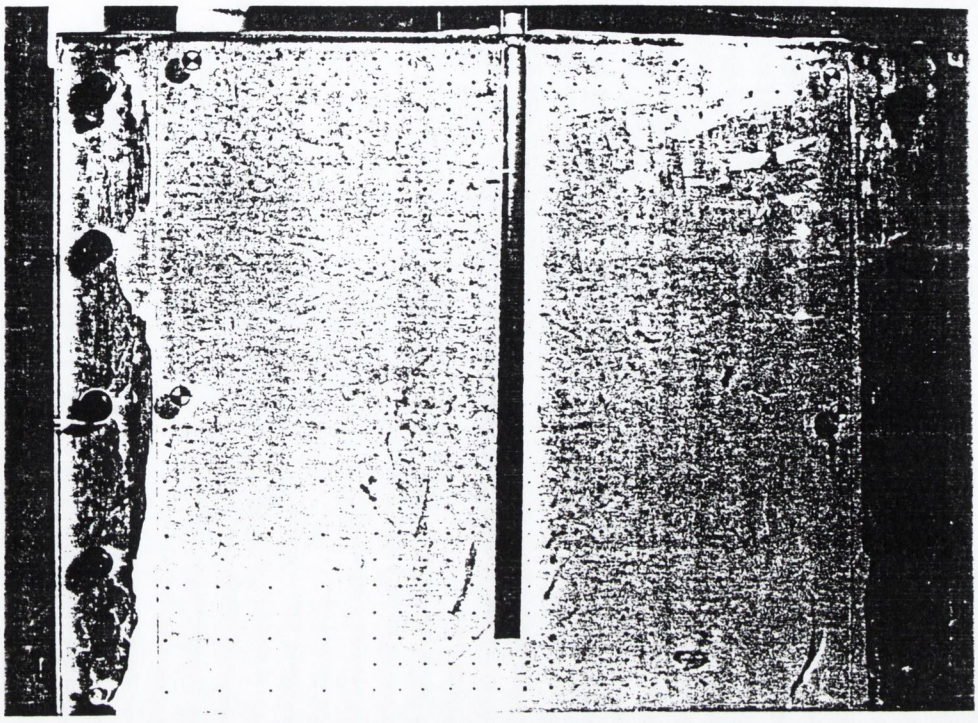

Figure 2.21. Photograph after driving a closed-ended pile (Gue, 1984)

The semi-cylindrical tests of Randolph *et al.* (1979) and Gue (1984) attempt to represent true 3-D behaviour by an axisymmetric representation of the penetrometer installation process with a perspex sheet on the plane of symmetry. The soil-perspex interface is lubricated in both studies to reduce the influence of this boundary on the soil movements. Gue (1984) described the results from these semi- cylindrical tests as 'qualitative'. A comparison study was, therefore, conducted with the 'quantitative' results obtained from full cylindrical specimens. The ground surface movements from both test types were found to have good agreement.

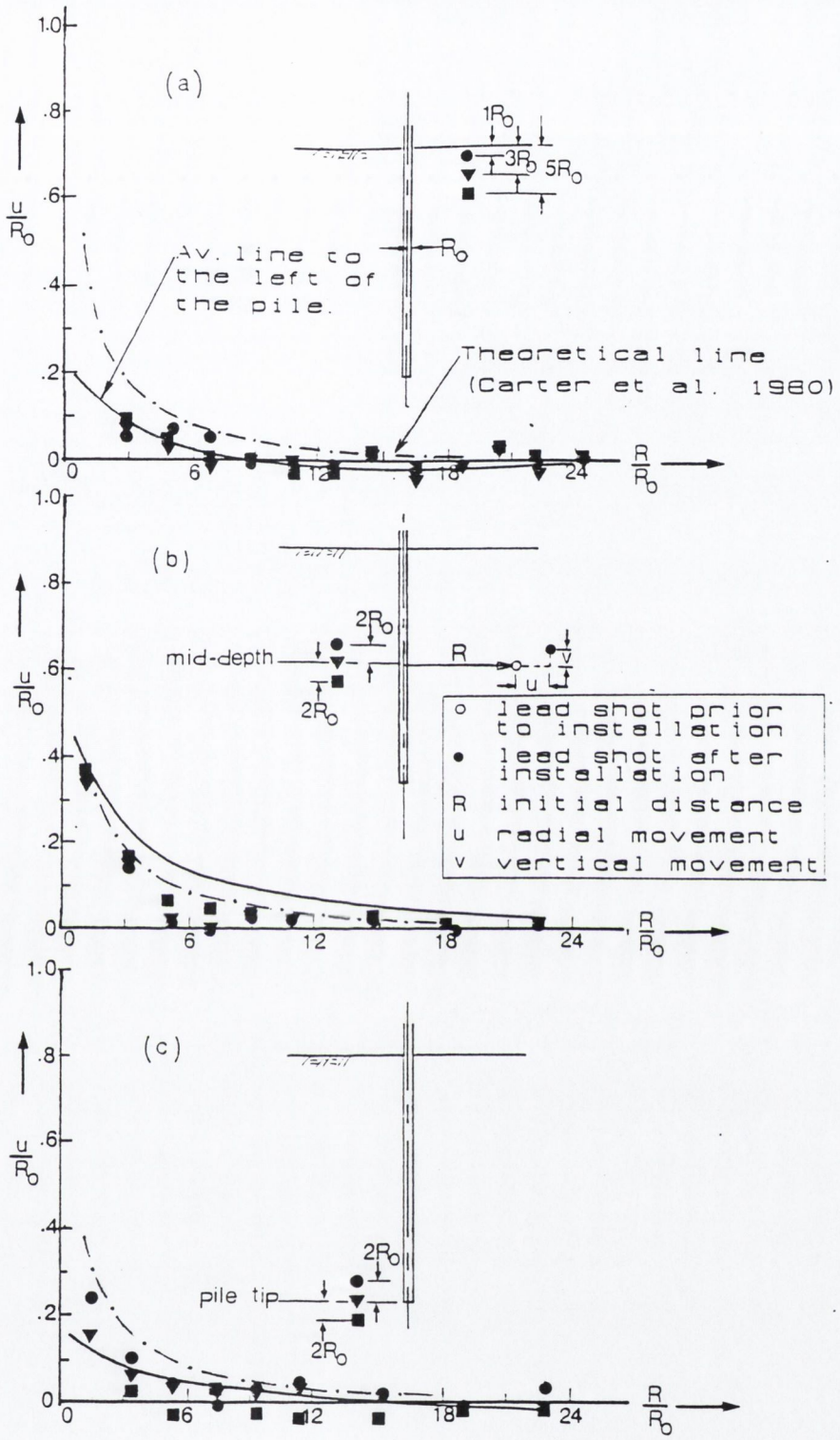

Figure 2.22. Radial soil movements from semi-cylindrical model pile tests (Gue 1984)

Another difficulty associated with this technique is the presence of voids between the vertical face of the sample and the perspex plate, and has been cited by Randolph *et al.* as the reason for no detectable ground heave being present in their results.

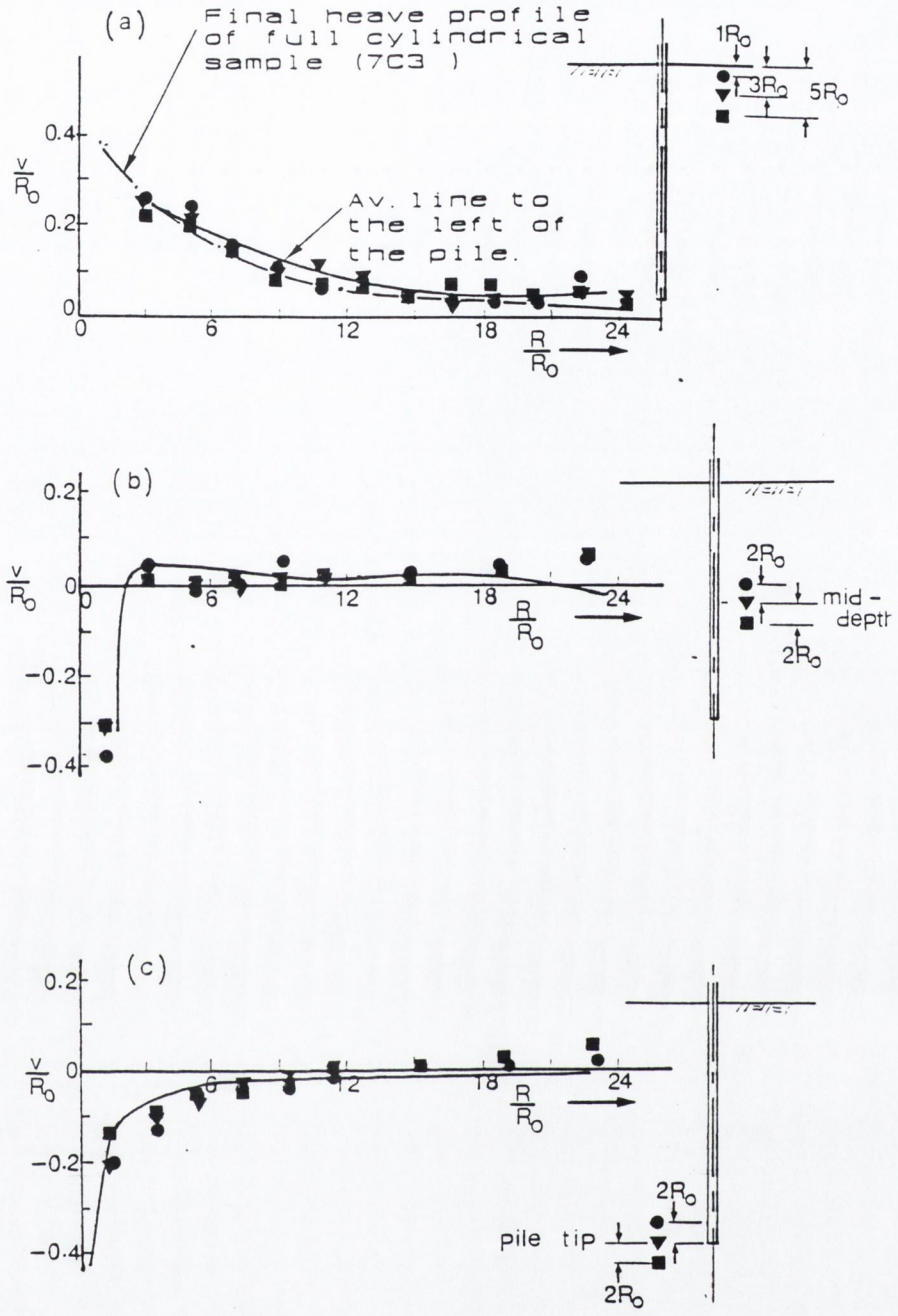

Figure 2.23. Vertical soil movements from semi-cylindrical model pile tests (Gue, 1984)

(iii) Model penetrometer tests in sand and crushed glass

A number of small scale laboratory tests have been conducted in materials such as sand and crushed glass. These tests are of more interest here for the experimental techniques used to measure deformation of the soil, rather than the results themselves.

Allersma (1988) conducted two dimensional penetrometer tests using a wedge shaped probe in a transparent granular material to determine the stress and displacement

distribution. The transparent granular material was made up of crushed glass and a fluid of a matched refractive index. The probe was pushed into the sample held between two sheets of glass 70 mm apart (shown in Figure 2.24a). The overall dimensions of the crushed glass sample were 70×600×600 mm, and the wedge shape aluminium probe had a rectangular section of 70×50 mm. This gave a far boundary distance of six shaft widths from the probe centreline. During testing, a vertical stress of approximately 5 kPa was applied on the free surface of the sample. The photo-elastic properties of crushed glass were used to determine the stress distribution around the penetrating wedge, as is shown in Figure 2.24b. A digital camera was used to determine the soil displacements by monitoring the movement of black markers distributed within the crushed glass.

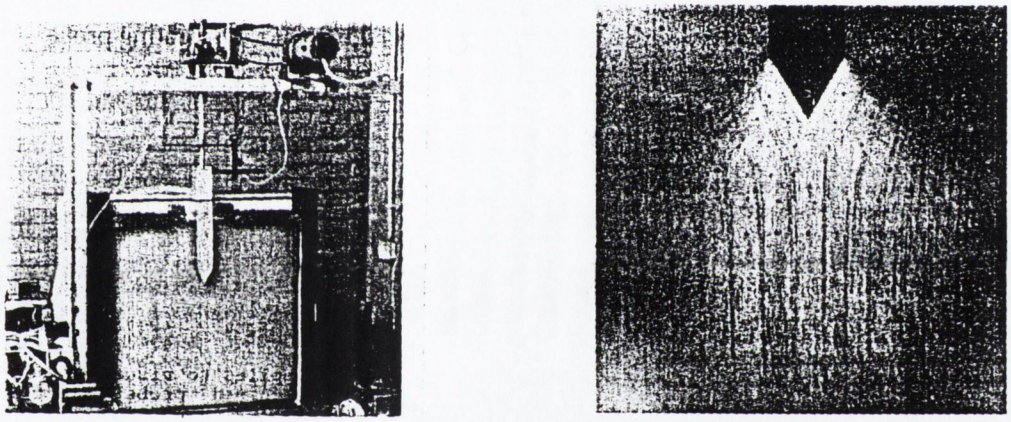

(a) (b)

Figure 2.24. 2-D model penetrometer test in crushed glass (Allersma 1988): (a) Test set-up; (b) stress distribution during penetration

The observations made by Allersma (1988) served to demonstrate the flowing nature of soil movement around the probe, and to highlight the differences between the movement of soil close to the penetrometer and the rest of the soil mass. Close to the tip and shaft of the probe, the soil movements are downward and horizontal in direction. However, upward motion was observed in the later stages of penetration after the tip has moved past that particular soil horizon and had moved deeper into the sample. Further away from the probe, at a distance of more than one shaft width, the soil markers showed only a sideways and upward motion.

Allersma's (1988) laboratory test was instructive but had a number of drawbacks including; (a) the test is fundamentally two dimensional in nature, (b) the effect of the glass panes is not accounted for and (c) the granular material is not truly transparent, but translucent.

The test is restricted to two dimensions by the translucent nature of the material since all the measured soil movements must be close to the front pane of glass. If the soil markers had been deeply imbedded within the material, as would be necessary for a three dimensional test, they would not have been visible.

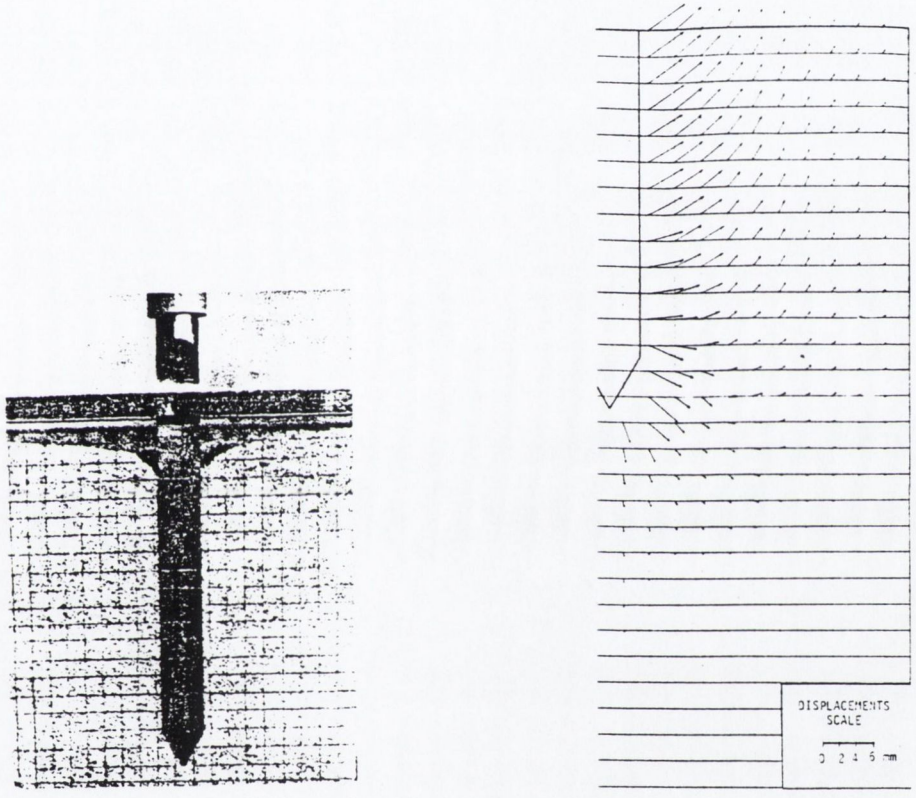

(a) (b)

Figure 2.25. Semi-cylindrical 60° cone tests in sand: (a) Probe penetrated into sand; (b) Displacement vectors for dense sand (Davidson & Boghrat, 1983)

Davidson & Boghrat (1983) conducted laboratory scale penetration tests with 60° cone and flat plate (dilatometer) shaped probes in sand (Figure 2.25). Testing was conducted in a container of dimensions 100×50×65 cm with a glass front panel (100×65 cm). Dummy test probes were manufactured from stainless steel and cut longitudinally in half. The test procedure consisted of pushing a probe, with a small hydraulic jack, into the sand with the flat, cut face against the glass. A stereo photographic technique (using two superimposed

images taken from different positions) on was used to accurately measure the displacements of sand grains at designated points in the viewed plane. As the probe penetrated the sand a series of eight photographs were taken from a rigidly fixed camera.

Volumetric and shear strains for a dense sand were calculated from the displacements using simple small strain theory and are shown on Figure 2.26. The photographic technique was claimed to be capable of measuring displacements to an accuracy of 0.005 mm, although the camera field of view for a resolution of this magnitude is not stated. A maximum error of 7 % was reported for the displacements was during penetration (no mention of the magnitude of the displacements was given). It is the view of the authors that the results should be regarded more qualitatively than quantitatively.

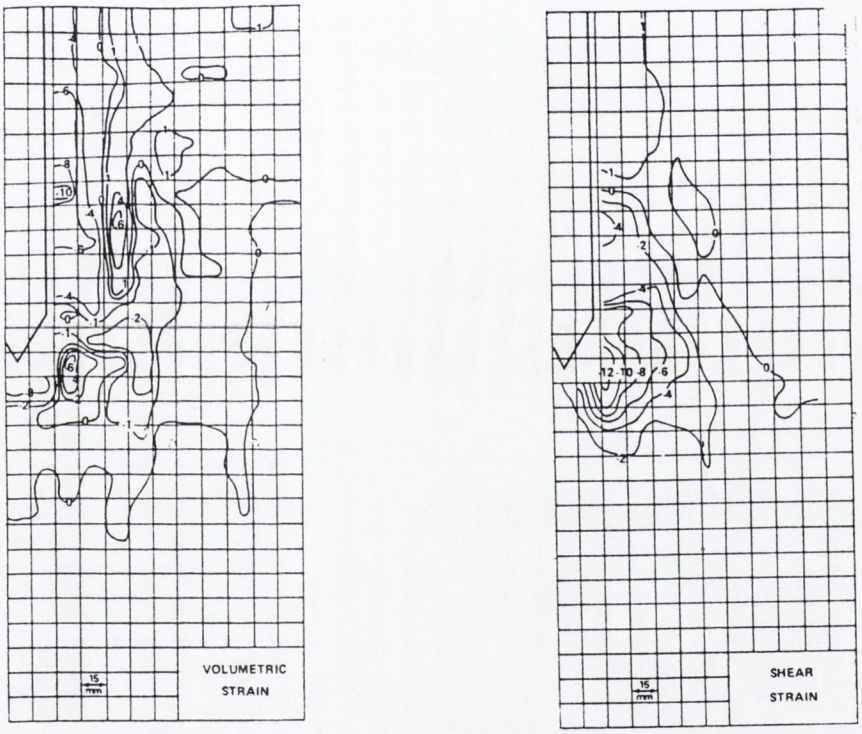

(a) (b)

Figure 2.26. Strain fields for a 60° cone test in dense sand: (a) Volumetric strains; (b) shear strains (Davidson & Boghrat, 1983)

2.3.3 Field Measurements

Cooke & Price (1973) and Cooke *et al.* (1979) conducted a series of field tests with instrumented tubular steel piles which were jacked into heavily overconsolidated London clay. The piles used in both investigations were 5m long and 84 mm in radius with a 60°

conical tip at the base. Vertical soil displacements were measured during installation using a series of settlement plates buried in the soil which gave a resolution of 0.0002 R. The radial movements measured by Cooke and Price (1973) using electrolytic level inclinometers immediately following installation are presented in Figure 2.20. The vertical movements were recorded by Cooke *et al.* (1979), also immediately following installation, at two depths beneath the ground, just below the surface at 0.5 m and at a mid-pile level of 2.2 m are shown in Figure 2.27.

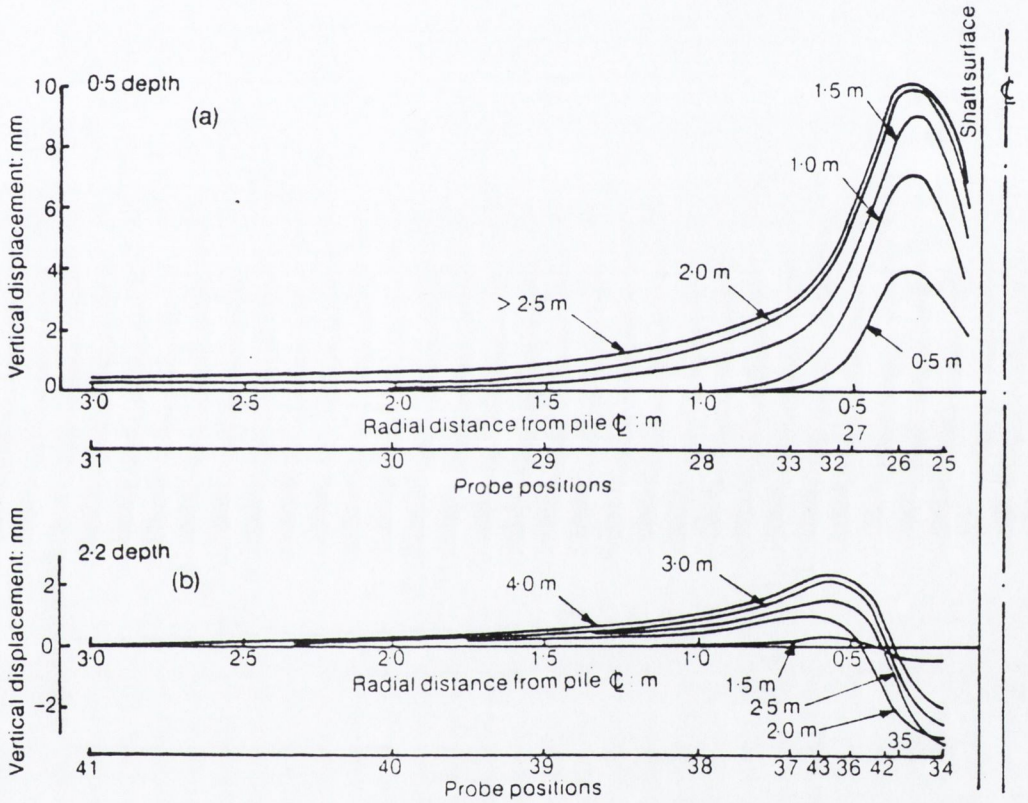

Figure 2.27. Vertical ground displacements from field tests (Cooke *et al.* 1979): (a) 0.5 m below the surface; (b) 2.2 m below the surface

The vertical displacements for the greater depth of 2.2 m display downward movement close to the pile and upward movements are recorded further out. The curves in Figure 2.27 have been fitted by Cooke *et al.* (1979) and points have been taken from the final vertical movements at 2.2 m (for a total pile penetration of 4 m) as a representation of this data for 'deep' penetration. This data, which is shown in shown in Figure 2.28 has been used in further analysis in this Thesis, although it should be noted that these field displacements are of a lower order of magnitude than the laboratory data. The measurements recorded

closer to the surface at 0.5 m showed greater heave (upward soil movement) which is typical of 'shallow penetration'.

2.3.4 Formation of Slip Planes During Penetrometer Installation

Slip planes have been shown to form in the soil immediately surrounding a penetrometer during installation in studies such as that by Bond (1989). Inspection of the soil fabric by Bond (1989) showed that the soil around a displacement pile is not remoulded by the action of installation, instead there is systematic shear distortion of the soil which diminishes with distance away from the pile wall. In stiff clays, the fabric is reoriented in a near vertical direction within a zone extending to 1.2R while the outer extent of the disturbance is about 4R.

Bond (1989) found significant differences between the type of slip planes that form in the soil due to jacking or driving of piles into the ground. Slow jacked piles were found to form a highly polished slip surface that is 0.75 to 1 mm from the pile. However, next to driven piles the shearing is more turbulent in nature with frequent discontinuous shear surfaces of irregular size and alignment. Further away from the pile there is little to distinguish between jacked and driven piles with the orientation of the fabric declining from the vertical at equal rates.

2.4 SUMMARY AND OUTLINE OF ADOPTED APPROACH

It is clear from the review of existing predictive methods for penetrometer installation that none of them provide a completely accurate or reliable solution to the penetration problem. In general, the techniques discussed fall into three categories; (a) methods that have lost their relevance and no longer have any real use, (b) analytical techniques which use simplifications but can provide useful results, and lastly, (c) promising numerical techniques which produce complete stress-strain solutions but require further development.

The spherical cavity expansion and bearing capacity theories fall into the first category as methods that have lost their usefulness in predicting what happens during penetrometer installation (although they still have relevance in other fields). Cylindrical cavity expansion and the Strain Path Method fall into the second category of analytical tools that provide a

simplified yet useful solution to what is a very complex problem. Finite Element Methods fall into the last category, and have shown steady improvement since being first applied to penetration problems in the mid-eighties.

The development of numerical methods in general, over the last decade or so, has seen a reduction in the use of analytical techniques for solving geotechnical problems. The switch in emphasis from analytical to numerical techniques has been mainly due to the increase in computer processor speeds. This has allowed complex finite element analyses (with features such as non-linear soil behaviour and coupled deformation and flow) to be conducted on desk top and portable computers. Under these conditions, the old analytical solutions, requiring drastic simplifications of the problem geometry and stress-strain properties can appear to lose their usefulness. However, they can still play an important role for the following reasons: (i) they are reference benchmarks for the results of numerical analyses; (ii) they can be used for sensitivity analysis and to identify problem variables; and (iii) in some cases they provide simple useful results. In the case of penetration problems in particular, the complex boundary conditions added to the difficulty of modelling soil behaviour creates enormous difficulties in providing useful numerical solutions.

The complexity of the problem has meant that FEMs are not yet so far developed that a solution can be provided that is directly useful in geotechnical practice, i.e., according to Van Den Berg *et al.* (1996) current solutions are qualitative not quantitative. The major difficulties for numerical modelling of penetrometer installation have been outlined here:

- The complexity of the problem has required the numerical techniques to adopt an advanced theory of mechanics which introduces material and geometric nonlinearities to examine the deformation behaviour of the soil during penetration.

- Modelling the penetrometer boundary has proved difficult and for cone penetration the shoulder region gives rise to problems in all the FE studies regardless of type. Kiousis *et al.* (1988) and Abu-Farsakh *et al.* (1998) encountered the separation of contact between the soil and penetrometer in a small region just behind the cone shoulder and Van Den Berg *et al.* (1996) have tried three different boundary conditions in this region.

- Modelling the constitutive soil properties is given added difficulty in penetration problems by the large deformations present. The high strains calculated raise the question of reliability of the soil models used since the vast majority of constitutive laws available have been developed for much lower strains (< 20%).

An alternative FEM approach which attempts to address some of the difficulties outlined above has been developed by Hu and Randolph (1998). It employs a remeshing technique to avoid problems caused by the complex formulations of large strain techniques, which, depending on the approach, are subject to; second order corrections to strain relationships allowing for rotation of elements (Lagrangian), or stress derivatives that allow for convection of material through the mesh (Eulerian). These are added complications to the conventional small strain finite element equations. The remeshing of elements to prevent them deforming excessively allows Hu and Randolph (1998) to use the simpler small strain approach. However, the remeshing technique brings its own difficulties to the problem, such as fluctuations in the load-deformation results and an increase in the requirement of computational resources.

The solution by Teh (1987) falls between categories (b) and (c) stated above. It is based on the analytical approach of the SPM and maintains some of its relative simplicity but uses a numerical technique to derive solutions to the cone penetration problem. A finite difference method was used for flow modelling and incorporated the actual shape of a 60° cone penetrometer, which was an improvement on the potential theory approach used by the SPM. The finite difference flow solutions by Teh (1987) were restricted to that of ideal inviscid irrotational flow.

Some current difficulties and complications to be overcome for the existing theoretical approaches to penetration installation are derived from introducing the effects of surface roughness on the penetrometer and soil shear strength. The complications these effects introduce to the problem are apparent from the FE analyses and the simplicity of the SPM is based on their omission. The application of material shear and surface roughness induces a different mode of soil deformation than is currently modelled by the SPM. It is clear, however, that accurate prediction of the strains and stresses must include the influence boundary friction and soil properties in some form. Other effects to be considered include the load cycling of pile driving and the rate of penetration on the soil. Teh (1987) and Whittle (1991) attempted to introduce material properties by the application of stress

models such as MIT-E3 and made some correction of the strain paths to satisfy equilibrium. This approach provides stress solutions for the SPM but has met with only limited success in providing more 'realistic' strain paths due to problems in achieving equilibrium in two dimensions.

The review of experimental data for displacements in the soil around penetrometers, highlights the need for more good quality test data to aid theoretical prediction. Accurate observations of radial and vertical movements in truly three dimensional model tests are required. Experimental data is also required of displacement paths (most existing data is only providing information on final positions). The experimental approaches which have been most successful in this area have either been field tests or model tests using radiographic techniques. Both types of test introduce difficulties; with field tests requiring large research resources, and the use of X-rays in model tests suffering from limitations in accuracy. A summary of the existing displacement data is presented in Figure 2.28. The existing data highlights the similarity of displacement measurements regardless of soil type, installation technique or rate. This provides some confirmation that penetration problems are kinematically constrained and as such are relatively insensitive to these factors (as first stated by Baligh 1985).

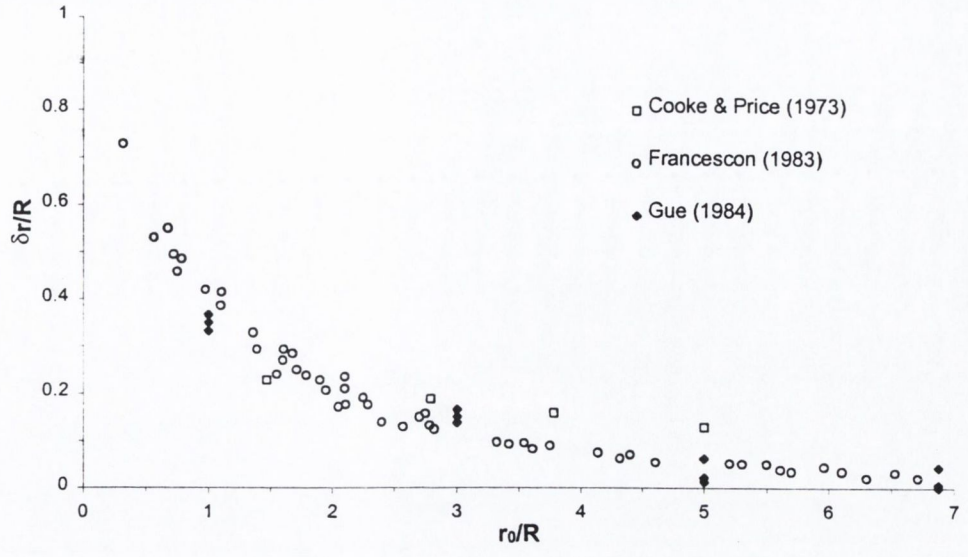

(a)

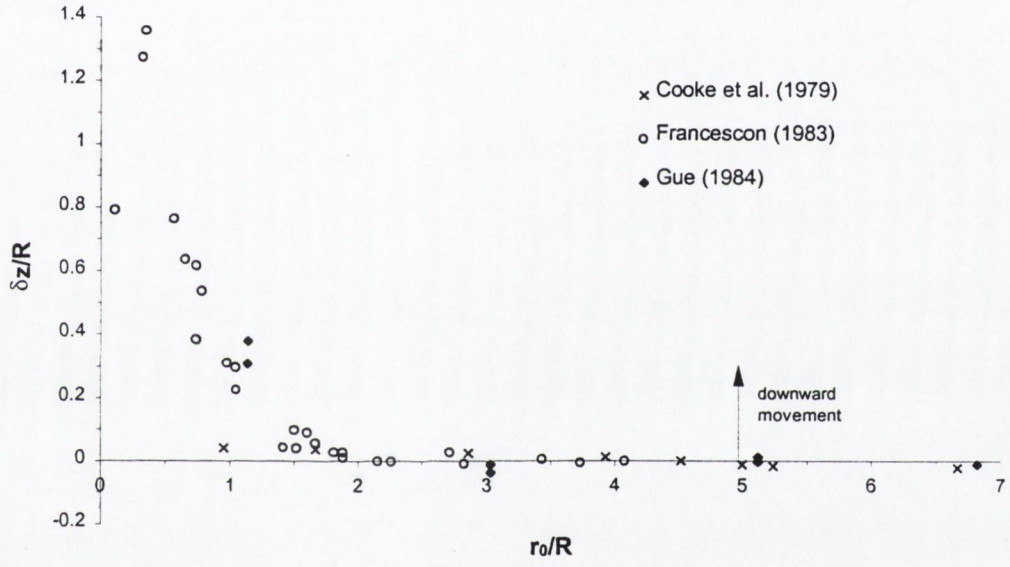

(b)

Figure 2.28. Experimental displacements measured in model pile tests; (a) radial movements, (b) vertical movements

CHAPTER 3
MODIFICATIONS TO THE STRAIN PATH METHOD APPROACH

Chapter 3

3.0 MODIFICATIONS TO THE STRAIN PATH METHOD APPROACH

3.1 INTRODUCTION

In this chapter the essential features of the original Strain Path Method (SPM) formulation are first outlined and the modifications which have been subsequently introduced to allow improved solutions are then described. Potential flow theory was used in the first applications of the SPM and the simplest case, that of the 'simple pile' presented by Baligh (1985), is used to demonstrate the theory. Modifications to the SPM are presented that were first introduced by Teh (1987) to allow strain rates be evaluated from the flow field of a finite difference model. In this Thesis a similar approach to that of Teh (1987) has been taken, only here a Finite Element (FE) approach is used in the modelling of flow fields. As will be described in later chapters, FE theory allows the introduction of addition parameters to the flow model and is capable of producing a wide variety of flow solutions. A study into the effects of different flow conditions, in later chapters, has allowed more representative solutions of strain fields than those of the SPM to be produced.

3.2 APPLICATION OF SPM

3.2.1 Outline

The SPM approach developed by Baligh (1985) has already been described in Chapter 2, and in this section, only the formulation used to apply the 'simple pile' solution is presented. This includes the development of the potential theory flow solution to the calculation of strain rates and strains. The procedure presented for the 'simple pile' is applicable to all SPM solutions, although flow modelling and techniques for the calculation of strains may change. A brief description is also given of a solution with a geometry close to that of a cone tipped penetrometer, found using potential theory; difficulties encountered in the approach are discussed.

3.2.2 Simple Pile Formulation

Baligh (1985) used potential flow theory to describe the soil movements around a penetrating axisymmetric body. The simple pile solution is modelled by the insertion a single spherical source in a uniform flow field and is developed in steps (i) to (iv) in the following. The equations for strain rates and the integration technique for evaluating strain are then developed. The solution for the simple pile has been reproduced in this Thesis on an MS Excel spreadsheet and has been used in later chapters for comparative studies with other solutions.

(i) Spherical cavity expansion

Consideration is first given to the expansion of a spherical cavity in an infinite incompressible, isotropic and homogeneous soil. If a spherical volume of this material is bounded by a radius, ρ_0 and has an initial volume V_0 then the expansion of a spherical cavity at its centre with radius, R causes an increase in volume, δV ($\delta V = 4/3\pi R^3$). After cavity expansion the new volume, V of the soil mass is given by;

$$V = V_0 + \delta V$$

$$\tfrac{4}{3}\pi\rho^3 = \tfrac{4}{3}\pi\rho_0^3 + \tfrac{4}{3}\pi R^3$$

and is enclosed by a radius:

$$\rho = \left[\rho_0^3 + R^3\right]^{1/3}$$

Accordingly at any time t, if the cavity radius $R(t)$ is known, then the radial location of a soil element can be related to its initial location, ρ_0 by the expression:

$$\rho(t) = \left[\rho_0^3 + R^3(t)\right]^{1/3} \tag{3.1}$$

(ii) Single spherical source

An equivalent method of simulating spherical cavity expansion is to consider a single spherical source, located at $\rho = 0$, emitting an incompressible material at a rate of volume

Q per unit time. Therefore at any time, t, the material occupies a spherical cavity with the radius given by:

$$R(t) = \left[\frac{3Q.t}{4\pi}\right]^{1/3} \tag{3.2}$$

Combining (3.1) and (3.2) allows the radial velocity, v_ρ, of at any point within the soil to be found by differentiation with respect to time;

$$\rho(t) = \left[\rho_0^3 + \frac{3Q.t}{4\pi}\right]^{1/3}$$

$$\frac{\partial \rho}{\partial t} = \frac{1}{3}\left[\rho_0^3 + \frac{3Q.t}{4\pi}\right]^{-2/3}\left(\frac{3Q}{4\pi}\right)$$

at $t = 0$, $\rho_0 = \rho$ and therefore:

$$\frac{\partial \rho}{\partial t} = \frac{Q}{4\pi}\left[\rho^3\right]^{-2/3}$$

$$v_\rho = \frac{\partial \rho}{\partial t} = \frac{Q}{4\pi\rho^2} \tag{3.3}$$

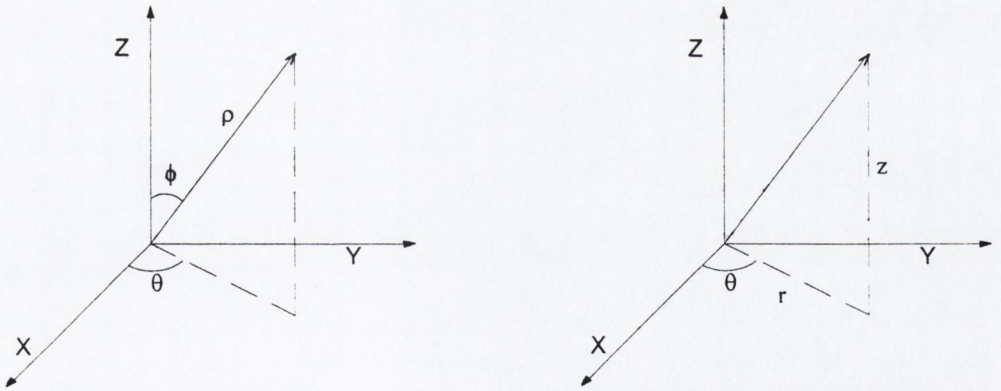

(a) Spherical Co-ordinate System (ρ, θ, ϕ)

(b) Cylindrical Co-ordinate System (r, θ, z)

Figure 3.1 Spherical and cylindrical co-ordinate systems

If a cylindrical co-ordinate system, as shown in Figure 3.1b, is adopted the conversion from the spherical components (ρ, θ, ϕ) to cylindrical components, (r, θ, z) are given by;

$$\rho = r^2 + z^2; \quad r = \rho\sin\phi, \quad z = \rho\cos\phi \tag{3.4}$$

and therefore the radial and vertical velocity components are:

$$v_r = v_\rho \sin\phi; \qquad v_z = v_\rho \cos\phi. \tag{3.5}$$

In potential flow theory a convenient, concise means of describing the form of any particular pattern of flow is the stream function, ψ which allows complicated flow patterns to be obtained by superimposing the stream functions of individual sources and sinks. In steady flow, this formulation has the added advantage that lines of constant stream function also represent particle paths. The velocity components and the stream function are related by the partial derivatives:

$$v_r = \frac{1}{r}\frac{\partial\psi}{\partial z}; \qquad v_z = -\frac{1}{r}\frac{\partial\psi}{\partial r} \tag{3.6}$$

The stream function at a point P with co-ordinates (r, z) due to a point source at the origin, discharging an incompressible material at a rate of volume Q per unit time is:

$$\psi_S = \frac{Q}{4\pi}\cos\phi \tag{3.7}$$

A stream function, ψ, is defined as the volume flow rate across any region joined to a point at which ψ is an arbitrary zero. Therefore, lines of constant stream function separate constant volumes of flow and the closer the streamlines for equal increments of ψ, the higher the velocity.

(iii) Simple pile solution

The simple pile solution, as stated previously, is obtained by superimposing a spherical source in a uniform flow field. The stream function of a uniform flow with velocity U in the positive z-direction is:

$$\psi_U = -\frac{r^2 U}{2} \tag{3.8}$$

By the principle of superposition, the stream function of a flow system consisting of a point source in a uniform flow is given by;

$$\psi = \psi_S + \psi_U$$

$$\therefore \psi = \frac{Q}{4\pi}\cos\phi - \frac{r^2 U}{2} \tag{3.9}$$

and by substituting equation (3.9) into (3.6) the cylindrical velocity components are obtained:

$$v_r = \frac{Q}{4\pi}\frac{\sin\phi}{\rho^2}; \qquad v_z = U + \frac{Q}{4\pi}\frac{\cos\phi}{\rho^2} \tag{3.10}$$

To give a solution that is independent of the dimensions of a pile or penetrometer, the radial and vertical co-ordinates (r, z) are normalised by the penetrometer radius, R. The radial position of a point with a vertical position, z/R along a given streamline with a constant stream function value, ψ is given by;

$$r/R = \sqrt{\frac{2}{UR^2}\left(\frac{Q}{4\pi}\cdot\frac{z/R}{\sqrt{(z/R)^2+(r/R)^2}} - \psi\right)} \tag{3.11}$$

where;

$$R = \left[\frac{Q}{\pi U}\right]^{1/2} \tag{3.12}$$

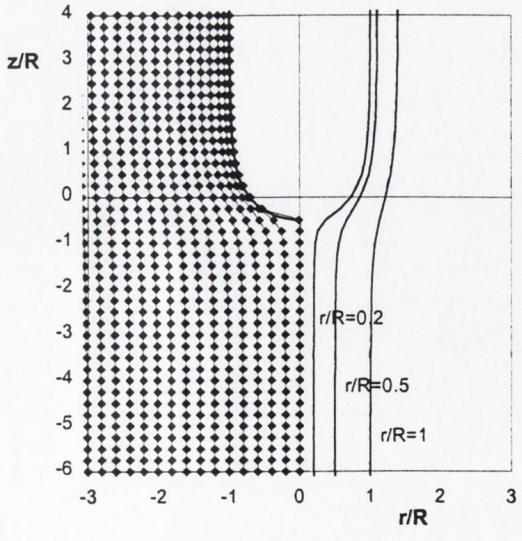

Figure 3.2. Prediction of grid deformation and streamlines due to simple pile penetration

i.e., the pile radius is a function of the source strength and uniform flow velocity.

In this Thesis, equation (3.11) has been used to calculate the positions for points at vertical increments of 0.25R along streamlines spaced at initial radial locations of 0.2R as is shown in Figure 3.2. The tip of the simple pile is defined as the point along the axis at which the vertical velocity component vanishes and is located at z/R = -0.5. The radius of a simple pile increases asymptotically to a value of R as z approaches infinity. For all practical purposes, however, it can be considered to be equal to R for z/R > 4, where r exceeds 99% R. The continual increase of the pile radius, R, with increasing vertical distance (albeit very small for z/R > 4) has influence on the inferred strains calculated from the SPM and this is described in later sections.

(iv) Strain due to simple pile penetration

The strain in the soil due to the simple pile is calculated by integrating the strain rates at points along the streamline paths followed by soil elements. In this way the complete strain history of an element during penetration is known. The strain at any point in the soil at time, t is given by;

$$\varepsilon_{ij} = \int_0^t \dot{\varepsilon}_{ij}\, dt \tag{3.13}$$

where $\dot{\varepsilon}_{ij}$ is the strain rate tensor (along the streamline). The geometry of the problem is illustrated in Figure 3.3 which shows an exaggerated streamline for a point moving around a 'simple' penetrometer.

The strain rates (which are considered negative when compressive) are evaluated from the gradients of the velocity as:

$$\dot{\varepsilon}_{rr} = \frac{\partial v_r}{\partial r} = \frac{Q}{4\pi\rho^3}\left(\cos^2\phi - 2\sin^2\phi\right) \tag{3.14}$$

$$\dot{\varepsilon}_{zz} = \frac{\partial v_z}{\partial z} = \frac{Q}{4\pi\rho^3}\left(\sin^2\phi - 2\cos^2\phi\right) \tag{3.15}$$

$$\dot{\varepsilon}_{\theta\theta} = \frac{v_r}{r} = \frac{Q}{4\pi\rho^3} \tag{3.16}$$

$$\dot{\varepsilon}_{rz} = \frac{1}{2}\left(\frac{\partial v_r}{\partial z} + \frac{\partial v_z}{\partial r}\right) = \frac{Q}{4\pi\rho^3}\left(-\tfrac{3}{2}\sin 2\phi\right) \tag{3.17}$$

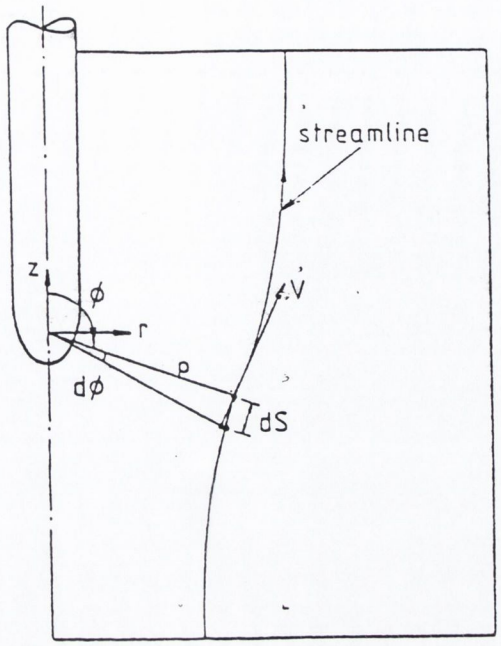

Figure 3.3. Geometry of the simple pile problem (Teh 1987)

These strain rates are integrated along streamlines to find ε_{zz}, ε_{rr} and $\varepsilon_{\theta\theta}$ which correspond to the direct vertical, radial and circumferential strains; and ε_{rz} which is the complimentary shear stain in the r-z plane. The strain paths can be described by three deviatoric strain components E_1, E_2 and E_3 proposed by Baligh (1985), which correspond to strains induced under vertical, cylindrical cavity expansion and direct simple shear loading respectively:

$$E_1 = \varepsilon_{zz} \qquad E_2 = \left(\varepsilon_{rr} - \varepsilon_{\theta\theta}\right)/\sqrt{3} \qquad E_3 = 2\,\varepsilon_{rz}/\sqrt{3} \tag{3.18}$$

The straining around the penetrometer can also be presented in terms of octahedral strain, γ_{oct} which gives a good measure of the level of shearing taking place. The octahedral strain is calculated from the three 'E' strain invariants;

$$\gamma_{oct} = \frac{1}{\sqrt{2}}\left(E_1^2 + E_2^2 + E_3^2\right)^{1/2} \tag{3.19}$$

and likewise the octahedral strain rate:

$$\dot{\gamma}_{oct} = \frac{1}{\sqrt{2}}\left(\dot{E}_1^2 + \dot{E}_2^2 + \dot{E}_3^2\right)^{1/2} \tag{3.20}$$

Figure 3.4 shows a plot of the octahedral strain rate contours around the 'simple pile', which consist of spheres centred on the origin, located R/2 behind the pile tip. The penetration velocity is 2 cm/s and the strain rate units are %/hr. The plot shows how the strain rates change as a particle moves along a given streamline, with the highest rates of strain occurring close to the tip.

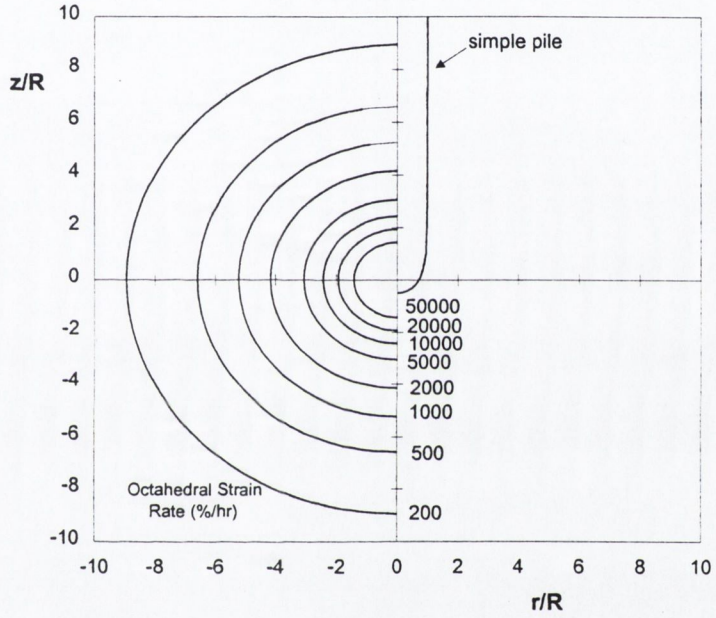

Figure 3.4 Octahedral strain rate contours during simple pile penetration

The deviatoric strain paths have been calculated along three streamlines with initial positions at r_0/R = 0.2, 0.5 & 1 (Figure 3.2). These strain paths, shown in Figure 3.5, plot vertical strain (E_1) against cylindrical expansion strain (E_2) and shear strain (E_3) against E_2. The predictions illustrate the relatively complex series of strain changes that soil elements are likely to experience adjacent to a penetrometer installation. The position of the soil element relative to the penetrometer tip (z/R) is indicated on the strain paths in Figure 3.5 at z/R = -1, 0, 1, 5 & 20. This allows the influence of the soil element's location on the strain paths to be assessed. Each component of strain has a maximum when the soil element is at a different location relative to the penetrometer tip. E_1 is at a maximum below the tip, whilst due to the geometry of the simple pile, E_2 continues to increase with z/R (although this is at a very reduced rate for z/R > 4). The shear strain, E_3 reaches a

maximum just after passing the penetrometer tip and then reduces before reaching a constant state. Likewise, E_1 is not monotonic but shows two reversals with the secondary reversal in the negative (compressive) direction. The values for all 'E' strains are almost identical at z/R = 5 & 20, showing that from just a short distance behind the tip there are no discernible changes in strain with increased z/R.

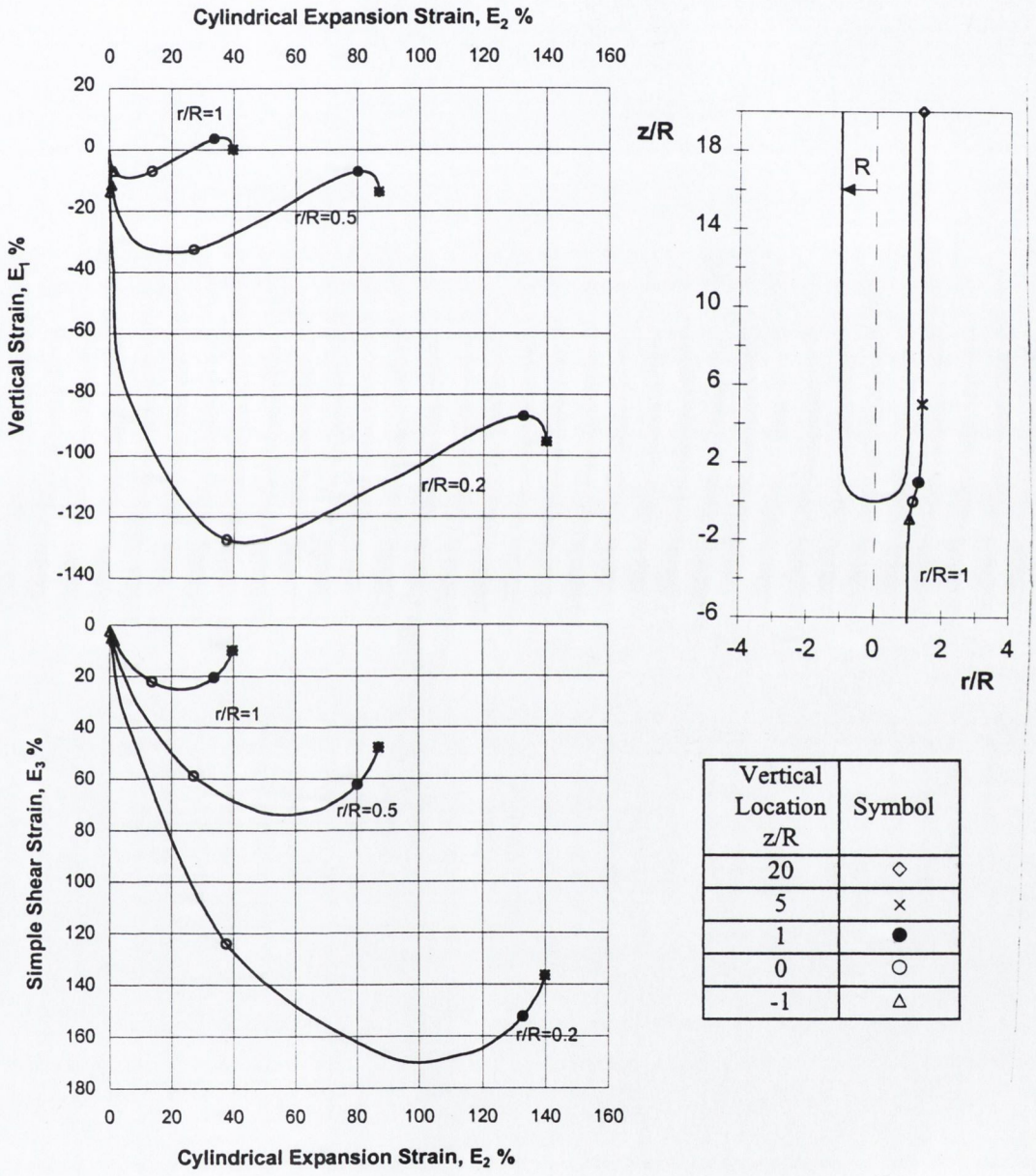

Figure 3.5. Spreadsheet prediction of strain paths during simple pile penetration

Due to the numerical integration procedure used to find strain, the accuracy of the strain path solutions is dependent on the distance between points along the streamlines. It was

necessary to find a spacing that would produce accurate strain results without utilising excessive amounts of computer time and storage space. The optimum grid point spacing was found to be 0.05 R (although this spacing is only critical in the region close to the tip as illustrated in Figure 3.4). The extent of the streamline ahead and behind the pile tip was also important accuracy consideration for calculating the strain. The grid needs to extend a distance of at least 10R below the pile tip and 4R above the pile tip, (where the shaft radius exceeds 99% R) if all the important zones of deformation are to be considered.

3.2.3 Modelling Different Shaped Penetrometers Using Potential Flow Theory

It is possible to produce flow solutions, using potential theory, for penetrometer geometries other than that of the 'simple pile' by a combination of point sources, line sources and sinks. This potential theory approach for modelling different geometries was investigated in this Thesis and solutions such as the 'cone' solution shown here were produced. The investigation also highlighted the difficulties of this type of analysis for modelling; (i) the geometries of real penetrometers, and (ii) different flow conditions.

The purpose of modelling different shapes is to produce strain path solutions for penetrometers, piles and samplers with more realistic geometry. The major difficulty in achieving this, with potential theory, is the approximation of straight lines and corners with differentiable curves. For example a 'cone' shape solution (shown in Figure 3.6) has been produced using a line source rather than a spherical source. This solution has a sharper penetrometer shape than that of the 'simple pile' but can be seen to have a rounded cone tip and shoulder. The 'cone' solution, as was the case for the 'simple pile', is found by first defining the flow in terms of the stream function and then solving the deformed grid in terms of the radial and vertical co-ordinates (r, z). For a line source the stream function is given by

$$\psi = -m - \tfrac{1}{2}Ur^2 \tag{3.20}$$

where m is the strength of the line source and U is the uniform steam velocity. The radial position for a given streamline and vertical position z is found from;

$$r = \sqrt{\frac{2}{U}\left[\frac{m}{a}\left(\sqrt{r^2+z^2} - \sqrt{r^2+(z-a)^2}\right) - \psi\right]} \tag{3.21}$$

where a is the length of the line source.

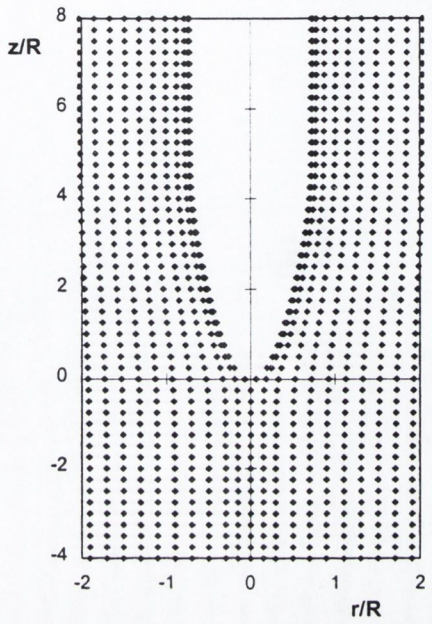

Figure 3.6. Flow pattern around a 'cone' shaped penetrometer using potential theory

3.3 APPLICATION OF FINITE ELEMENT FLOW MODELLING TO SPM

3.3.1 General Description Of FE Model

In the SPM the first step in modelling the penetration process is to solve the flow problem of a fixed penetrometer in a uniform velocity field. Previous applications of SPM have estimated strain fields for a variety of penetrometer geometries using the velocity fields of ideal fluids. In this Thesis, fluid flow modelling has been conducted with a finite element fluid dynamics package which has allowed a variety of flow cases with different fluid properties and boundary conditions to be solved. Many of the flow cases examined are also described in Gill & Lehane (1998) and Gill & Lehane (1999).

The finite element modelling in this Thesis was conducted using the ANSYS general purpose engineering package. The FLOTRAN CFD (Computational Fluid Dynamics) option within the ANSYS product provides a tool for analysing two dimensional and three

dimensional fluid flow fields (penetrometer installation is simulated as a two dimensional axisymmetric problem). All the fluid flow solutions presented in this Thesis are steady-state incompressible Newtonian flow analyses of either laminar or turbulent flow which were meshed with four-noded quadrilateral elements. In laminar flow analyses, the velocity field is very ordered and smooth, as it is in highly viscous, slow moving flows. Turbulent flow analyses deal with problems where velocities are high enough and the viscosity is low enough to cause turbulent fluctuations.

Flow velocities are obtained from the conservation of momentum principle, and the pressure is obtained from the conservation of mass principle. The solution of all the governing equations constitutes a 'global' or complete iteration. The number of iterations required to achieve a converged solution depends on the grid meshing and stability of the problem. The analyses conducted for fluids with high viscosities produced smooth, ordered velocity fields and converged easily. Convergence of flows with very low viscosities was more difficult and, following the recommendations of the ANSYS authors', involved a number of analyses, each of which began iterations from the results of a preceding analysis which had been performed for a higher viscosity.

Results from ANSYS flow solutions are given in a nodal format (i.e., as properties for each node in the mesh). The results files are subsequently used to evaluate strains and displacements. These calculations are performed in Microsoft Excel, but before this can be done the ANSYS files must be converted into compatible format. This conversion procedure is described in Appendix B.

3.3.2 Modelling Flow Around A Fixed Penetrometer

In a finite element solution the flow around a fixed penetrometer is modelled in a two-dimensional axisymmetric co-ordinate system with the penetrometer (an axisymmetric fixed body) located on the axis of symmetry. The boundary conditions adopted for modelling the flow distribution around a cone penetrometer, of radius, R, are shown on Figure 3.7. For all solutions, a uniform vertical velocity (U) is applied at the inlet AF (upstream) and far field boundary (FE). On the axis of symmetry (r = 0 axis), the velocity normal to the flow (the r-direction) is set to zero but is unconstrained in the z-direction. A zero normal velocity is applied on the penetrometer face and, unlike the conventional SPM,

the tangential velocity (v_{pent}) is assigned a value between zero (termed no-slip) and the flow field velocity, U (full slip). A zero relative pressure is specified at the outlet (DE) for all solutions.

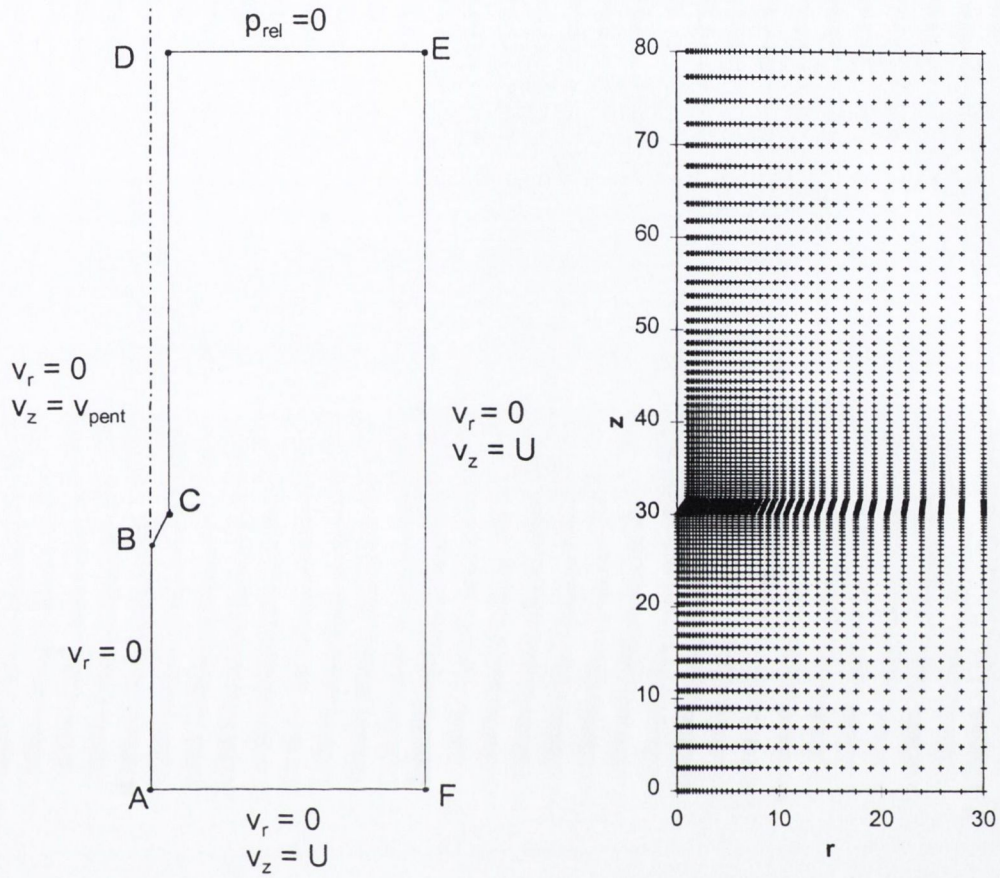

Figure 3.7. Flow Model: (a) boundary conditions; (b) nodal grid

The solutions of finite element models are dependent on the density of the element mesh particularly for fluid flow solutions in the regions close to surface boundaries. Consideration was given to the effect of the mesh density on the solutions given in this Thesis. Figure 3.8 shows the vertical and radial velocity profiles close to the penetrometer at a height of five radii above the tip (z/R = 5) for 'full slip' flow and for two meshes: Mesh 'A' (with 4080 elements) and Mesh 'B' (with 11,140 elements). Significant differences between the predicted velocities of the two meshes only occur very close to the penetrometer and these are relatively small. Given that the interpolation procedure discussed below resulted in smoother profiles, Mesh 'A' was selected as the best compromise between accuracy and computational/data processing time and is used to produce all the solutions presented in this Thesis (a considerable amount of data

manipulation is required to find strains and displacements). The size of the output files from ANSYS was most critical at the post analysis stage where a large amount of data processing was required. Due to a 'bug' in the flow solver it was necessary to mesh the flow area in a particular sequence to avoid errors in the nodal stream function values. This problem, and the means of avoiding it, are described in detail in Appendix B (Section B6).

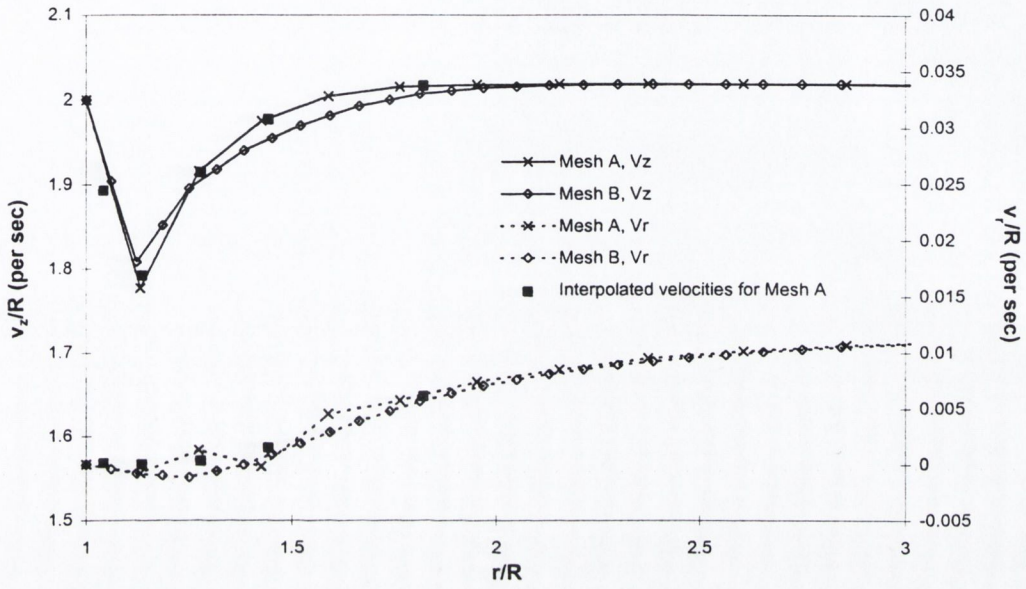

Figure 3.8. Velocities for the 60° cone at z/R = 20 for two FE meshes

3.3.3 Interpolating Flow Paths

The SPM derives strains in the soil by integration of strain rates along streamlines (or flow paths) followed by the fluid flow. Each streamline is defined by a constant value of ψ, termed the stream function (which is given directly by potential theory). The standard ANSYS package does not, however, predict the location of streamlines but instead outputs the ψ value at each node, which are derived from the calculated velocities and stored on a nodal basis at the end of each iteration. The location of streamlines therefore has to be found by interpolating for a constant stream function through the nodal grid as is shown in Figure 3.9. A polynomial interpolation function that could be integrated or differentiated without difficulty was used for this purpose.

In two dimensions, a complete nth-order polynomial in the r-z plane may be written as (e.g., see Huebner *et al.*, 1995):

$$P_n(r,z) = \sum_{k=1}^{T_n^{(2)}} \alpha_k r^i z^j , \qquad i+j \le n \tag{3.22}$$

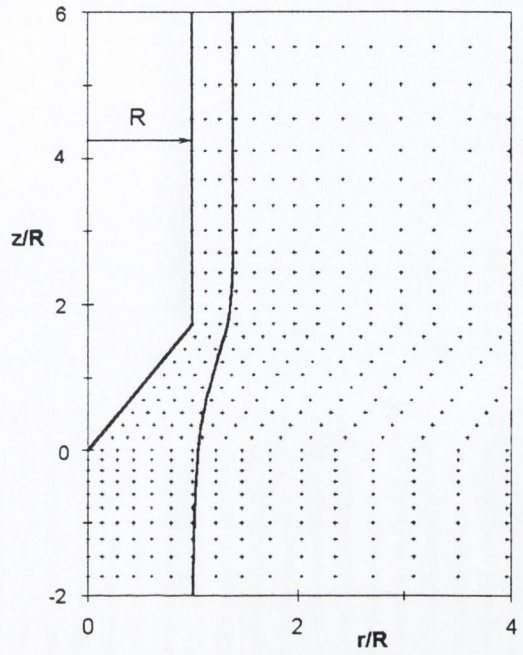

Figure 3.9. Interpolated streamline in the nodal grid

where the number of terms in the polynomial is

$$T_n^{(2)} = (n+1)(n+2)/2$$

and the coefficients (α_k) control the magnitude of the distribution of the two-dimensional field variable. Using the local co-ordinates (ξ, η) in a nine-node local mesh system (also used by Teh, 1997) which is shown in Figure 3.10, the polynomial used to describe the variation of ψ becomes:

$$\psi(\xi,\eta) = \alpha_0 + \alpha_1\xi + \alpha_2\eta + \alpha_3\xi^2 + \alpha_4\xi\eta + \alpha_5\eta^2 + \alpha_6\xi^2\eta + \alpha_7\xi\eta^2 + \alpha_8\xi^2\eta^2 \tag{3.23}$$

The corresponding matrix formulation for (3.23) is:

$$\{\psi\} = [M]\{\alpha\} \tag{3.24}$$

where [M] is a square (9x9) matrix. $\{\alpha\}$ is then found from:

$$\{\alpha\} = [M]^{-1}\{\psi\} \tag{3.25}$$

This set of simultaneous equations gives $\{\alpha\}$ for the central node in the local mesh and is applied to every node in the grid (except the boundary nodes). Interpolation of streamline paths (of constant stream function, ψ) through the nodal grid can then be achieved by simply solving for ξ at each horizontal grid row (when the local y-direction co-ordinate, η, is zero) using (3.23), which is reduced to the following quadratic equation.

$$\psi = \alpha_0 + \alpha_1\xi + \alpha_3\xi^2 \tag{3.26}$$

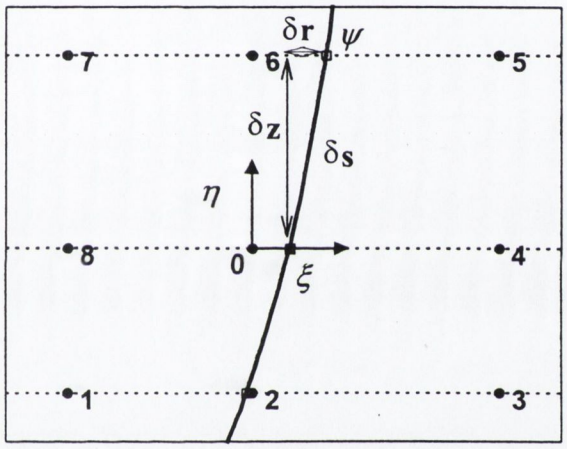

Figure 3.10. Streamline interpolation through the nine-node local mesh

3.3.4. Calculation Of Strains And Displacements

The calculation of strains from the ANSYS results files is an adaptation of the method presented by Teh (1987) for use with finite difference flow solutions. Following the derivation of the streamline location, as outlined, the determination of strains involves calculation of the velocities and strain rates at each interpolated point along the flow path. The accumulated strain can then be calculated along the streamline by integration of the strain rates at each interpolated point.

The velocities and strain rates are obtained from differential forms of equation (3.23). Radial and vertical velocities (v_r and v_z) may be written in terms of the stream function (ψ) as:

$$v_r = -\frac{1}{r}\frac{\partial \psi}{\partial z} \qquad v_z = \frac{1}{r}\frac{\partial \psi}{\partial r} \tag{3.27}$$

The radial, vertical, circumferential and shear strain rates are expressed as:

$$\dot{\varepsilon}_{rr} = \frac{\partial v_r}{\partial r} \qquad \dot{\varepsilon}_{zz} = \frac{\partial v_z}{\partial z} \qquad \dot{\varepsilon}_{\theta\theta} = \frac{v_r}{r} \qquad \dot{\varepsilon}_{rz} = \frac{1}{2}\left(\frac{\partial v_r}{\partial z} + \frac{\partial v_z}{\partial r}\right) \tag{3.28}$$

Then from (3.23) and converting to the local co-ordinate system (note the local and global co-ordinates can simply be interchanged in the differentiation process as $\delta r = \delta\xi$ and $\delta z = \delta\eta$):

$$v_r = -\frac{1}{r}\left(\alpha_2 + \alpha_4\xi + 2\alpha_5\eta + \alpha_6\xi^2 + 2\alpha_7\xi\eta + 2\alpha_8\xi^2\eta\right) \tag{3.29}$$

$$v_z = \frac{1}{r}\left(\alpha_1 + 2\alpha_3\xi + \alpha_4\eta + 2\alpha_6\xi\eta + \alpha_7\eta^2 + 2\alpha_8\xi\eta^2\right) \tag{3.30}$$

$$\dot{\varepsilon}_{rr} = \frac{1}{r^2}\left\{\alpha_2 + \alpha_4(\xi - r) + 2\alpha_5\eta + \alpha_6\xi(\xi - 2r) + 2\alpha_7\eta(\xi - r) + 2\alpha_8\xi\eta(\xi - 2r)\right\} \tag{3.31}$$

$$\dot{\varepsilon}_{zz} = \frac{1}{r}\left(\alpha_4 + 2\alpha_6\xi + 2\alpha_7\eta + 4\alpha_8\xi\eta\right) \tag{3.32}$$

$$\dot{\varepsilon}_{\theta\theta} = -\frac{1}{r^2}\left(\alpha_2 + \alpha_4\varepsilon + 2\alpha_5\eta + \alpha_6\varepsilon^2 + 2\alpha_7\xi\eta + 2\alpha_8\xi^2\eta\right) \tag{3.33}$$

$$\begin{aligned}\dot{\varepsilon}_{rz} = \frac{1}{2r^2}\big[&-\alpha_1 + 2\alpha_3(r - \xi) - \alpha_4\eta - 2\alpha_5 r + 2\alpha_6\eta(r - \xi) \\ &- \alpha_7(2\xi r + \eta^2) - 2\alpha_8\xi(\xi r + \eta^2)\big]\end{aligned} \tag{3.34}$$

The strain accumulated along a streamline is then calculated by dividing the streamline along its length into linear segments, each of which is an approximation of the path length (δs) between the established points. Each strain increment is calculated at the mid-point

between the streamline points and the integration moves from the bottom grid (boundary *AF* in Figure 3.7) upwards in the direction of flow. The cumulative strain is given by:

$$\varepsilon_{ij} = \sum_{k=1}^{n} \dot{\varepsilon}_{ij} \frac{\delta s}{\bar{v}_s} \tag{3.35}$$

where $\bar{v}_s$ is the average velocity in the direction of the streamline between points i and j and $\dot{\varepsilon}_{ij}$ is the strain rate between these points.

The radial displacement at any node n (δr_n) is simply the radial shift of the streamline (equation 3.36). The increment of vertical displacement is given by the difference between the vertical and free flow field velocity multiplied by the time over which these velocities act. This time is given by the distance travelled along the streamline (ds) divided by the average velocity along that segment of the streamline, $v_{s(avg)}$. The total vertical displacement (δz_n) at each streamline point is the sum of these increments (equation 3.37).

$$\delta r_n = r_n - r_0 \tag{3.36}$$

$$\delta z_n = \sum_{k=1}^{n} \left(v_{rel} . t\right)_k = \sum_{k=1}^{n} \left(\left(v_z - U\right) \frac{ds}{v_{s(avg)}} \right)_k \tag{3.37}$$

The expression in (3.37) for the calculation of vertical displacements is an approximate one. It calculates the vertical displacement relative to the penetrometer for points in the flow with respect to their position in an uninterrupted uniform flow where $v_z = U$ (as is specified on the far field boundary). Use of this expression does, however, in theory allow a discrepancy to occur between vertical straining and vertical displacement under certain conditions. These conditions arise if the vertical velocity, at large values of z/R, reaches a constant state where $v_z \neq U$. The vertical displacement, therefore, continues to increase although there is no further increase in vertical strain since $\delta v_z = 0$. In practice small changes in the vertical velocity were found to occur even at large distances behind the tip (up to z/R = 50) and a constant state was not reached, although for most flow types and 'full slip' flow in particular, v_z was very close to U.

The accuracy of the interpolation technique is demonstrated using the example shown on Figure 3.8. The velocities derived from the interpolated stream functions are shown to

compare very well with those outputted directly from the Mesh 'A' solution. In fact, it is evident that the interpolation process smoothens small irregularities associated with the discrete nature of the FE mesh.

CHAPTER 4
SOLUTIONS FROM MODIFIED STRAIN PATH METHOD APPROACH

Chapter 4

4.0 SOLUTIONS FROM MODIFIED STRAIN PATH METHOD APPROACH

4.1 INTRODUCTION

This chapter presents the solutions to the Strain Path Method for different flow conditions using the ANSYS finite element model presented in Chapter 3. The effect that different fluid viscosity and penetrometer boundary conditions have on the strains and displacements is investigated. A comparison is also made between the 60° cone tip and the flat-ended penetrometer to determine the influence of tip geometry on deformation of the soil.

The introduction of viscosity to the flow model gives some representation to the possible effects of soil shear strength. The velocity condition on the penetrometer boundary can be adjusted to model the effect of shear stress (i.e., friction) on this surface. Solutions for a broad range of flow types around the two penetrometer shapes (60° cone and flat tip) have been produced. The strain paths are presented for a selection of the flow types that highlight the influence of the flow model boundary conditions and fluid properties on the inferred strain and displacement in the soil.

4.1.1 Introduction of Two Flow Parameters

The two flow parameters that are introduced in this modified SPM analysis are fluid viscosity, μ, and relative velocity on the penetrometer boundary, v_{pent}/U. The effect of these parameters is to introduce shear strength to the fluid and friction/shear stress on the penetrometer boundary. However, these fluid flow parameters are not found to be directly comparable to real soil properties such as strength, stiffness nor do they give consideration to effects arising from the rate of installation. Instead, μ introduces a factor that allows the flow to replicate heave in the far field and down drag of material close to the penetrometer and v_{pent}/U controls the magnitude of this down drag.

4.2 STRAIN PATH PREDICTIONS

4.2.1 Solutions for 60° Cone

The influence of fluid viscosity and shear stresses on the penetrometer boundary (as a consequence of the relative velocity on the penetrometer boundary, v_{pent}/U, being less than 1) are investigated for the 60° cone by examining the strain paths predicted in seven separate ANSYS analyses. The relevant details of each analysis, designated flows 'A' to 'G', are summarised in Table 4.1. Comparison of the flow analyses is conducted using strain path predictions performed for a streamline located at an initial radial distance of one penetrometer radius from the centreline, i.e. $r_0/R = 1$. The initial vertical position of the soil element is limited by the boundary extents in the fluid problem, i.e., on the upstream boundary which is thirty radii ahead of the penetrometer tip ($z_0/R = -30$). The final position is taken at a point on the streamline twenty radii behind the pile tip ($z/R = 20$). The extents of the mesh were found to be sufficient to include all the significant features of the flow problem (Teh 1987 also used similar mesh extents). The strain paths in these, and all other plots, are marked at five vertical positions along the streamline ($z/R = -1$, 0, 1, 5 and 20). This allows the influence of the vertical location relative to the pile on the strain paths of an element to be assessed.

Table 4.1. ANSYS flow solution for 60° cone

Flow	Viscosity, μ (N s m^{-2})	Velocity on Penetrometer Boundary, v_{pent}/U	Reynolds Number, Re†	Flow Type Description
A*	1×10^{-60}	1	1.2×10^{62}	Very low viscosity full slip flow
B	1.2	0	2000	Non-slip viscous flow
C	1.2	1	2000	Full-slip viscous flow
D	100	1	24	High viscosity full slip flow
E	1×10^{4}	1	0.24	High viscosity full slip flow
F	1.2	0.975	2000	Partial-slip viscous flow
G	1.2	0.75	2000	Partial-slip viscous flow

* Fluid density, $\rho = 1$ kg/m^3 and uniform flow field velocity, $U = 2$ m/s. For all other solutions $\rho = 2000$kg/m^3 and $U = 0.02$ m/s

† For internal duct flows; $Re = \rho V D_h/\mu$, where D_h is the hydraulic diameter and V is the fluid velocity (Note that D_h is twice the inlet height of 30m).

4.2.1.1 Comparison with SPM

Teh (1987) presents the strain path for a streamline with $r_0/R = 1$ for an inviscid flow around a 60° cone. This has been reproduced in Figure 4.1 and may be considered as a benchmark representing the SPM solution for this streamline. Flow 'A', which adopted a very low viscosity and a v_{pent}/U ratio of unity, closely approximates the conditions modelled by the SPM. A comparison of the strain paths predicted by this flow (see Figure 4.2) indicates very good agreement with the SPM solution apart from the fact that E_3 experiences a reversal at z/R = 3 and increases subsequently as z/R increases. This E_3 response predicted at large z/R values for Flow A is more marked than for the other 'full slip' flows with higher viscosity (C, D & E). This is due to the relatively uniform vertical velocity (v_z) variation with radial distance (r/R) from the penetrometer brought about by the

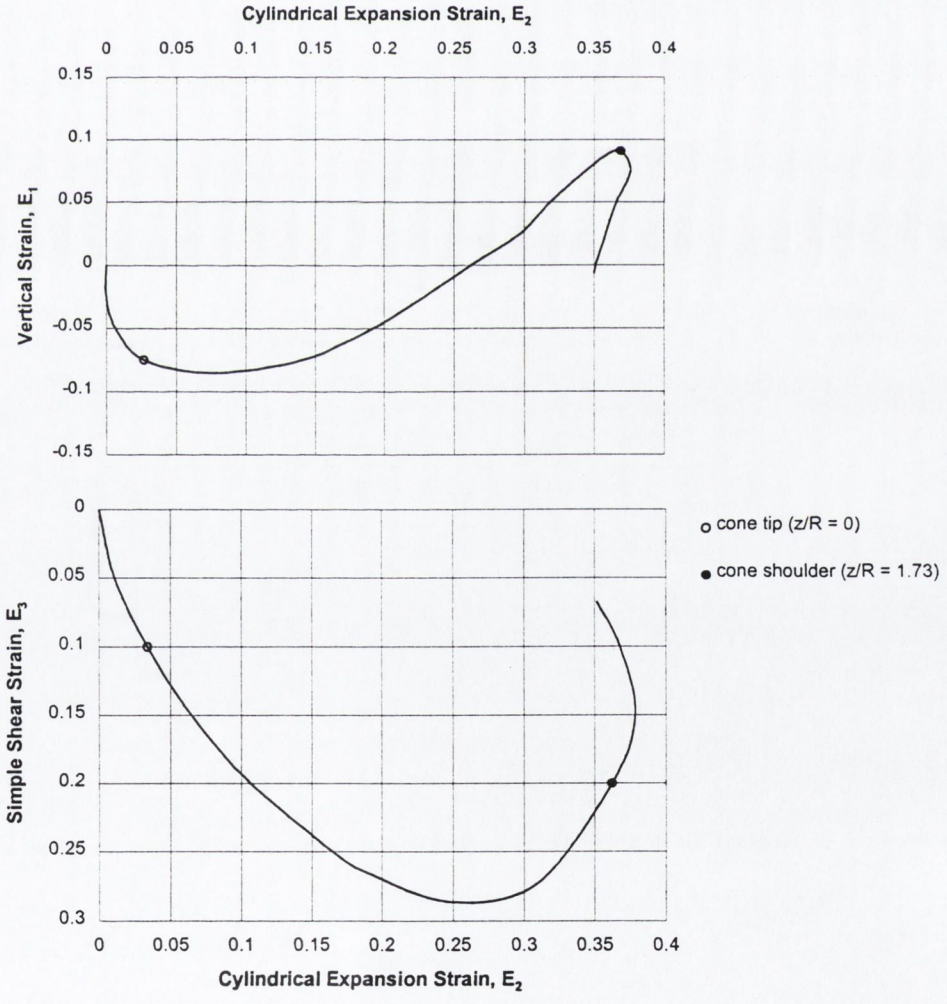

Figure 4.1. Teh's (1987) solution for SPM: strain path at $r_0/R = 1$ for 60° cone

low viscosity and due to the fact the flow does not revert completely to the uniform flow field velocity, U, which was specified at the inlet. This is most apparent for the low viscosity flows which are able to maintain small differences in velocity, while for high viscosity flows the fluid tends to move more as a single 'block' as resistance to shear in the fluid is higher.

4.2.1.2 The effects of fluid viscosity (μ)

The predictions plotted on Figure 4.2 illustrate the effect of fluid viscosity (μ) on 'full slip' flow ($v_{pent}/U = 1$) for the 60° cone. It is evident that high viscosity flows with low Reynolds numbers (Re), i.e., Flows D & E, produce somewhat different strain paths to flows with lower viscosity (A & C). Further points of note include:

- High μ results in greater compressive strains (note that E_1 is negative when compressive) as the penetrometer tip approaches. The elements for Flows D & E are seen in Figure 4.2 to have a net vertical compression throughout the penetrative process.
- E_2 and E_3 are generally lower for high μ flows with 'full slip'. However, the other analyses indicated that friction on the penetrometer can lead to higher E_2 and E_3 values for high μ flows.
- The strain paths produced are most sensitive to changes in viscosity over the range from 1 to 100 Ns/m^2 (compare Flows C and D).

In general, all analyses performed (including those involving partial slippage on the penetrometer surface) indicated that the overall effect of increasing the fluid viscosity is to increase the range of influence of the penetrometer and its specified boundary conditions on the surrounding elements. The reason for the significant differences between Flows C & D, despite the relatively small difference in Re (2000 compared to 24), is that the flow behaviour changes form one of low viscosity (C) to that of high viscosity (D) where the fluid moves almost as a single block.

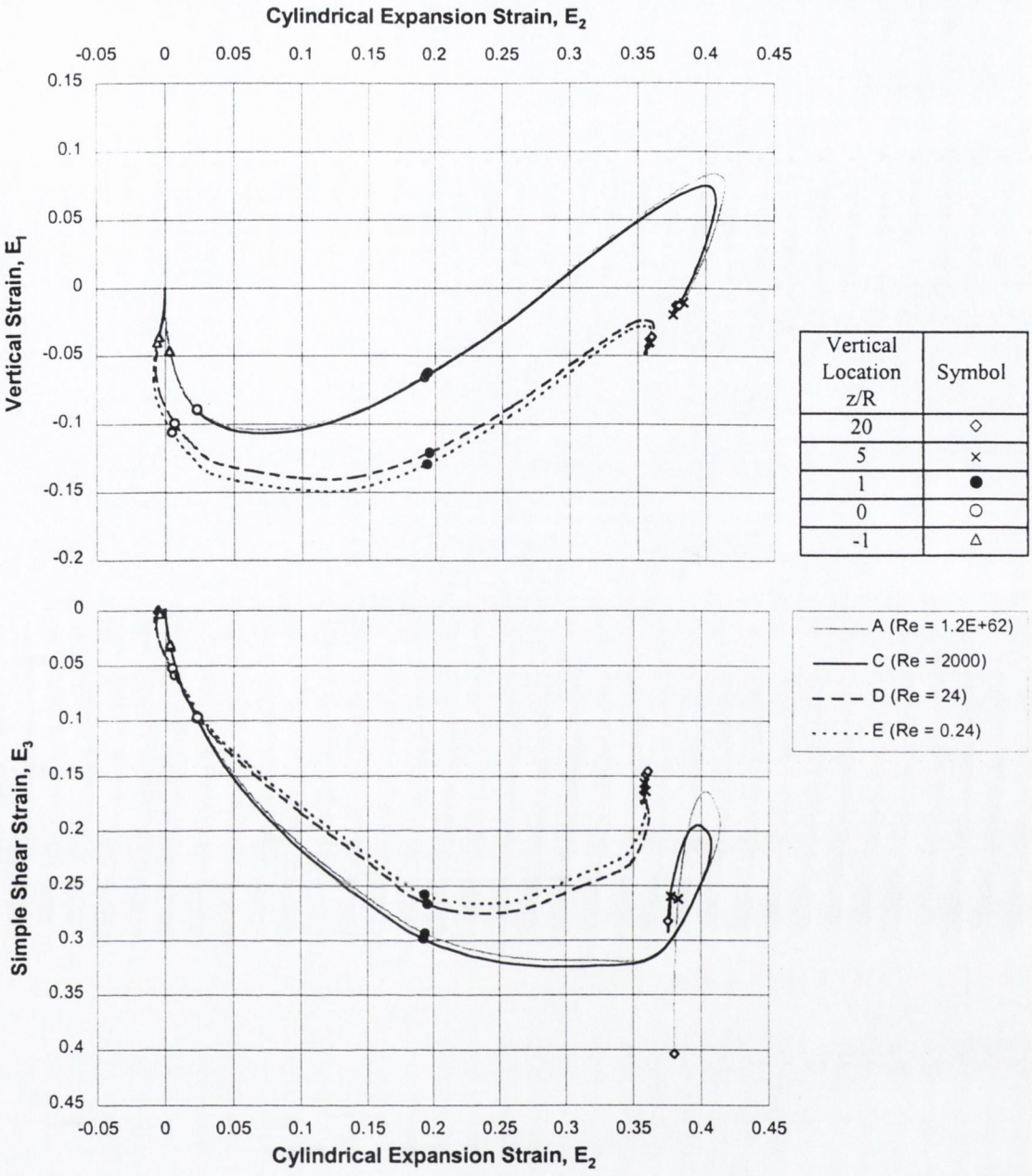

Figure 4.2. Deviatoric strain paths at $r_0/R = 1$ during penetration of a 60° cone for 'full slip' flow

4.2.1.3 Relative velocity on penetrometer boundary

The predictions plotted on Figure 4.3 examine the influence of the slip condition on the boundary of the penetrometer for a fluid with a viscosity approximately 1000 times that of water. The strain paths for flows with 'full slip' (C), 'no-slip' (B), and two 'partial slip' conditions (F & G) are presented. Reducing the relative velocity of the penetrometer increases the friction on its surface and this results in;

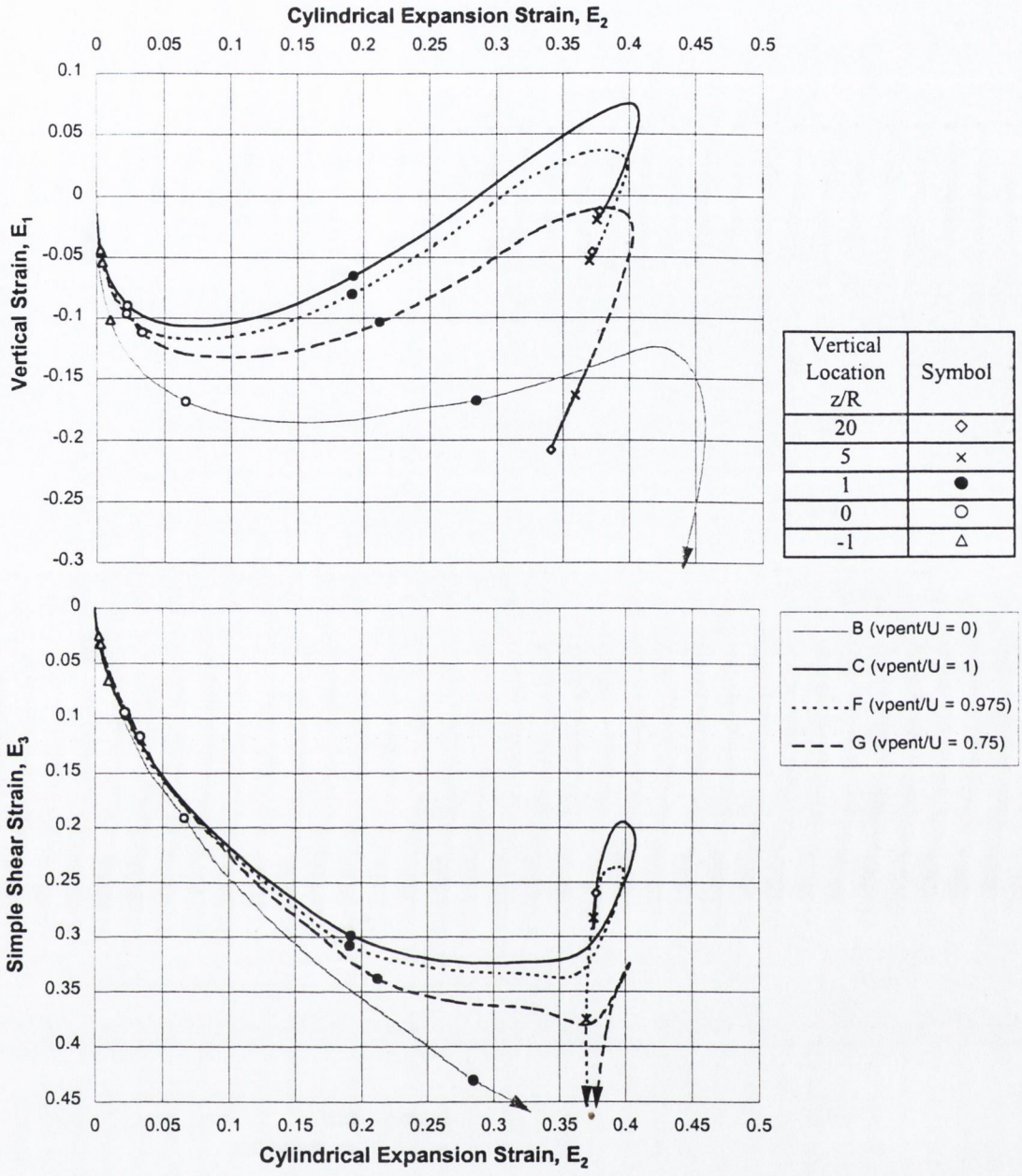

Figure 4.3. Deviatoric strain paths at $r_0/R = 1$ during penetration of a 60° cone for different boundary conditions with constant viscosity

- large increases in the shear strain (E_3) once the cone shoulder has passed (particularly evident in Flows B & G)
- increased vertical compressive strain (E_1 remains compressive throughout the penetrative process in Flows B & G)
- greater peaks in E_2 (the cylindrical expansion strain) at the cone shoulder, but also greater reductions in E_2 as the distance above the tip (z/R) increases.

4.2.1.4 The effects of initial radial distance (r_0/R)

The proximity of a soil element to the penetrometer has a large influence on the shape and magnitude of the strain paths followed during the installation process. Figure 4.4 plots the strain paths for three soil elements with initial positions at r_0/R = 0.5, 1 & 2. The greater the distance from the penetrometer the more rounded the strain paths become and show less influence of the penetrometer tip geometry. A comparison of the strain paths at r_0/R = 0.5 and 2, highlights the level of strain concentration close to the penetrometer with E_1 reducing by 15 times, E_2 by 10 times and for E_3 by 5 times as we from the r_0/R = 0.5 streamline to the r_0/R = 2 streamline.

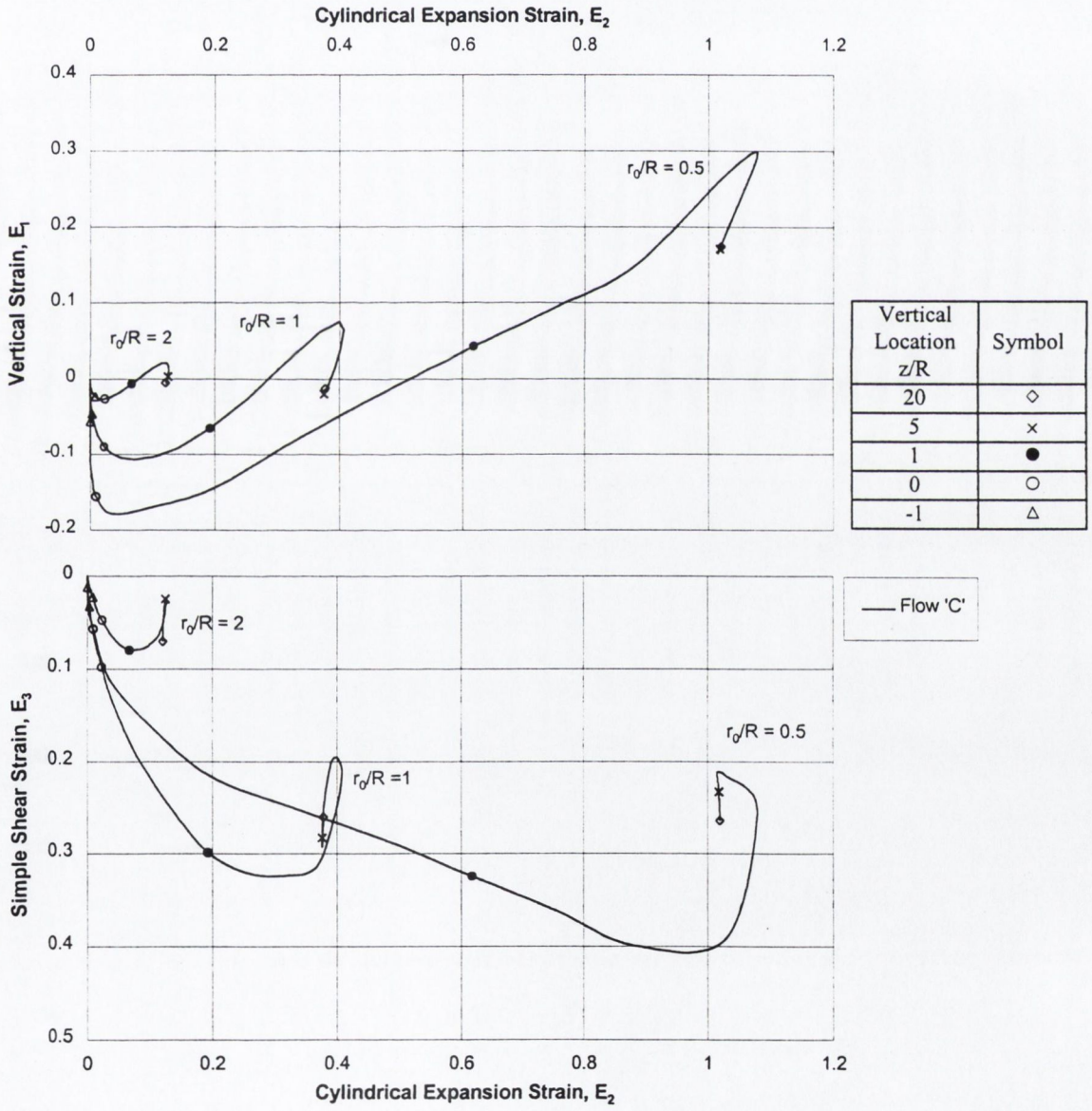

Figure 4.4. Deviatoric strain paths at r_0/R = 0.5, 1 & 2 for 'full slip' flow conditions (v_{pent}/U = 1) and viscosity, μ = 1 Nsm^{-2} (Re = 2000)

4.2.2 Solutions For Flat-Ended Penetrometer

Five flow predictions, designated flows 'H' to 'L' for a flat tipped penetrometer are presented here for comparison and the relevant details of each are described in Table 4.2. The effects of viscosity and the penetrometer boundary velocity condition on the strain paths for the flat ended geometry are assessed here in a manner similar to that conducted in Section 4.2.1 for the 60° cone shape. All the strain path predictions were performed for a streamline located at $r_0/R = 1$. The boundary extents of the ANSYS model are the same as were used for the 60° cone solutions.

Table 4.2. ANSYS flow Solutions for flat-ended penetrometer

Flow*	Viscosity, μ (N s m^{-2})	Velocity on Penetrometer Boundary, v_{pent}/U	Reynolds Number, Re†	Flow Type Description
H	1×10^{-3}	1	2.4×10^{6}	Low viscosity full slip flow
I	0.25	1	9600	Full slip viscous flow
J	1	1	2400	Full slip viscous flow
K	1	0.95	2400	Partial-slip viscous flow
L	1	0.9	2400	Partial-slip viscous flow

* Fluid density, $\rho = 2000$ kg/m^3 and uniform flow field velocity, U = 0.02 m/s.
† For internal duct flows; $Re = \rho V D_h/\mu$, where D_h is the hydraulic diameter and V is the fluid velocity (Note that D_h is twice the inlet height of 30 m).

4.2.2.1 The effect of viscosity (μ)

The predictions plotted on Figure 4.5 illustrate the effect of fluid viscosity (μ) on 'full slip' flow for the flat ended penetrometer. Three flows are presented with the viscosity ranging from that approximating water (Flow H) to viscosity 250 times (I) and 1000 times (J) greater. It is evident that Flows H & I produce similar vertical strain paths and that for shear strain the greater similarity lies between Flows I & J. Further points of note include:

- High μ results in greater compressive straining of the soil. The element for Flow J has a net vertical compression throughout the penetrative process.
- E_2 shows similar behaviour for all three flows, with a reductions in E_2 evident after the tip has passed followed soon after by a gradual increase in strain with increasing z/R.

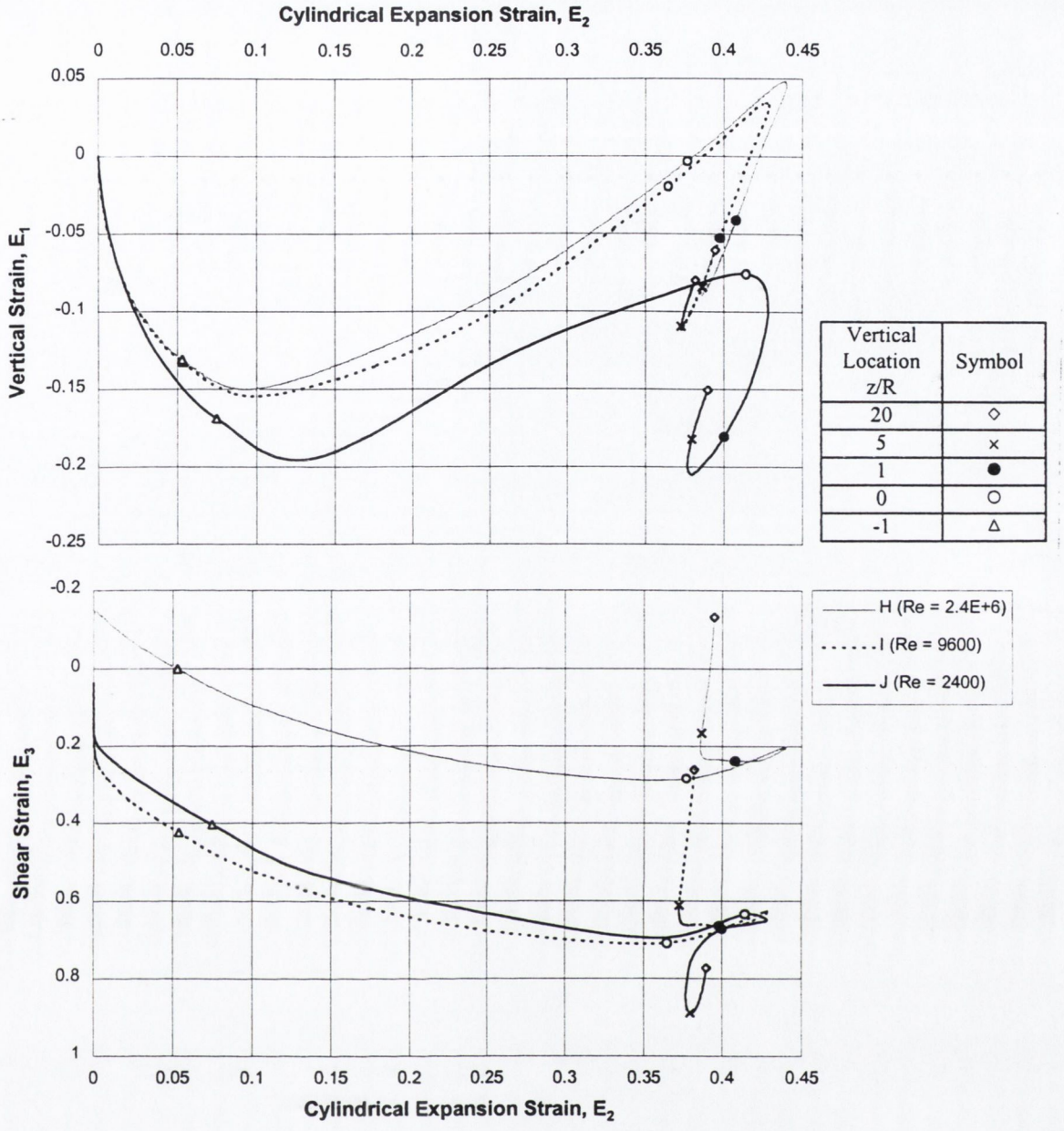

Figure 4.5. Deviatoric strain paths at $r_0/R = 1$ during penetration of a flat ended penetrometer for 'full slip' flow

- For E_3, high μ flows with 'full slip' display greater reductions in shear strain with increased distance above the tip. (Note that for Flow H, E_3 is initially negative before increasing and a second reversal brings E_3 back into the negative region).

4.2.2.2 Penetrometer boundary effects

The influence of the slip condition on the boundary of the penetrometer is examined from the three predictions plotted on Figure 4.6 for a fluid with a viscosity, $\mu = 1$ (approximately

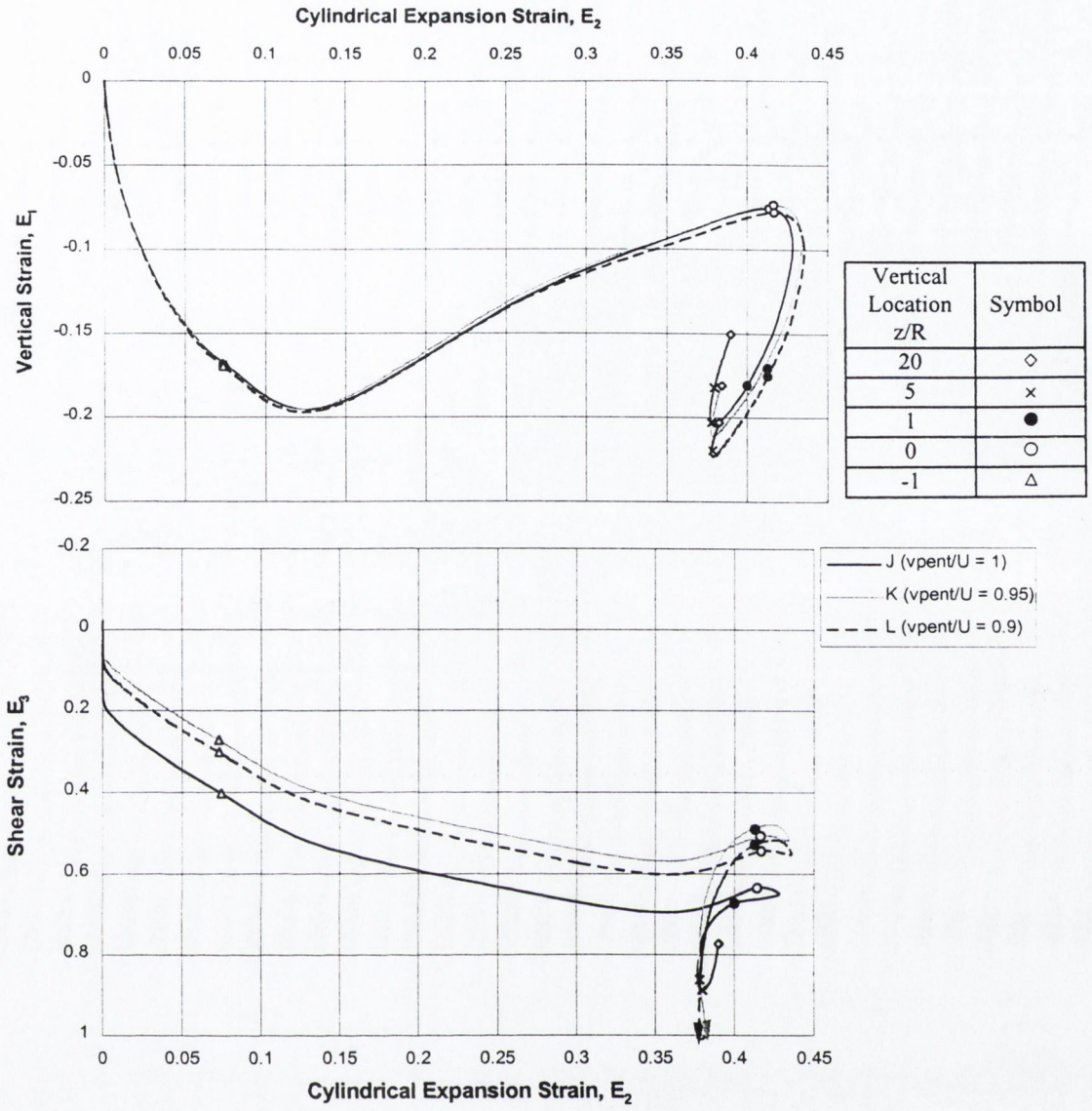

Figure 4.6. Deviatoric strain paths at $r_0/R = 1$ during penetration of a flat ended penetrometer for different boundary conditions with constant velocity

1000 times that of water). The strain paths for flows with 'full slip' (J) and two 'partial slip' conditions (K & L) are presented. As has been stated, the effect of reducing the relative velocity of the penetrometer is to increase the friction on its surface and for a penetrometer with a flat tip this results in:

- Increased vertical compressive strain. Although there appears to be little difference between the three flows, the 10% reduction in velocity on the penetrometer, from Flow J to L, results in a 30% increase in vertical strain at z/R = 20.

- Greater peaks in E_2, which occur between z/R = 0 and 1, with greater reductions in E_2 also taking place after the tip has passed.
- Large increases in the shear strain (E_3) once the cone shoulder has passed. Ahead of the tip, however, there is little difference between the flows with Flow J ('full slip' flow) in fact showing the greater shear strain at this stage.

4.2.3 Comparison Of 60° Cone and Flat-Ended Penetrometers

The effects of penetrometer geometry are examined by a comparison of two flows with similar fluid properties for the 60° cone (C) and flat ended penetrometer (J). These 'full slip' flows are compared in Figure 4.7 and show that:

- E_1 shows greater compressive strain for the flat ended penetrometer, which reverses just before the tip is reached. A larger reduction in vertical strain as the soil element moves from z/R = 5 to 20 is also evident for the flat geometry.
- E_2 shows a greater peak for the flat tip and subsequently a greater reduction, but also shows a larger increase in the cylindrical cavity strain for z/R > 5.
- The behaviour of the shear strain for both tip geometries show similar trends but is more exaggerated for the flat shape which shows greater peaks and reversals, and overall shows more shear straining.

Note that these comparisons are only for one streamline (i.e., above observations are not general).

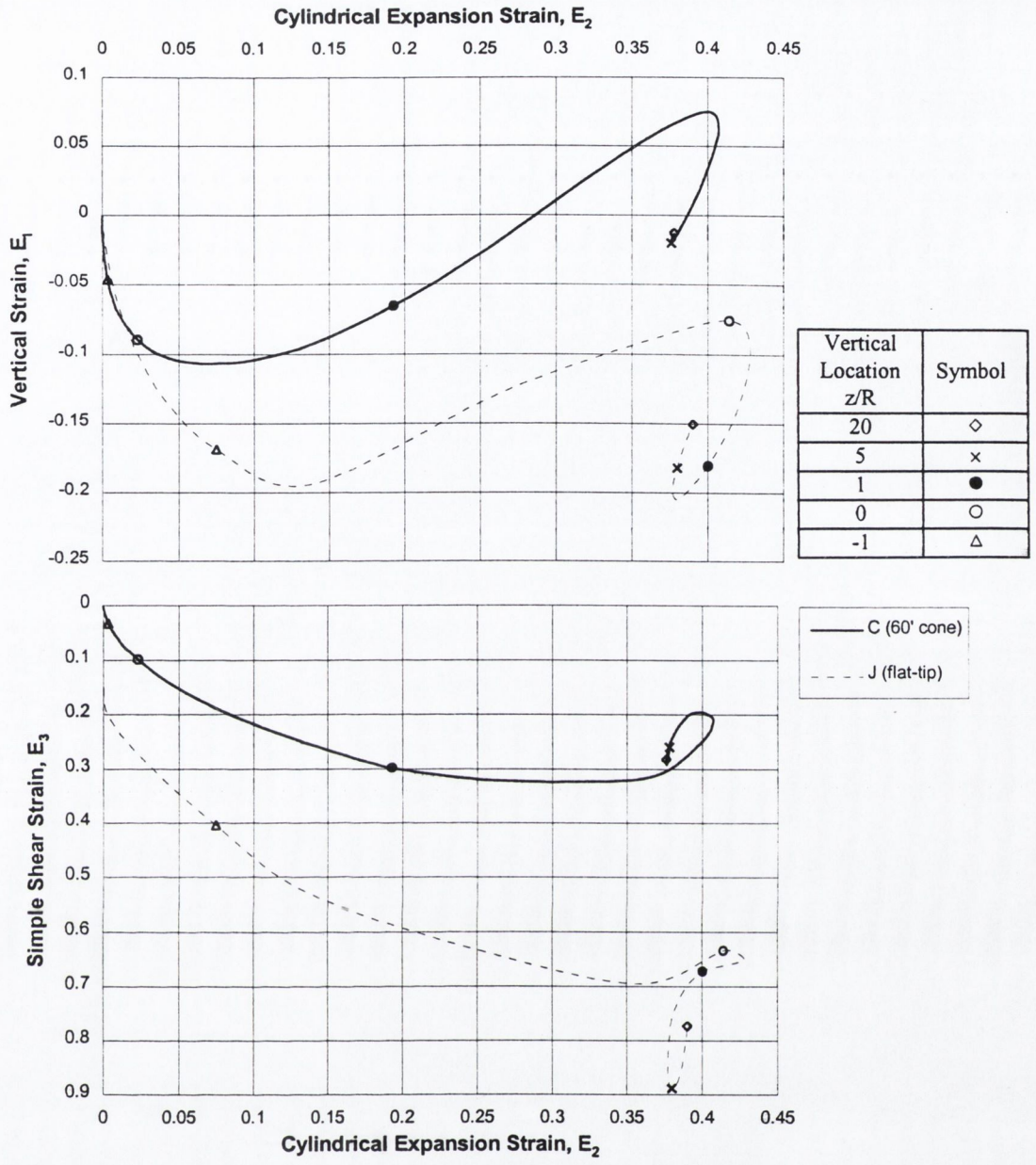

Figure 4.7. Comparison of deviatoric strain paths at $r_0/R = 1$ for penetrometers with 60° cone and flat tips with 'full slip' flow ($v_{pent}/U = 1$)

4.3 DISPLACEMENT PREDICTIONS

4.3.1 Outline

In this section the effect of flow type on the deformation in the soil around 60° cone and flat ended penetrometers is examined. The displacement distributions are compared for both penetrometer geometries and show the large influence that viscosity and friction on the penetrometer have on predicted soil movements.

4.3.2 Displacements around 60° Cone

The radial and vertical displacements for the flow solutions summarised in Table 4.1 are used to illustrate the influence of viscosity and penetrometer friction on the deformations. The displacements are shown at z/R = 20 for soil elements with initial radial distances ranging from close in to the penetrometer centreline ($r_0/R \approx 0$) up to $r_0/R = 7$.

4.3.2.1 Effect of viscosity (μ)

The influence of viscosity on the ground displacements is shown in Figure 4.8. This plot presents solutions for four different viscosities (Flows A, C D and E), all of which apply a

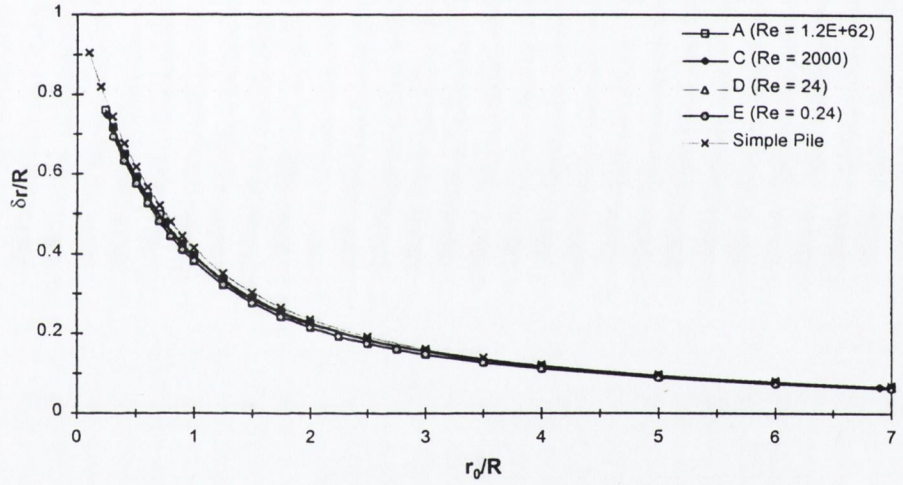

(a) Radial displacements

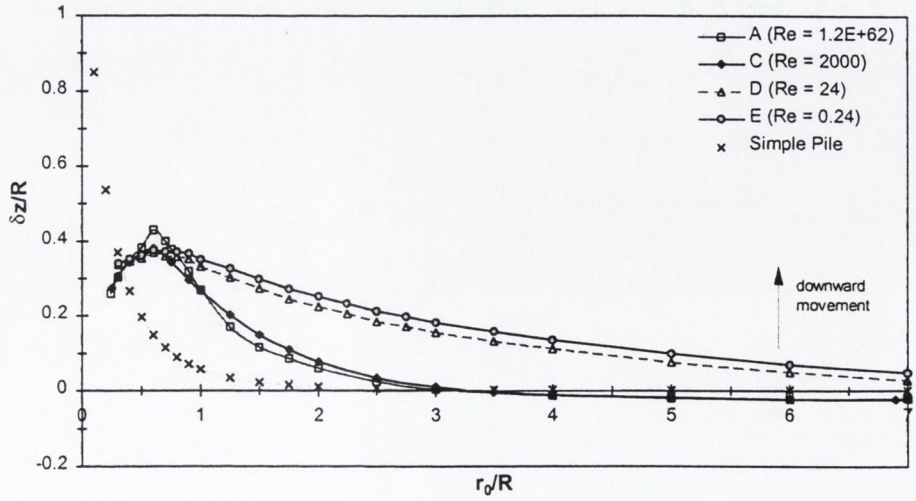

(b) Vertical displacements

Figure 4.8. Displacements at z/R = 20 around a 60° cone for 'full slip' flow

slip velocity condition on the penetrometer. Baligh's solution for the 'simple pile' is also shown in Figure 4.8 to demonstrate the differences between the SPM and the modified approach taken in this Thesis. The vertical deformation distribution for all four flow solutions show close similarities in the near field area around the penetrometer. However for $r_0/R > 1$ the low viscosity flow types show lower vertical soil disturbance than the more viscous flows. For the viscous flows F and G all the ground movements are downwards but for A and C upward deformation occurs for $r_0/R > 3$. The plots of radial displacement show that only small differences occur for flows with varying viscosities. These radial displacements compare closely with those predicted by the simple pile and cavity expansion predictions, though clear differences are evident for the vertical displacements.

4.3.2.2 Effect of slip condition

Figure 4.9 plots the displacements for flows of the same viscosity ($\mu = 1.2$ Ns/m^2) but with different velocity conditions on the penetrometer boundary (Flows B, C, F & G). The plot clearly shows that increases in the friction on the penetrometer for 'no-slip' (B) and 'partial slip' flow (F & G) increases both the radial and vertical soil movements. In particular, the vertical displacements close to the penetrometer are sensitive to small changes in the velocity on the boundary. For $r_0/R > 4$ the soil under goes a net upward displacement although the magnitude of this movement is small compared to the downward movement close to the penetrometer.

The penetrometer boundary slip condition and the fluid viscosity can each be seen to have a different effect on the distribution of displacements. The influence of the slip condition can be generalised as being the predominant influence on the soil close to the penetrometer ($r_0/R < 2$) and for further away ($r_0/R > 2$), the displacements are more dependent on the fluid viscosity. Therefore, in effect, the fluid viscosity determines the penetrometer's range of influence on the soil. This generalised description pertains more to relatively small changes in these properties than the more extreme flow conditions presented, e.g., 'no-slip' flow and highly viscous flow.

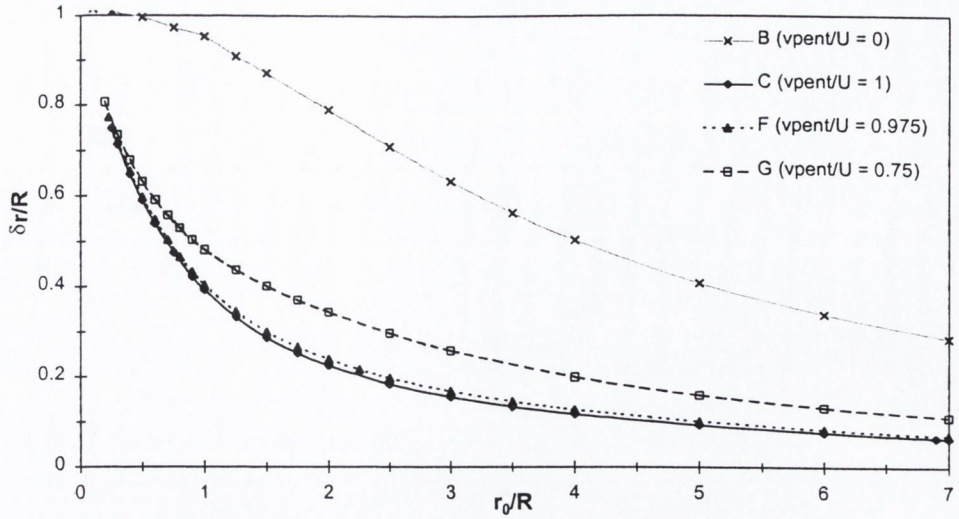

(a) Radial displacements

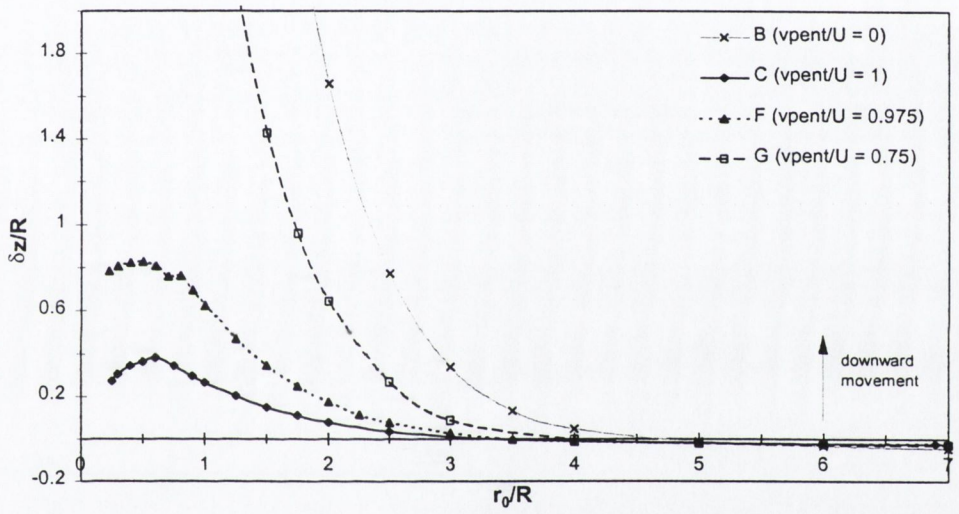

(b) Vertical displacements

Figure 4.9. Displacements at z/R = 20 around a 60° cone for constant viscosity

4.3.2.3 Effect of z/R on displacements

The influence of the vertical location of a soil element behind the penetrometer tip is investigated using the 'partial slip' Flow F at two horizontal soil horizons located at z/R = 5 & 20 (Figure 4.10). The radial movements show only small differences with the greater depth of penetration at z/R = 20 resulting in slightly larger radial displacement in the far field. The vertical displacements show differences in both the near and far fields; close to the penetrometer ($r_0/R < 3$) there is greater downward movement at z/R = 20 than at z/R = 5 caused by the 'drag down' motion of the soil in this region, for $r_0/R > 3$ an upward (heave)

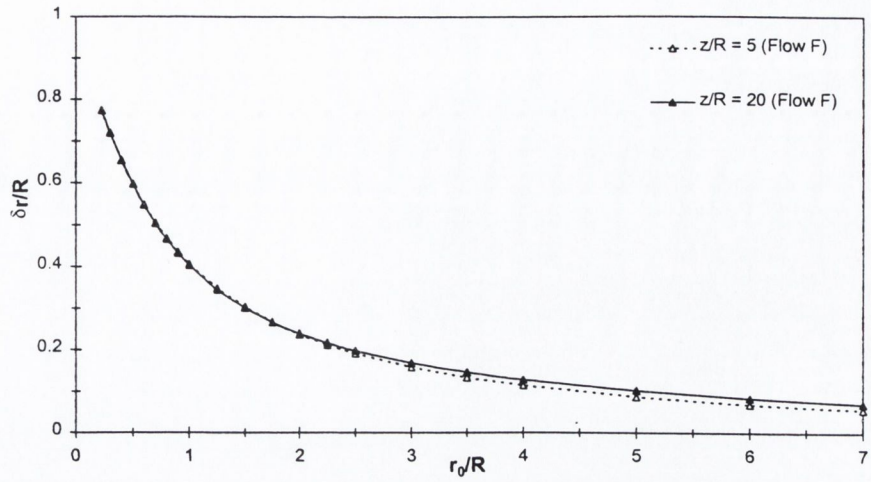

(a) Radial displacements

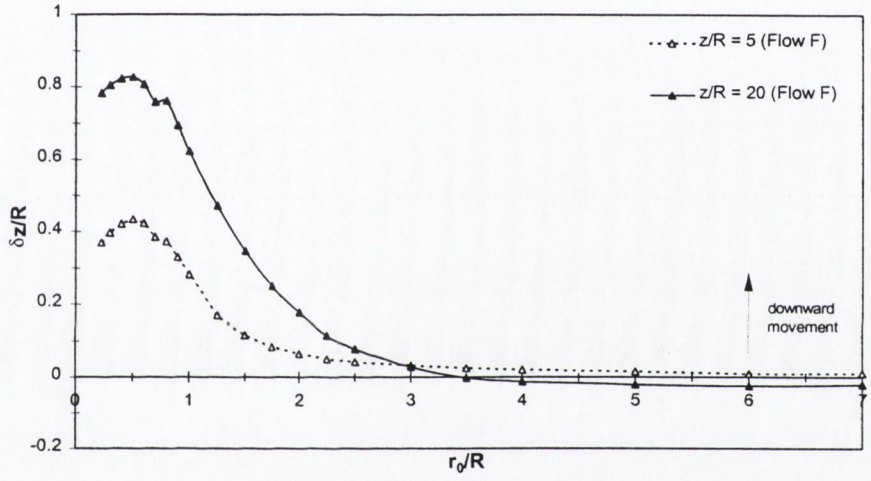

(b) Vertical displacements

Figure 4.10. Comparison of displacements at z/R = 5 & 20 for 'partial slip' flow ($v_{pent}/U = 0.975$) around a 60° cone

movement of the soil occurs at z/R = 20, while at z/R = 5 only net downward displacements occur.

4.3.2.4 Displacement paths for 60° cone

The computed displacement paths are shown for four soil elements with initial radii, r_0/R = 0.5, 1, 2 & 4 in a 'full slip' flow (C) around a 60° cone (Figure 4.11). These paths illustrate the deformation behaviour present at different radial distances from the penetrometer and also show the influence of vertical location on the displacements. The process by which soil in the far field showed heave occurring at z/R = 20 but not at z/R = 5 (discussed in

Section 4.3.2.3) is shown more clearly by the displacement path at $r_0/R = 4$. Although upward movement is present shortly after the tip has passed, it is not sufficient to show net upward displacement until after z/R=5. The 'drag down' motion of soil movement is evident close to the penetrometer for $z/R > 5$ but is most prominent for $r_0/R = 1$ (at $r_0/R = 0.5$ the 'full slip' nature of the flow reduces this effect). All the paths show that a reversal in the downward movement takes place close to the cone shoulder ($z/R \cong 1.7$).

The effect on the displacement paths from changes in μ or v_{pent}/U can be inferred from the strain paths and displacements solutions presented elsewhere in this chapter. An increase in viscosity would have the effect of causing a small increase in the magnitude of the radial displacement paths at all initial radii, and a large increase in the vertical displacement paths for elements at $r_0/R > 1$, although little effect on the soil at $r_0/R < 1$ (inferred from Flows D & E in Figure 4.8). A reduction in the velocity on the penetrometer (i.e., $v_{pent}/U < 1$) would increase the radial displacements throughout the soil and in the vertical direction would increase the downward 'drag' behind the tip ($z/R > 0$) for soil elements close to the penetrometer $r_0/R < 3$, but have little effect in the far field (inferred from Figure 4.9).

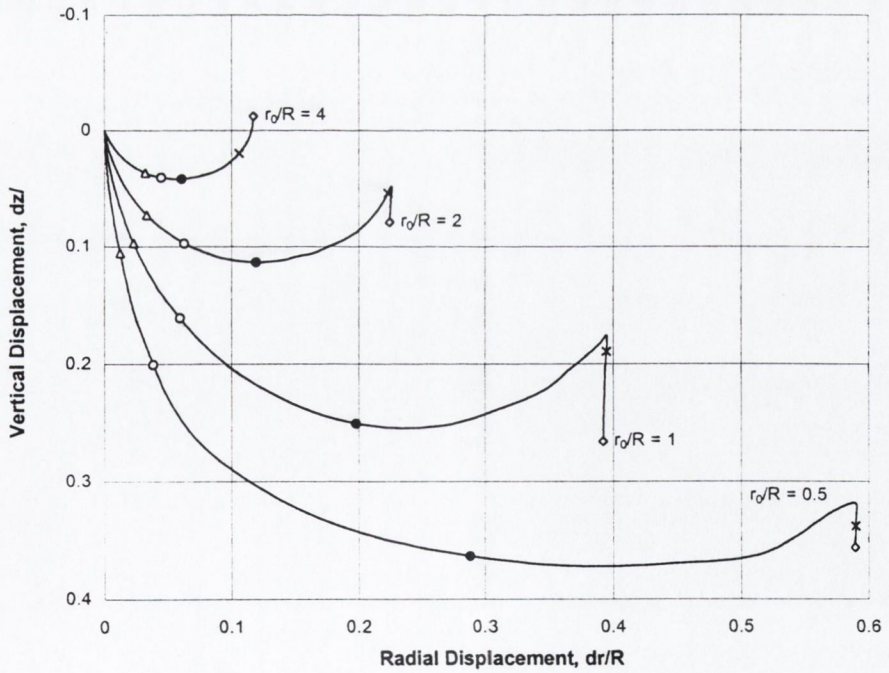

Figure 4.11. Displacement paths at r0/R = 0.5, 1, 2 & 4 for a 60° cone with 'full slip' flow conditions (Flow C) and $\mu = 1.2$

4.3.3 Displacements Around Flat-Ended Penetrometer

A comparison of the displacements for the 60° cone (Figures 4.8 & 4.9) and the flat-ended penetrometers (Figures 4.12 & 4.13) reveals the radial displacements for the flat ended are greater than for the cone tip, and the vertical displacements, particularly those very close to the penetrometer are significantly higher for the flat-ended tip. The radial displacements are approximately 10% higher for the flat tip close to the penetrometer and this difference reduces with increasing distance from the penetrometer. For flows with similar properties, vertical displacements are typically 2-3 times higher for the flat-ended penetrometer for $r_0/R < 2$, but become more similar to the cone-ended tip with increasing radial distance for the penetrometer.

4.3.3.1 Effect of viscosity (μ)

The effect of the fluid viscosity on the displacements around a flat-ended penetrometer is illustrated in Figure 4.12 using the 'full slip' flows H, I & J. Lower viscosity has the effect of reducing both the radial and vertical displacements. It should be noted that although the viscosity of Flow I is 250 times greater than Flow H their vertical movements are a closer match than Flows I and J, for which the viscosity differs only by a factor of four. This is because Flow I behaves as a low viscosity flow and Flow J, with Re = 2400, is close to the transition between laminar and turbulent flow and as such behaves more like a viscous flow.

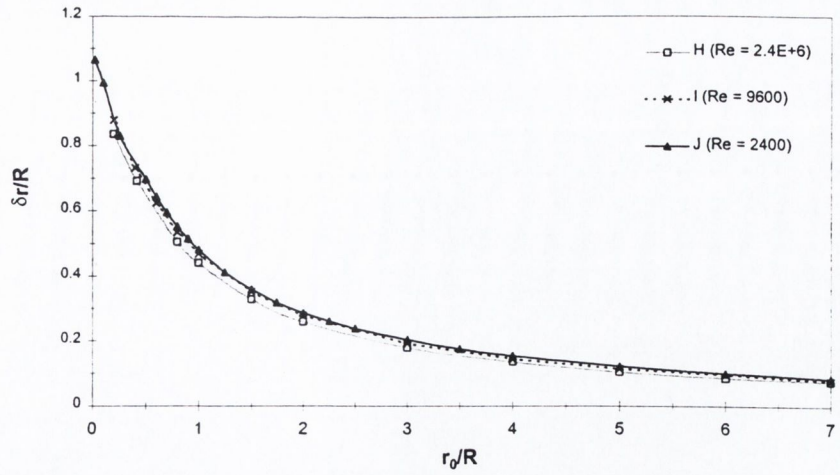

(a) Radial displacements

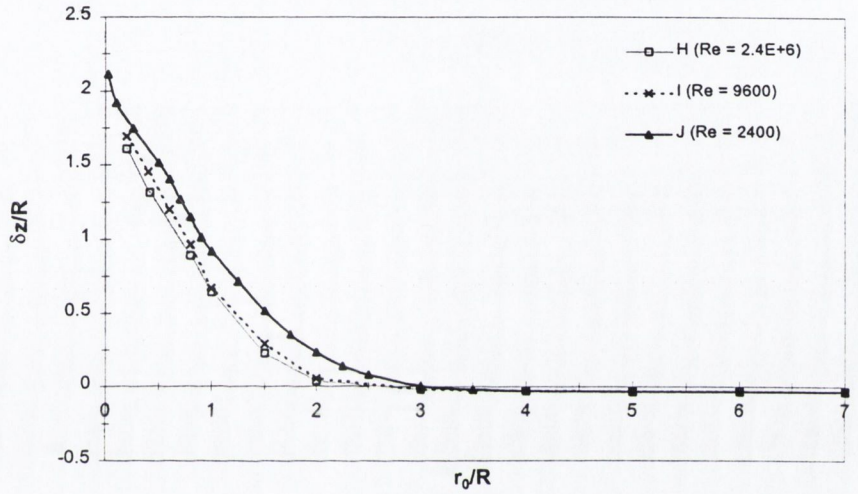

(b) Vertical displacements

Figure 4.12. Displacements at z/R = 20 around a flat-ended penetrometer for 'full slip' flow

4.3.3.2 Effect of slip condition

Increasing the friction on the penetrometer by reducing the velocity applied on its surface has the effect of increasing the radial and vertical displacement in the soil around it (Figure 4.13). This is most evident in the vertical movements, which show the partial slip flows of K & L (v_{pent}/U = 0.95 & 0.9, respectively) have considerably greater downward movement for $r_0/R < 3$ (approximately a 30 % and 60 % increase, respectively).

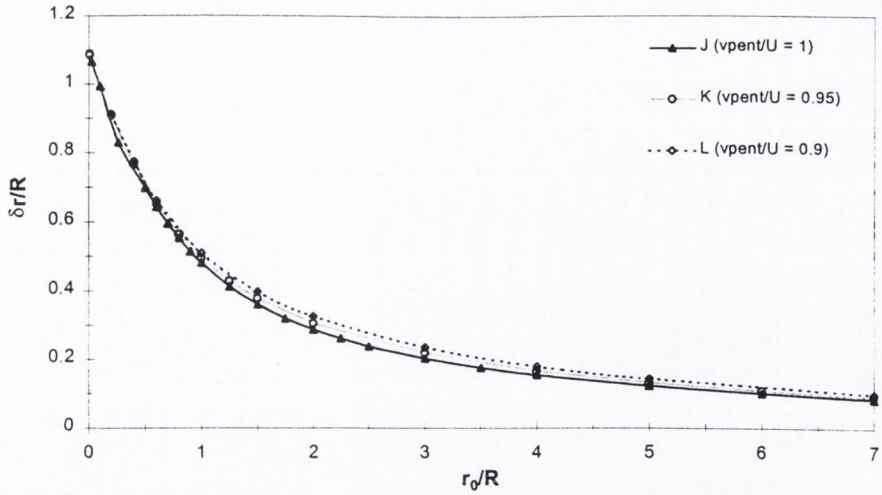

(a) Radial displacements

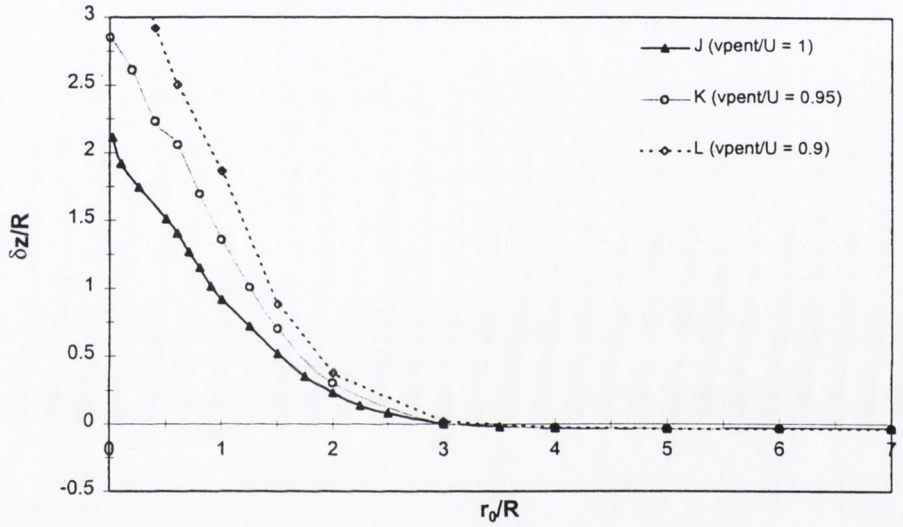

(b) Vertical displacements

Figure 4.13. Displacements at z/R = 20 around a flat-ended penetrometer for constant viscosity

4.3.3.3 Displacement paths for flat tip

The displacement paths around a flat ended penetrometer are investigated for four elements (r_0/R = 0.5, 1, 2 & 4) in Figure 4.14. For the elements close to the penetrometer (r_0/R = 0.5 & 1) a relatively large proportion of the downward vertical movement takes place behind the tip (i.e. $z/R > 0$). There are considerable differences between the displacement paths computed, for the 60° cone and flat tips; these may be summarised as:

- Close to the penetrometer ($r_0/R < 2$) vertical movements for the flat tip are typically 3 times greater than for the cone tip.

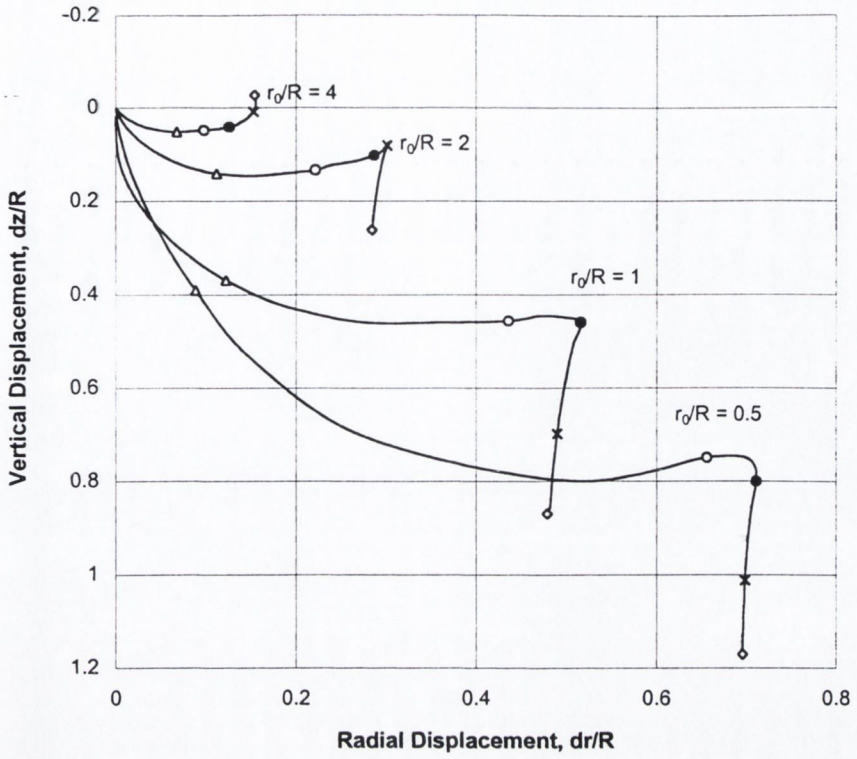

Figure 4.14 Displacement paths at $r_0/R = 0.5$, 1, 2 & 4 for a flat tip with 'full slip' flow conditions (Flow J) and $\mu = 1$

- Flat tip displacement paths show greater radial displacements.
- For the flat tip, the radial displacements in general reach a peak value close to tip ($z/R \approx 0$), although this maximum position moves further behind the tip with increased radial distance from the penetrometer (i.e., at $r_0/R = 4$ the peak radial displacement is at $z/R = 20$). For the 60° cone, peak radial movements close to the shaft occur behind the cone shoulder at $z/R \approx 3$-4 but peak radial movements occur at $z/R = 20$ for the streamline with $r_0/R = 4$.

4.4 SUMMARY OF FLOW EFFECTS

It has been shown that it is possible to predict a wide variety of strain paths using moderately different types of flow solutions. The effects of fluid viscosity, the velocity/slip condition on the penetrometer boundary and the tip geometry have been investigated and the main points are:

- Viscosity increases the range of disturbance caused by the penetrometer to the flow.

- Reducing the relative viscosity (i.e., introducing partial slip) increases both vertical and shear stain, respectively.
- A sharp penetrometer tip reduces disturbance and strain reversals.

The findings in this chapter from the investigation into the effects of the flow parameters are now summarised:

Strains

1. Increased viscosity has the effect of increasing the vertical compression and shear strains and, in general, increases the range of influence of the penetrometer and its specified boundary conditions on the surrounding soil elements.
2. Reducing the relative velocity (v_{pent}/U) on the penetrometer increases vertical compression and the shear strain. The cylindrical cavity strain shows a greater peak value but also a greater reversal and reduction with increased distance behind the tip.
3. The sharp tip of the 60° cone has a less disturbing effect on the soil than that of the flat ended penetrometer which shows greater E_1, E_2 and E_3 strains, although the flat tip also shows greater reversals for these strains.

Displacements

1. In general, lower viscosity reduces the disturbance to the soil of the penetrometer, and in particular reduces its range of influence in the radial direction.
2. Increasing friction on the penetrometer (by reducing the velocity) increases both the radial and vertical displacements. The vertical movements close to the penetrometer ($r_0/R < 2$) are most affected and even small changes in v_{pent}/U cause large increases in δz.
3. Vertical displacements are 2-3 times higher for the flat-ended shape close to the penetrometer ($r_0/R < 2$).
4. The radial displacements are typically ~10 % higher for the flat tip than for the cone, and peak values occur close to the tip of the flat-ended penetrometer ($z/R \approx 1$), and some distance behind the shoulder for the cone ($z/R > 3$).

Overall the strain and displacement paths indicate a smoother movement of soil around the cone shape, with peak behaviour occurring some way behind the tip. The flat shape causes greater disturbance to the soil and most peak behaviour occurs close to its tip.

CHAPTER 5
DEVELOPMENT OF A TRANSPARENT SOIL

Chapter 5

5.0 DEVELOPMENT OF A TRANSPARENT SOIL

5.1 INTRODUCTION

Chapter 2 reviewed the literature on experimental data for soil displacements around penetrometers, including the visual measuring techniques that have been used successfully with transparent granular material (e.g., crushed glass). It is proposed, in this Thesis, to add to the literature on soil displacements around penetrometers in clay, using a visual experimental measuring technique. It was necessary, therefore, to develop a transparent material with properties similar to clay and yet sufficiently transparent to allow a truly three dimensional test to be conducted. The actual laboratory model penetrometer test is described in Chapter 6, but the development of a transparent soil and a description of its geotechnical properties are presented in this chapter. A brief review of other studies in the area of transparent soils is first given to set in context the work done in this Thesis.

5.2 REVIEW OF TRANSPARENT SOILS

This section makes a brief review of previous studies into the development of transparent, porous materials which are capable of 'mimicking' the geotechnical properties of soils. To date, there have, strictly speaking, been two types of transparent 'soils' developed; the first is a transparent granular material developed by Allersma (1988), and the second is a transparent clay-type material which was developed by Mannheimer and Oswald (1993), and further researched by Iskander *et al.* (1994). This latter material with clay sized particles, was developed to study the transport of fluid through soil, and it was proposed to use a similar transparent 'soil' in this research for studying the deformation around penetrometers.

5.2.1 Transparent Granular Soil

Allersma (1988) developed a transparent two-phase medium for the purpose of observing, in two dimensional tests, the stress and displacement distribution during the installation of

a penetrometer (described in Section 2.3.2.2). The material used consisted of crushed glass and a fluid with a matching refractive index. When the crushed glass, which had a particle size of 2-3 mm, was submerged in this fluid it created a transparent medium. The crushed glass also possesses an additional photoelastic property which was used to indicate visually the distribution of stress around a penetrometer.

Shear box and triaxial tests conducted on the material found its constant volume friction angle to be 32° and 38° from these tests, respectively. The limited amount of testing performed on the crushed glass indicated its mechanical properties were similar to those of sand. An important characteristic of the material was the rapid degradation of transparency with increasing thickness. This imposes limitations on the type of tests that can be performed with this granular material, and Allersma (1988) was thus restricted to a 2-D laboratory test for a 3-D problem. The crushed glass with matching refractive fluid is therefore not truly transparent, but merely translucent. Despite these drawbacks, the simple formula of creating a soil-like material from solid particles and a fluid with a matched refractive index forms the basis of all transparent soils.

5.2.2 Transparent Clays

5.1.2.1 Initial investigations by Mannheimer and Oswald (1993)

Mannheimer and Oswald (1993) developed an approach for making transparent porous media for the purpose of observing 3-D flow processes. This approach involved consolidating suspensions of amorphous silica in liquids with matched refractive indices. The result was a porous material for which the porosity and permeability could be made comparable to a wide range of soils by the appropriate choice of particle size and consolidation pressure. This material was very different to the porous media produced by glass beads or crushed glass, which are rendered translucent rather than transparent due to local differences in the refractive index of the glass.

Silica with two different median particle sizes, of 1.6 μm and 25 μm respectively, were used by Mannheimer and Oswald (1993) in their study of transparent media. The silica was suspended in a blend of two oils; a medium viscosity white mineral oil and a low viscosity paraffinic solvent. The oil blend which produced the clearest suspension had a 1:1 ratio of

the two oils by weight, and resulted in a refractive index of 1.447 at 25°C. The viscosity and density of the oil at 23°C were 0.005 Pa s and 806 kg/m^3, respectively.

The superior optical transparency reported by Mannheimer and Oswald (1993) for the amorphous silica compared to that of glass beads or crushed glass is partly explained by the fact that the silica is made up of aggregates of primary particles that are in the order of 0.02 μm in size. These fine particles are smaller than the wavelength of light and thus do not cause it to scatter, hence improving transparency. A further reason is the porous nature of the aggregates, which allows them to absorb the pore fluid (of matched refractive index) and completely displace air from the internal pores that would prevent them from becoming transparent. The amount of absorbed oil was estimated to be 2.1 cm^3 of oil per gram of silica.

The main purpose of the investigations of Mannheimer and Oswald (1993) was to produce a transparent porous media for use in flow visualisation experiments, and therefore, the only material property tests conducted were with regard to the flow of pore fluid through the medium. The permeability and effective porosity (i.e., the porosity available for flow) were investigated for both silica sizes for different consolidation pressures. Constant head permeability test results were used to find the intrinsic permeability, k_i, calculated using Darcy's law;

$$k_i = \frac{Q\mu L}{A\Delta P} \tag{5.1}$$

where Q is the average flow rate, μ is the viscosity of the liquid, A is the cross-sectional area and ΔP is the pressure drop. The hydraulic conductivity, k, was then calculated using;

$$k = \frac{k_i \rho g}{\mu} \tag{5.2}$$

and this gave a hydraulic conductivity range of between 2.3×10^{-9} and 2.5×10^{-7} m/s. This range of permeability is comparable to the range typically reported for clays and silts. Mannheimer and Oswald (1993)

5.1.2.2 Further study by Iskander *et al.* (1994)

Iskander *et al.* (1994) extended the research of Mannheimer and Oswald (1993) by investigating the geotechnical properties of this transparent clay. The same type of silica, with particle sizes of 1.6 μm and 25 μm was used. The transparent soil was also made in the same way, by the consolidation of amorphous silica in an oil blend with a matching optical refractive index. After mixing, the suspension was transferred into a one-dimensional 'consolidometer' where it was subjected to pressures ranging between 70 and 700 kPa. Iskander *et al.* (1994) then performed conventional consolidation, permeability and triaxial compression tests on specimens trimmed from the consolidated samples.

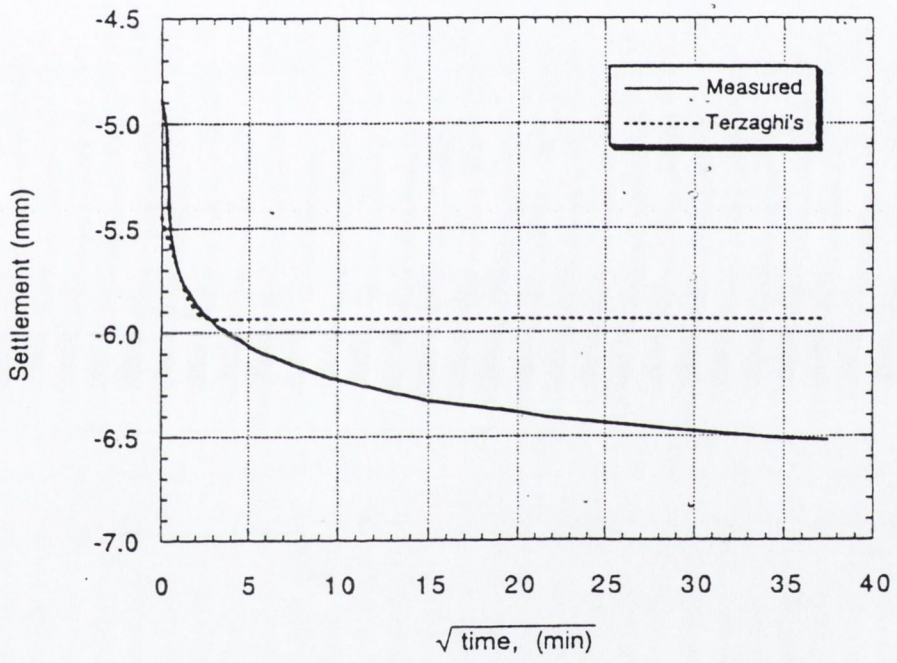

Figure 5.1. Measured and theoretical time settlement curves (Iskander *et al.*, 1994)

(i) Consolidation tests

The transparent soil consists of porous aggregates made up of smaller primary particles and after mixing with oil, the voids are filled with pore fluid. Iskander *et al.* (1994) speculated that the change in void ratio during consolidation represents the change in both the voids within and between the silica aggregates. Comparison between theoretical time settlement curves computed using Terzaghi's theory of consolidation and measured time settlement curves indicated that large secondary consolidation occurs (Figure 5.1). Iskander *et al.*

(1994) thought that two consolidation processes take place when a load is applied on a specimen; the first consolidation process involves the pores between the silica aggregates, while the second involves the pores inside the silica aggregates. It was found that most of the volume change occurred in the first hour after loading or unloading. The compression index, C_c, and recompression index C_r, were found to be 2.35 and 0.23, respectively. These values are somewhat higher than the values typically reported for natural clays, although the ratio of C_r to C_c is 0.1 and is within the range typically reported for natural clays. The coefficients of consolidation of the specimen were reported to be between 0.001 and 0.002 cm^2/s (3.2-6.3 m^2/year).

(ii) Triaxial tests & shear characteristics

Iskander *et al.* (1994) made some observations of the behaviour of transparent soils under loading from consolidated drained and undrained triaxial tests. The shape of the volumetric strain curves during shear were described as typical of soft clays and very loose sands. Large axial and volumetric strains were observed and explained by the continuous shear deformation of the silica aggregates as shear stress is applied. As discussed previously, silica aggregates adsorb significant amounts of fluid into internal voids and therefore may deform significantly more than the solid particles in natural soils when subjected to shear stress. Shear deformation of the silica aggregates allows an increasingly tighter packing arrangement of the aggregates so that more pore fluid is expelled and larger strains occur. In this respect, Iskander *et al.* (1994) speculated that transparent soils may resemble highly flocculated clay soils which can deform into tightly packed arrangements under loading.

Strains during shear were found to be characteristic of soft normally consolidated clays, although the peak strength of transparent soils was defined at 20% strain, which is larger than for most natural clays. The strength was consistent with the properties of stronger clays due to the low plasticity of the silica particles.

The initial and final void ratios of the tested specimens were also recorded. An oil residue was retained in the specimens after standard drying procedures were performed. Accordingly, void ratios were determined using corrected fluid contents, which were calibrated to account for incomplete fluid drying. The total void ratio is representative of the voids both within and between the silica aggregates and therefore does not correlate well with typical void ratios of natural soils. The interaggregate void ratio is thought to be

more representative than the total void ratio for geotechnical purposes (this is discussed later). The interaggregate void ratios computed ranged between 0.1 and 0.4, which are 10 to 50 times smaller than the corresponding total void ratios and are somewhat smaller than those for most natural soils.

5.3 TCD TRANSPARENT CLAY

5.3.1 Objective

The aim of this part of the dissertation was to produce a porous transparent material which exhibits geotechnical properties representative of natural clays, and could then be considered suitable for use in model penetrometer tests in 'undrained clay'. The transparent soil developed here is based on the work of Mannheimer and Oswald (1993) and Iskander *et al.* (1994). It is, however, different in the respect that it is made from different types of silica and oil to those previously used and is therefore referred to in the text as TCD transparent clay. For reasons of economy and convenience the materials were chosen for their availability locally. The material and geotechnical properties of the TCD transparent clay are described in the following section.

5.3.2. The Silica

The silica, or silicon dioxide (SiO_2) as it is also known, used in this and previous studies to make transparent media with soil-like properties, falls under the general term of *amorphous* silica. This distinguishes it from the crystalline form of silica, of which by far the commonest type is quartz, the main constituent of common sand. Common amorphous forms of silica consist of ultimate (primary) spherical particles of silica less than 0.1 μm in diameter. These particles may be separate or linked together as aggregates with siloxane bonding at the points of contact, as in gels, or in voluminous open networks of aggregated particles as in *fumed* silica and silica powders. Amorphous silica can be divided into two broad categories:

1. Anhydrous amorphous silica particles formed at high temperature, such as *pyrogenic* or *fumed* silica, and recovered from the gas phase as voluminous, extremely finely divided powders.

2. Surface hydroxylated amorphous silica particles grown from supersaturated aqueous solutions. The soluble silica comes out of solution as spherical amorphous particles and are aggregated into a gel network or are coagulated as a *precipitate*.

5.3.2.1 Precipitated Silica

The silica type used in the studies of Mannheimer and Oswald (1993) and Iskander *et al.* (1994) is termed *precipitated* silica and falls in the second category. This precipitated silica is formed when the ultimate (primary) silica particles are coagulated in an aqueous medium, recovered, washed and dried. The ultimate particle sizes for the silica in these studies was reported to be approximately 20 nm. When the ultimate particles are larger than 5-10 nm, as is the case, they may only be joined weakly together in an open packed condition and can be subsequently easily broken apart and dispersed in liquids such as oil.

5.3.2.2 Fumed Silica

The silica used in this study is termed *fumed* silica and falls in the first category described. Fumed silica powders are made by condensing silica from the vapour phase at elevated temperature. The powder consists of aggregates of submicron particles that are linked together in extremely weak networks. In powders the ultimate or primary particles are always aggregated into what have been variously called 'secondary particles', 'clusters' or most commonly 'aggregates' and are not dispersible without mechanical rupture. Theoretically, a silica powder might consist of separate, discrete silica particles, but when the particle diameter is less than 100 nm, the particles spontaneously adhere together in loose aggregates. It is only when the particles are much larger, that is, 5-50 microns that the cohesive forces become so low that the particles do not attract each other.

The fumed silica used here is manufactured by Sigma and its properties are given in Table 5.1. The manufacturers describe the fumed silica as: "extremely fine, snow white, fluffy powder with interesting thickening and thixotropic properties, and an enormous external surface area". The primary particles, which have a diameter of 0.014 μm, are said to form "branched, chain-like aggregates a few tenths of a micron long".

In its original form as a fluffy powder, the fumed silica is very bulky by nature, as indicated by its density of 36.8 kg/m^3 in an uncompacted state, and this makes it difficult to determine any definite pores. The particle packing for this type of silica has been studied experimentally and reported by Iler (1979). Very fine silica powders, of uniform particle size in a voluminous state of low bulk density, have been mechanically compressed and the surface area and porosity measured. In the voluminous state, each silica particle touches only two, and at most three other particles, but when it is mechanically compressed there are more and more inter-particle contacts. The particle arrangements for different silica packing densities are shown in Figure 5.2. As the confining pressure is increased, the surface area as well as the porosity of the silica, is reduced. This relationship between the co-ordination number (the number of particle contacts) and the pore volume is also shown in Figure 5.2.

The manufacturers description of the fumed silica as forming branched, chain-like aggregates a few tenths of a micron long indicates its initial particle structure is one of a loose packing arrangement with large voids such as given by the co-ordination numbers 3-2-3 or 3-2-2-3. This is also compatible with the bulk density of the uncompacted fumed silica (37 kg/m^3) which has a pore volume of 58 cm^3/g.

COORDINATION NUMBER	VOLUME %		PORE VOL.
	SOLID	PORES	$cm^3 g^{-1}$
12	74.5	25.5	0.155
6	52	48	0.42
3	5	95	8.6
3-2-3	1.3	98.7	35
3-2-2-3	0.83	99.17	54

Figure 5.2. The relationship between the co-ordination number (number of particle contacts) and the pore volume (Iler, 1979)

Table 5.1. TCD Transparent soil: material properties

Material†	**Crystal Light Liquid Paraffin**	**Mineral Spirits**	**Oil Blend‡**	**Fumed Silica**
Manufacturer	Morris Lubricants	Aldrich Chemicals	-	Sigma
Density (kg m^{-3}) at 20°C	845	752	817.1	2200*
Measured density (kg m^{-3})	840	747	812.7	2150
Viscosity (mPa s)	19	0.08	8	-
Refractive index	1.469	1.424	1.456	1.46
Particle Size (μm)	-	-	-	0.014
Surface Area (m^2 g^{-1})	-	-	-	200 ± 25

† All properties at 20°C

* Uncompressed fumed silica; bulk density = 36.8 kg m^{-3}; particle density, ρ_s = 2200 kg m^{-3}

‡ 70% Crystal light liquid paraffin and 30% mineral spirits

When the silica is initially mixed with the blended oil it forms a viscous liquid. After mixing, sedimentation while in storage caused by gravity results in the formation of a concentrated viscous layer at the bottom of the oil-silica mixture. Application of consolidation pressure to the slurry, while allowing drainage to take place, increases the packing density and decreases the oil content, thus creating a material with more clay-like properties. Electron microscope images of the compressed silica show the soil to be made up of colloids (aggregates) approximately 0.08 to 0.35 μm in diameter after consolidation to 225 kPa, as can be seen in Figure 5.3. The electron microscope pictures of the soil were obtained after conventional oven drying to remove excess oil. This was deemed necessary as the oil vaporises in the vacuum of the microscope creating problems with imaging. The colloidal aggregates shown are made up of the primary 0.014 μm diameter particles in structures similar to that given by a co-ordination number of 3, as shown in Figure 5.2 (this is discussed in detail in Section 5.3.4.4). The spherical shape of the silica aggregates in Figure 5.3 can be contrasted with the 'plate-like' structure of the natural clay minerals in Figure 5.4 (of Boston Blue clay).

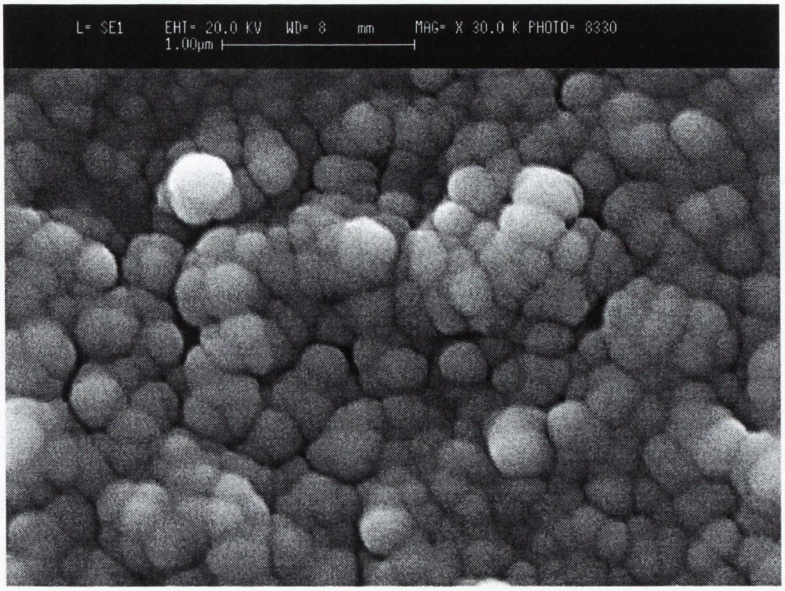

Figure 5.3. Electron microscope image of TCD transparent clay magnified 30,000 times (after consolidation to 225 kPa).

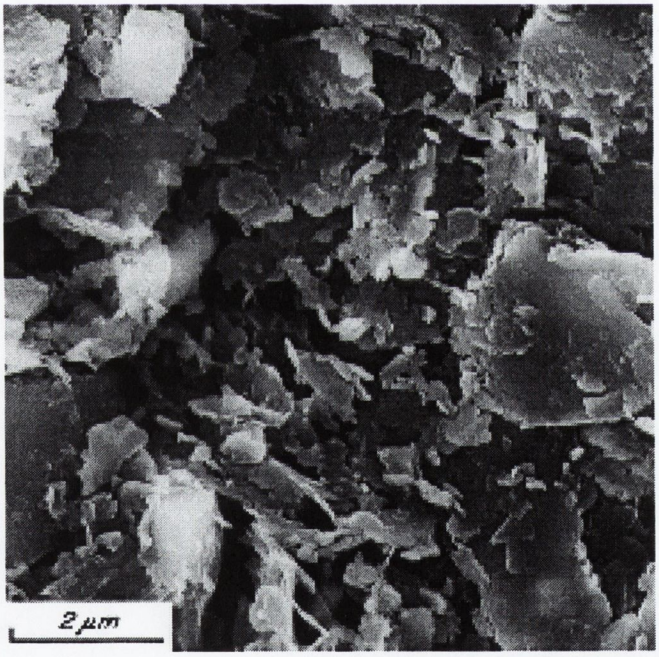

Figure 5.4. Electron microscope image of undisturbed Boston Blue clay (Mesri & Ali, 1999)

5.3.3. Properties Of The Pore Fluid

5.3.3.1 Determining the optimum refractive index for the pore fluid

To create a transparent porous media, it is necessary, to match the refractive properties of the pore fluid with the solid particles. In this Thesis, a blend of two oils was used to

achieve the refractive properties that give the best soil transparency; crystal light liquid paraffin and mineral spirits, the properties of which are given in Table 5.1. It was possible to achieve different refractive index values by changing the blend ratios of the two oils. Before a successful blend could be achieved, it was first necessary to set a target refractive index for the soil, although it was not initially certain what this target refractive index should be.

The silica used, which is a type that falls under the general label of *amorphous*, was reported by the manufacturers to have a refractive index of 1.46. This value is confirmed by the graph in Figure 5.5, taken from Iler (1979), which plots refractive index against density for different types of silica, including the amorphous type used here. Information on the silica from the literature and from the manufacturers, therefore, suggested 1.46 to be the optimum refractive index. However, previous work in the area of transparent soils by Mannheimer and Oswald (1993) and Iskander *et al.* (1994) found that a value of 1.447 for the refractive index produced the clearest soil, using a similar though not identical silica. To achieve target refractive indices of 1.46 or 1.447 using the oils in this research, required ratios of the liquid paraffin and mineral spirits of approximately 80:20 and 50:50 respectively. These are obviously two very different mixes, each with different properties.

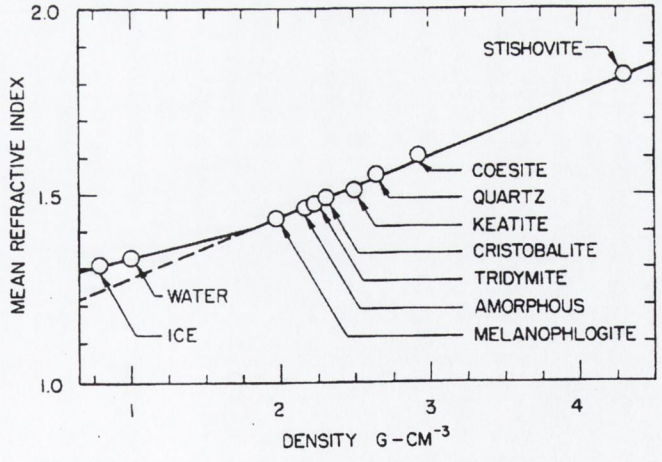

Figure 5.5. Density versus refractive index for various forms of silica (Iler, 1979)

The lack of definitive information regarding the optimum refractive index together with the temperature dependant nature of oil properties, meant it was important to conduct a visual assessment of different oil blends to determine the best mix. Each oil and silica mix was

assessed for clarity by placing beakers containing the slurries over paper marked with a fine square grid. It was then a simple inspection process to find the optimum oil ratio. The temperature factor was an important consideration, not least because the refractive properties of the transparent soils used by Mannheimer and Iskander have been quoted at 25°C, and the refractive properties of oil are normally given at 20°C. It was necessary, therefore, to interpolate all refractive properties to a base temperature of 20°C. The comparison studies were conducted at room temperature (approximately 20°C) and these indicated the clearest mixtures to be those at ratios of 70:30 and 80:20, of liquid paraffin to mineral spirits. It was not possible to visually determine a difference in quality between these two oil blend ratios.

5.3.3.2 Viscous effects of silica concentration

These comparison studies also allowed an assessment of the effects of different concentrations of the fumed silica on the slurry's viscosity. If the concentration of silica is too high, the mixture becomes too viscous for the air bubbles to come out of suspension and it becomes an opaque white paste. It is important, however, that the silica concentration is as high as possible in order to minimise the quantity of fluid within a soil sample. Mannheimer and Oswald (1993) and Iskander *et al.* (1994), used initial concentrations of 20 % by weight for silica with a mean particle size of 25 μm, and 9 % for a particle size of 1.6 μm. The smaller particle sizes cause a greater increase in viscosity and hence require a lower initial concentration, due primarily to their greater surface area per unit weight. The primary particles of the silica used in this research had a mean size of 0.014 μm and a large surface area of 200 ± 25 m^2/g. The initial concentration of silica was therefore expected to be lower than that used in the other studies.

The viscosity of the oil blend, before silica was added, also had a large influence on the quantities of silica that could be added to the mixture. Increasing the percentage of mineral spirits decreases the viscosity and allows greater concentrations of silica, thus reducing the amount of consolidation necessary to produce a solid sample. It was advantageous, therefore to choose the oil blend ratio of 70:30, which has a lower viscosity than the 80:20 blend. It was found that for this blend the maximum initial concentration of silica was approximately 7% by weight (it was 6% for a 80:20 ratio). Although the 80:20 blend was calculated to have a refractive index of 1.46 at 20°C, it was expected that the model pile

testing would be conducted at slightly lower temperatures and this would increase the oil refractive index by small amounts.

In summary, the oil blend found to have the most advantageous properties was a 70:30 ratio of liquid paraffin to mineral spirits and this produces an oil with a refractive index of 1.456 and a density of 817.1 kg/m^3 at 20°C. This density is slightly higher than the oils used by Mannheimer and Oswald (1993) or Iskander *et al.* (1994), which had densities of 804 kg/m^3 and 806 kg/m^3 at 23°C respectively. The bulk modulus, K of the oil blend is approximately 1.6 GPa (at atmospheric pressure and at 20°C) and is therefore assumed to be incompressible (K for water is 2.05 GPa).

5.3.4 Geotechnical Characteristics of the TCD Transparent Clay

5.3.4.1 Phase relationships for slurry and soil

The techniques and formulae used to calculate the solid and liquid phase relationships, both as a soil and in the initial state as a slurry, are outlined here. The maximum silica content by weight that could be added to the oil blend in the initial mixing phase, for viscous reasons, was approximately 7%, as mentioned above. This weight fraction of silica resulted in a mixture that could be de-aired within a few hours. The disadvantage of a low silica content was that it increased the volume of slurry necessary to create a sample. At the mixing stage the weight fraction of the silica present is known and the density of the silica-oil mixture, ρ_m, can be found from;

$$\rho_m = \frac{\rho_s \rho_l}{\rho_s x_l + \rho_l x_s} \tag{5.3}$$

where ρ_s and ρ_l are the known silica particle and pore oil densities, and x_s and x_l are the weight fractions of the solid and liquid parts, respectively. However, if the weight fraction is not known, which was the case after consolidation, this can be found by measuring the soil density (ρ_m) and by rearranging (5.3):

$$x_s = \frac{\rho_s(\rho_m - \rho_l)}{\rho_m(\rho_s - \rho_l)} \tag{5.4}$$

The volume per unit weight for solids, V_s, and for the pore fluid, V_l can then be found;

$$V_s = \frac{m_s}{\rho_s} \qquad V_l = \frac{m_l}{\rho_l} \tag{5.5}$$

The soil is assumed to be fully saturated and therefore, $V = V_s + V_l$. The void ratio, e, and the porosity, n, can then be found;

$$e = \frac{V_l}{V_s} \qquad n = \frac{V_l}{V} = \frac{e}{1+e} \tag{5.6}$$

Both the oil and silica particles are considered to be incompressible and so, therefore, is the oil-silica blend if it is completely de-aired.

5.3.4.2 Consolidation tests on TCD transparent clay

The test results from a series of consolidation tests to 25, 50, 100 and 200 kPa are shown in Table 5.2. Consolidation was performed in a 60 mm square shear box, and following consolidation the samples were sheared.

Table 5.2. Soil properties measured during consolidation tests

Consolidation Pressure, σ'_v (kN/m^2)	**25 (NC)**	**50 (NC)**	**100 (NC)**	**200 (NC)**	**25 (OC)***
Coeff. of Volume Compressibility, m_V (m^2/MN)	4.90	5.42	2.61	1.18	0.42
Coeff. of Consolidation, c_V (m^2/year)	13.34	1.65	0.41	0.24	0.93
Compression Index, C_c/C_s	5.76	6.99	6.85	5.37	0.34
Slope of normal compression line, λ,	2.50	4.14	2.98	2.33	-
Secondary Compression Index, C_α	0.418	0.263	0.209	0.196	0.257
Hydraulic Conductivity for oil, k (m/s)	1.66×10^{-8}	2.89×10^{-9}	2.74×10^{-10}	7.15×10^{-11}	1.1×10^{-10}
NC - Normally consolidated; OC - Overconsolidated *OCR = 8.					

The void ratio-consolidation pressure relationship of this sample of transparent soil is shown in Figure 5.6 for primary consolidation only (changes in void ratio due to secondary

creep are not included). For an incremental increase in effective stress from σ_0' to σ_1' and a decrease in void ratio from e_0 to e_1, the coefficient of volume compressibility, m_v, and the compression index, C_c, are given by:

$$m_v = \frac{1}{1+e_0}\left(\frac{e_0 - e_1}{\sigma_1' - \sigma_0'}\right) \tag{5.7}$$

$$C_c = \frac{e_0 - e_1}{\log(\sigma_1'/\sigma_0')} \tag{5.8}$$

The swelling index, C_s likewise, is given by (5.6) on the swelling line.

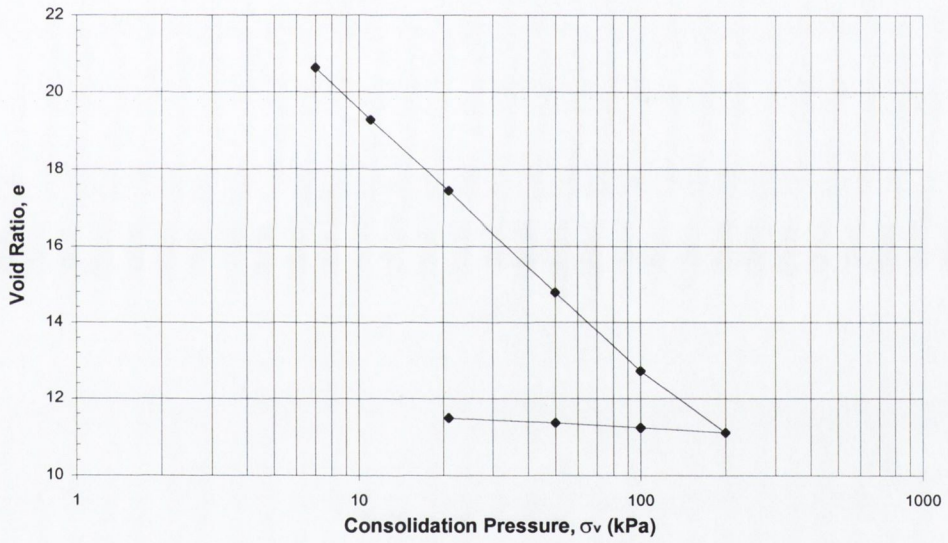

Figure 5.6. 1-D consolidation test on TCD transparent soil

The slope of the normal compression line, λ, and the slope of the unloading-reloading line in the v:lnσ_v' plane are given as:

$$\lambda \cong \frac{C_c}{\ln 10} \; ; \qquad \kappa \cong \frac{C_s}{\ln 10} \tag{5.9}$$

The value of the compression index in a normally consolidated state ($C_c \approx 6$) is very high but reflects the large reduction in fluid content during these 'formation' stresses, i.e., while a stiff sample is created from the initial slurry state.

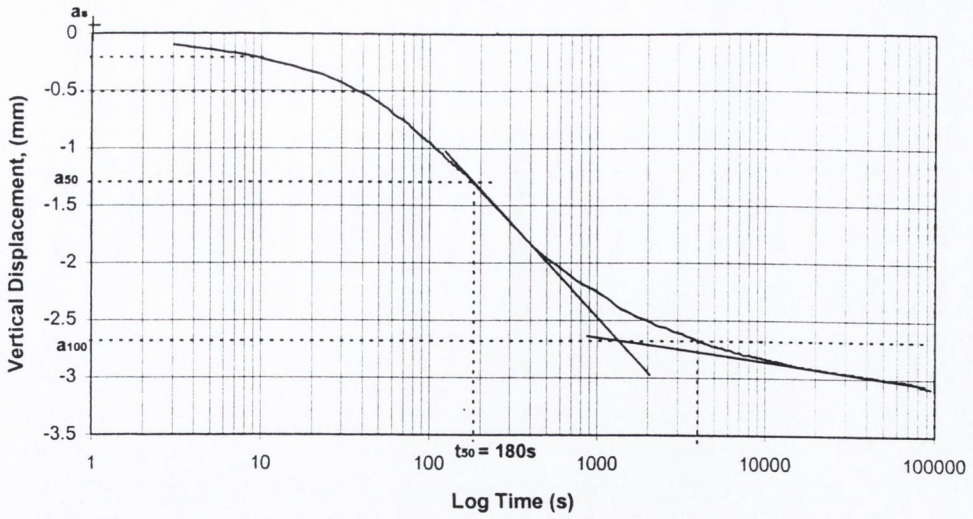

Figure 5.7. Settlement-log time consolidation plot for transparent clay; increment 25 → 50 kPa

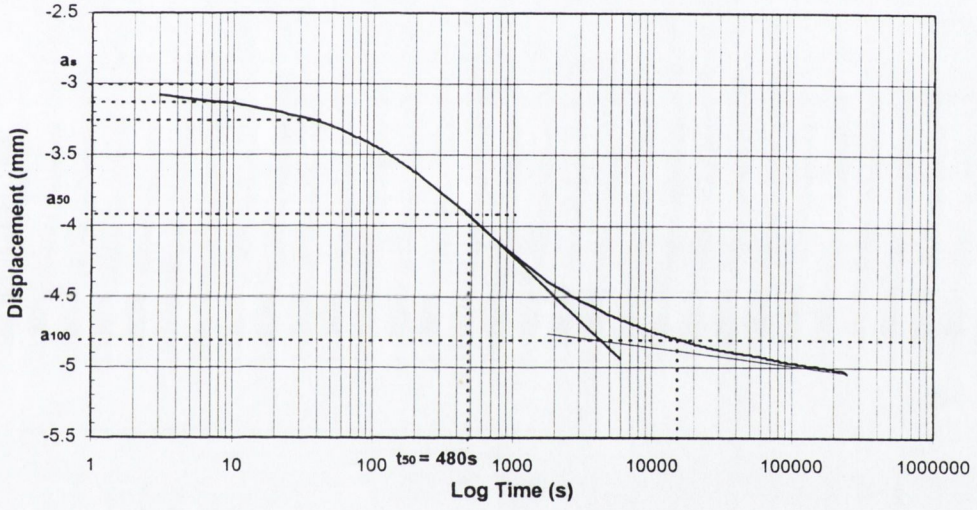

Figure 5.8. Settlement-log time consolidation plot for transparent clay; increment 50 → 100 kPa

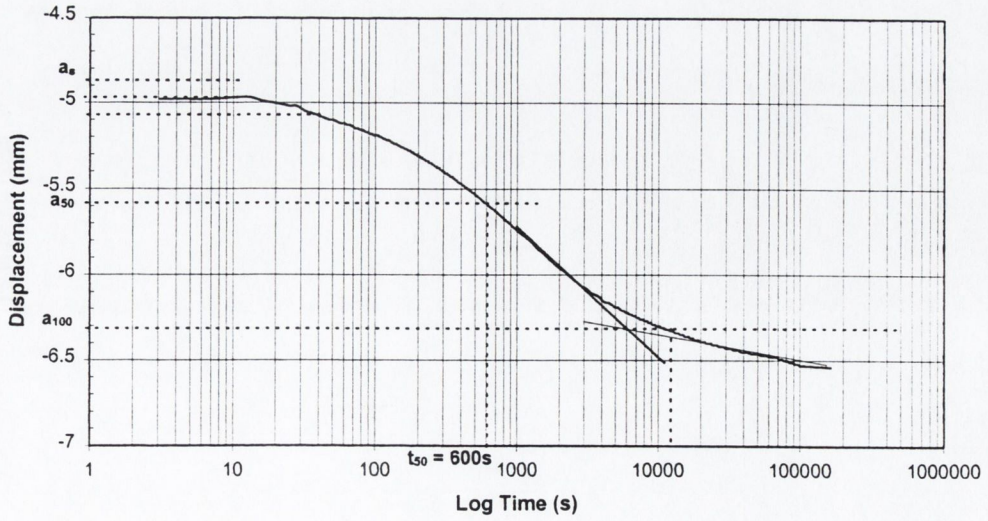

Figure 5.9. Settlement-log time consolidation plot for transparent clay; increment 100 → 200 kPa

The compression-log time curves at consolidation pressures of 50, 100 and 200 kPa are shown in Figures 5.7, 5.8 & 5.9 respectively. The curves are marked to show the settlement values a_s, a_{50} and a_{100} that correspond to the initial starting point (accounting for initial compression), 50% and 100% primary consolidation. Where the lines marked for these 'a' values intersect the time-settlement curve the times for 100% and 50% consolidation can be found (i.e., t_{100} and t_{50}). The coefficient of consolidation, c_v, is found from these time settlement curves using the Casagrande method to find the start and end of primary consolidation, and then by applying;

$$c_v = \frac{0.196d^2}{t_{50}} \tag{5.10}$$

where d is the maximum length of the drainage path and t_{50} is the time for 50% primary consolidation.

Beyond the end of primary consolidation, the compression of the soil continues at a slower rate for an indefinite period, and this is the secondary compression. The rate of secondary compression can be defined by, C_α, the secondary compression index (or coefficient of secondary consolidation) and is found from the final (or post primary) part of the compression-log time curve. C_α is the change in void ratio over a log cycle of time, and if this time increment is given by t_0 and t_1, then:

$$C_\alpha = \frac{e_0 - e_1}{\log(t_1/t_0)} \tag{5.11}$$

The secondary compression index, as can be seen from Table 5.2, lies within the range 0.19-0.42 for the TCD transparent clay. This range is extremely high and is comparable only to highly plastic clays or organic soils. However, in a heavily overconsolidated state unload time-settlement curves show the secondary compression index to be significantly lower, in the order of 0.02, which is comparable to natural clays. The ratio of $C_\alpha/C_c \approx 0.05$ is high, but not untypical of natural clays.

Once m_v and c_v values have been obtained for a particular stress increment, the coefficient of permeability (or hydraulic conductivity) can be found from;

$$k = c_v m_v \gamma_l \tag{5.12}$$

where γ_l is the unit weight of the pore fluid. The permeability values obtained are plotted in Figure 5.10 against the consolidation pressure, and are shown alongside the values found by Mannheimer and Oswald (1993). There is a clear relation, evident from this plot, between the aggregate particle size and permeability of these transparent soils. The strongly non-linear k:σ'_v relationship displayed by the TCD transparent soil is thought to be partly due to changes in aggregate size during consolidation is discussed further in Section 5.3.4.4. It should be noted that the viscosity of the oil blend has an influence on permeability of the transparent soil, and therefore has some temperature dependence although this was not investigated with all consolidation tests conducted at approximately 20 °C.

The values for the coefficient volume compressibility, m_v found from the consolidation tests provide a reliable comparison of the compressive properties of the transparent clay with natural clays. The m_v values are not dependent on the absolute values of the void ratio, which appear high due to the nature of the material, but are a measure the volume changes in the soil under compression. The transparent clay was found to have an m_v range of 1.18-5.4 m^2/MN (Table 5.2), which is comparable with normally consolidated alluvial clays (high compressibility, 0.3-1.5 m^2/MN) and very organic alluvial clays and peat (very high compressibility, >1.5 m^2/MN).

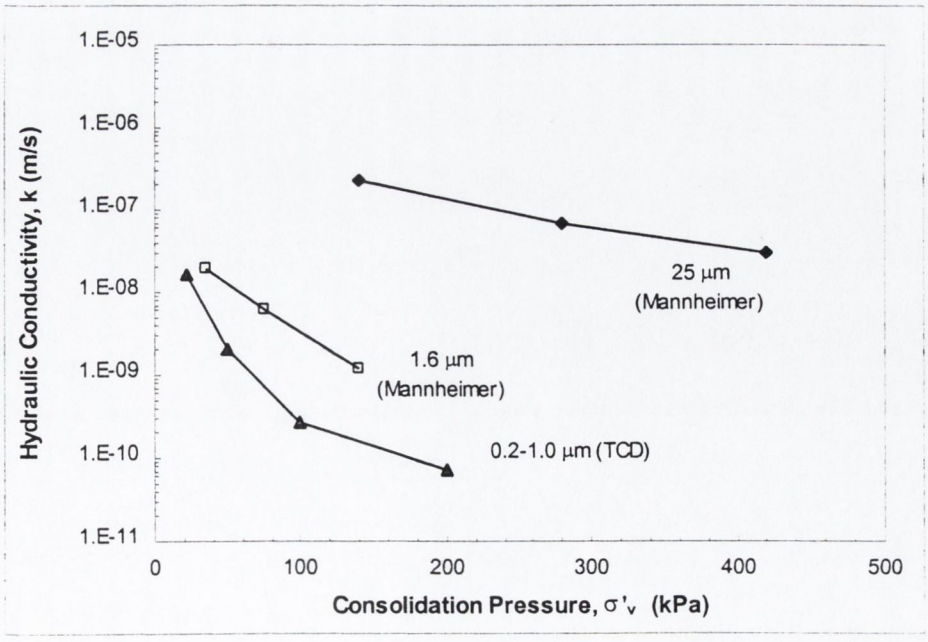

Figure 5.10. Effect of consolidation pressure and particle size on permeability of transparent soil

Likewise, the values obtained for c_v, which are in the range 0.24-1.65 m^2/year, are comparable with typical values for a normally consolidated alluvial clay (0.4-1.7 m^2/year for a soft alluvial clay that underlies Tokyo International Airport). However the high values obtained for the compression index, C_c = 5.4-7.0, result from the high void ratio of the material and are approximately 10 times higher than values typically reported for natural clays. As has been mentioned, this is reflected by the high liquid-solid ratio (e) of the transparent clay, which at the slurry stage is in the region of 30:1. This is ten times higher than is typically required to achieve a slurry state for kaolin, which requires a void ratio, $e \cong 3.1$ (Al-Tabbaa & Wood, 1987).

The properties of the transparent clay in an overconsolidated state at 25 kPa (OCR = 8) are also given in Table 5.2 and are particularly relevant as the soil used in the model tests is heavily overconsolidated. The values of m_v (0.42 m^2/MN), c_v (0.93 m^2/year) and compression index (0.34) for overconsolidated transparent clay are consistent with the geotechnical properties of soft clay.

5.3.4.3 Effective porosity and interaggregate void ratio

The high porosity and void ratio of the transparent clay, which is evident in Table 5.2 and Figure 5.6, is due in main to the porous nature of the colloids that make up the soil. Even after standard drying procedures were performed an oil residue was retained in the specimens. The total void ratio, e, is representative of the voids both within and between the silica aggregates, and therefore does not correlate well with typical void ratios of natural soils. Iskander *et al.* (1994) considered the interaggregate void ratio to be more representative than the total void ratio for geotechnical purposes. The interaggregate void ratio can be estimated using the hydraulic conductivity and the average estimated aggregate size from the Blake-Kozeny equation;

$$\frac{(e^*)^3}{(1+e^*)} = \frac{150k\mu}{\gamma_l D_p^2} \tag{5.13}$$

where,

e^* = interaggregate void ratio,

D_p = aggregate size, estimated in this case from electron microscope images,

k = hydraulic conductivity, determined from c_v and m_v values measured during consolidation,

μ = absolute viscosity of the pore fluid, taken as 8×10^{-3} Pa s,

γ_l = unit weight of pore fluid, which for the oil used was 8.2 kN/m^3.

The effective porosity, n^*, which is the porosity available for flow, may also be more comparable to the porosity of a natural soil and is found from;

$$n^* = \frac{e^*}{1+e^*} \tag{5.14}$$

5.3.4.4 Aggregate-pore fluid relationship in TCD transparent clay

Within the TCD transparent clay, unlike natural clays, a large percentage of the pore fluid is not free to drain during consolidation, or evaporate even when dried in an oven. Instead, a large percentage of the total pore fluid is 'locked' within the aggregate particles, or bound to individual silica particles as adsorbed fluid.

It is thought that the oil within the transparent clay can be in one of three possible states with regard to drainage, (this is demonstrated schematically in Figure 5.11):

(A) The first possible state for the pore oil is to be outside the aggregate particles, and is thus free to drain should conditions so dictate. The movement of this oil is thought to be the main contributor to the permeability characteristics of the soil and it dominates the period of primary consolidation. Thus, if the volume of this 'free' oil within the soil is reduced (as it is during consolidation) the permeability will also reduce accordingly.

(B) The second possible state for the pore oil is to be within the actual aggregate particles themselves, as is shown in Figure 5.10. This fluid does not have the same freedom to move within the material as the oil described in (A). Its volume within the soil mass is, however, sensitive to any particle rearrangements within the aggregates, such as increased packing during consolidation. The porous nature of the aggregates suggests they are permeable and this characteristic is clearly dependent on the density of packing of the ultimate particles. However, it is the view of the author that the overall

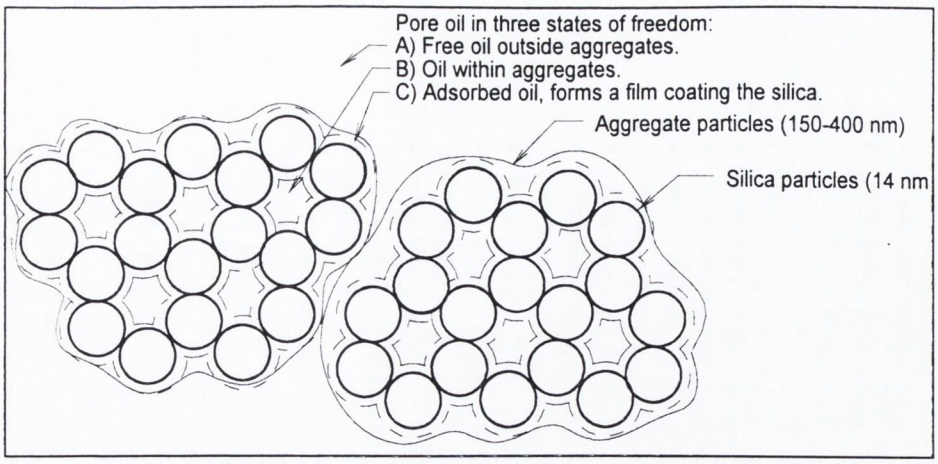

Figure 5.11. Schematic diagram showing three states for pore fluid within silica

contribution of this oil to the permeability of the material is small (especially after consolidation to pressures greater than 50 kPa).

(C) The third state for the pore fluid is as a residual oil that is bound to the individual spherical silica particles. The adsorbed oil, which coats each particle, is chemically bound to it by strong surface forces (Iler, 1979). The volume of this adsorbed oil is dependent on the particle size, and for a diameter of 14 nm this residue of oil is estimated to be approximately 1.6 cm^3 per gram of silica. This figure is estimated from studies by Kieslev reported by Iler (1979) of water adsorption in silica with different particle sizes.

The particle packing scheme present within the aggregates shown in Figure 5.11 has been deduced from Figure 5.2 which shows the packing arrangements corresponding to pore volume percentages. A co-ordination number of 3 corresponds to a pore volume of 95%, which is close to the pore volume range of 94.6-90.6 % present during consolidation from 25-200 kPa (calculated from the changes in void ratio). The changes in the distribution of the pore fluid within the soil during consolidation is shown in Table 5.3. The reduction in the volume of 'free' oil with increasing pressure is consistent with the reduction of permeability found during consolidation tests.

The permeability of the transparent soil is considered to be linked to the 'free' pore oil rather than the total volume of voids and this is investigated in Figure 5.12, which plots adjusted void ratios against consolidation pressure. Three relationships for the

Table 5.3. Distribution changes of the pore fluid within the soil during consolidation

Consolidation Pressure	Estimated Aggregate Size	A. 'Free' Pore Fluid		B. 'Unbound' Aggregate Pore Fluid		C. Adsorbed Oil	
(kPa)	(μm)	(cm^3/g)	(%)	(cm^3/g)	(%)	(cm^3/g)	(%)
25	1.0	0.86	10.7	5.52	69.0	1.6	20.2
50	0.5	0.65	9.8	4.03	66.4	1.6	23.8
100	0.3	0.51	8.8	3.14	63.6	1.6	27.7
200	0.2	0.34	7.0	2.45	61.3	1.6	31.2

interaggregate void ratio, e^*, which represents the oil free to drain, are plotted. Two of these relationships are based the Blake-Kozeny equation in (5.13):

(i) e^* has been calculated from the Blake-Kozeny equation and the permeability values found from consolidation tests, by assuming a constant aggregate size D_p (found from electron microscope images which were taken after normal consolidation to 225 kPa).

(ii) The Blake-Kozeny equation is also plotted using adjusted values of the aggregate size, D_p to give a linear e^*:logσ'_v relationship. The estimated changes in aggregate size at the lower consolidation pressures were based on the observed aggregate size at the end of consolidation (i.e., at 225kPa), and are given in Table 5.3.

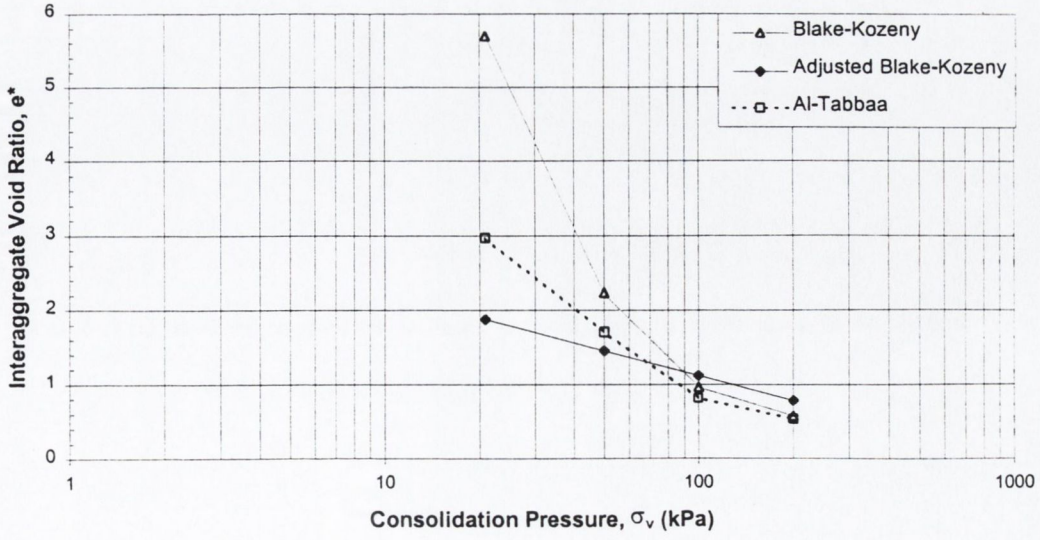

Figure 5.12. 1-D consolidation for 'free' pore fluid

The linear relationship of the normal consolidation line for the adjusted Blake-Kozeny method reinforces the point of view that aggregate size changes take place during consolidation.

A third relationship for reconstituted clays has been applied in Figure 5.12, which was developed from experimental studies by Al-Tabba & Wood (1987) on kaolin, between the void ratio and permeability of clays, and is given by:

$$k = 0.53(e^*)^{3.16}\left(\times 10^{-9} ms^{-1}\right) \tag{5.15}$$

This relationship has been used with permeability values for the TCD transparent clay found from consolidation tests, and this gave void ratios that are typical of natural clay (plotted in Figure 5.12). It should be noted that the Al-Tabba & Wood relationship is for water and no adjustment has been made for the difference in viscosity of the oil (~8 times higher). The author is unsure how to account for this but since the relationship has been used for purely demonstrative purposes this is not considered to be very significant. These void ratios are considered to be effectively the interaggregate void ratio (e*) of the soil and are shown to be far closer to e* found from the Blake-Kozeny equation than to the total void ratio (e) of the soil. The values of total and interaggregate void ratio for the transparent soil can be compared in Table 5.4. The total void ratio is approximately 10 times the interaggregate void ratio.

Table 5.4. A comparison total and interaggregate pore fluid

Consolidation Pressure (kPa)	**25**	**50**	**100**	**200**
Total Void Ratio, e	17.56	13.83	11.55	9.68
†Interaggregate Void Ratio, e*	1.88	1.45	1.12	0.78
e/e*	9.3	9.5	10.3	12.5
Porosity, n	0.946	0.93	0.92	0.91
Effective porosity, n*	0.65	0.59	0.53	0.44

† calculated using the adjusted Blake-Kozeny method

5.3.4.5 Consolidation of the TCD transparent clay within the test chamber

The glass chamber, which is described in Chapter 6, and is used to contain the transparent soil for the model penetrometer tests, has an internal volume of almost 35 litres. To mix the

quantity of the silica-oil slurry needed to fill the chamber, required suitably sized mixing equipment. A concrete mixer with a very low speed was used for this purpose and it was important that mixer, and all other equipment used, was dirt and dust free to ensure the minimum degradation of soil transparency. The objective was to produce a soil sample that was approximately half the depth of the test chamber (~0.4 m) after consolidation. Predictions from consolidation tests suggested that the material would lose in the region of two thirds of its original volume at a pressure of 250 kPa. It was necessary, therefore, to add additional quantities of the slurry into the test chamber during consolidation but without creating a non-homogeneous material. This was a simple matter as the greatest volume changes took place under self weight directly after placing the slurry in the chamber and, therefore, could be topped up as the slurry level dropped. The e:logσ'_v curve for primary consolidation only, measured within the test chamber is shown Figure 5.13.

Table 5.5. Phase relationships for transparent clay before and after 1-D consolidation to 225 kPa

	Before Consolidation (in slurry form)	After Consolidation to 225 kPa and unloaded to 0.7 kPa
Density, ρ (kg m^{-3})	854.7	922.0
Weight fraction of solids, x_S	0.07	0.181
Volume fraction of solids, v_S	0.0261	0.0759
Void ratio, e	37.3	12.12
Porosity, n	0.9739	0.9241
Effective void ratio, e*	-	2.57
Effective porosity, n*	-	0.72

The initial mixture density was found by calculation to be 854.7 kg/m^3 for a weight fraction of 7% silica. This was confirmed by density measurements using the standard pycnometer method. Since the density of the transparent soil is low compared to natural soils, white spirits rather than distilled water was used in the density tests as the displacing fluid (ρ = 782 kg/m^3). Density measurements were also taken after the end of consolidation. The phase relationships given in (5.3)-(5.6), have been used in Table 5.5 to describe the transparent clay in its initial slurry form and then after consolidation to 225 kPa in the test chamber.

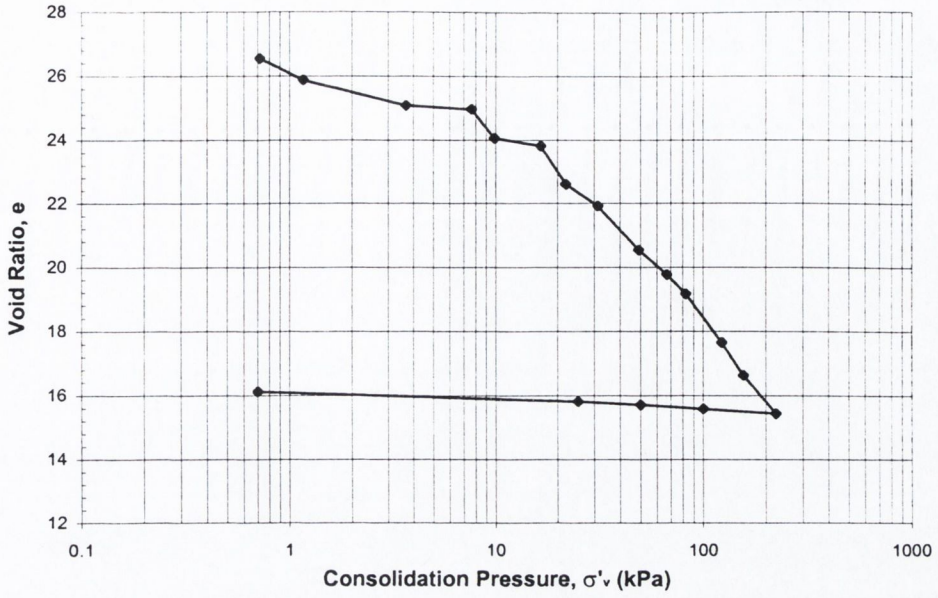

Figure 5.13. Test chamber *e*-log σ' curve (for 100% primary consolidation)

5.3.4.6. Dissipation analysis

It was important to assess to what degree, if any, drainage took place during the model pile tests. To do this it was necessary to find c_v appropriate to the stress condition existing during pile installation. c_v was found to be 0.93 m^2/year from the unload part of settlement-log time curves for the increment 50-25 kPa (this is four times larger than the c_v inferred for the increment 100 to 200 kPa during normal consolidation) and is assumed to be close to that present in the model test chamber after unloading to σ'_v = 0.7 kPa. Using this value for c_v with the dissipation curves around a penetrometer predicted by Teh (1987) (Figure 5.14) it is possible to estimate the pore pressure dissipation at various points along the model penetrometer shaft during testing. The time factor, T is found from;

$$T = \frac{c_v t}{R^2} \tag{5.16}$$

where t is the time after driving and R is the pile diameter. For a conventional consolidation test conducted in an oedometer, the length of the longest drainage path is used as the characteristic dimension in the definition of T. The time factor, for the dissipation curves in Figure 5.14 is normalised in this instance by R which characterises the zone of soil subjected to excess pore pressure.

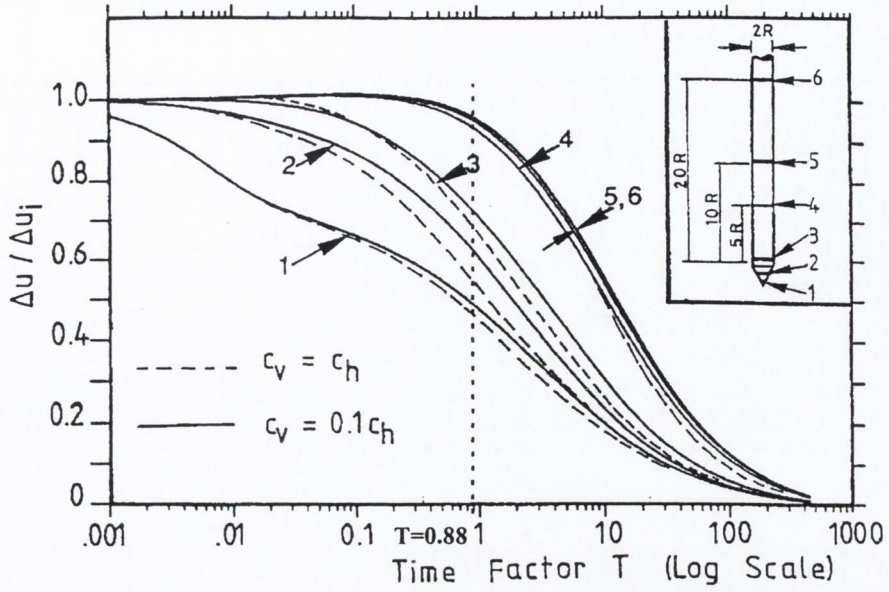

Figure 5.14. Dissipation of pore pressures at various points along penetrometer shaft (after Teh, 1987)

The drainage time, t during the penetrometer tests was taken as the time for the penetrometer to move from a position where the greatest pore pressures are generated in the soil, at h/R = 0, to the position where the final displacements were recorded, at z/R = 20. Typically, this took approximately 20 min and this gives a time factor value of T = 0.88. Along the shaft of the penetrometer it is found from the dissipation curves in Figure 5.14 that there is very little dissipation of pore pressures (~5 %), although for a region close to the tip, within zone of approximately one radius there is up to 50 % dissipation of pore pressures. However, within this region significant dissipation occurs within seconds, irrespective of the speed of penetration, and for practical purposes the test can be considered undrained. It should be noted that the penetrometer used in this instance was flat ended, whereas Teh's dissipation curves are for a 60° cone, but this is thought to have little impact on the overall shape of the curves.

5.3.4.7 The behaviour of TCD transparent clay in direct shear

Both drained and undrained direct shear tests were performed in a conventional 60 mm square shear box. Measurements were obtained using electrical displacement transducers. For the drained tests a horizontal displacement rate of 0.0048 mm/min was used, and was

designed to ensure drained conditions. The undrained horizontal displacement rate was 0.9144 mm/min.

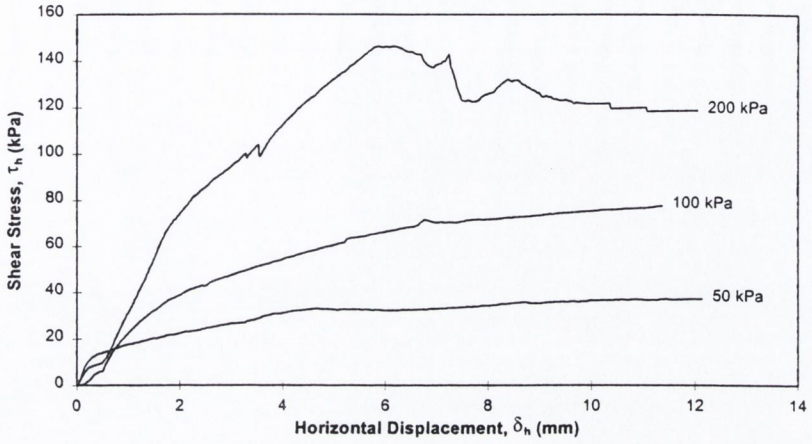

(a)

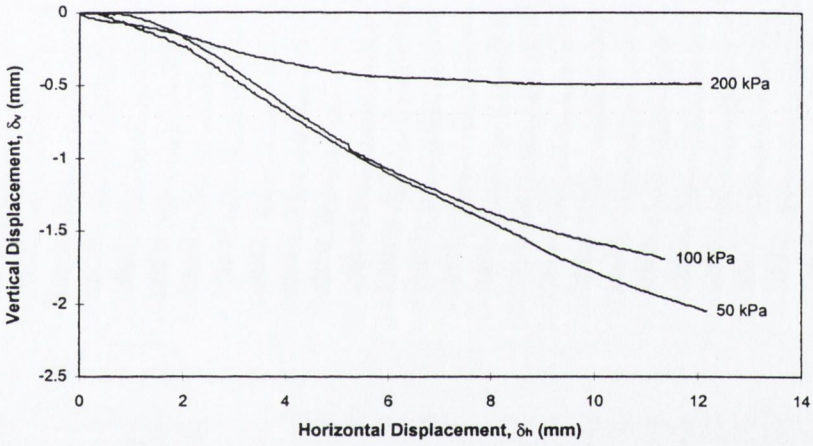

(b)

Figure 5.15 (a) & (b). Direct drained shear tests on normally consolidated transparent soil

In Figure 5.15(a) the drained horizontal shear stress is plotted against horizontal displacement for normally consolidated samples with vertical stresses of 50, 100 and 200 kPa. The 50 and 100 kPa curves exhibit flat shear stress-horizontal displacement curves with no pronounced peak strength, but instead continue to show small increases in shear stress with increased horizontal displacement. At 200 kPa, however, peak and post rupture strength characteristics are evident with the post rupture plateau occurring after approximately 10 mm of horizontal displacement. Figure 5.15(b) shows that minor or insignificant changes in vertical displacement are observed after peak strength for the 200 kPa curve, which is indicative of critical state. The vertical displacements at 50 and 100 kPa show no such flattening, which indicates a critical state has not been reached.

The behaviour in shear of the normally consolidated transparent clay is typical of the behaviour of soft normally consolidated or lightly overconsolidated clays. The difference in behaviour between the samples normally consolidated to 50 and 100 kPa and to 200 kPa is most likely due to the increased packing and particle rearrangement that occurs during the shearing process at the lower stresses. On the Mohr diagram in Figure 5.16, the slope of the peak failure line is found to be $\phi' = 36.7°$, assuming $c' = 0$. A failure line has also been drawn through the post rupture strength value for a normal stress of 200 kPa, and has a slope of $\phi' = 30.8°$.

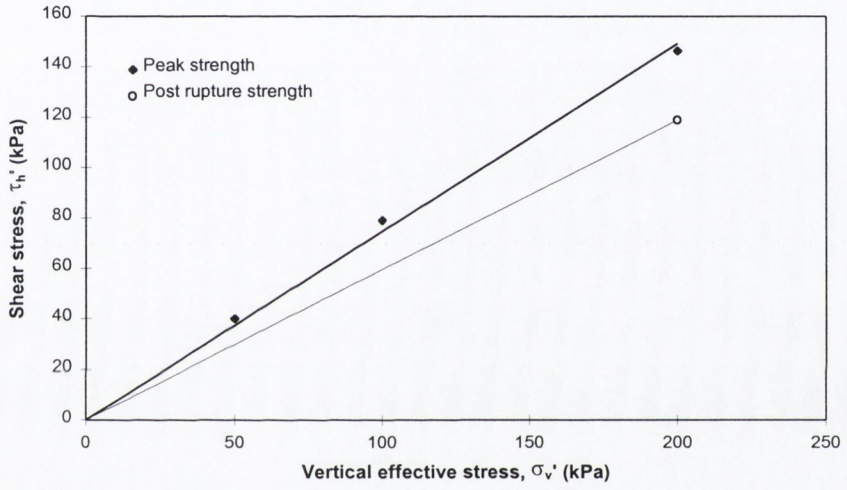

Figure 5.16. Mohr diagram for normally consolidated transparent clay

Figure 5.17 plots the undrained horizontal shear stress against horizontal displacement for a sample subjected to $\sigma'_v = 25$ kPa and overconsolidated to OCR = 8 showing a peak shear stress of 42.5 kPa. This is close to the conditions during model penetrometer testing, i.e., in an overconsolidated state. It is possible to infer the undrained strength, c_U, of the soil within the chamber (for $\sigma_v' = 0.7$ kPa and OCR = 321) from the empirical relationship;

$$\frac{c_U}{\sigma'_v} \cong (0.3 \pm 0.1) OCR^{0.8} \tag{5.15}$$

This gives $c_U \cong 23$ kPa, which approximates the undrained strength found from hand vane tests in the chamber, although using the relationship in (5.15) for such a high OCR value is questionable.

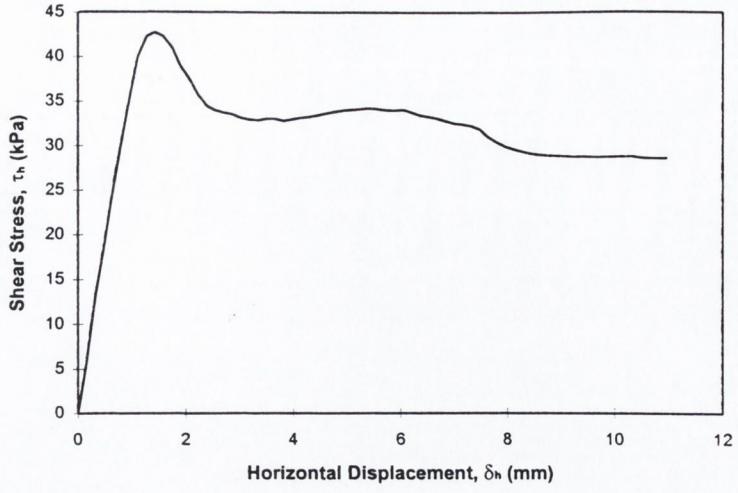

Figure 5.17. Direct undrained shear tests on overconsolidated transparent soil at σ'_v = 25 kPa (OCR = 8)

5.3.4.8. Undrained strength from triaxial and hand vane tests

The undrained strength of the transparent soil in the test chamber was measured after the model penetrometer tests by hand vane and from unconsolidated undrained triaxial tests. A 33 mm diameter hand vane was used to determine the undrained strength of the soil while still within the test chamber. This was carried out at radial distances of 40-50 mm (6-8 R) from the penetrometer after both of the model tests (labelled Tests 1 & 2). The undrained strength measured after both tests, and the depth they were taken at are shown in Table 5.6.

The hand vane readings from both tests indicate that a slight variation of strength exists and gives higher values closer to the drainage points at the top and bottom of the sample. The average peak shear strengths for Tests 1 & 2 were found to be 21.8 kPa and 26.5 kPa, respectively. The slight increase of strength of the second test, which despite re-mixing, is attributed to the recycling of soil from the first test. An average value of strength for constant rotation of the vane was 13.5 kPa, i.e., the post rupture strength.

Table 5.6. Undrained shear strengths from hand vane tests for soil in test chamber

Test 1		*Test 2*	
Shear Strength, Cu (kPa)	**Depth (mm)**	**Shear Strength, Cu (kPa)**	**Depth (mm)**
24.5	100	30	100
19.5	200	24	200
21.5	300	25.5	300

Unconsolidated undrained triaxial tests were also performed on samples taken using a sampling tube from the model penetrometer test chamber after penetrometer installation. The triaxial samples were taken from the top 100 mm of the soil in the chamber at approximately 65 mm (10R) from the penetrometer. Figure 5.18 plots the shear stress against axial strain for these unconsolidated undrained triaxial tests. The average peak undrained shear strength was found to be 41.3 kPa (the peak values measured from the two tests undertaken were 38.1 kPa and 44.5 kPa).

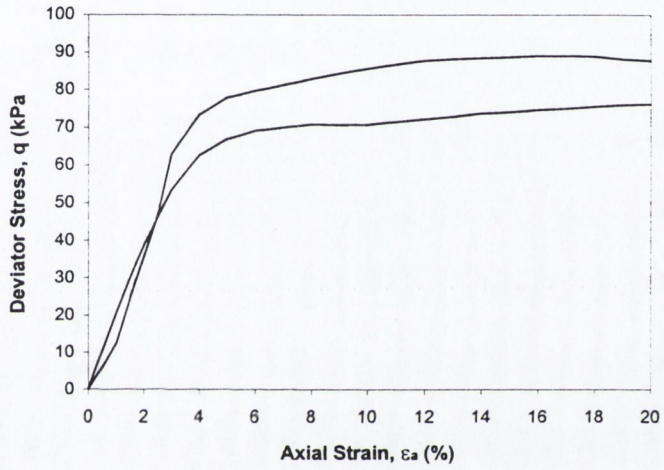

Figure 5.18. Unconsolidated undrained triaxial test on transparent clay (cell pressure = 200kPa).

5.4 SUMMARY

A transparent material was developed with geotechnical properties consistent with normally consolidated clay. Previous work in the development of transparent soils for flow visualisation experiments has been used to produce a new material termed TCD transparent clay. The TCD transparent clay is a two phase media, consisting of fumed silica and a pore fluid blended from two oils to give a refractive index of 1.456 at 20°C. The primary particle size of the silica is 0.014 μm and it was found from electron microscope images that these form larger aggregate particles after consolidation in the order of 0.1-0.4 μm. The pore oil is blended from 70 % crystal light paraffin and 30 % mineral spirits and has a density of 817.1 kg/m^3 at 20°C.

The soil is initially mixed as a slurry and is 7 % silica, by weight and after consolidation to 200 kPa is approximately 18 % silica by weight. The properties of the transparent soil after consolidation within the test chamber are given:

$e = 12.1$ ($e^* = 2.6$),

$m_v = 0.42$ m^2/MN,

$c_v = 0.97$ m^2/yr,

Compression Index = 0.34,

$C_\alpha = 0.02$ (in an overconsolidated state),

$k = 1.1 \times 10^{-10}$ m/s.

The behaviour in compression was shown to be similar to soft clay, although the secondary compression was particularly high and comparable only to highly plastic or organic soils. The interaggregate void ratio, which considers only the pore fluid 'free' for drainage, was found to be more representative than the total void ratio for geotechnical purposes. The values of interaggregate void ratio were typically 10 times lower than total values and compared better with values for natural soils.

In drained shear box tests the transparent soil, which behaved like a normally consolidated clay, was found to have high strength and gave friction angles of $\phi' = 37°$ for peak behaviour and $\phi' = 31°$ at post peak rupture. The range of undrained peak strengths from shear box, hand vane and triaxial tests are given:

UU Triaxial:→ 38.1 to 44.5 kPa.

Hand Vane:→ 21.8 to 26.5 kPa (post rupture strength = 13.5kPa).

Undrained Shear Box:→ 23 kPa (corrected for OCR using the empirical equation in 5.15).

The relatively high strength behaviour of the transparent soil is thought to be due to the low plasticity of the silica particles.

CHAPTER 6
MEASUREMENT OF SOIL DISPLACEMENTS DURING PENETROMETER INSTALLATION

Chapter 6

6.0 MEASUREMENT OF SOIL DISPLACEMENTS DURING PENETROMETER INSTALLATION

6.1 INTRODUCTION

This chapter describes a laboratory experiment, conducted to measure the soil movements around a model penetrometer during its installation into a test chamber. A visual measuring technique using a video camera system was employed to record the displacement of markers within a transparent soil. The aim of the experiment was to improve the understanding of soil behaviour during penetrometer installation and to add to the experimental data in the literature (Chapter 2) by providing good quality measurements. The experimental results are also used in Chapter 8 to aid the theoretical prediction of displacements and strain. This chapter describes the test chamber, the visual measuring system, and the experimental procedure undertaken.

6.2 DESIGN OF A MODEL PENETROMETER EXPERIMENT

6.2.1 Outline Of Design Process

The objective of the experimental work was to design an test that allowed the soil displacements caused by the installation of a model pile or penetrometer to be measured. Key to achieving this were three fundamental decisions regarding; (a) the technique used to measure the soil displacements, (b) the type of soil medium in which to conduct the tests, and (c) the size and type of testing chamber required.

(a) A visual measuring technique, which provides a non-intrusive method capable of measuring displacements to a high resolution, was chosen to record the soil movements in the laboratory experiment. It is also free from some of the difficulties associated with X-ray measurement, which is the alternative non-intrusive technique referred to in the literature; (discussed in Section 2.3.2.1). Radiographic techniques require the use of specialist equipment and have been shown have a maximum resolution of 0.05 mm, which the visual

technique was expected to improve upon. The video camera system used is capable of *continuously* monitoring the movement of suitable targets to a high resolution (see Chapter 7). Distinct markers within the transparent soil medium provided visual targets that could allow the camera to record the effect of penetrometer installation within the sample.

(b) The choice of soil medium, in which to conduct the experiment, was determined by the choice of measuring technique; this required either the use of a transparent soil medium or the use of a transparent interface through which soil movement could be monitored (as employed by Gue, 1984). It was considered that the effects of an interface on the soil movements would be difficult to account for and that to conduct a truly three dimensional test would require the use of a transparent medium. This led to the development of a material that could both allow visual inspection of displacements within the material and possess soil-like properties. The transparent clay developed for this purpose has been described in Chapter 5.

(c) It was then necessary to design a test chamber that could both withstand the pressures during soil consolidation and allow an unobstructed view of the penetration process (see Section 6.2.2). The chamber needed to be sufficiently large to allow reliable measurements be taken and to limit the effect of the boundaries on movements. The dimensions of the chamber was, however, limited by the difficulties associated with increased size, such as handling, cost and particularly by the high pressures required during consolidation.

6.2.2 The Test Chamber

The test chamber was designed to meet demands unique to this type of test, namely to;

- allow an unobstructed, undistorted view of any soil movements taking place during the penetrometer installation process,
- accommodate the high pressures required to consolidate the soil within the chamber,
- provide adequate drainage to the soil during the consolidation phase,
- allow access for penetrometer installation.

The most difficult of these requirements to meet, was to allow the visual observation of the soil displacements during penetrometer installation, whilst also being able accommodate

the high pressures that are necessary during consolidation phase of the test. The result was a test chamber comprising of a glass inner chamber surrounded by removable steel casing designed to function differently during these two phases of the experiment. During consolidation, the soil pressures are resisted by the steel casing and during penetrometer installation, the steel could be removed to leave the transparent glass inner chamber.

The chamber design is shown in Figure 6.1 and consists of a four sided glass container which fits tightly inside a similar four sided steel casing, which is held together by bolts. The dimensions of the chamber were most influenced by the need to design a sufficiently large chamber to negate the effects of the boundaries and the size restrictions imposed by the large shear box apparatus (discussed in Section 6.2.2.3).

6.2.2.1 Glass inner chamber

(i) Requirements of the glass chamber

Glass, rather than perspex, was chosen as the material for the inner chamber sides, which was mainly due to the greater hardness of glass which doesn't scratch or get dulled as easily as the softer perspex, thus giving a clearer view. It was required that at least one surface of the container be flat, to give the video camera an undistorted view of the soil movements. This meant that a container more suitable to the resistance of consolidation pressures, such as a bored glass cylinder, could not be used. A four sided glass box, which meets the visual requirements, could also meet the consolidation requirements by providing external support, as has been described. The test chamber is left open at the top to allow loading of the soil, and the bottom, to allow drainage through a porous stone.

(ii) Bonding the glass

The four sides of the glass chamber were bonded together using silicone sealant. The glass was assembled and glued within the steel casing to ensure the best fit between glass and steel was achieved. The use of silicone rather than super-glue as a bonding agent gave some flexibility to the joins between the glass panes. This meant that as consolidation pressure was applied, the glass panes could move by small amounts, if necessary, so as to lie perfectly flat against the steel casing. The silicone bonds were also non-permanent, which gives the added advantage that should a pane of glass break it can be replaced individually rather than replacing the whole chamber.

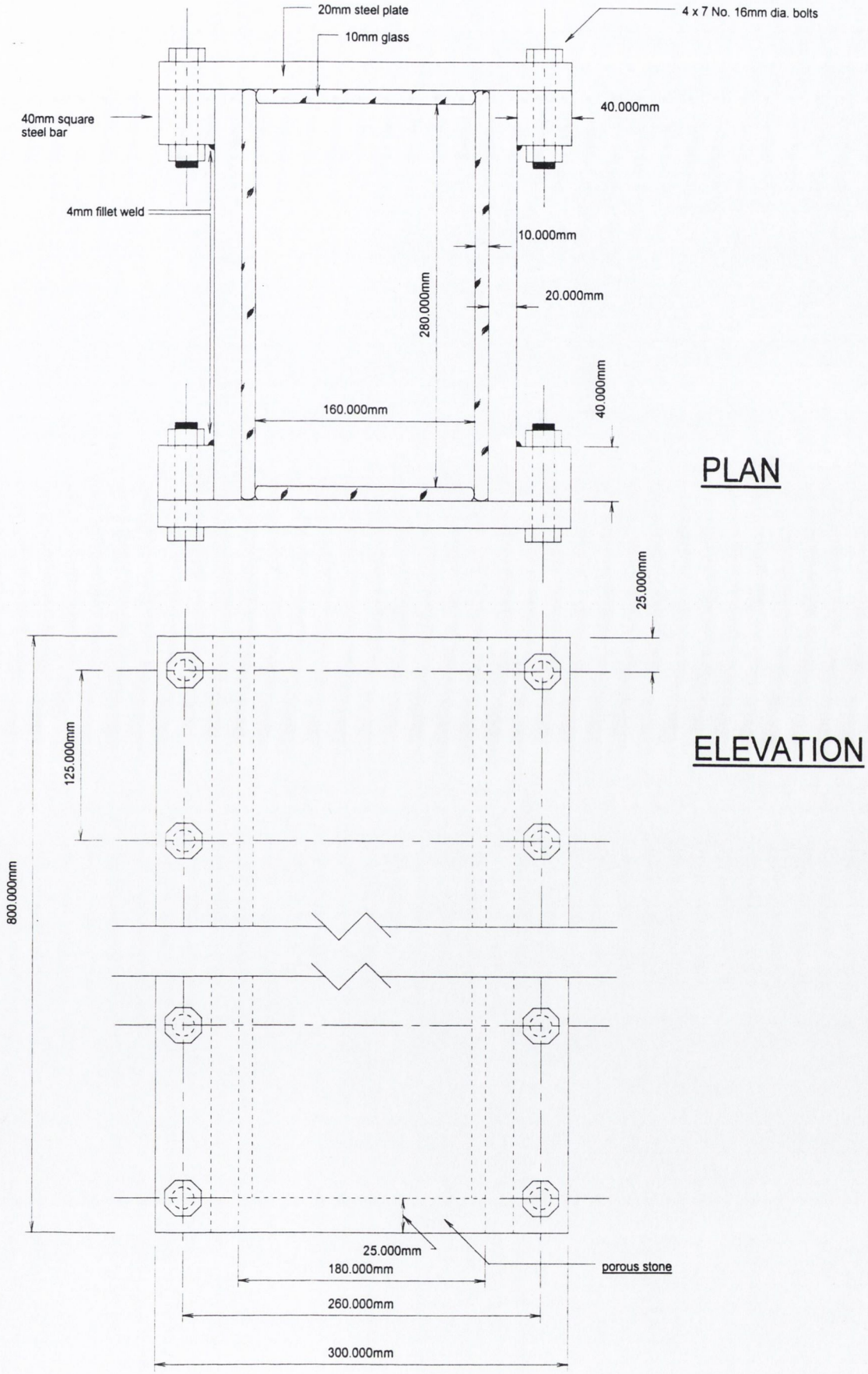

Figure 6.1. The test chamber in plan and elevation.

(iii) Glass type and thickness

To determine the most suitable type and thickness of glass for the chamber, a series of three point tests were conducted. The thickest glass available at an economical cost was 10 mm plate glass and 11.5 mm laminated glass. The laminated glass was found to be stiffer and failed at a higher load, as is evident from Figure 6.2. The 10 mm plate glass, however, is more flexible and fails at a deflection of 0.5mm in the centre of the 255 mm span, compared to 0.2 mm deflection for the laminated glass. The plate glass, therefore, was chosen for use in the chamber because of its greater flexibility, which gives greater latitude in the design of the outer steel box.

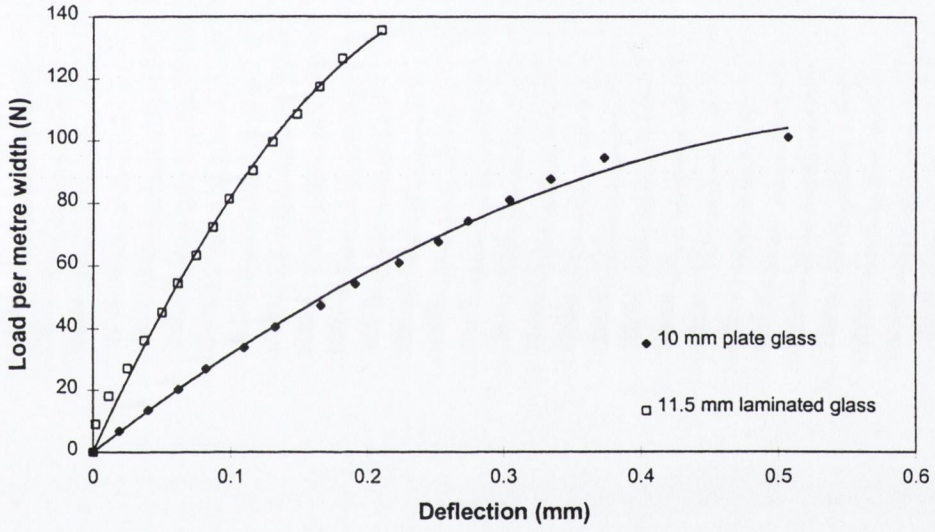

Figure 6.2. Load versus deflection for three-point test with laminated and plate glass

6.2.2.2 Steel outer casing

The glass chamber on its own would be unable to resist the soil pressure during consolidation. Therefore, during this phase of the test a steel casing was placed around the glass to provide support. The design of the steel casing was based on the allowable deflections for the glass and the pressures likely to be present during consolidation. The simple calculations in (i) to (iv) show how a design for the steel casing, which could withstand the range of consolidation pressures expected, was reached.

(i) Maximum bending moment of the glass

The maximum bending moment of the glass, before failure is reached, needed to be determined before other calculations could proceed. The maximum bending moment was calculated using the load-deflection results from the three-point test conducted on the 10 mm plate glass, which imposes a point load at the centre of simply supported 'beam' of glass. If the span length, L was 255 mm and a maximum load of W_{ss} = 101.2 N was applied in the centre of the span before failure, then;

$$M_{\max} = \frac{W_{ss} L}{4} = \frac{(101.2)(0.255)}{4} = 6.45 Nm \tag{6.1}$$

where M_{max} is the maximum bending moment for the simply supported 10 mm plate glass with a concentrated load at the centre. This could subsequently be used to find the maximum deflection the glass could endure under the loading conditions imposed within the chamber.

(ii) Loading conditions within the chamber.

Consolidation pressures within the chamber impose a uniformly distributed loading condition on the glass that differs from that of the three-point test. The support provided by the steel casing with its rigid connections causes it to behave in a manner close to that of a beam fixed at both ends. The maximum uniformly distributed load, w, which can be supported by the glass (only) under these conditions, can be found by rearranging (6.2);

$$M_{\max} = \frac{\omega L^2}{12} \tag{6.2}$$

to give,

$$w = \frac{12 M_{\max}}{L^2} \tag{6.3}$$

and if L is taken to be the internal dimension of the longer side of the chamber (280 mm, as shown in Figure 6.1) then the maximum uniform load is w = 0.988 kNm^{-1}. The maximum allowable deflection for the glass under a uniformly distributed load for fixed end conditions, and hence within the test chamber, is given by;

$$\delta = \frac{1}{384}\frac{\omega L^4}{E_{glass} I_{glass}} = 0.229mm \tag{6.4}$$

where:

$E_{glass} = 8.27 \times 10^8\ Nm^{-2}$ (found from the three point test)

$I_{glass} = 8.33 \times 10^{-8} m^4$

This is the deflection allowable in bending of the glass panel (derived from test results) and does not include any movement of the silicone seals that hold the glass chamber together.

(iii) Steel plate thickness

The thickness of the steel plate for the outer casing of the test chamber was designed to prevent failure of the glass for a consolidation pressure of 1600 kPa. This gave a very conservative design as the maximum pressure actually applied during testing was 225 kPa. Nonetheless, for a maximum uniform load of 1600 kPa, the thickness of the steel surrounding the glass was found from (6.5) and (6.6):

$$I_s = \frac{\omega_{\max} L^4}{384 E_s \delta_{\max}} \tag{6.5}$$

The Young's Modulus of steel was taken as $E = 210\times10^9$ Nm^{-2} and the second moment of area for the steel was found to be $I_s = 0.5326\times10^6$ m^4 and for a rectangular section:

$$d = \left(\frac{12 I_s}{b}\right)^{\frac{1}{3}} \tag{6.6}$$

$$\therefore d = 18.6mm$$

A 20 mm steel plate, therefore, was chosen for the sides of the chamber, which in theory allows a maximum consolidation pressure of 2000 kPa. The load taken by the glass was ignored in the calculations since this is only a tiny fraction of the load taken by the steel. The calculations also assume that failure of the glass occurs in bending only and not by any other means, such as uneven loading or the presence of point loads. To ensure this condition is closely achieved, the steel was carefully smoothened to remove any bumps and possible point loads, allowing the glass to lie flat against the steel plate. During testing a

layer of thin cardboard and plastic sheeting was placed between the steel and glass to further reduce the possibility of point loads occurring. The maximum consolidation pressure reached in testing was 225 kPa, which gives a deflection of 0.026mm, almost 10 times less than at failure.

(iv) Bolt and weld connections

Once the required thickness for the steel plate had been determined, the connections to hold the steel in place during loading were designed. The four sides of the steel box were bolted together through 40 mm square steel bars which were welded to two of the plates; see Figure 6.1. Bolt holes were drilled through the 40 mm bars and matching holes through the other two 20 mm steel plates. The consolidation pressures are translated into tension and shear forces on the bolts holding the casing together, as shown in Figure 6.3. The maximum shear force, F_S, and tensile force, F_T, on the bolts was found for a consolidation pressure of 2000 kPa and a soil depth within the chamber of 0.6 m (this is a conservative value for soil depth since at 225 kPa it was 0.4 m):

$$F_S = p_c A = 2000 \times (0.28 \times 0.6) = 336kN$$

$$F_T = p_c A = 2000 \times (0.16 \times 0.6) = 196kN$$

The bolts used were 16 mm, Grade 8.8 bolts and had a shear strength, P_S = 75.3 kN and a tensile strength, P_T = 70.6 kN. A bolt spacing of 125 mm was chosen to ensure minimum steel and glass deflection between the bolts and this could comfortably deal with the worst possible case scenario for consolidation considered. The design was also well within the bearing capacity of the steel plate and the bolts. A total of 28 bolts were used to hold the casing together; 7 bolts at each of the four corners which were spaced at 125 mm along the 800 mm length of the chamber.

The 40 mm square steel bars were welded onto two of the 300×800×20 mm steel plates using a weld size, s, of 4 mm and this gives a weld strength, P_w, of 0.6 kN/mm from;

$$P_w = 0.7sp_w \tag{6.7}$$

where p_w = 215 kN/m. The welding was done in 100 mm lengths between the seven bolt holes at each corner, giving approximately 600 mm of weld, which more than meets the requirements of any possible loading condition. For example to resist the forces on the

chamber in the tensile direction (F_T) for a consolidation pressure of 2000 kPa and 0.6 m depth of soil in the chamber, the total weld length required at each corner of the box is 327 mm.

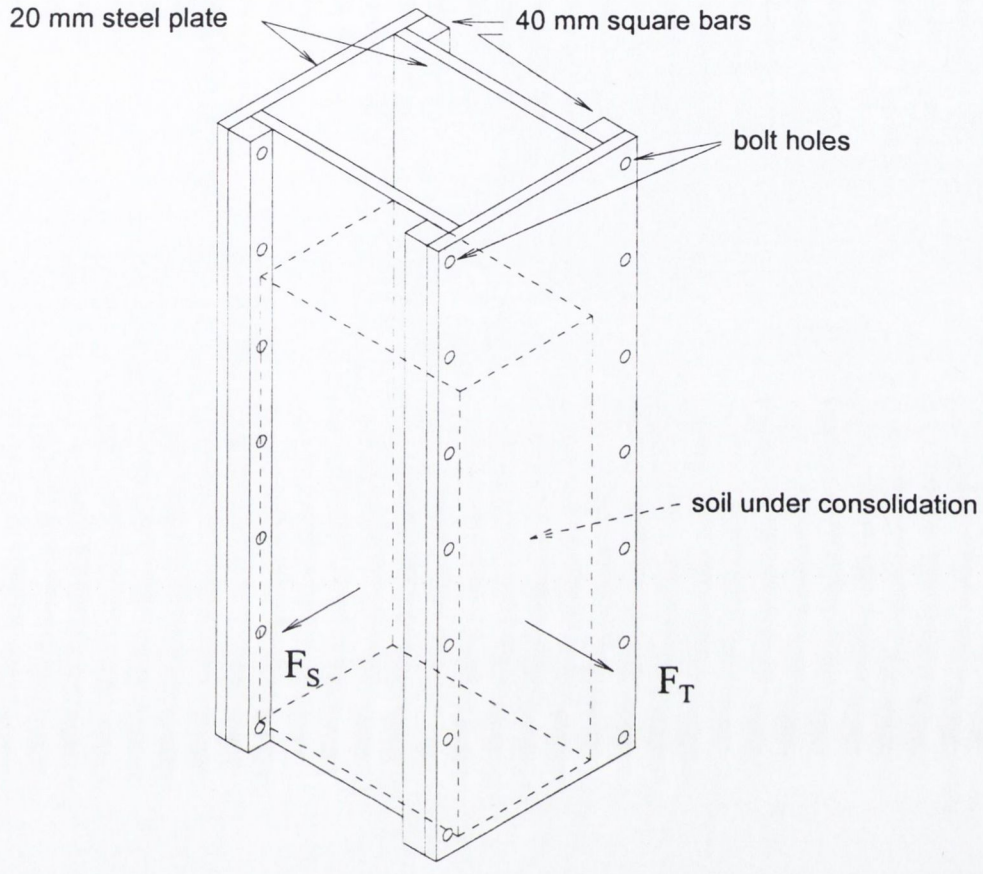

Figure 6.3. The forces on the sides of the test chamber during consolidation.

6.2.2.3 Loading the soil

During the consolidation phase it was necessary to apply a range of loads to the top of the soil sample. The loading conditions ranged from low pressure, while the liquid content was high and the soil was very soft, to the high pressures necessary to produce a moderately compact material. In an undrained state the bulk stiffness of the silica-oil blend is taken to be 1.6 GPa (the same as the oil) and is effectively incompressible.

The transparent soil was introduced to the chamber as a slurry and initially the material consolidated under self weight. When the soil had achieved a jelly-like consistency, it was possible to place a loading platen on top of the sample, through which the top of the soil could then be loaded evenly. The loading platen was required to be both sufficiently strong

to withstand the applied loads and be non abrasive to the glass sides of the chamber. A wooden platen met these requirements and was made up of three layers of 22 mm thick mahogany cut to fit inside the glass chamber, leaving a gap of approximately 1 mm on all sides. A detachable bottom layer, held to the top two layers by screws, had a 30 mm hole drilled through its centre. After unloading, the platen could then be separated to leave the bottom layer on the soil sample, and this allowed a surcharge to be applied during penetrometer installation.

The vertical loading system of a large shear box apparatus was used to apply the high vertical loads required in the later stages of consolidation. The large shear box is capable of taking specimens up to 300 mm square and has a 100 kN vertical load capacity. The vertical force is produced by a hydraulic system, which once adjusted manually to the desired load, automatically maintains that load. The test chamber was placed on the carriage of the shear box machine (as is shown in Figure 6.4) in the place of the shear box normally used to hold soil samples. The load is applied to the sample via the top platen through a vertical loading yoke consisting of a crossbeam and two tension bars. It was necessary to make up extended tension bars for the shear box apparatus to allow loading of the 800 mm high test chamber (under normal conditions, 200 mm high samples are tested).

The low consolidation pressures, in the range 0.7-30 kPa, were achieved by placing weights (29-1400 N) on the platen. Loads greater than these were achieved using the vertical loading system of the shear box. A maximum load of 10 kN was applied in these tests giving a consolidation pressure of 225 kPa, although pressures up to 10 times higher were within the range of the system.

6.2.2.4 Drainage

Drainage of the transparent soil within the chamber was achieved through a ceramic porous stone with a pore size of 1 μm. The porous stone was 1 inch (25.4 mm) thick and was cut to fit at the bottom of the test chamber (160×280 mm). The inner glass chamber rested on top of the porous stone and was sealed using silicone sealant. During the first test, filter paper was used to ensure there was no leakage of the very small (0.014 μm) silica particles. It was found, however, that this was not necessary due the agglomeration of the silica into

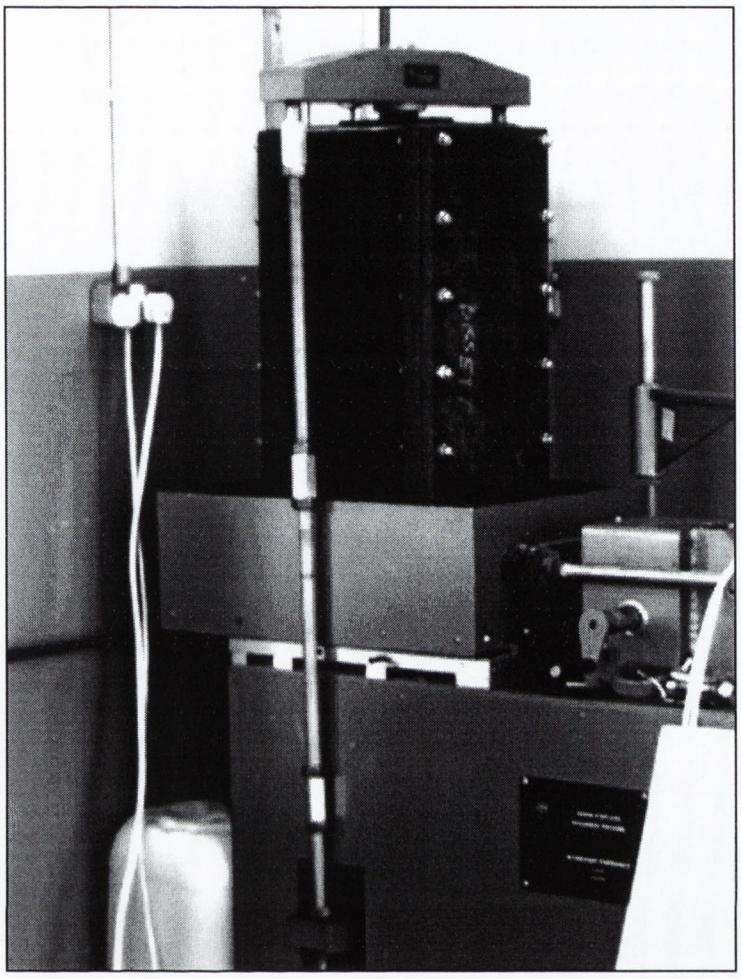

Figure 6.4. Consolidation of a soil sample within the test chamber using the vertical loading system of the large shear box apparatus

larger aggregates. These aggregates were found not to pass through the porous stone. The second test therefore did not use filter paper.

Although there was no porous stone on the top surface of the sample during loading, some drainage was considered to take place through this surface. This was due to the 1-2 mm gap left between the wooden loading platen and the glass sides of the chamber. This allowed excess fluid (and some soil) to drain from the sample using the natural filtering mechanism of the material itself, somewhat like a sponge.

6.3 THE MODEL PENETROMETER TEST

6.3.1 Outline

In all, two model penetrometer tests were conducted in the chamber. The low number of tests was due primarily to the length of time it took to set up the chamber, prepare the transparent soil and, in particular, to consolidate it within the chamber, all of which took three to four months for each test. In both tests a flat-ended penetrometer was installed and the resulting soil movements were recorded with the video camera system. The operating procedures and accuracy capabilities of the Videoextensometer dot measuring system are described in detail in Appendix C. A description of the two main parts of the experiment are described the following section; (1) preparation of a transparent soil sample within the chamber; (2) installation of a model penetrometer into the soil and the measurement of displacements.

6.3.2 Preparation Of A Soil Sample

The procedure for setting up the chamber and preparing a soil sample for penetrometer testing is described in the following:

(i) Test chamber assembly

The test chamber was assembled on the carriage of the large shear box machine, with the steel casing bolted around the four sided glass box (Figure 6.4). The network of threads used to position the soil markers, which is described in (iii), is positioned within the glass box prior to assembly of the steel around the chamber.

(ii) Soil introduction

The transparent soil sample, prepared in a slurry form (described in Chapter 5), is then poured slowly into the chamber, with care taken to ensure that air is not trapped in the slurry. The chamber, which has internal dimensions of 775×280×160 mm requires almost 35 litres (0.03472 m^3) to fill. This sample is then consolidated, first under self weight, and then loaded incrementally to a vertical pressure of 225 kPa.

(iii) Soil marker positioning

Markers were positioned within the soil mass to allow soil movements to be monitored during penetrometer installation using the video camera system. These soil markers consisted of small black beads (approximately 2 mm in diameter, but slightly oval in shape) positioned within the soil sample using thread that was removed at an early stage during consolidation. The thread was strung horizontally across the centreline of the chamber at a number of different vertical locations, prior to the introduction of the soil slurry. The threads were held by 'loops' fixed by PVC tape to the inner side of the glass walls at the two narrow ends of the chamber (i.e., d_{wall} = 160 mm). These threads were released and pulled from the soil when it had become sufficiently solid to hold the beads in position (i.e., in a jelly-like state), which was typically about 24 hours after introduction of the slurry to the chamber. The markers and the surrounding soil were unaffected by the removal of the threads. The final result is an (almost) horizontal line of soil markers, positioned across the centreline of the chamber. The camera view of two rows of soil markers, during testing, is shown in Figure 6.5. The curve in the lines of markers is due to the settling of the soil that occurred before the threads were removed.

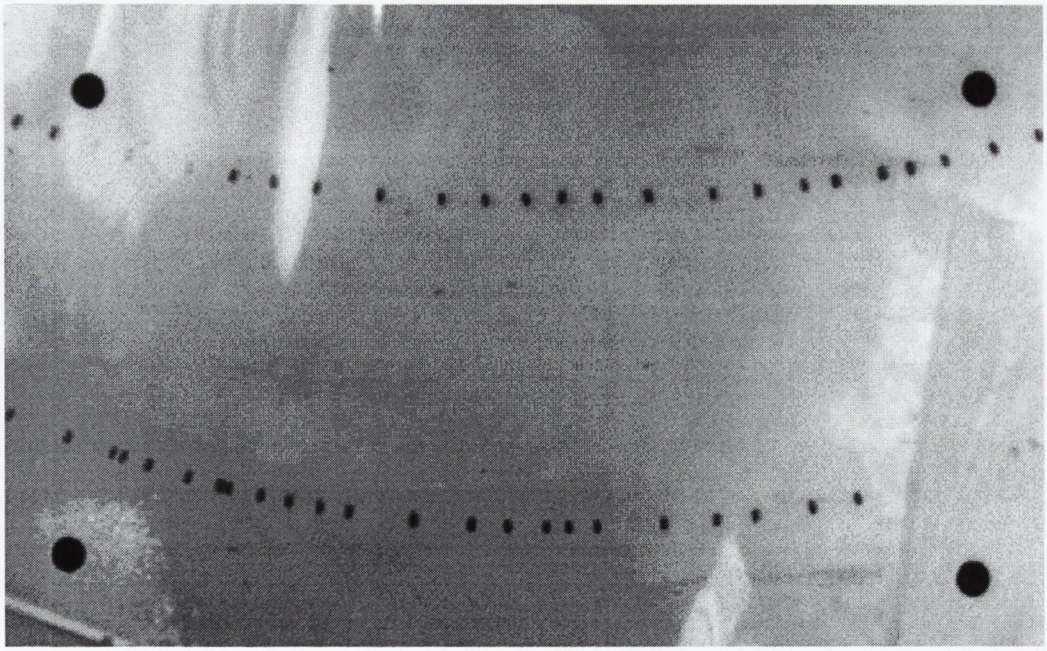

Figure 6.5. Two rows of soil markers (beads) at mid-depth in the test chamber prior to penetrometer installation (as seen by the video camera, field of view = 192×144 mm)

(iv) Loading the soil

When the soil sample was sufficiently solid and the threads used to position the soil markers had been removed, the loading platen could be placed on top of the sample and a vertical load applied. Incremental loads were left on the sample for at least 24 hours and often longer if significant vertical settlements were still taking place. For both tests the maximum consolidation pressure applied was 225 kPa, which was considered to be sufficiently high to give a stiff sample, while also giving a large factor of safety (FOS $\approx$ 10) against failure of the glass.

The transparent soil possess very high secondary creep (see Chapter 5) and this meant that the settlement under high loads appeared to continue almost indefinitely; therefore, to allow the addition of further load increments, the consolidation process was considered to be complete when primary consolidation had ended. This could be assumed to be the case after 24hrs for the relatively low consolidation pressures (< 25 kPa), but at higher pressures the permeability of the soil reduces considerably (i.e., < 10^{-9} ms^{-1}) and the time for 100% primary consolidation increases accordingly. To ensure 100% primary consolidation was achieved at pressures greater than 25 kPa, the c_v values found from 1-D consolidation tests (Section 5.3.4.2) were used to estimate the time for primary consolidation and settlement-time curves such as that shown in Figure 6.6 were plotted. The consolidation results and properties of the test sample are described in Section 5.3.4.5.

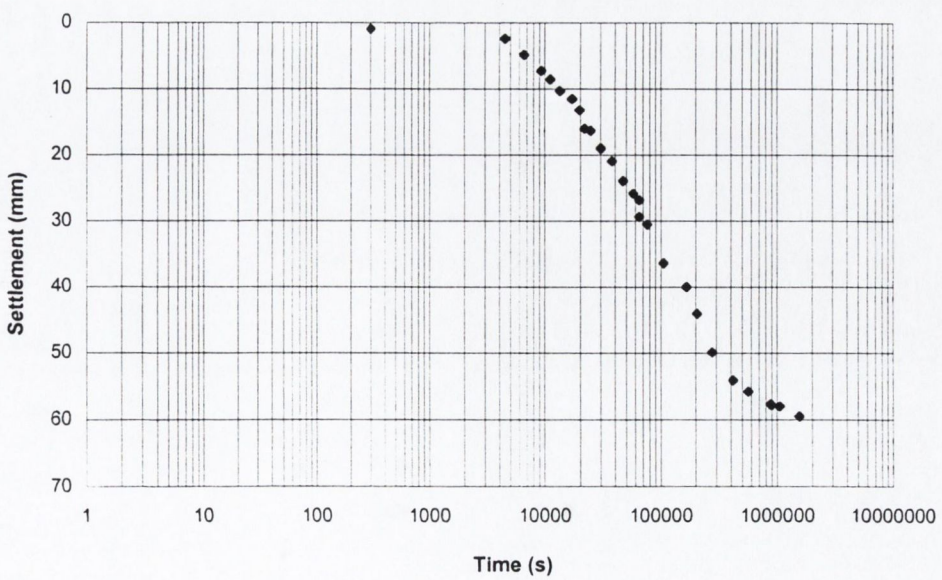

Figure 6.6. Settlement-log time consolidation plot for transparent soil within the test chamber for load increment 100→150 kPa.

Primary consolidation at 225 kPa was complete after 3 months in Test 1 and 2½ months in Test 2. The time taken to achieve full primary consolidation for each load increment is illustrated in Figure 6.6, which shows it took approximately 2 weeks for the increment 100 150 kPa.

(v) Unloading the soil

When primary consolidation at 225 kPa was achieved the sample was then unloaded incrementally. The steel plate casing was removed from around the glass chamber once all loads had been removed for a sufficient period of time. Full equalisation was considered to have been achieved when, after two weeks, no further heave was detectable. The top section of the wooden loading platen was removed leaving the bottom (22 mm) section resting on top of the soil, which allowed a small overburden pressure of 0.7 kPa to be applied to the soil during testing. In this state the soil had an OCR = 321 throughout due to its negligible self weight and the properties in this state are given in Chapter 5.

6.3.3 Penetrometer Installation

The procedure for installation of the model penetrometer and simultaneous recording of soil movements is described in the following.

(i) Penetrometer alignment

The penetrometer was installed by pushing it through a 'guiding' tube fixed to the wall of the laboratory. This consisted of a vertical steel tube, fixed by steel bars to the wall, and positioned above the centre of the chamber, over the hole in the platen (Figure 6.7). The steel tube ensures the penetrometer is practically vertical as it is pushed into the soil. The penetrometer itself, consists of a 12.7 mm ($^1/_2$ inch) stainless steel bar with a circular cross section, approximately 2 m long, with a flat tip.

(ii) Camera set-up

The Videoextensometer camera system, used to measure the soil displacements during the penetrometer installation process, requires that the soil markers be clearly defined against a contrasting background. This was achieved by positioning lights behind the glass chamber in a manner that provided even illumination of the sample. This allowed the markers within

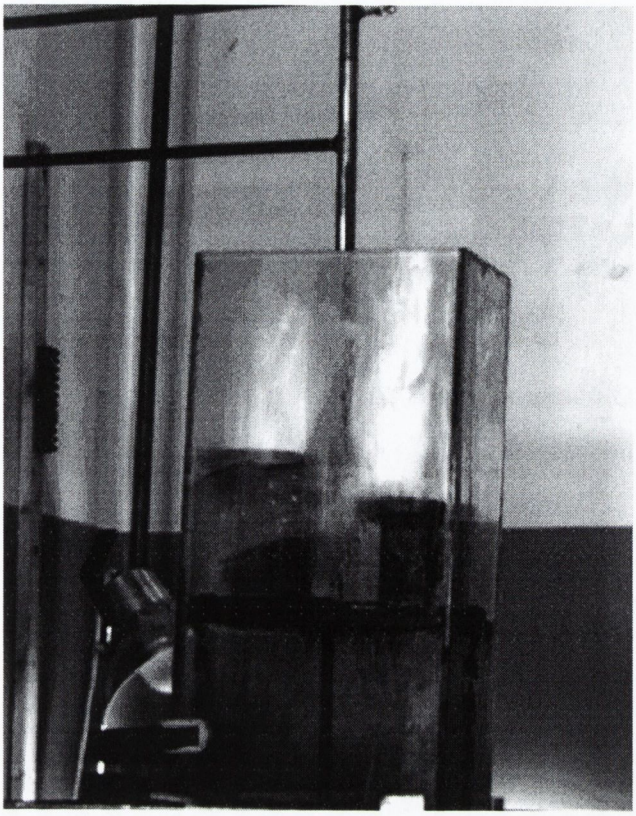

Figure 6.7. The penetrometer after installation into the glass chamber has been completed

the soil to be clearly defined as black dots on a light grey background, which can be seen in Figure 6.5. The normal procedures for setting up the camera system are described in Appendix C. In the penetrometer test, the camera was mounted on a tripod and placed in front of the glass chamber. Special care was taken to ensure the camera was;

- set up perpendicular to the centre of the front face of the glass chamber,
- levelled in the horizontal plane,
- focused on the soil markers within the soil.

(iii) Camera field of view

It was important to select a field of view (FOV) for the camera that allowed a large number of soil markers to be tracked (including points in the far field) and that also gave a high resolution for the measurements taken. The camera FOV chosen for both tests was approximately 200×150 mm and this took in two rows of soil markers which were located at approximately mid-depth in the soil sample, where the influence of the top and bottom boundaries is at minimum (Figure 6.5). In each test, approximately 25 soil markers, that

were clearly defined, were chosen as targets for the camera. Points that were subsequently obscured by the penetrometer or pushed out of its FOV were 'lost' and could no longer be tracked.

It was also necessary to carefully calibrate the field of view with two clearly defined dots, a known distance apart. Black, round stickers on the front pane of glass were used for this purpose (see Figure 6.5) and also doubled as reference markers during the test to account for any movement of the camera or chamber. The distance between the reference markers (centre to centre) was measured carefully with callipers (accurate to 0.1 mm) before using them to set the FOV.

(iv) Vertical location of the penetrometer

It was important that the position of the pile tip relative to the soil markers be known throughout penetrometer installation. To achieve this, the top section of the penetrometer (which does not enter the sample) had notches positioned on it at 5 mm intervals, and this allowed the installation to be conducted in incremental stages; the notches were aligned with the top of the steel guiding tube so that, at any stage of installation, the depth of the penetrometer tip was known. The soil movements during each 5 mm increment were recorded in separate data files (see Section 7.2), allowing the test to be broken into stages where the position of the penetrometer is know at the start and end of each stage of penetration. The total depth of installation for tests 1 & 2 was 367 & 355 mm, respectively. The total time for penetrometer insertion was approximately 90 min, although despite this the installation was effectively conducted in undrained conditions due to the low permeability of the soil (the drainage during the model pile tests is discussed in Section 5.3.4.6).

(v) Camera images

It was possible to record images of the installation process with the camera (as bitmap files) throughout the test. Pictures were taken at the end of each penetrometer increment as an aid to data processing and to illustrate the sequence of penetration. A close up view of a single row of soil markers during the penetration process, in Figure 6.8, shows six images at various stages of penetrometer installation. The z/R values which are given for images 1 to 6, refer to the position of the penetrometer relative to the soil markers in the far field, where soil movement is of a small magnitude. The sequence of pictures show that clearly

defined movement of the soil markers is restricted to a region close to the penetrometer. A 'wedge' of soil moving ahead of the penetrometer tip is made apparent by the movement of one soil marker, just left of the centreline, in pictures 4 & 5. The soil marker is shown to be pushed ahead of the penetrometer when the tip is approximately 2 radii from the row of markers. The results from displacement measurements from the penetration tests are presented in the following chapter.

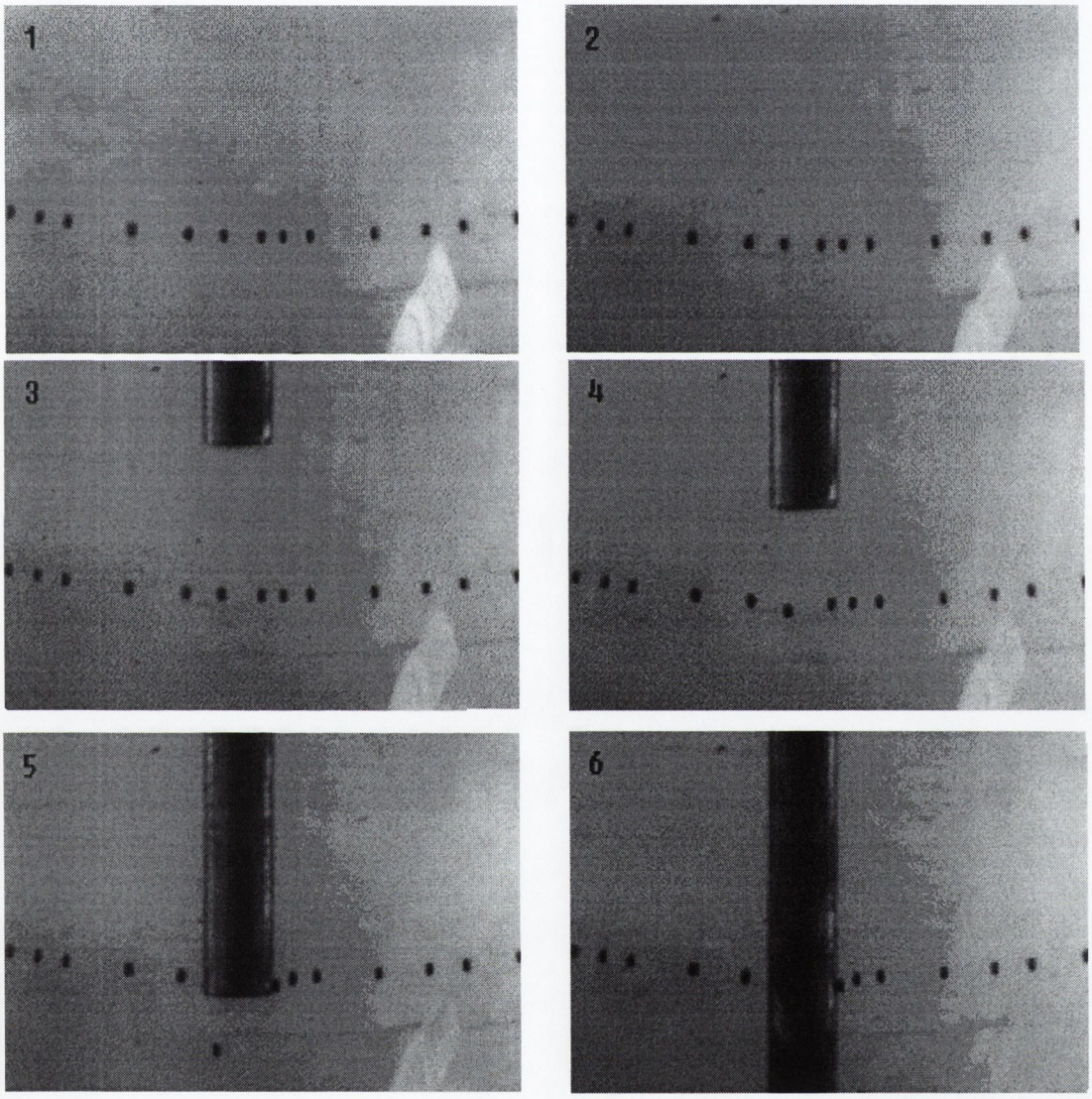

Figure 6.8. Camera images of penetrometer installation at: (1) z/R = -20; (2) z/R = - 10; (3) z/R = -4; (4) z/R = -2; (5) z/R = 2; (6) z/R = 20

CHAPTER 7
EXPERIMENTAL RESULTS - MODEL PENETROMETER TEST

7.0 EXPERIMENTAL RESULTS - MODEL PENETROMETER TEST

7.1 INTRODUCTION

This chapter presents the results from the model penetrometer tests and outlines the procedures taken to minimise inaccuracies and remove the effects of external factors from the data. The experimental results are presented as radial and vertical soil movements, displacement paths, strain paths and strain contours; the strains were derived from the displacements using a curve fitting procedure and numerical differentiation.

7.2 CORRECTIONS APPLIED TO CAMERA MEASUREMENTS

7.2.1 General

The visual nature of the experiment, i.e., the use of the video camera system, requires that external influences, which were not real features of the installation process, be filtered out. Corrections were made to the displacement results logged by the camera to account for such factors as;

- movement of the chamber or camera,
- misalignment of camera and penetrometer,
- eccentricity of soil markers from centreline of penetrometer.

These corrections are discussed later in this chapter.

Results from the camera are recorded in the form of (X, Y) horizontal and vertical co-ordinates with the origin located in the top left corner of the field of view. The position of selected targets, which in this case are soil markers and reference points, are tracked for as long as the measuring system is active or until they disappear from the view of the camera. (N.B. The set-up and operating procedures of the Videoextensometer measuring system are presented in Chapter 6 and Appendix C).

A reliable and convenient way to determine the location of both the soil markers and the penetrometer during the test was to find the marker positions before and after known incremental movements of the penetrometer. These incremental movements needed to be small enough to give sufficient number of data points during penetration, yet large enough to allow the penetrometer to be installed at a rate sufficient to achieve undrained penetration. It was decided that incremental penetrometer movements of 5 mm, which gave a total installation time of approximately 90 minutes, would meet both of these requirements. The penetrometer was typically installed to 360 mm, which gives 72 incremental movements. The experiment was thus conducted in a series of incremental steps for which the monitoring of soil movement (with the camera) was started and stopped before and after each step. The measurement data observed by the camera is recorded in a log file to the hard drive of the Videoextensometer controlling PC. The soil movements for each 5 mm increment were recorded in separate log files. The logging rate (or sample rate) of the camera during measurement was every 0.5 seconds (i.e., 2 Hz) and the total duration of logging during each penetrometer increment was approximately 30 seconds. This gives approximately 60 data readings for each soil marker for each 5 mm increment of penetrometer movement.

The penetrometer was pushed into the soil specimen by hand (through the 'vertical guiding' tube) and therefore the force required to cause penetration could not be measured precisely. However, the soil was sufficiently stiff to ensure this was a difficult process and it was estimated the vertical force required to insert the penetrometer was approximately 200 to 250 N at 300 mm of penetration. The main reason for not providing a mechanical means of installation was the extra cost and difficulty in constructing such an arrangement. Since the main focus of this research was the measurement of strains and displacements it was not considered to be absolutely necessary to provide an exact measurement of the force required for installation of the penetrometer.

A consequence of the installation process is the pile is not installed in one movement (i.e., monotonic installation) but instead is pushed in increments. A discussed in the Chapter 2, the installation process (jacking or driving) has been shown by Bond (1989) to have a significant influence on the formation of shear bands in the soil around a pile. Although the installation is this research is incremental it is considered to be effectively the same as

jacking due to the gradual application of force to cause penetration, as opposed the impact nature of pile driving.

7.2.2 Data Averaging

The first step taken to improve the accuracy of the soil marker displacement measurements was to average ten camera readings immediately prior to and following each penetrometer increment. A significant improvement could therefore be made on the accuracy of the camera measurements, which were found to show a random error of 0.01-0.02 mm (0.0015-0.003 R) for the model penetrometer tests. The averaging procedure was conducted using a simple MS Excel macro programme which could deal efficiently with the large volume of data recorded by the camera. These averaged readings, taken as the soil marker positions at each pile penetration, can then be corrected for external influences and used to find the soil displacement resulting from penetrometer installation.

7.2.3 Camera-Test Chamber Relative Movement

The relative movement of the test chamber and the camera during testing could be accounted for using reference markers on the front pane of glass of the chamber. The glass chamber was mounted on a porous stone and held in place by silicone bonds which allowed small movements of the chamber (less than 1 mm) to take place during pile installation. The reference markers were circular stickers adhered to the glass within the field of view of the camera and by monitoring the movements of these points, any movement of the test chamber during testing could be filtered out of the displacement results and accounted for.

The reference markers were, however, closer to the camera lens than the soil markers located in the centre of the chamber by virtue of their position on the front pane of the glass chamber; this led to a scale effect which had to be accounted for and is illustrated in Figure 7.1. It may be seen how distances measured at the front of the chamber are exaggerated compared to those at the mid-section of the chamber, i.e., distances X and X'. This effect can be reduced, but not completely eliminated, by increasing the camera-chamber distance D. This distance was approximately 1 m for the penetrometer tests. Two of the reference markers, of known distance apart (carefully measured with a Vernier scale callipers) were

used to calibrate the camera field of view. The ratio of X : X' is used as a factor to convert the apparent movement of the soil markers, as recorded by the camera, to actual movements. The distance factor, F_{dist} applied to the soil marker displacement results is found from;

$$X' = \frac{X}{D} \times (D + d) \tag{7.1}$$

$$F_{dist} = \frac{X'}{X} \tag{7.2}$$

where, D is the camera-chamber distance and d is the distance of the soil markers from the front face (half the width of the chamber).

For the two tests conducted, the distance factors used to multiply the soil displacements were 1.0949 & 1.0834 respectively. The external movement of the chamber/camera was removed from the displacement results by simply subtracting the factored horizontal (δX_{ref}) and vertical (δY_{ref}) averaged movements of the reference markers;

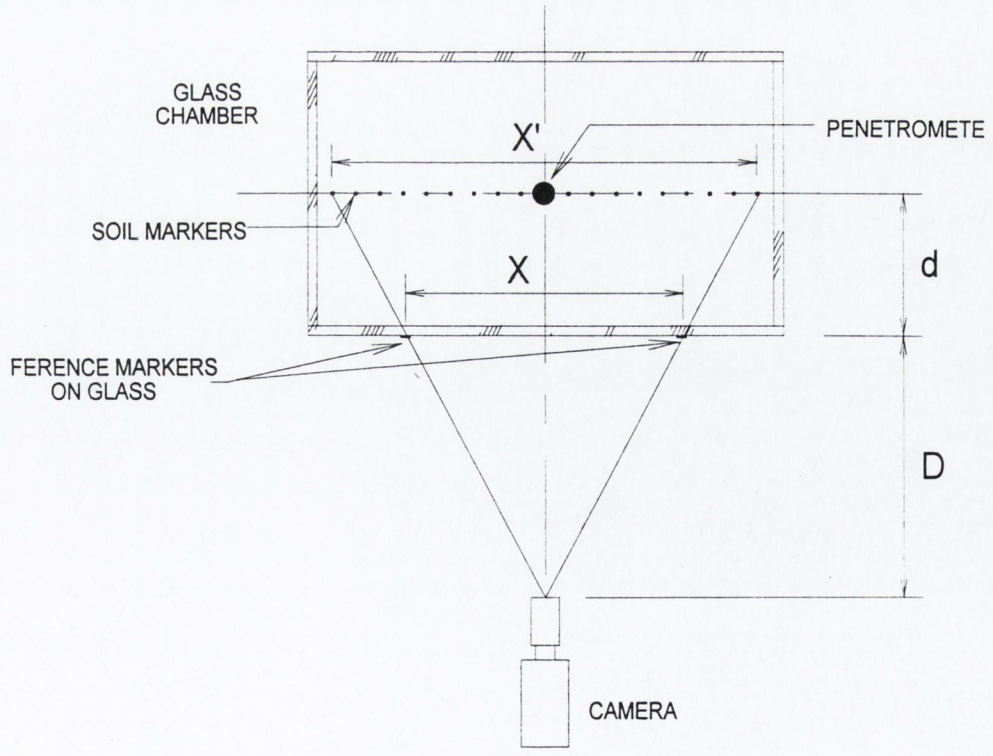

Figure 7.1. Distance effect of using reference markers on front of chamber

$$\left(X_n, Y_n\right) = \left[\mathrm{F}_{disp} \times \left(X'_n, Y'_n\right) - \left(\delta X_{ref}, \delta Y_{ref}\right)\right] \tag{7.3}$$

where (X'_n, Y'_n) are the unfactored co-ordinates of a soil marker, n and (X_n, Y_n) are the adjusted co-ordinates. During testing values for the external horizontal and vertical movement (δX_{ref} and δY_{ref}) were as much as 0.08 and 0.14 mm (0.013 and 0.022 R) respectively. It should be noted that the effects of refraction at the glass-air interface have not been accounted for but due to the positioning of the camera (~1 m from the glass), they are considered to be small.

7.2.4 Rotation of the Camera Reference Frame

The analysis of camera images from both of the experimental tests (such as the image in Figure 7.2 taken from Test 2) show that installation of the penetrometer occurred at very slight inclinations to the vertical axis of the camera. Despite the small magnitude of the angles involved, the effect of this inclination of the penetrometer on the results has been corrected for. This was done by rotating the *X-Y* plane defined by the camera to align with the centre axis of the penetrometer, which is shown to an exaggerated scale in Figure 7.3.

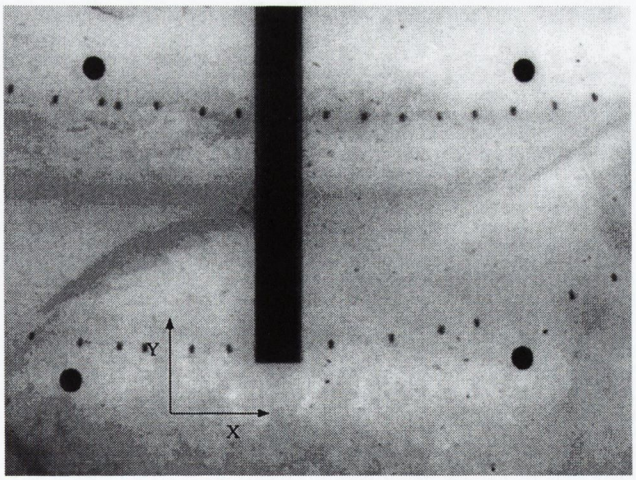

Figure 7.2. Image taken from Test 2, which illustrates the very slight inclination of the penetrometer to the X-Y plane

Small adjustments, thus have been made to the horizontal and vertical results and by the following equations;

$$x = x_n \cos\theta - y_n \sin\theta$$

$$y = y_n \cos\theta - x_n \sin\theta \tag{7.4}$$

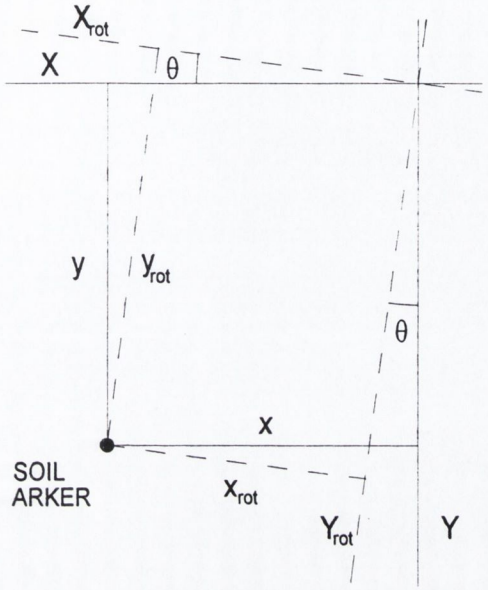

Figure 7.3. Rotation of the X-Y co-ordinate plane to allow for any misalignment of the penetrometer

where the angle, θ is measured from camera images taken of the penetrometer during its insertion and x and y are the horizontal and vertical distances to the initial position of the penetrometer along the centre axis of penetration. For both tests $\theta \approx 1°$ and the subsequent adjustments made to the soil movements were found to be greatest in the vertical direction, with the maximum correction found to be 0.02 mm (0.003 R).

7.2.5 Eccentricity of Soil Markers

Deviation of either the soil markers or the penetrometer from the presumed vertical plane being measured has a misleading effect on the observed movements. The true radial distance of the markers from the penetrometer and their radial displacement cannot be measured correctly if either soil marker or penetrometer deviate from this plane. This is illustrated in Figure 7.4 which shows a soil marker that is offset from a line perpendicular to the camera view through the centre of the penetrometer. The distances, a and δa are measured by the camera instead of the radial distances, r and δr. This eccentricity was accounted for by first measuring the distance, b of the soil markers from a line through the

centre of the penetrometer (shown in Figure 7.4) with a steel measuring tape. The initial radial position of the marker can then be found from;

$$r = \sqrt{a^2 + b^2} \tag{7.5}$$

where a is the initial horizontal distance measured by the camera. To find the change in radial distance, δr the eccentricity is corrected for using;

$$\delta r = \sqrt{(a + \delta a) + (b + \delta b)} - r_0 \tag{7.6}$$

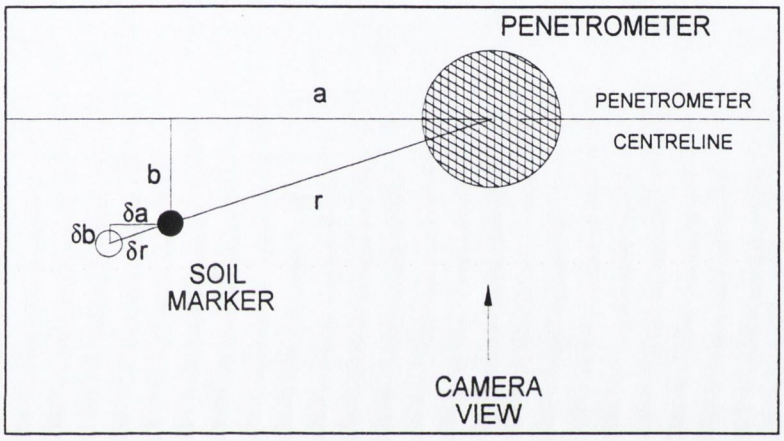

Figure 7.4. Schematic diagram of eccentric effect of soil markers on camera displacement measurements

where $a + \delta a$ is the current distance to the penetrometer centre measured by the camera and δb is found using similar triangles from:

$$\delta b = \frac{b}{a}(a + \delta a) - b \tag{7.7}$$

The effect of eccentricity is greatest for soil markers closest to the penetrometer with the maximum corrections made to the initial radius, r_0, of 0.4 mm (0.06 R) and to radial displacements, δr, of 0.24 mm (0.04 R).

7.2.6 Calculating Soil Marker Position Relative to Penetrometer (z/R)

The relative position of the penetrometer tip has a large influence on the mode of deformation experienced by the soil at any one time. For this reason it was important to

determine as accurately as possible the vertical position of the penetrometer tip relative to the soil markers during installation. In this research, this vertical distance which is normalised by the radius of the penetrometer is termed the z/R value. The z/R value at any stage during the test could be determined from the incremental nature of the penetrometer installation which allows the depth of the tip within the soil to be known during penetration. The initial position of the penetrometer tip was measured before starting the test relative to one of the reference markers on the chamber thus allowing it to be tied in later with the camera results. It was also necessary to take into account any non-verticality of the penetrometer installation, as has been presented in Section 7.2.4. This is shown schematically in Figure 7.5 where the influence of both the current position and inclination of the penetrometer are demonstrated.

To maintain consistency of notation the horizontal and vertical co-ordinates remain in terms of X and Y (although displacements are presented later in this chapter in terms of the cylindrical co-ordinates r and z). The vertical distance from a soil marker to the current position of the penetrometer tip is given by;

$$y = \left(X - X_{p_0}\right)\sin\theta + \left(Y - Y_{p_0} - \Delta Y_p\right)\cos\theta \tag{7.8}$$

where;

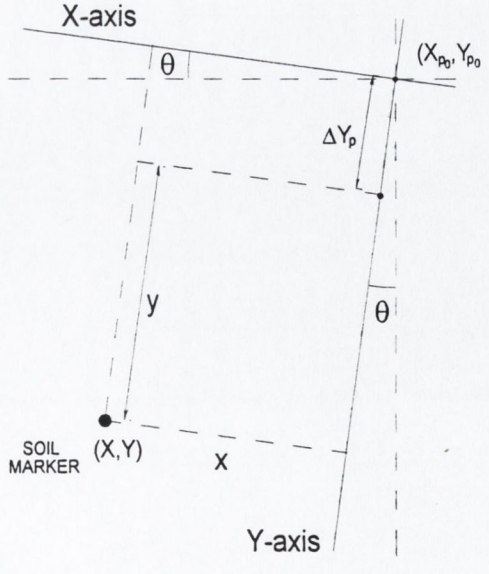

Figure 7.5. Determining z/R for soil markers during penetration

(X_{p0}, Y_{p0}) are the co-ordinates of the starting position of the penetrometer,

(X, Y) are the current co-ordinates of the soil marker,

ΔY_p is the depth of penetration of the penetrometer.

7.3 SOIL DISPLACEMENTS

The radial and vertical soil displacements measured from the model penetrometer tests using the video camera system are presented in this section. The soil movements are presented in the form of soil displacement fields around the penetrometer as well as displacement paths experienced by individual points in the soil. The results presented have been corrected for the factors, listed in Section 7.2, which could mask any of the real penetrometer-soil installation effects. After the adjustments have been made, the displacements display a random scatter which is typically in the order of 0.03 mm (0.005 R). The radial and vertical displacements presented in this section have been carefully checked to ensure they lie within the 'centre' of any scatter present in the results and, therefore, it is estimated the improved accuracy is to the order of 0.01 mm (0.0016 R).

7.3.1 Displacement Fields

7.3.1.1 Results from Tests 1 & 2

The radial and vertical displacements (dr and dz) for Tests 1 & 2, shown in Figures 7.6 to 7.9, have been normalised by the penetrometer radius (R) and are plotted against their initial radial position, r_0/R. It should be noted that downward movements have a positive sign and upward heave is therefore negative. The displacement fields are shown for two soil horizons behind the penetrometer, z/R = 5 (Figures 7.6 & 7.7) and z/R = 20 (Figures 7.8 & 7.9). Where possible the displacement plots have a logarithmic scale on the axes to give a better representation of the large range of soil movements occurring at different radii from the penetrometer. The negative vertical displacements (heave) that occur in the far field cannot, however, be presented on a log scale and have been shown separately in Figures 7.7(b) & 7.9(b).

The displacements are presented in a manner that identifies the test from which they were measured. The distinction between the tests is maintained as after conducting the first test, the procedures which ensured optimum accuracy were better understood for the second test, and therefore there is greater confidence in the results from Test 2. A further consideration was the cracking of the glass chamber whilst unloading the sample during the consolidation phase of Test 1. The lower part of the front pane was damaged but held place with clamps and is thought to have caused only minimal disturbance to the sample. The small degree of uncertainty introduced by this, however, reduced confidence in the results from Test 1.

7.3.1.2 Displacement trends

For the purpose of comparison with other data and in particular for fitting a theoretical prediction, it was important to present a definitive set of displacement results. The displacement fields from Tests 1 & 2 show some scatter, which is most pronounced for the points furthest away from the penetrometer. This is due in part to the exaggerating effect of the log plot and to the greater effect of any measuring errors on the smaller displacements. An attempt has been made to reduce the scatter in the results and present a clearer representation of soil movements experienced during the test. This was done by carefully selecting the most reliable data and conducting some averaging.

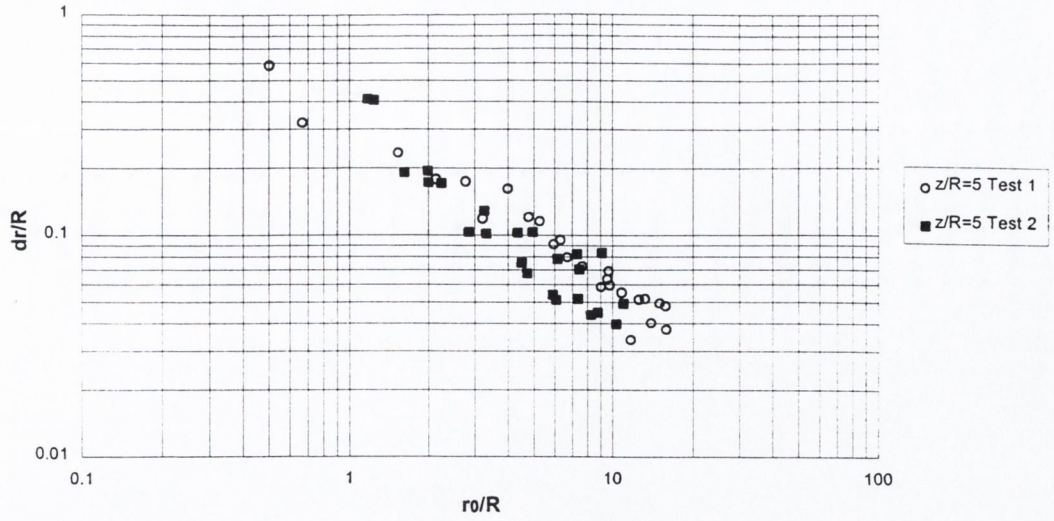

Figure 7.6. Radial displacements for Tests 1 & 2 at z/R = 5.

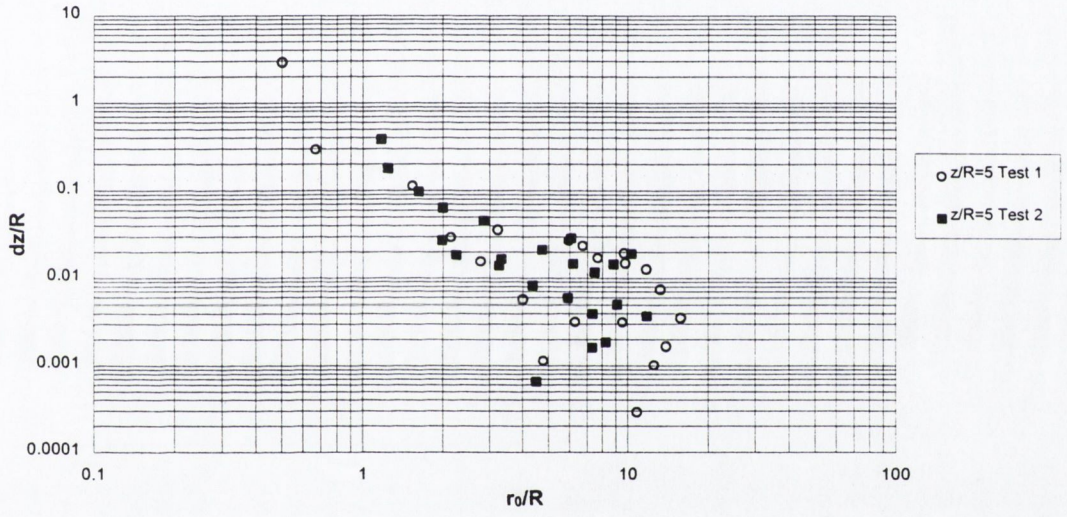

(a)

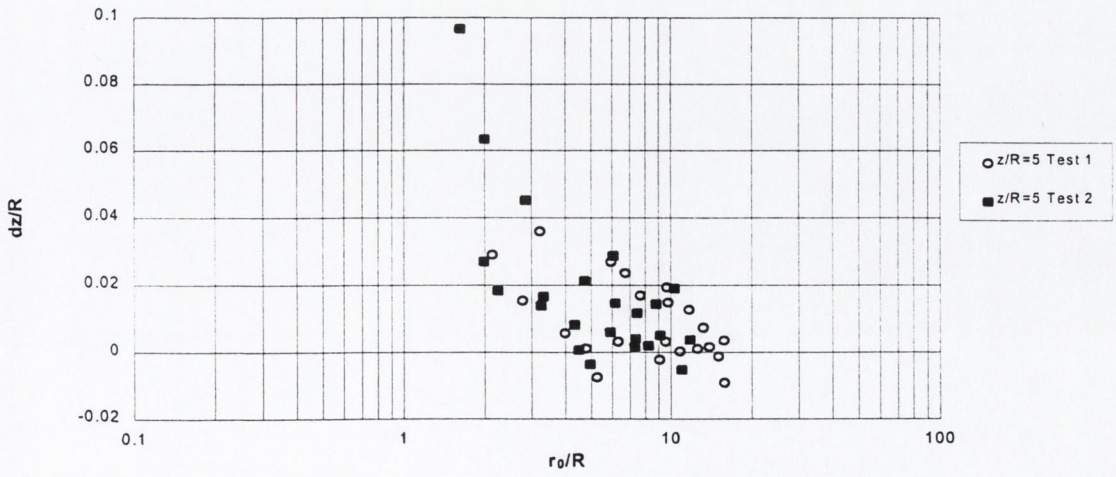

(b)

Figure 7.7. Vertical displacements for Test 1 & 2 at z/R = 5 with: (a) negative values not shown; (b) negative values shown.

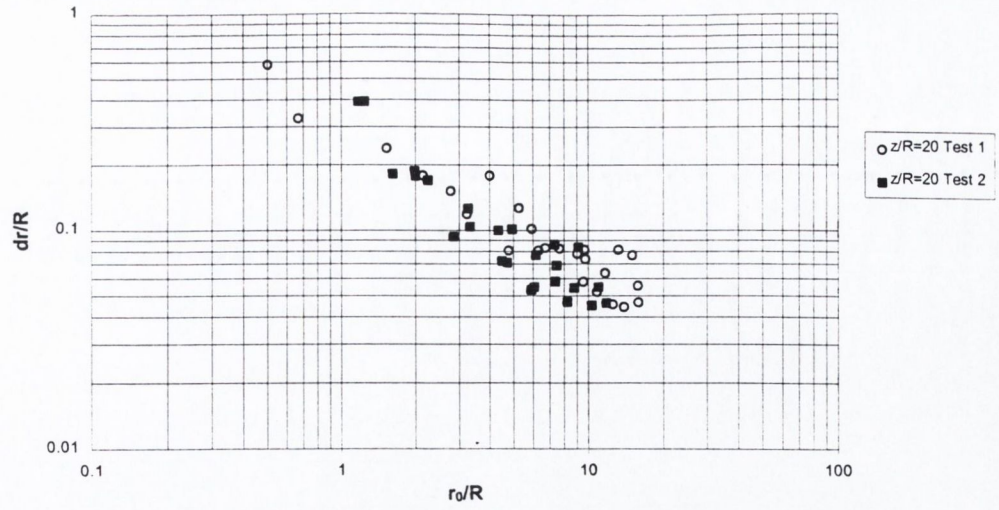

Figure 7.8. Radial displacements for Test 1 & 2 at z/R = 20.

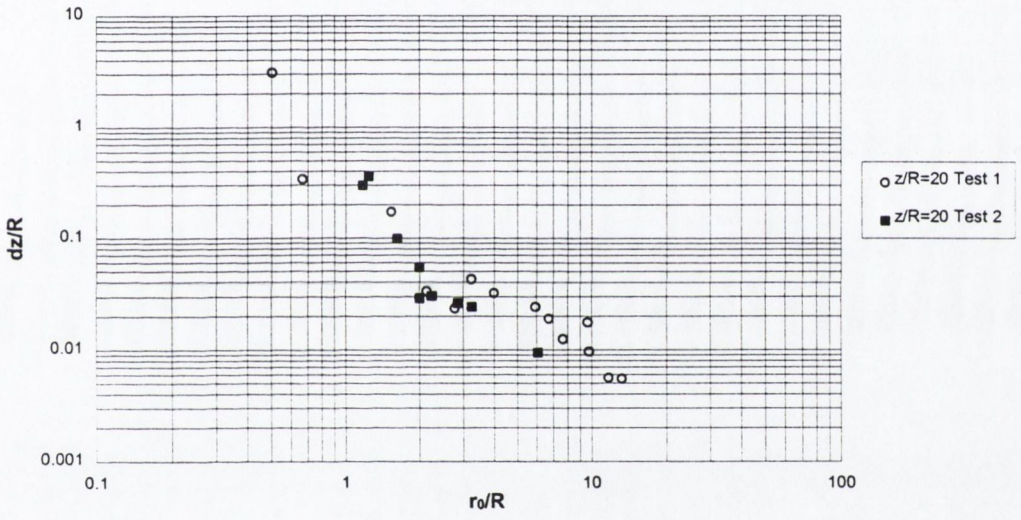

(a)

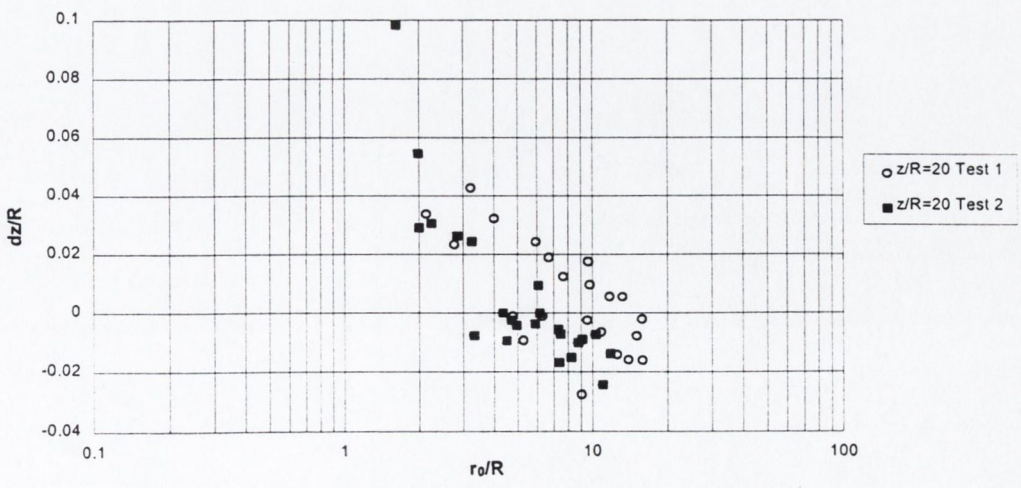

(b)

Figure 7.9. Vertical displacements for Test 1 & 2 at z/R = 20: (a) negative values not shown; (b) with negative values shown

Instead of using all the experimental data measured by the camera, only that which was found from clear and well defined soil markers was used. The points which failed to meet this criterion were easily distinguished from the camera images and were also made apparent by the erratic nature of these results. Some points with similar initial radii, particularly in the far field, were averaged to improve accuracy and reduce the effect of any measuring errors in the results. Employing this more careful treatment of the experimental results yields the displacement fields shown in Figures 7.10 & 7.11. Also plotted, for comparison, are the displacements from model penetrometer tests by Francescon (1983) and Gue (1984) which are described in Chapter 2.

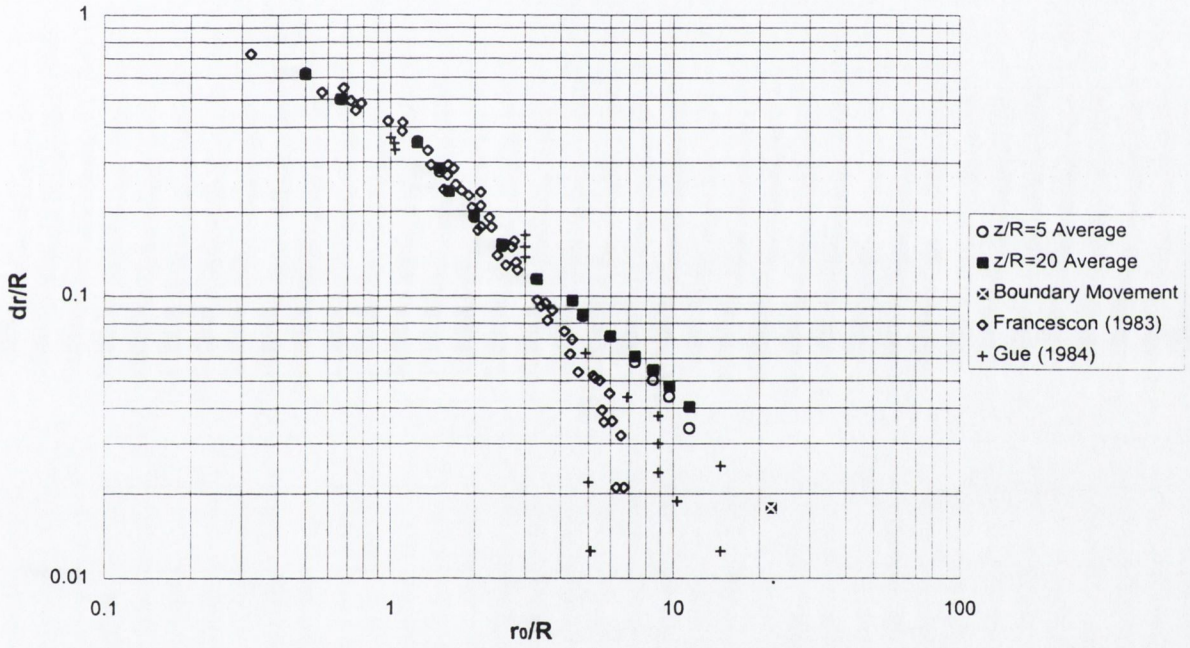

Figure 7.10. Comparison of radial displacements at z/R=5 & z/R=20 with other experimental data

It has also been easier to deduce trends from this set of displacement data. The radial displacements in Figure 7.10 show that:

1. Close to the penetrometer ($r_0/R < 3$) the movements are very similar for all the displacement data (including for both of the z/R values).
2. At large initial distances from the penetrometer ($r_0/R > 7$) the radial displacements measured at z/R = 20 are greater than those at z/R = 5.

3. A divergence of the results from this investigation and that of Francescon (1983) & Gue (1984) occurs for $r_0/R > 3$. This is due, in main, to the influence of the far field boundary; which for Francescon (1983) is located at 13R, for Gue (1984) at 28R and in the TCD model it is at 22R. Francescon's results thus show the greatest restriction to the far field movements, while the results of Gue (1984) fall between these and the TCD results. The reason for the latter trend is the semi-fixed nature of the chamber walls used in this research. The glass chamber used to hold the soil sample was held together by silicone which allows a small amount of elastic movement on these joints. These bonds also showed some deterioration caused by the consolidation process, which allowed some additional movement during penetrometer installation.

Theoretical movement of the far field boundary was calculated to be 0.11 mm (0.018 R) from the additional volume of the penetrometer introduced into the soil, and is plotted in Figure 7.9. This theoretical boundary movement is found to fit well with the radial soil displacements (dr) as an extension of their general trend, suggesting a minimal influence of the boundary on dr. The influence of the rectangular shape of the chamber, rather than cylindrical, cannot be fully known but is considered to be negligible due the distance to the far field boundary (~22R) and is certainly of less influence than that of other tests, i.e., Francescon (1983) where it is at 13R.

The definitive vertical displacement fields for the TCD model penetrometer tests at z/R distances of 5 & 20, are shown with results from Francescon (1983) and Gue (1984) results in Figures 7.11. It can be seen that:

1. The displacements close to the penetrometer ($r_0/R < 2$) show greater downward movement at z/R = 20 than at z/R = 5 due to a 'drag down' effect; see Figure 7.11(a).
2. The reverse is true for $r_0/R > 2$ where the soil at z/R = 20 starts to show upward vertical rebound and thus display lower values than at z/R = 5. This upward rebound is translated into net upward heave of the soil at distances greater than r/R > 4 (Figure 7.11b) while the soil at the z/R = 5 horizon only experiences net downward (positive) movement.
3. Close to the penetrometer the TCD results show slightly greater downward movement than those of Francescon (1983) but are similar to the limited number of Gue (1984) measurements in this region.

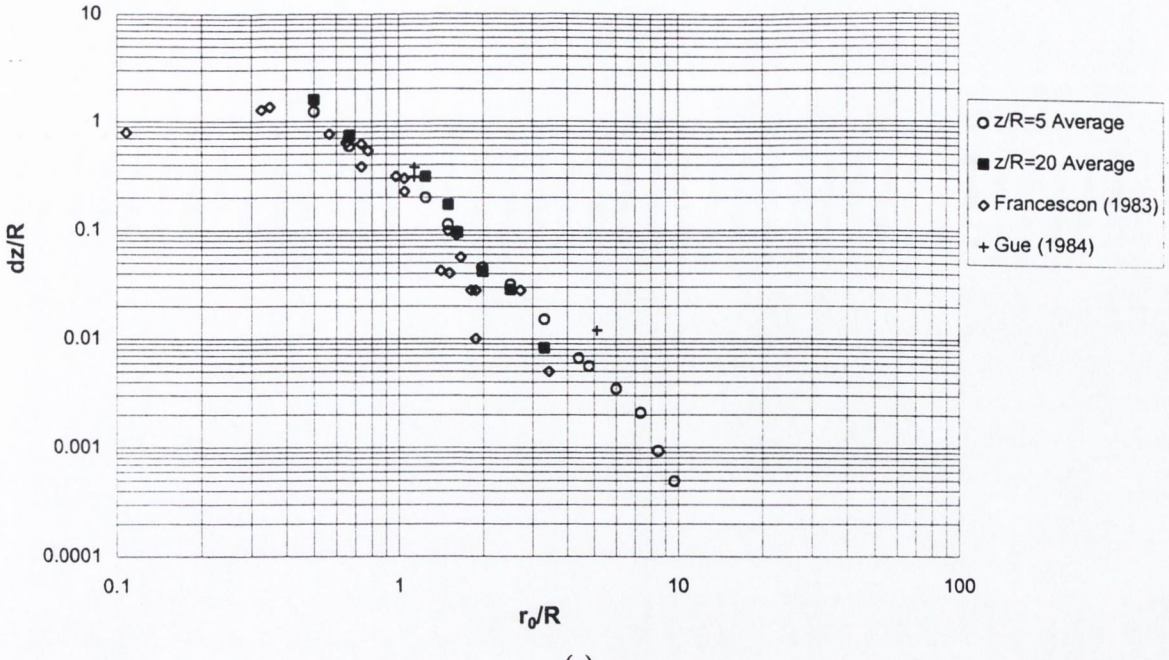

(a)

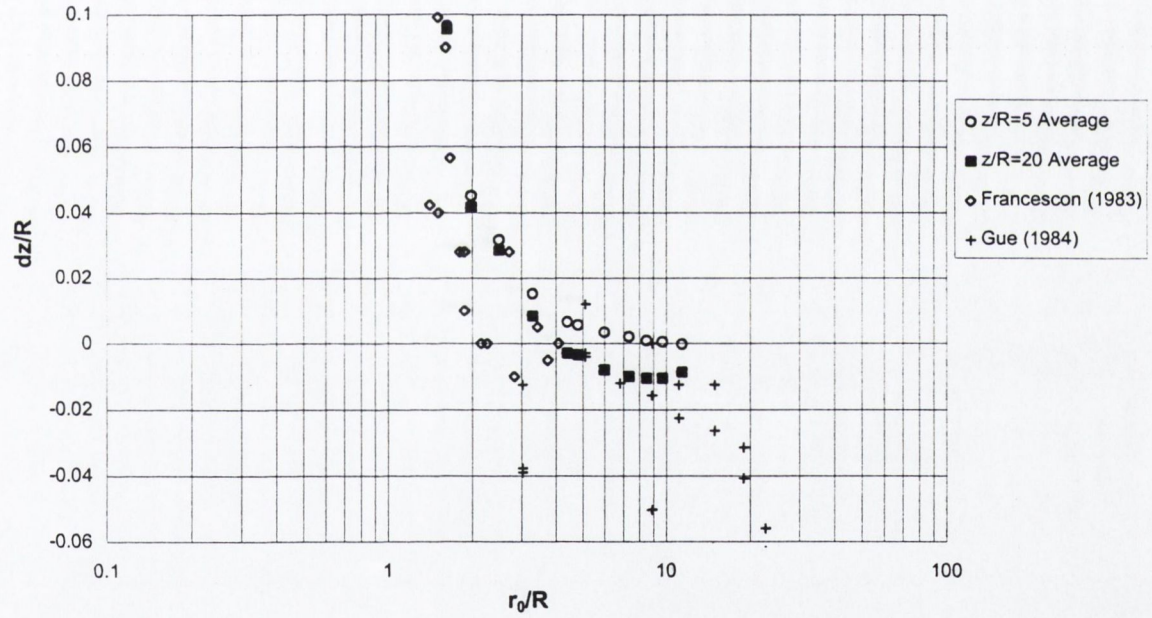

(b)

Figure 7.11. Comparison of vertical displacements at z/R=5 & z/R=20 with other experimental data: (a) negative values not shown; (b) with negative values shown

4. For r/R >3 the Gue (1984) results show net heave greater than that shown in the TCD tests, whilst for r/R > 2.5 the Francescon (1983) data shows small amounts of heave.

The comparison of the Gill (1999) displacement data with that of Francescon (1983) and Gue (1984) has highlighted that the radial movements are insensitive to tip geometry but

have a large influence on vertical movements close to the penetrometer. The similarity, in all the tests, of the radial displacements and to an extent the medium to far field vertical displacements, despite the different soil types used, reinforces the view of Baligh (1985) that soil movements are insensitive to the material properties. The data from this Thesis, however show the importance of the vertical distance (z/R) from the tip on the movements, which is not fully accounted for in the other data.

7.3.2 Displacement Paths

The Videoextensometer system used to record the soil displacements allowed continuous measurement of movements throughout the installation process. The displacement paths of the soil markers could therefore be traced and are presented for a representative number of points throughout the soil mass in Figure 7.12. The displacement paths shown have been 'smoothed' of the random scatter present in the results after the correction procedures in Section 7.3 have been conducted (which was typically in the order of 0.005 R or 0.03 mm).

The soil paths at all radii show an initial downward phase of movement and then a reversal after the penetrometer tip has passed. This reversal is only slight interruption in a general downward movement for soil close to the penetrometer, while for soil further away the upward trend continues resulting in soil heave. In between these two extremes of behaviour a complicated series of reversals in vertical movement takes place. The key features of soil movement shown by the displacement paths are;

- downward drag of soil close to penetrometer ($r_0/R < 1.6$)
- for soil in the region $1.6 < r_0/R < 5$ the vertical movements undergo three reversals with the final movement in the upward direction
- for $r_0/R > 5$ after an initial downward phase of vertical movement there is a reversal resulting in upward heave
- radial movement is outward in general although for $r_0/R < 9$ a reversal occurs once the tip has passed.

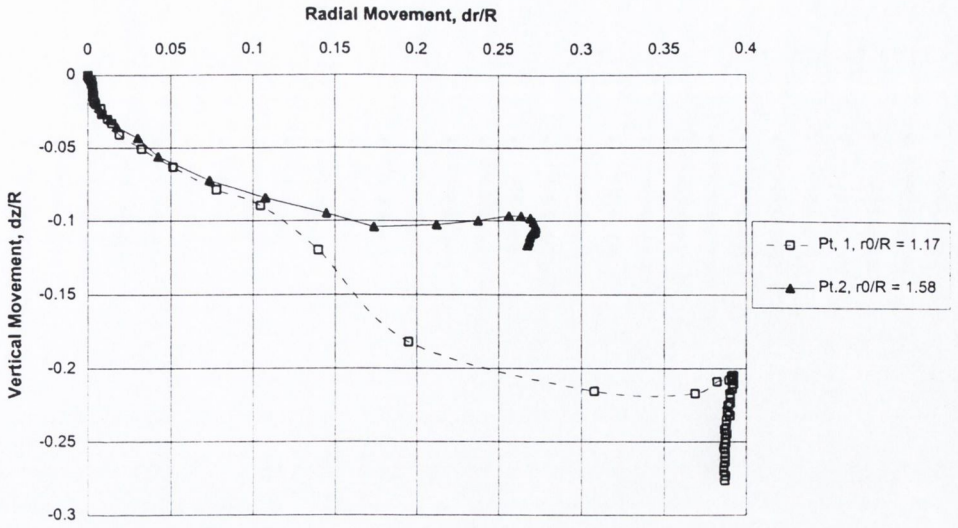

(a)

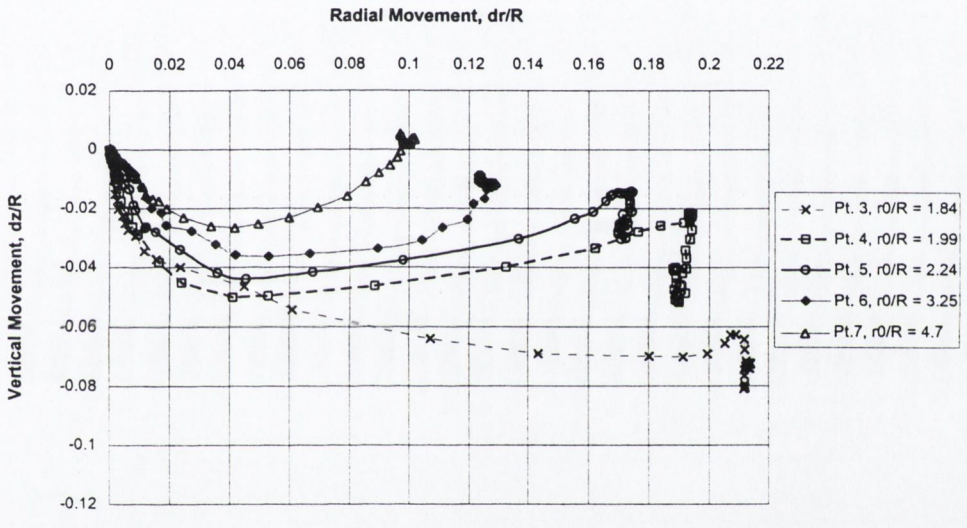

(b)

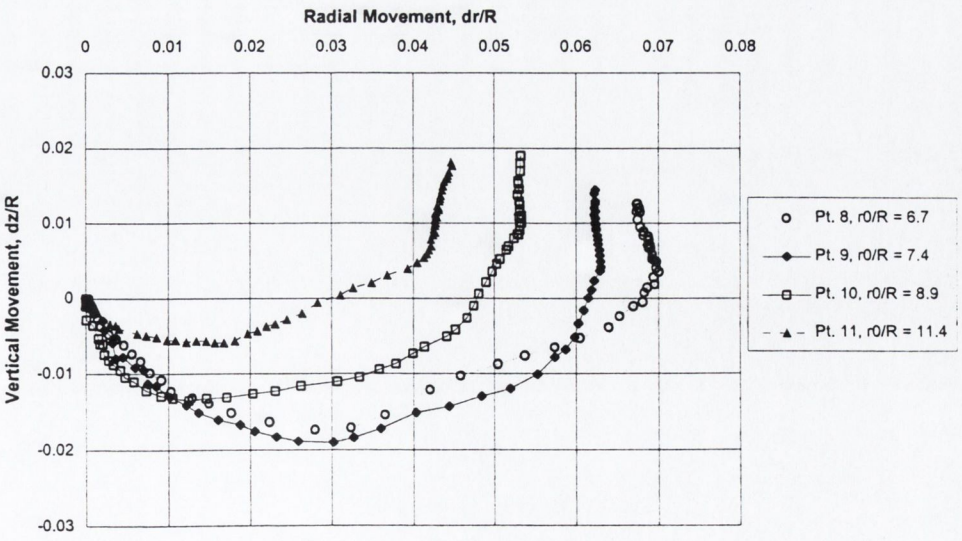

(c)

Figure 7.12. Displacement paths during penetrometer installation: (a) $r_0/R < 1.6$; (b) $1.6 < r_0/R < 5$; (c) $r_0/R >$ 5

7.4 SOIL STRAIN

7.4.1 Strain Paths

The strain experienced by elements within the soil mass during penetrometer installation has been calculated from the displacement measurements. The strains are presented in the form of strain paths represented by three deviatoric strains E_1, E_2 & E_3 (defined in Chapter 3) which provide a clear picture of the shearing modes of the soil. The strain paths calculated correspond to points represented by the displacement paths shown in Section 7.3.

Strain is calculated by differentiation of the soil displacements in the radial and vertical directions and in this Thesis a curve fitting procedure to the displacement data rather than numerical differentiation has been used to achieve this. The curves, which are fitted to the radial and vertical displacements plotted with respect to the vertical distance from the tip (z/R), are described by equations that could be readily differentiated. This provides a convenient means of calculating strain and allows the strain to be found at any point along the displacement/streamline paths. This is especially convenient close to the penetrometer tip where the large deformations increase the difficulty in interpolating between the known points using a numerical technique.

The curve equations used to fit the displacement data are a combination of polynomial and exponential formulation (see Equation 7.9). The general purpose mathematical package, MATLAB was used to fit least squares solutions to the radial and vertical displacement data. This was done by providing an initial estimate for the coefficients of the curve fitting equation. The general formulation of fitting the radial (dr/R) and vertical (dz/R) displacements with respect to the vertical position (z/R) was, after careful consideration, selected to be of the form;

$$dr_n \quad or \quad dz_n = a_0 . \frac{b_0 + b_1 z_n + b_2 z_n^2 + b_3 z_n^3 + b_4 z_n^4}{1 + \exp\left(-a_1 z_n\right)} \tag{7.9}$$

where,

$$dr_n = dr/R$$
$$dz_n = dz/R$$
$$z_n = z/R$$

and a_i and b_i are the constants for the least squares solution found using MATLAB. Different variations of this equation were used depending on the shape of the curve being fitted (and typical solutions are shown in Figure 7.13 & 7.14). More reversals in the displacement direction required a higher order polynomial part of the curve equation. The displacements (dr, dz) are often called (u, v) and differentiation of (7.9) in terms of z gives:

$$\frac{\partial(u)}{\partial z} \text{ or } \frac{\partial(v)}{\partial z} = \begin{bmatrix} \left(1+\exp\left(-a_1 z_n\right)\right).\left[b_1 + 2b_2 z_n + 3b_3 z_n^2 + 4b_4 z_n^3\right] \\ -\left(b_0 + b_1 z_n + b_2 z_n^2 + b_3 z_n^3 + b_4 z_n^4\right).\left[-a_1 \exp\left(-a_1 z_n\right)\right] \end{bmatrix} \Bigg/ \left(1+\exp\left(-a_1 z_n\right)\right)^2 \tag{7.10}$$

If the flow analogy of the Strain Path Method is used in relation to the displacement paths followed by the soil elements around the penetrometer, the experimental data gave eleven streamlines to represent the soil movement. Equation (7.10) allows differentiation with respect to vertical position (z/R) to take place at an infinite number of points along the streamline. Differentiation in the radial direction, however, can only take place between selected points on the eleven streamlines, and this is demonstrated schematically in Figure 7.15. The radial and vertical displacement derivatives along flow path '0' are found from the following equations, for which values of u and v were obtained by direct substitution into the equation of each 'streamline'.

$$\frac{\partial u}{\partial r} = \frac{1}{2}\left[\frac{u_2 - u_0}{\Delta r_2} + \frac{u_0 - u_1}{\Delta r_1}\right]; \qquad \frac{\partial v}{\partial r} = \frac{1}{2}\left[\frac{v_2 - v_0}{\Delta r_2} + \frac{v_0 - v_1}{\Delta r_1}\right] \tag{7.11}$$

where $\Delta r_1 = r_0 - r_1$ and $\Delta r_2 = r_2 - r_0$ respectively. The number of soil elements tracked thus restricts the accuracy of differentiation in the radial direction. The values obtained from Equations (7.9), (7.10) & (7.11) at any point along one of the flow paths are used to find the radial, vertical, circumferential and shear strain which are given by;

$$\varepsilon_{rr} = \frac{\partial u}{\partial r}; \qquad \varepsilon_{zz} = \frac{\partial v}{\partial z}; \qquad \varepsilon_{\theta\theta} = \frac{u}{r}; \qquad \varepsilon_{rz} = \frac{1}{2}\left(\frac{\partial u}{\partial z} + \frac{\partial v}{\partial r}\right) \tag{7.12}$$

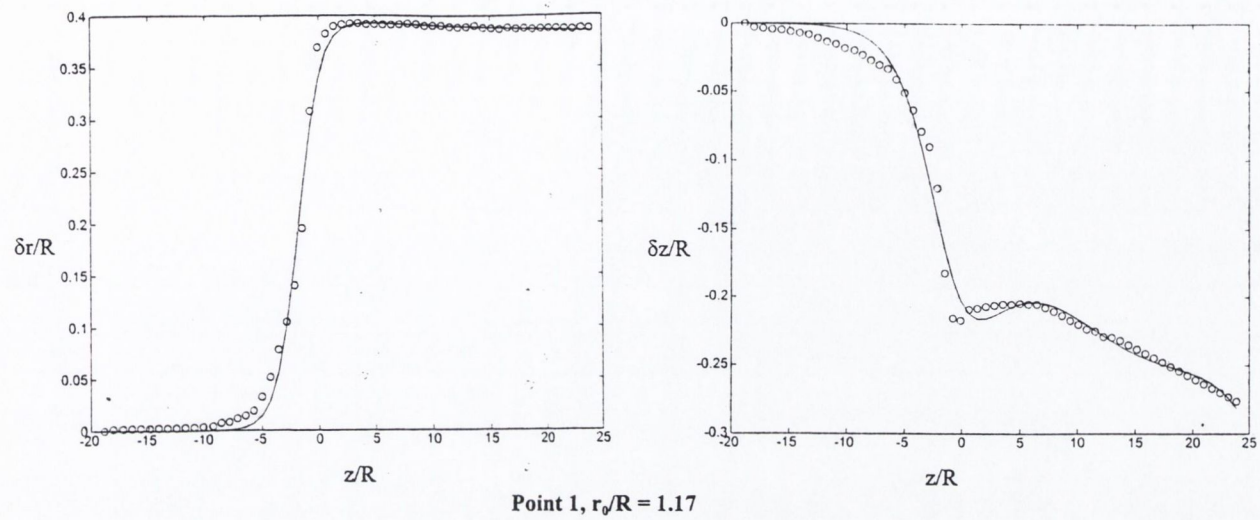

Point 1, $r_0/R = 1.17$

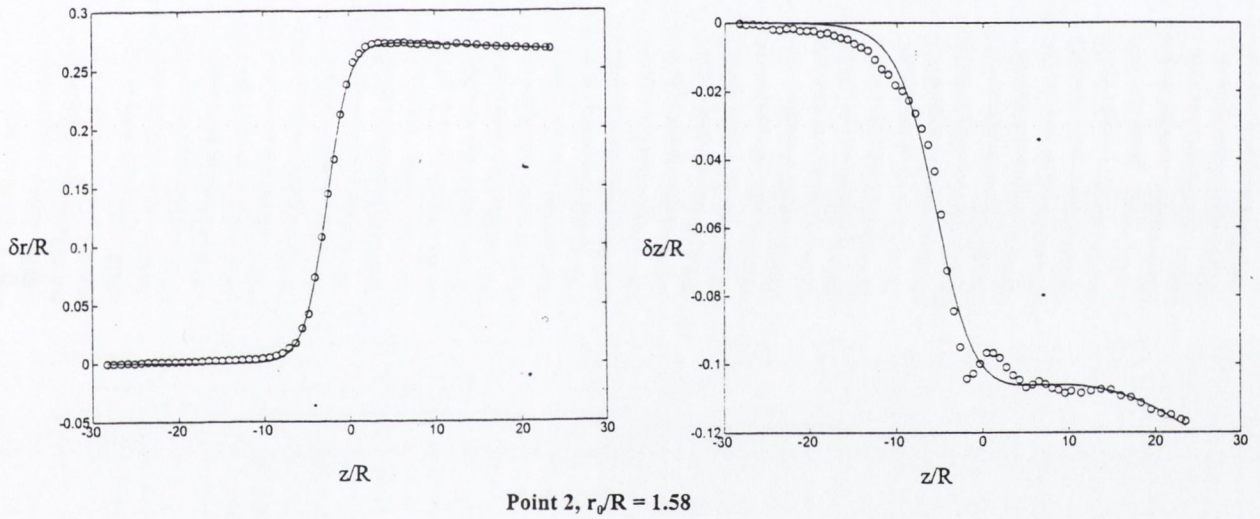

Point 2, $r_0/R = 1.58$

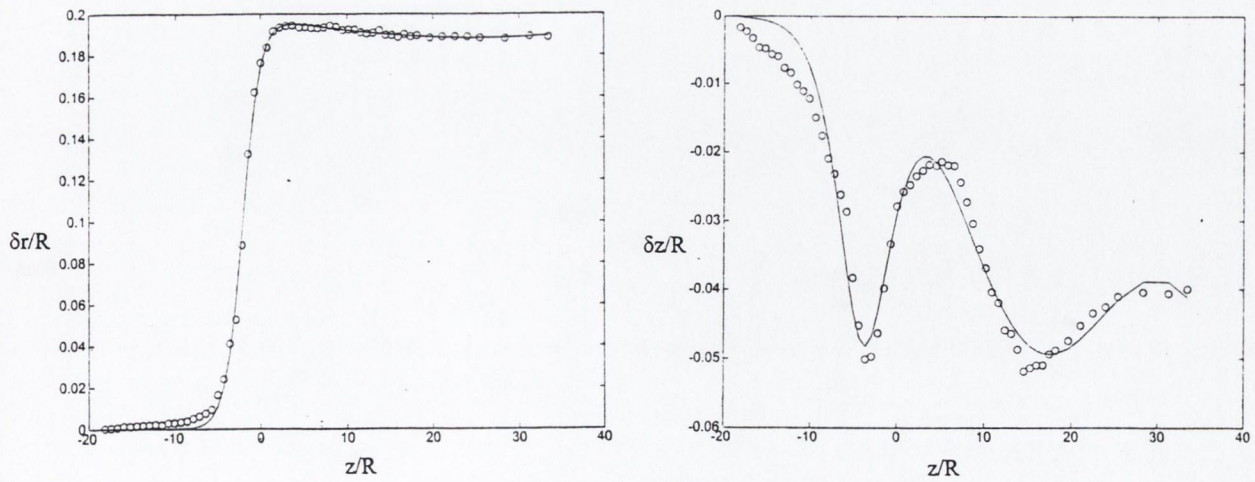

Point 4, $r_0/R = 1.99$

Figure 7.13. Curves fitted to displacement data using MATLAB ($r_0/R < 3$)

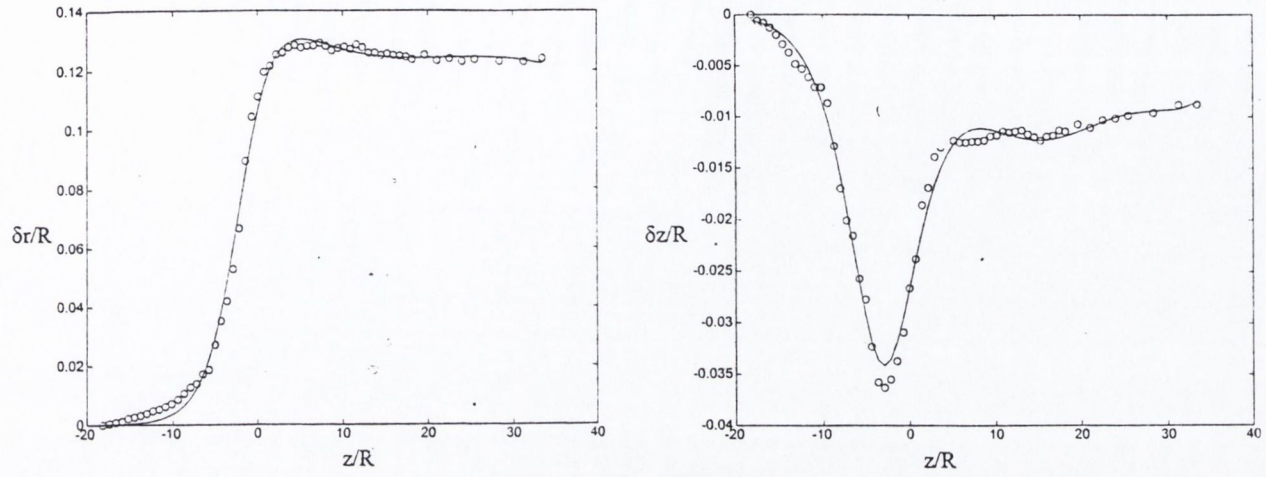

Point 6, $r_0/R = 3.25$

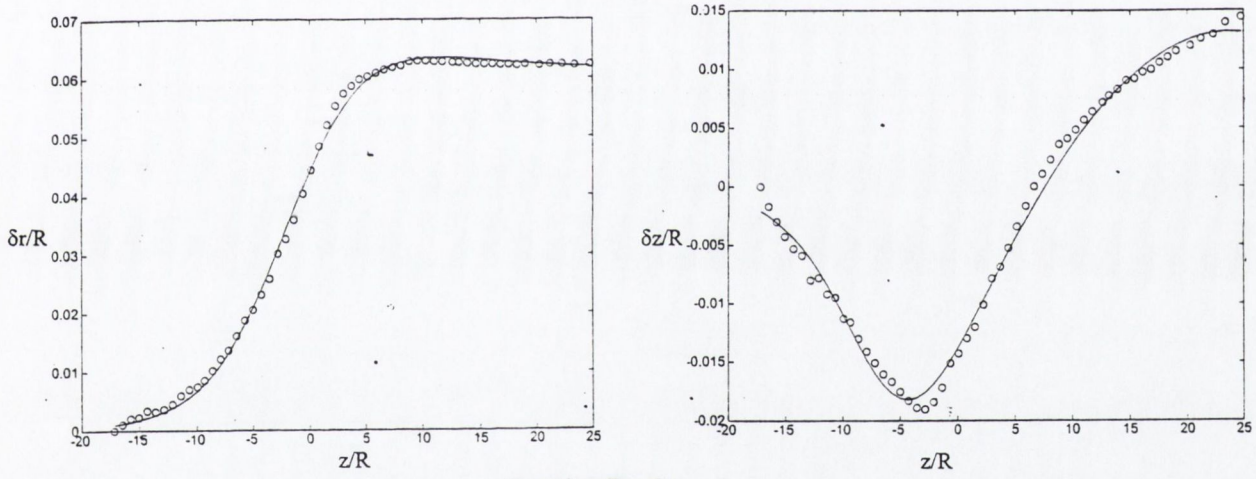

Point 9, $r_0/R = 7.4$

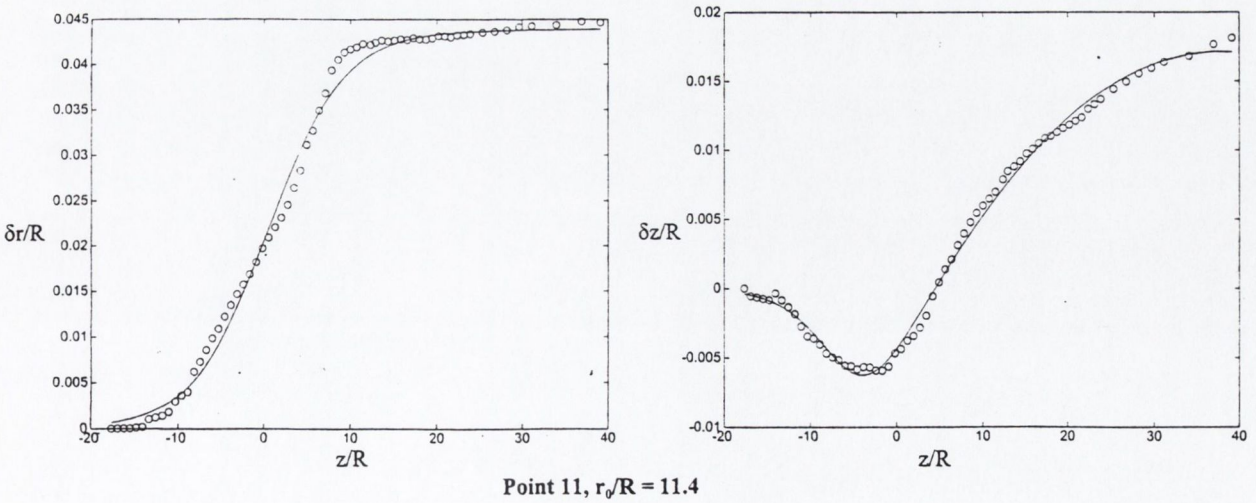

Point 11, $r_0/R = 11.4$

Figure 7.14. Curves fitted to displacement data using MATLAB ($r_0/R > 3$)

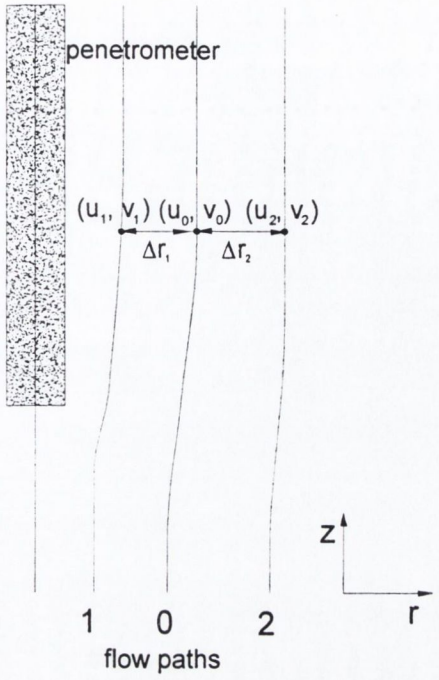

Figure 7.15. Schematic diagram showing differentiation in the radial direction with points along 'flow paths'

The approximate nature of the strain paths is illustrated in Figures 7.16 to 7.19, particularly in the vertical strains close to the penetrometer. While it has not been possible to quantify the approximation made to the data by curve fitting, peak displacements never differ by more than 10% from the approximated value. As such the strains should be seen as representative of a region of soil but not as exact measurements.

The main features of the strain paths followed by soil elements in the model penetrometer tests are now described for four regions at increasing radial distance from the penetrometer:

(i) $r_0/R < 1.5$ (Figure 7.16)

- high compressive values of E_1 occur beneath the penetrometer which reduce at $z/R \cong -3$ and are tensile at $z/R \cong 1$
- a final reversal of E_1 occurs at $z/R = 4$ after the tip has past with E_1 ending in compression
- E_2 reaches a maximum at $z/R = -1$ (just before the tip passes) and then reverses before reaching an approximately constant value at $z/R = 4$
- E_3 increases steadily before reversing at $z/R = 0$ with a second reversal in shear strain occurring at $z/R = 10$ so that the final direction of E_3 is increasing with

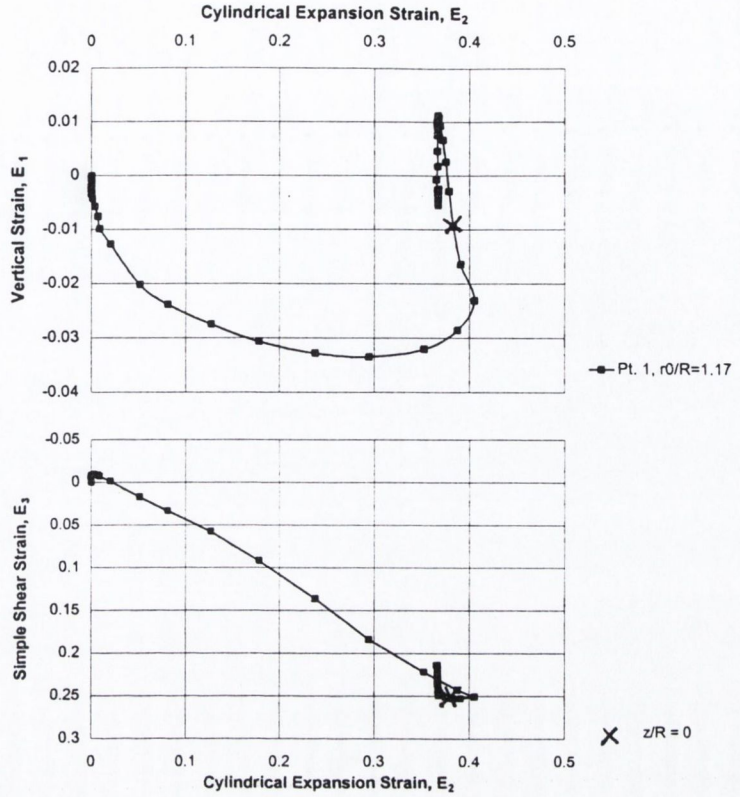

Figure 7.16. Strain paths followed by soil elements during penetrometer installation ($r_0/R < 1.5$)

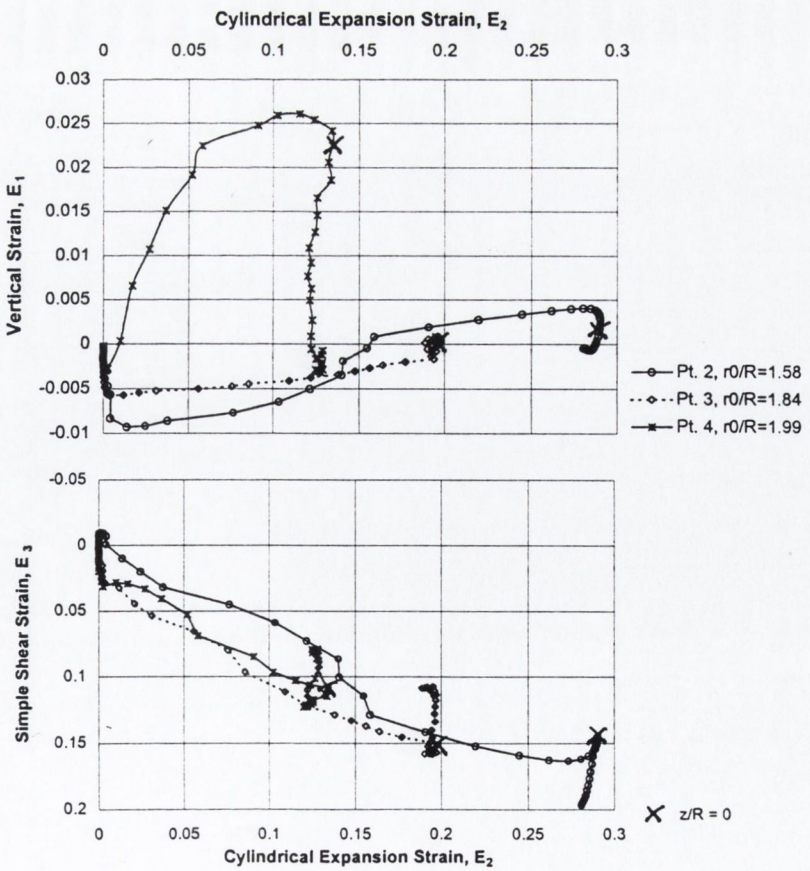

Figure 7.17. Strain paths followed by soil elements during penetrometer installation ($1.5 < r_0/R < 2$)

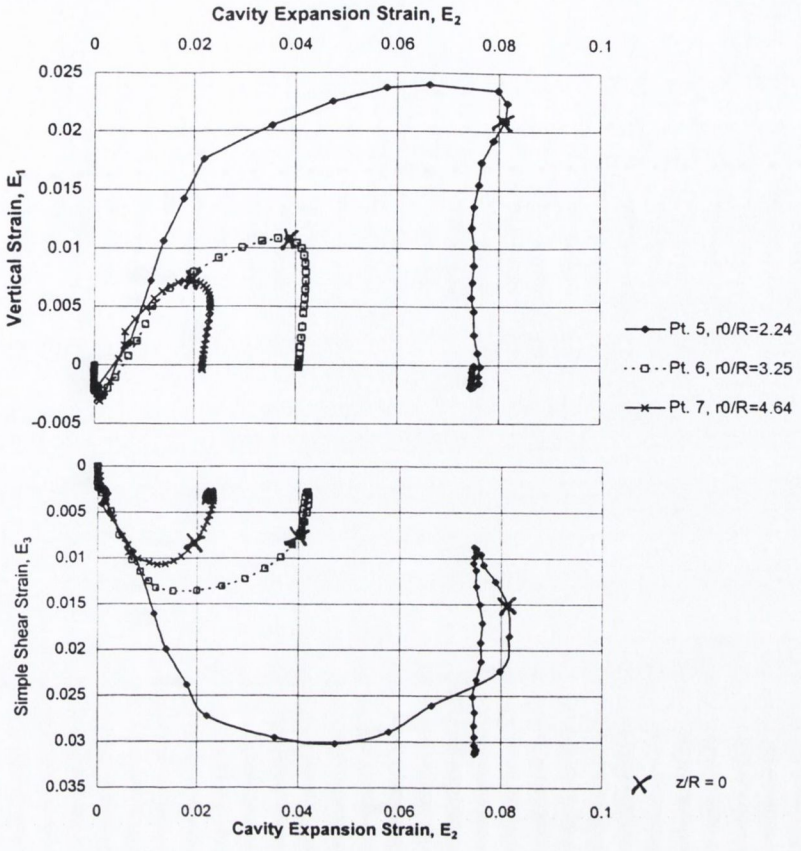

Figure 7.18. Strain paths followed by soil elements during penetrometer installation ($2 < r_0/R < 5$)

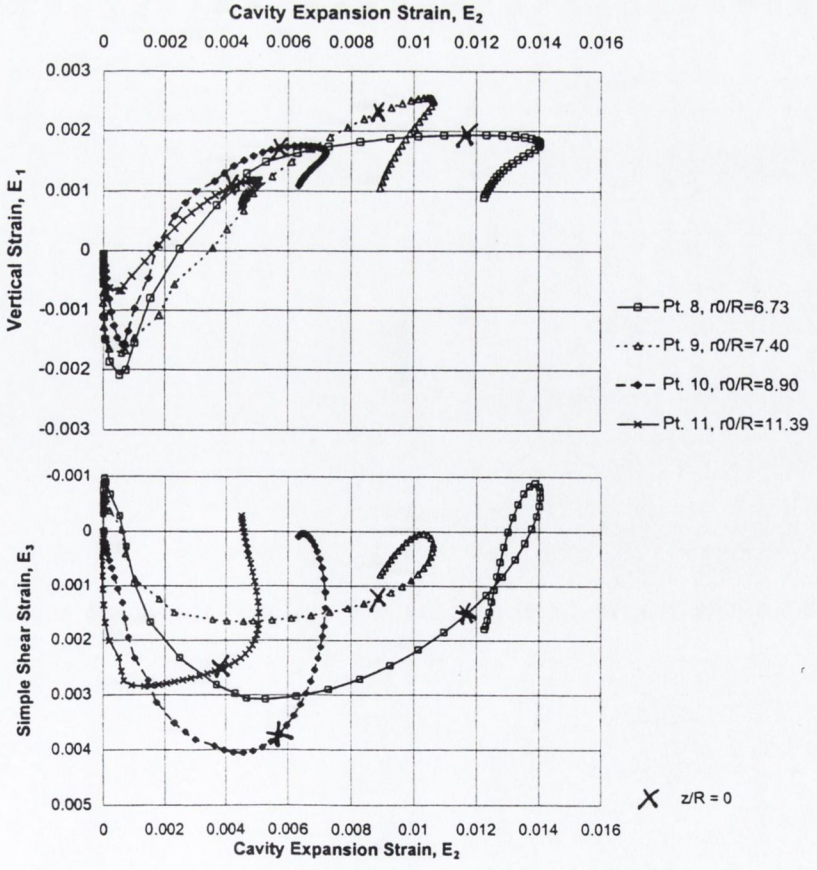

Figure 7.19. Strain paths followed by soil elements during penetrometer installation ($r_0/R > 5$)

further penetration (this is evident from the data but is more difficult to see from Figure 7.16)

(ii) $1.5 < r_0/R < 2$ (Figure 7.17)

- an initial compressive phase of E_1 occurs beneath the penetrometer which reverses typically at z/R = -10 and a second reversal of E_1 occurs at z/R = -4 leaving E_1 with a net compression value
- E_2 reaches a maximum at z/R = -2 before reversing and then continues to reduce at slow rate
- E_3 increases steadily before reversing typically at z/R = 4 and continues to decrease with further penetration (however, the strain path at $r_0/R = 1.58$ reverses before the tip has passed at z/R = -2, then reverses again at z/R= 0 and continues to increase thereafter)

(iii) $2 < r_0/R < 5$ (Figure 7.18)

- after initially going into compression E_1 reverses at z/R = -9 and goes into tension before another reversal of E_1 occurring at z/R = 0 brings E_1 back into a final compression value
- E_2 reaches a maximum typically at z/R = 4 (for $r_0/R = 2.24$ the peak is at z/R = 0) before undergoing a slight reversal and continues to reduce slowly as penetration increases
- E_3 is initially positive before undergoing a reversal typically at z/R = -3, with a second reversal causing E_3 to increase again when the tip has passed (between z/R = 4 & 8); this second reversal is more pronounced for points closer to the penetrometer

(iv) $5 < r_0/R < 12$ (Figure 7.19)

- E_1 undergoes compression before reversing at z/R = -10 and goes into tension, with a final reversal of E_1 occurring at z/R = 4 (although E_1 remains in tension)
- E_2 reaches a maximum between z/R = 4 & 6 before reversing and reducing steadily as penetration increases

- E_3 initially increases before undergoing a reversal (which is typically at z/R = -5) with a second reversal at z/R = 10 causing E_3 to increase again (although there is no second reversal in E_3 at r_0/R = 11.4 the point furthest from the penetrometer)

7.4.2 Strain Contours

The strain contours due to the penetration of the flat ended penetrometer used in the model test have been produced from the experimental results and are shown in Figures 7.20 to 7.24. The strain data used for contouring was the same as that used to produce the strain paths shown in Section 7.4.1. The strain contours were plotted using Surfer, a surface mapping package, and have been found for radial (ε_{rr}), circumferential ($\varepsilon_{\theta\theta}$), vertical ($\varepsilon_{zz}$), and shear strains ($\varepsilon_{rz}$). The sign convention used shows compressive strain as negative and therefore tensile strain is positive. Figure 7.20 presents all four strain plots together and Figures 7.21 to 7.24 shows each plot individually to allow a closer view of the contouring detail (note that, for reasons previously explained, there are no data for the region directly beneath the penetrometer). The Surfer contouring package was also limited by the small number of data points in certain high strain gradient areas, and therefore the program will misrepresent the exact strain state in these areas.

The radial strain contours (Figure 7.21) are compressive everywhere except for a region far ahead of the penetrometer (z/R $\cong$ -8). Large strains (> 5 %) are located in a zone around the penetrometer extending 2R radially and 5R ahead of the tip. Far behind the tip, the strain contours for both ε_{rr} and $\varepsilon_{\theta\theta}$ are approximately parallel to the axis of the penetrometer. The circumferential strains (Figure 7.22), which are tensile, also have a similar sized zone to the radial strains where large straining is taking place, although differences are apparent close to the penetrometer. For ε_{zz} (Figure 7.23), the soil is in compression in the region ahead of the penetrometer tip when r/R < 2, although this compressive zone widens at z/R = -6 (i.e., far ahead of the tip). The rest of the soil in the vicinity of the penetrometer is in tension except for 'pockets' of compression close to the penetrometer shaft. The shear strain (Figure 7.24) is located predominately in a 'bulb' shaped zone close to the penetrometer (up to 20 %), which is widest ahead of the tip.

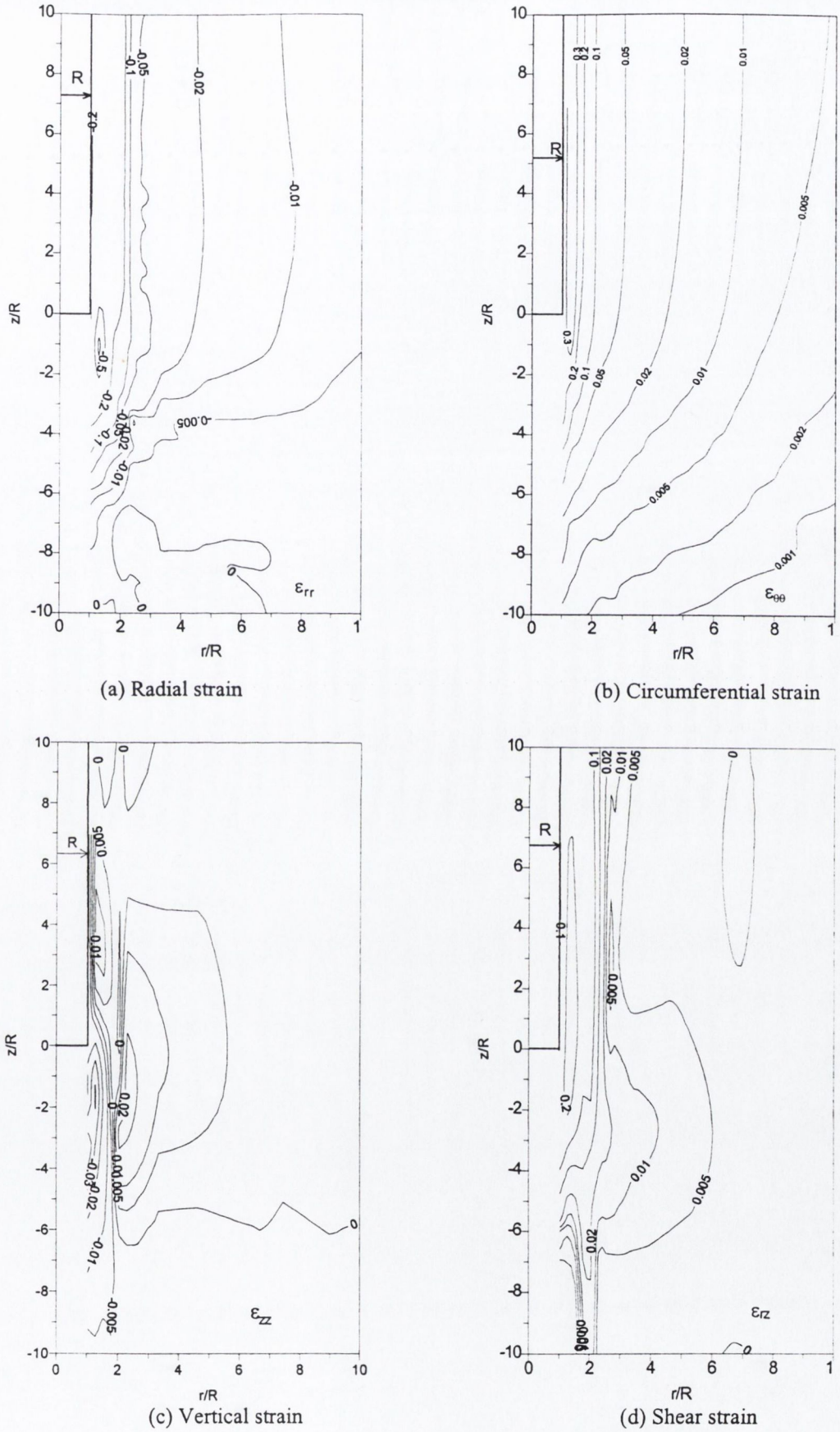

(a) Radial strain

(b) Circumferential strain

(c) Vertical strain

(d) Shear strain

Figure 7.20. Strain contours around a flat ended penetrometer

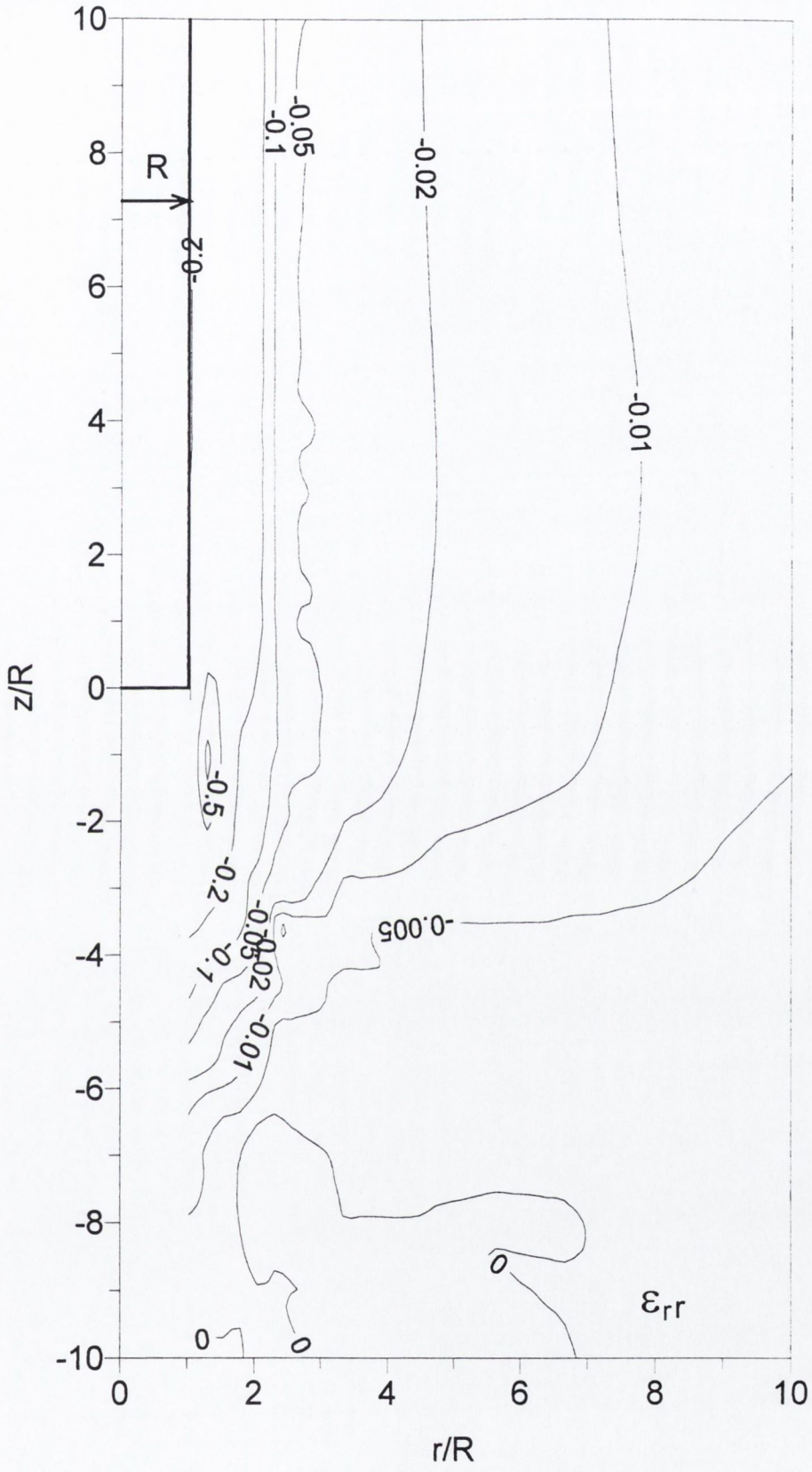

Figure 7.21 Radial strain contours around a flat ended penetrometer

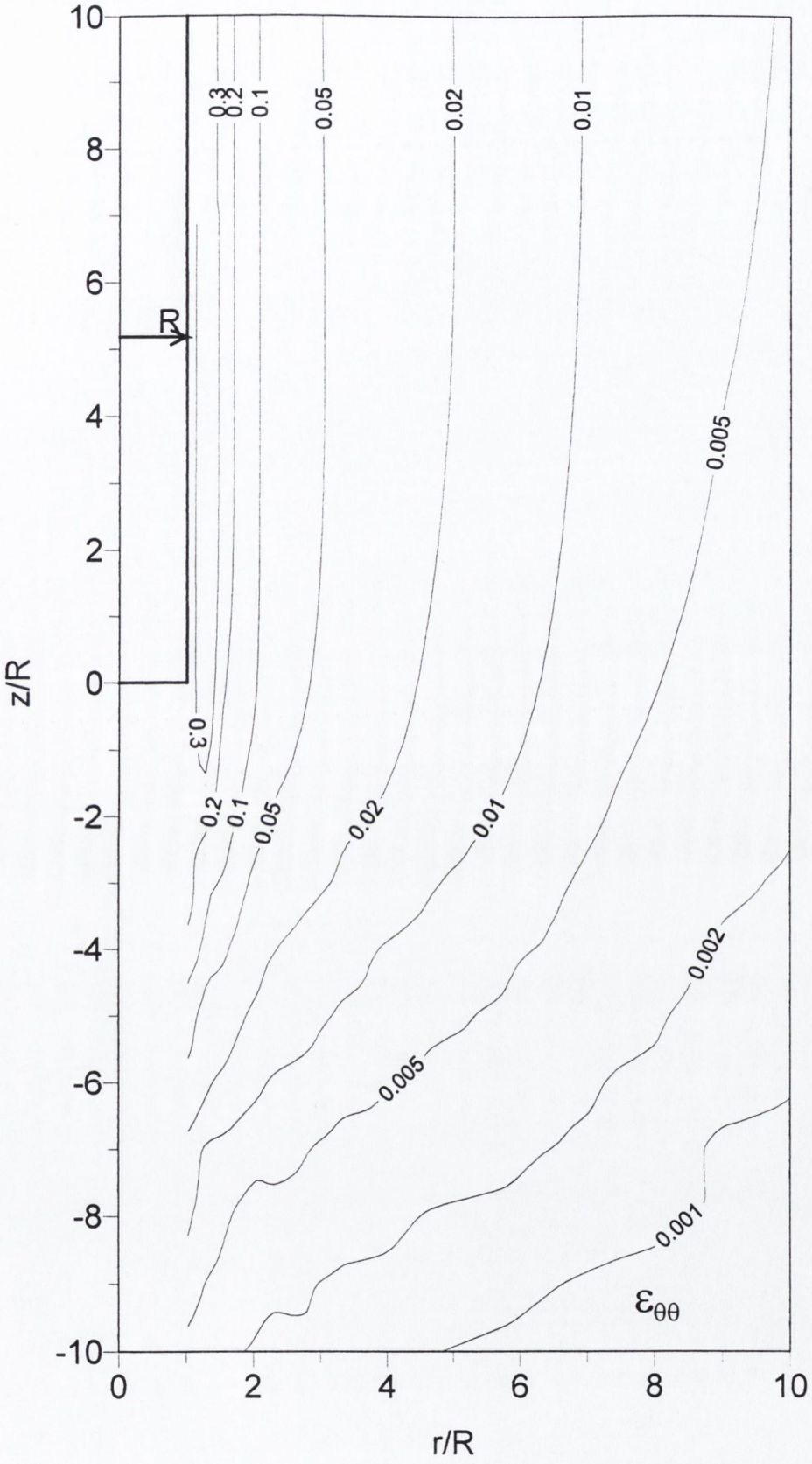

Figure 7.22 Circumferential strain contours around a flat ended penetrometer

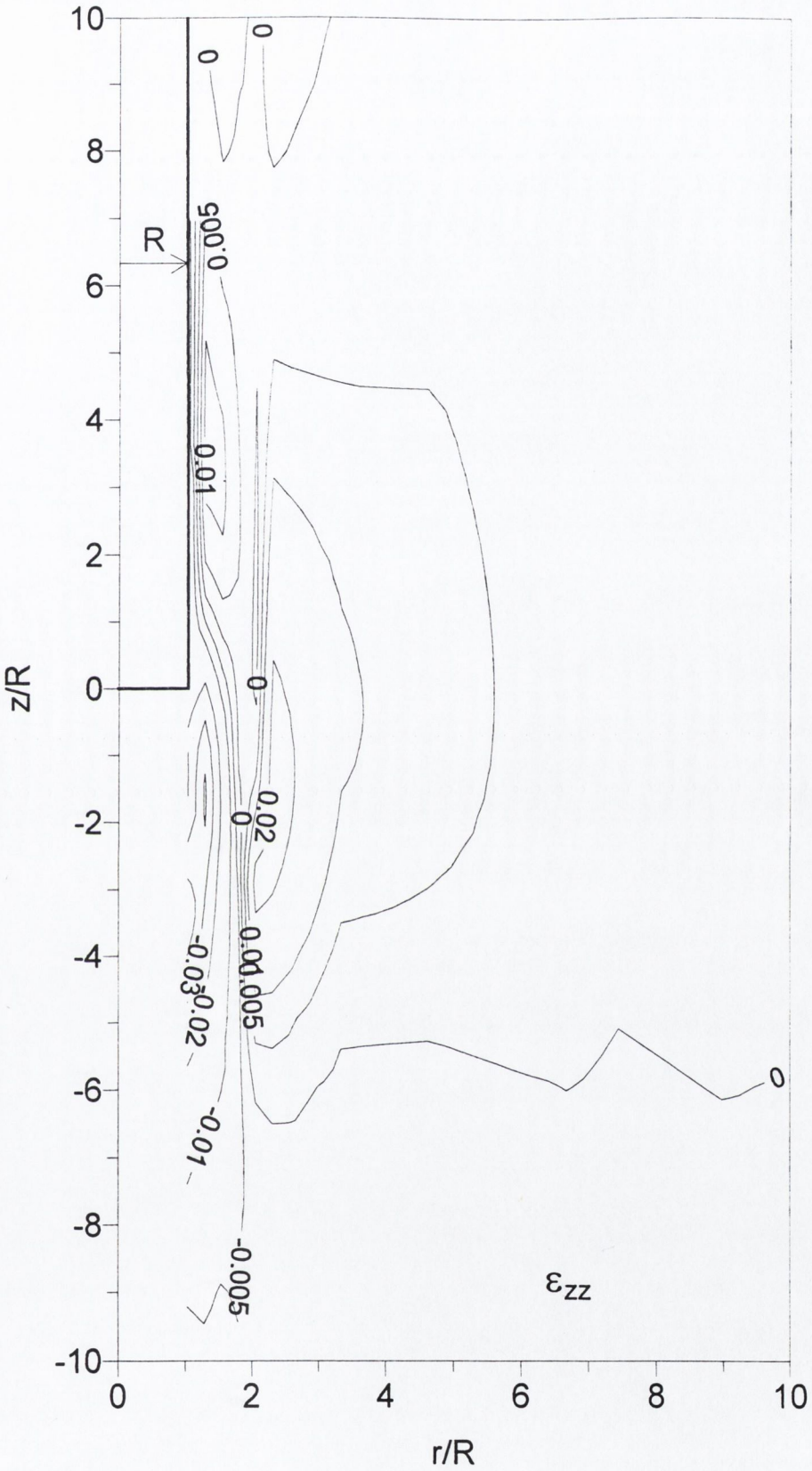

Figure 7.23 Vertical strain contours around a flat ended penetrometer

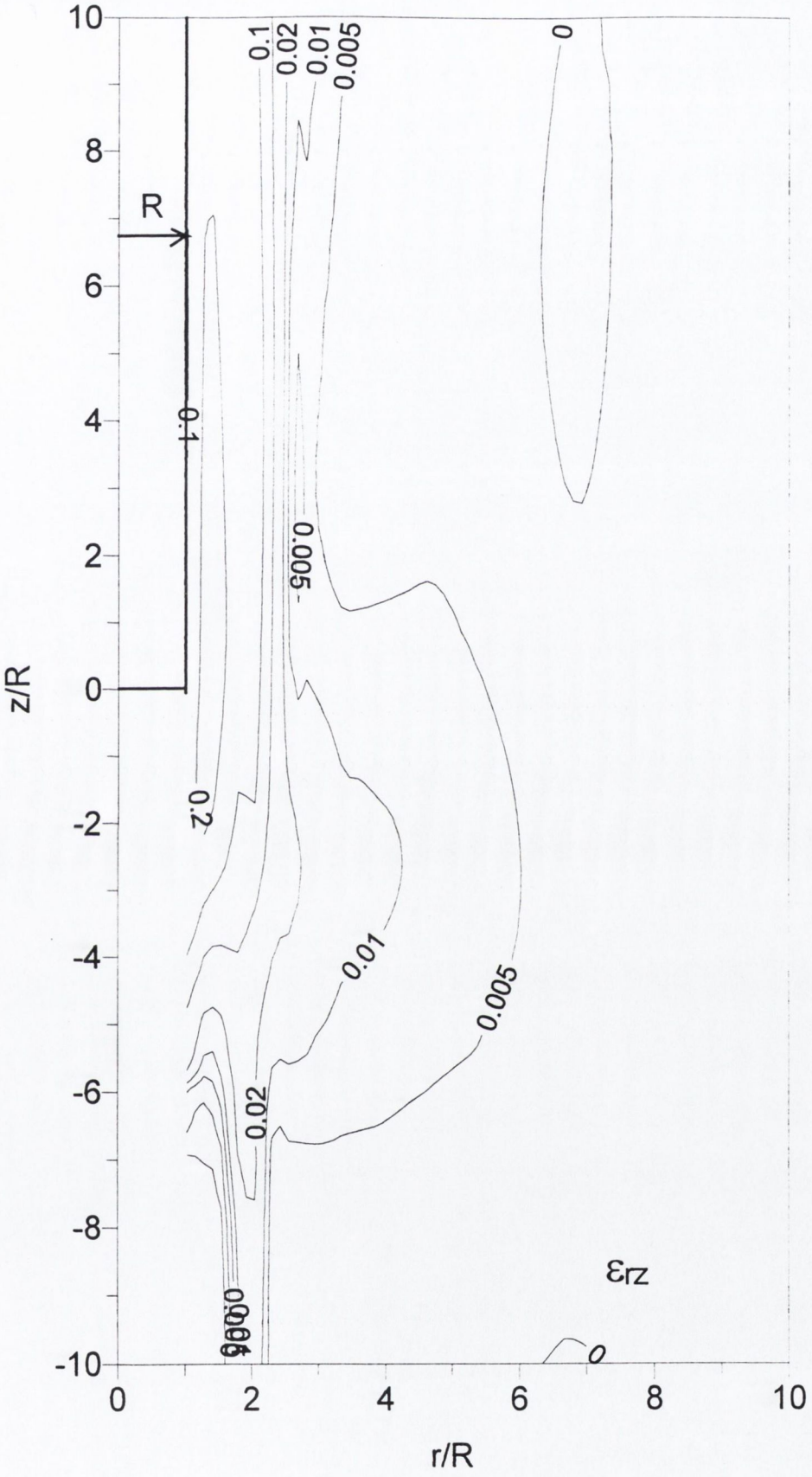

Figure 7.24 Shear strain contours around a flat ended penetrometer

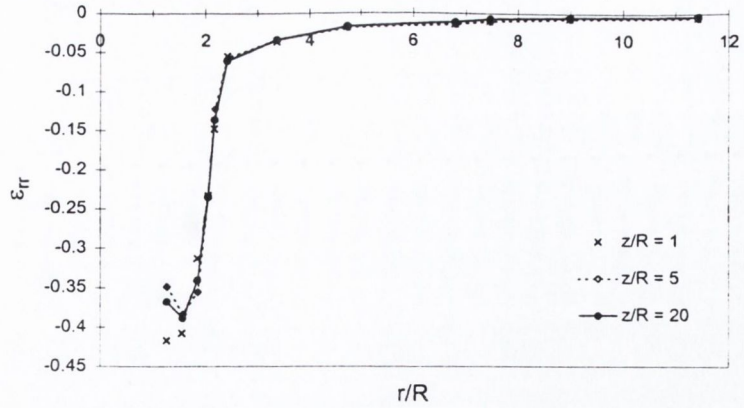

(a) Radial strain

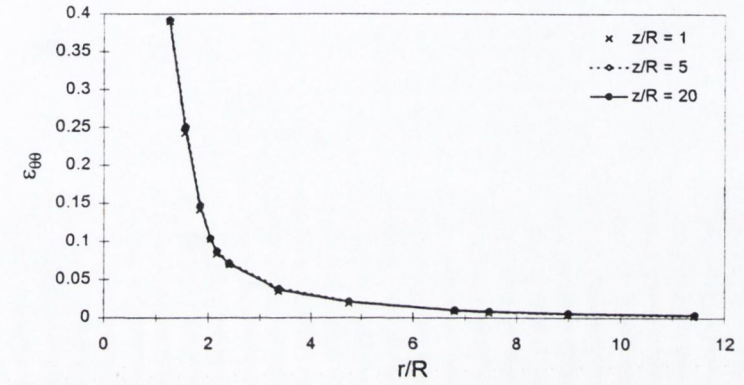

(b) Circumferential strain

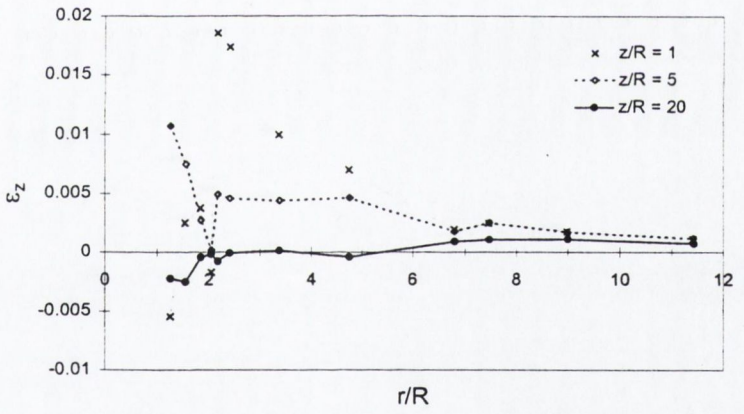

(c) Vertical strain

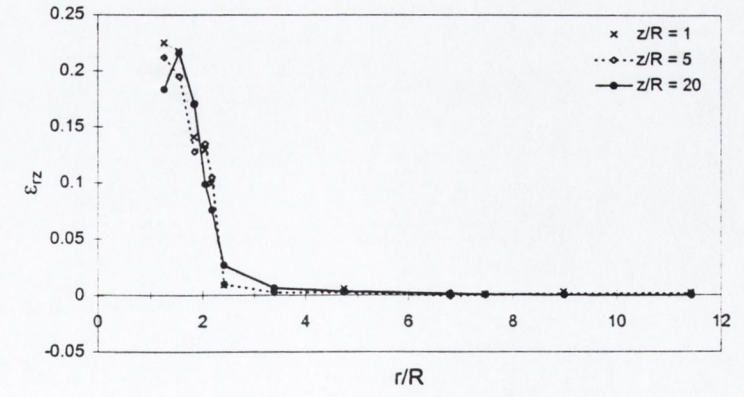

(d) Shear strain

Figure 7.25. Radial distribution of strain at z/R = 1, 5 & 20

The radial distribution of ε_{rr}, $\varepsilon_{\theta\theta}$, ε_{zz} & ε_{rz} has also been found at three horizontal horizons behind the penetrometer tip (z/R = 1, 5 and 20) and are shown in Figure 7.25. The strain distributions show that for ε_{rr}, $\varepsilon_{\theta\theta}$, & ε_{rz} the strain is concentrated in the region close to the penetrometer shaft and is relatively small when r/R > 2. There are reductions in ε_{rr} and $\varepsilon_{\theta\theta}$ close to the penetrometer with increased z/R (although, the magnitude of ε_{rr}, is greater at z/R = 20 than that at z/R = 5). The three horizons show large differences in ε_{zz}; at z/R = 1 the soil is in compression close to the penetrometer but has a high tension value at r/R = 2, at z/R = 5 the soil is in tension but with a lower magnitude than at z/R = 1 while at z/R = 20, the soil is in compression for r/R < 5.

7.5 DISCUSSION ON DATA QUALITY

The resolution of soil movement is considered to be to within 0.01 mm (or 0.0016 R) for the model tests conducted in this Thesis after the appropriate corrections in Section 7.2 have been made (the accuracy capabilities of the Videoextensometer measurement system in general are discussed Appendix B). This resolution is not always reflected in the displacement results for Tests 1 & 2 (as shown in Figures 7.5 to 7.8) which show a degree of scatter that is considered to be due to the uncertain nature of soil deformation around the penetrometer. A second set of displacement results derived from those found in Tests 1 & 2 were presented in Figures 7.10 & 7.11 and showed the general trend of movement with a far lower degree of scatter in the results. These 'average' plots were produced for three main reasons;

a) the partial obscurement of some points called their reliability into question
b) some averaging of points was considered to improve accuracy
c) soil movements close to the penetrometer were more irregular than those at $r_0/R > 2$

Representation of the movements close to the penetrometer was difficult as the range of vertical movement varied from up to 4R to as low as 1R for points in almost identical positions ($r_0/R \approx 0.5$). The uncertain nature of the vertical deformation in this region reflects the complexities involved at very high shear strain levels. Another major, but unrelated, difficulty encountered in this region was in the measurement of the displacements for soil markers initially positioned directly beneath the penetrometer ($r_0/R <$

1). This was due to the inability of the video camera system to track soil markers once they came in contact with, or very close to the penetrometer since the target boundaries must remain clearly defined. This can be seen from images taken by the camera during penetration, shown in the previous chapter, on Figure 6.7. Unfortunately, therefore there are only a limited amount of data for this complex region of deformation.

The experimental results obtained at the end of penetration in this research compared well with the reported data of Francescon (1983) and Gue (1984). The main differences between the measured radial movements occurred in the far field which was due to different model boundary conditions of each test. The influence of the penetrometer tip is potentially partly the reason for the differences between the displacements recorded by Gue (1984) and in this Thesis with those of Francescon (1983) who used a penetrometer with a 45° conical tip cut off close to the apex.

The accuracy of the experimental results has a large influence on the dependability of the deduced strain paths which were calculated by differentiating the soil displacements with respect to the radial and vertical directions. The strain resolution depends not only on the displacement resolution but also the magnitudes involved. In general, any error in the displacements is magnified in the calculation of strains. Approximations introduced by the curve fitting procedures may also have had a distorting influence on the strain results. The strain paths presented in Figures 7.16 to 7.19 are, therefore, considered to be useful for identifying the type of straining occurring in the soil during penetration but approximate from a quantitative view point.

In summary, however, it is believed that the data presented in this chapter represent a considerable improvement on what has existed up to now. Accurate measurements of the displacement paths have not been reported in the literature even though these paths are essential to the testing of any numerical approach.

CHAPTER 8
COMPARISON OF THEORETICAL AND EXPERIMENTAL RESULTS

8.0 COMPARISON OF THEORETICAL AND EXPERIMENTAL RESULTS

8.1 INTRODUCTION

This chapter compares the theoretical prediction of soil deformation during penetrometer installation using the modified Strain Path Method (SPM) approach, developed in Chapter 3, with experimental measurements. The investigation, in Chapter 4, of the effect different flow solutions have on the SPM prediction of strain and displacement has led to the selection of the solutions presented in this chapter. The two solutions presented, for the 60° cone tip and the flat-ended penetrometer, respectively, provide the 'best' or closest fit to the experimental data that could be obtained by adjusting the fluid flow parameters μ and v_{pent}/U. The 'best' fit solutions are shown to provide a closer approximation to the experimental data than existing SPM solutions by Baligh (1985) and Teh (1987) and are therefore deemed to be more realistic.

A solution for a flat-ended penetrometer fitted to the experimental soil displacements measured from model penetrometer tests conducted in this Thesis has been found and is termed the 'best fit' solution. The strains from this 'best-fit' solution for a flat tip have subsequently been compared with the strains interpreted from the experimental data in Chapter 7. The 'best-fit' flow parameters (μ & v_{pent}/U) found for the flat tip were also applied to a solution for a 60° cone tip and this is compared with existing experimental displacement results in the literature and the standard SPM predictions.

8.2 BEST FIT SOLUTION FOR FLAT-ENDED PENETROMETER

8.2.1 General

The objective of this section is to find the SPM solution for a penetrometer with a flat tip that can be considered to be most representative of the soil deformation actually occurring during penetrometer installation. This was achieved by the selection of a SPM solution that provides the 'best' fit to the soil displacement measurements from the laboratory tests

conducted in this Thesis for a flat ended penetrometer. The strains predicted for this 'best-fit' flow solution are also compared here with the experimental strains derived from the model test results presented in Chapter 7.

The parametric study, conducted in Chapter 4, of the influence the flow properties have on the inferred strain and displacement fields around a flat-ended penetrometer has led to the selection of the 'best-fit' flow described in Table 8.1. The solution is termed 'Flow N' to distinguish it from other flow solutions presented in this Thesis.

The two parameters adjusted were the relative velocity on the penetrometer, v_{pent}/U and the fluid viscosity, μ. Since the radial displacements were found to be relatively unaffected by small changes in these two parameters, the vertical displacements ($\delta z/R$) were used to determine the 'best fit' solution. v_{pent}/U was adjusted to give a good fit to $\delta z/R$ close to the penetrometer (values at z/R = 5 & 20 were checked). Fluid viscosity was then adjusted to give the closest distribution of $\delta z/R$ with radial distance from penetrometer to the experimental data. The fluid density, ρ, was kept constant throughout ($\rho = 2000$ kg/m^3) and was chosen as a nominal value at the beginning of the process to be representative of soil. It was subsequently found that the fluid properties were not physically representative of real soil properties (discussed in Section 8.2.1.1) but this value for ρ was maintained.

Table 8.1. Flow properties of the 'best-fit' solution for a flat-ended penetrometer (Flow N)

Flow Type Description for 'Flow N'	Low viscosity partial slip flow
Viscosity, μ (Ns/m^2)	0.01
Relative Velocity on Penetrometer Boundary, v_{pent}/U	0.985
Reynolds Number, Re	2.4×10^5
Fluid density, ρ (kg/m^3)	2000

8.2.1.1 Physical Significance of the Fluid Flow Parameters

The values derived for μ and v_{pent}/U to give a 'best fit' solution produce a low viscosity fluid flow for which Re = 2.4×10^5, i.e., turbulent flow since Re > 2000. These flow parameters result in a relatively low disturbance being caused to the flow by the penetrometer. However, despite the relative velocity on the penetrometer being close to unity ($v_{pent}/U = 0.985$) this results in sufficient down drag to mimic the experimentally

measured vertical displacements close to a flat-ended penetrometer. A viscosity of 0.01 Ns/m^2 is applied to the flow, which is relatively low (10 times greater than water) but allows sufficient disturbance to the flow to give a displacement field that has down drag close to the penetrometer and upward heave in the far field.

The physical significance of the shear stress generated on the penetrometer boundary from the fluid flow (by introducing μ and v_{pent}/U) was also investigated to determine if any quantitative correspondence with soil shear stress exists. The shear stress, τ, at the boundary was calculated using the relationship;

$$\tau = \mu \frac{\partial v_z}{\partial r} \tag{8.1}$$

where ∂v_z is the change in vertical velocity with the change in radial distance ∂r. The average shear stress calculated on the penetrometer shaft for Flow N ('best fit' solution to the experimental results) was 2×10^{-5} N/m^2. The estimated average shear stress generated on the model penetrometer during penetration was approximately 15-20 kPa. This confirms that there is no relation between the shear stress imposed on the penetrometer boundary by the fluid flow and real shear stresses measured in the soil during penetrometer installation.

8.2.2 Displacements

The displacement data that have been used here to aid the refinement of the predictive method, are the average experimental measurements presented in Chapter 7, which were described as the definitive set of displacement results. The results from the model tests give the vertical location of the soil element relative to the penetrometer tip (the z/R value), which is not available for other experimental displacement data. It has been possible, therefore, to compare the predicted and measured displacement data at many different locations (horizons); z/R values of 5 & 20 are chosen for demonstration purposes here. The radial and vertical displacements ($\delta r/R$ and $\delta z/R$) are plotted to both linear and logarithmic scales. The use of a log scale allows the features of the near field soil movements and the smaller far field displacements to be seen clearly on the same plot (although the negative vertical movements cannot be shown).

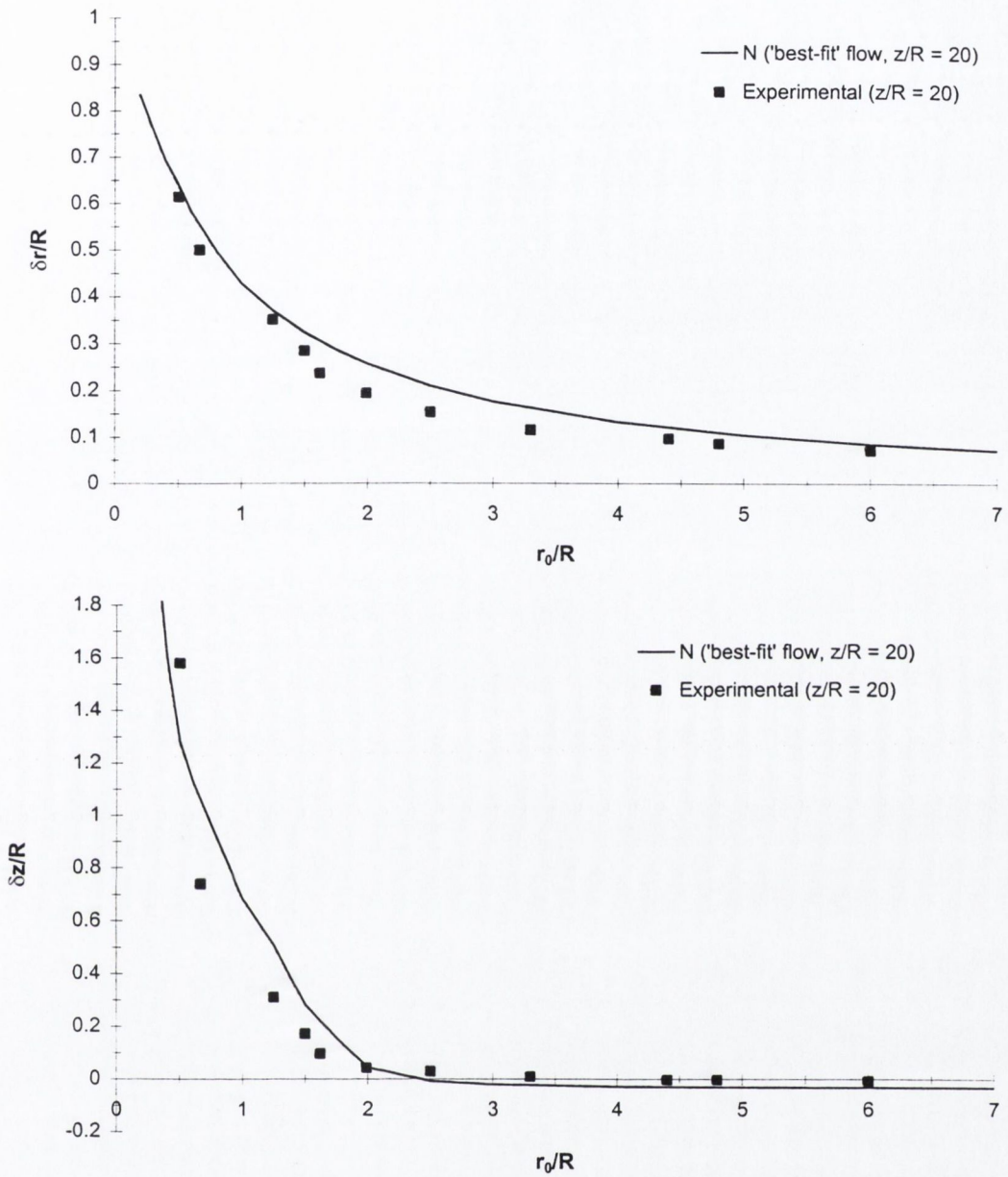

Figure 8.1. Radial and vertical displacement fields at z/R = 20 during penetration of a flat-ended penetrometer for 'best-fit' flow and experimental measurements

The displacements at z/R = 20 for Flow N and for the experimental data are shown in the linear and log plots of Figures 8.1 and 8.2, respectively. The best-fit theoretical prediction provides a reasonable approximation to the experimental data, although the plots show that Flow N;

- over predicts the experimental $\delta r/R$ in the region $1.5 < r_0/R < 6$ (by up to 20 %)

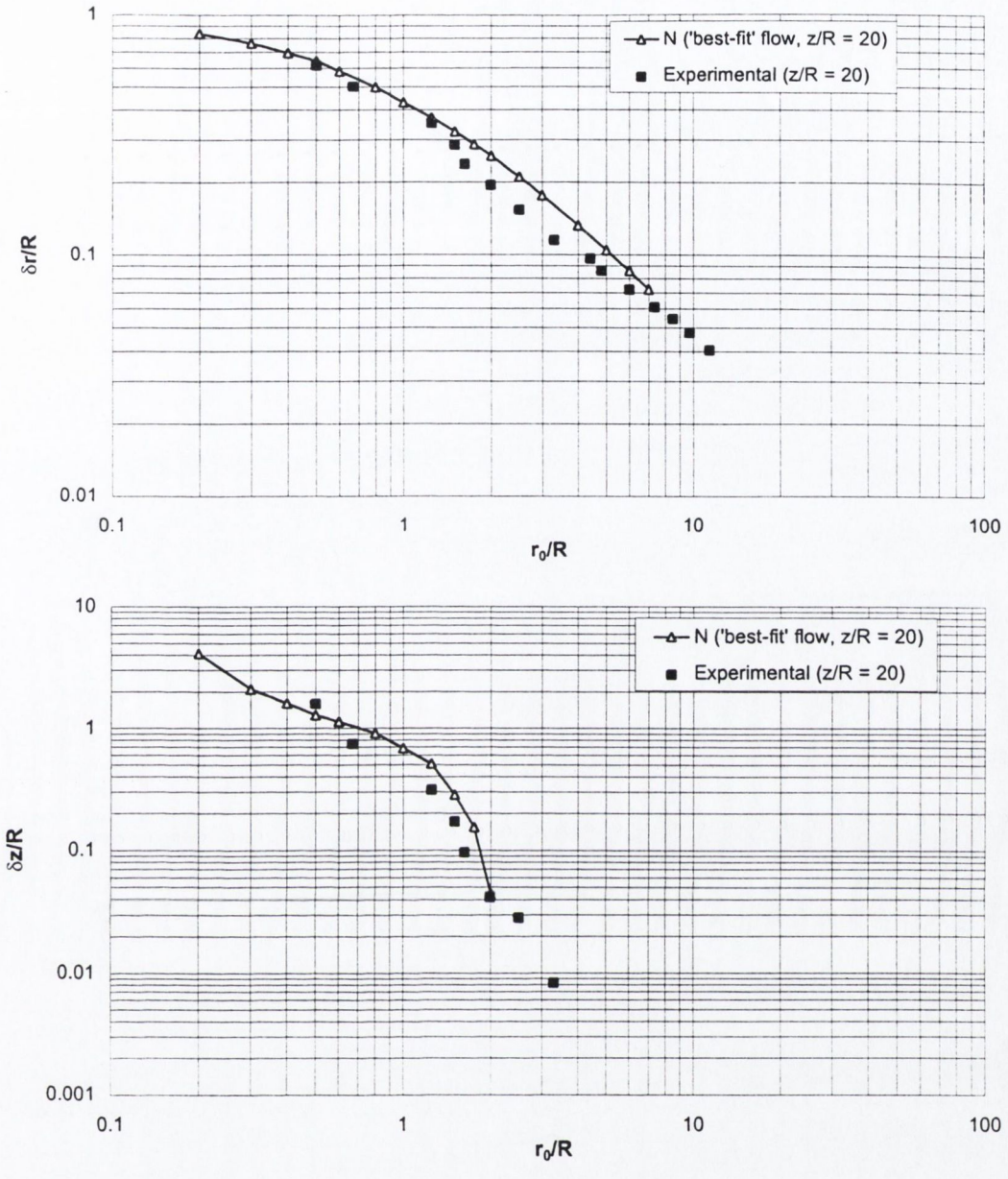

Figure 8.2. Log plot of the radial and vertical displacements at z/R = 20 during penetration of a flat-ended penetrometer for 'best-fit' flow and experimental measurements

- over predicts the downward vertical movement (δz/R) of the experimental results in the near field of the penetrometer ($0.7 < r_0/R < 2$) and also over predicts the upward heave in the far field ($r_0/R > 2.5$).

Predicted displacements at z/R = 5 are also presented on a log scale (only) in Figure 8.3. The 'best-fit' solution displays similar trends to those shown at z/R = 20, although a slightly closer fit is evident for both the radial and vertical data. The experimental radial displacements are over predicted by the theoretical values in the region $1.5 < r_0/R < 6$. The δz/R predictions, however, show few deviations from the experimental measurements.

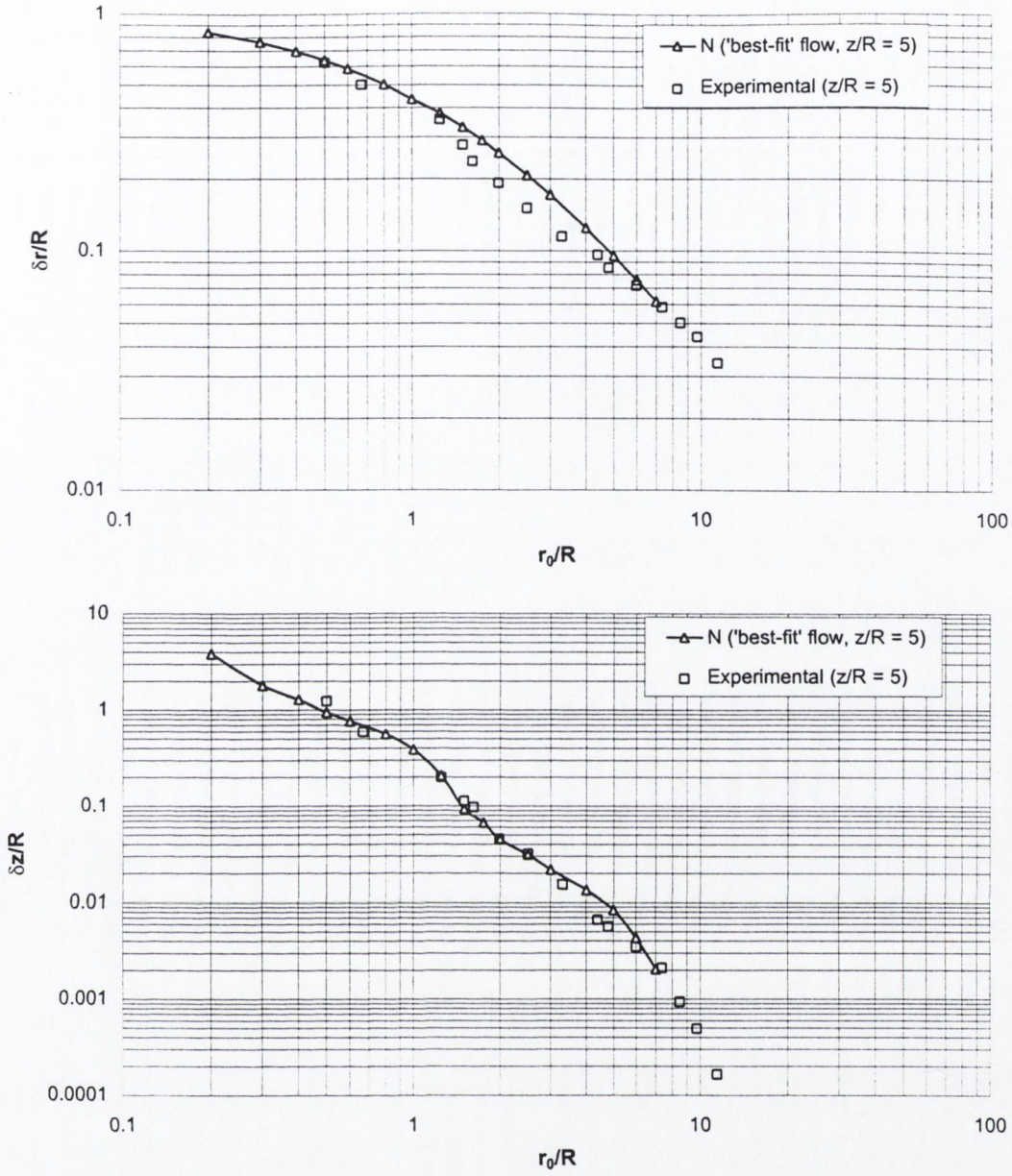

Figure 8.3. Log plot of the radial and vertical displacements at z/R = 5 during penetration of a flat-ended penetrometer for 'best-fit' flow and experimental measurements

The displacement paths for elements at initial radii of r_0/R = 0.5, 1, 2, 4 & 6 are shown in Figure 8.4. The magnitude of the soil movement close to the penetrometer is, as expected, considerably greater than the movements further away. A clear distinction, however, can also be seen between the trends of movement shown by the near and far field displacement paths. Downward movement of the soil after the penetrometer tip has passed (i.e., $z/R > 0$), is evident for elements at r_0/R = 0.5 & 1. This is considered to be due primarily to the influence of friction on the penetrometer shaft, but is also attributed to an interruption of the flow by the flat tip of the penetrometer. The zone of soil which experiences this

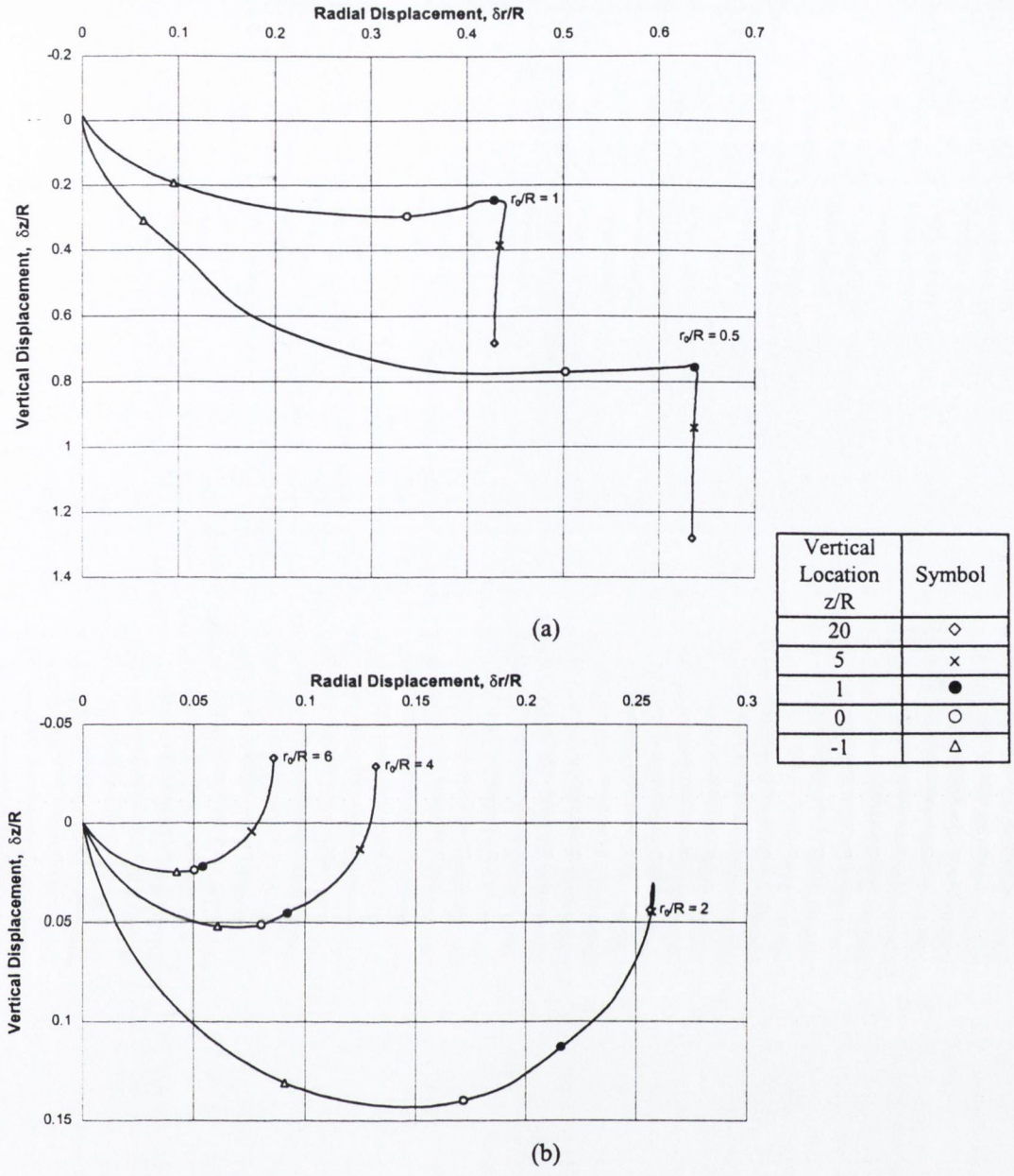

Figure 8.4. Displacement paths during penetration of a flat ended penetrometer for the 'best-fit' flow solution (Flow N): (a) in the near field $r_0/R \leq 1$; and (b) in the far field $r_0/R > 1$

downward 'drag' with further penetrometer movement, extends as far as $r_0/R = 2$ where a second reversal at $z/R > 5$ results in further downward vertical movement of the soil. The soil elements shown at larger radial distances, i.e., at $r_0/R = 4$ & 6, show upward vertical movements only, after the penetrometer tip has passed.

8.2.2.1 Comparison of theoretical and experimental displacement paths

The predicted displacement paths for the 'best-fit' solution (shown in Figure 8.4) are compared here to the experimental displacement paths for the model tests which were

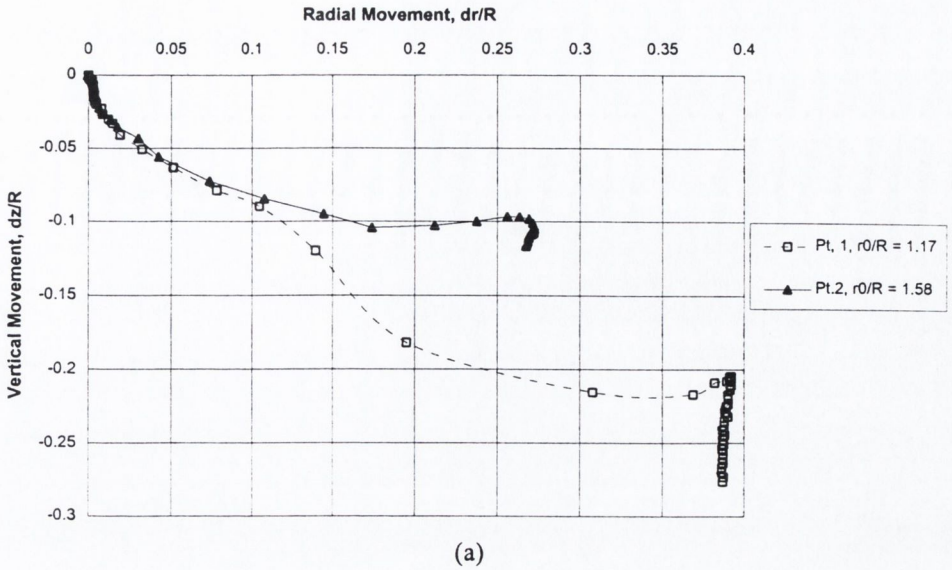

(a)

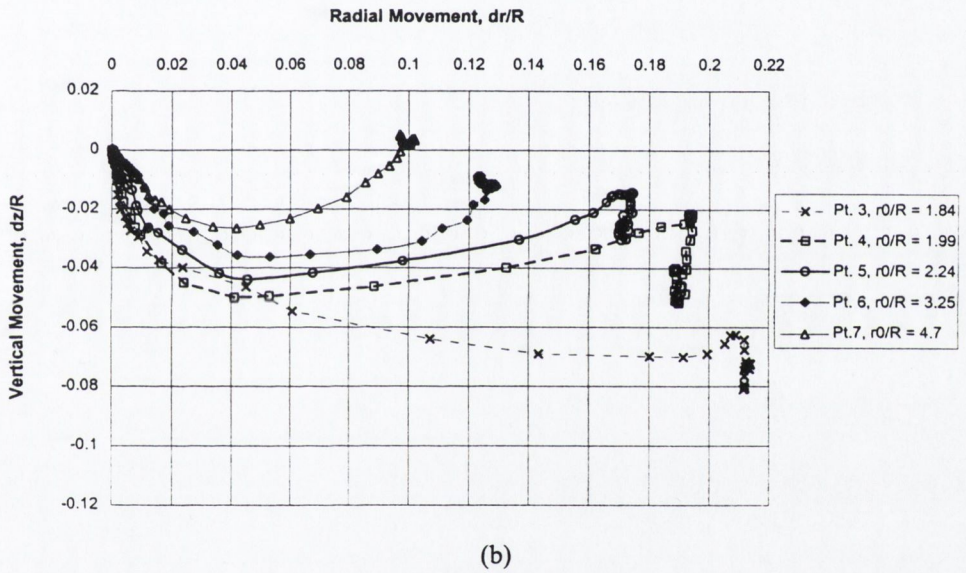

(b)

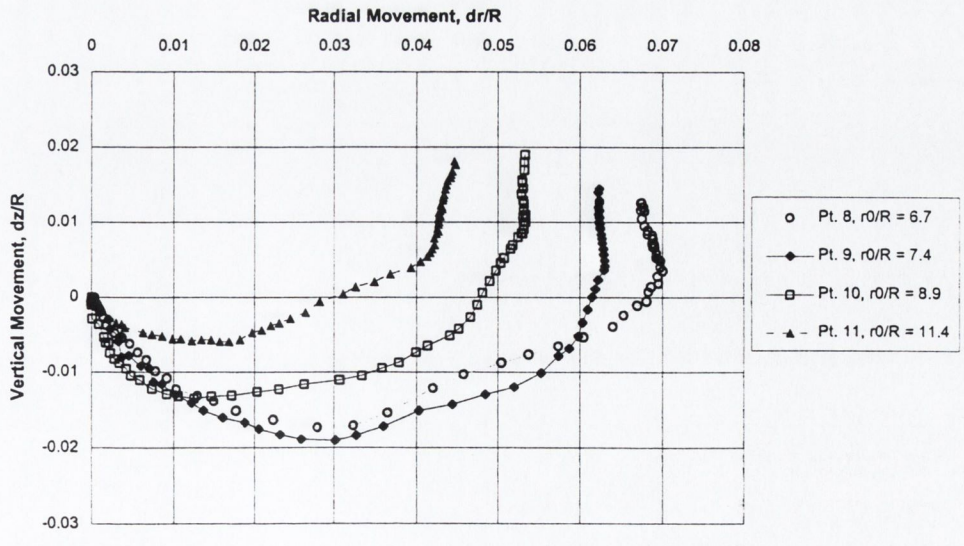

(c)

Figure 8.5. Experimental displacement paths during penetrometer installation: (a) $r_0/R < 1.6$; (b) $1.6 < r_0/R < 5$; (c) $r_0/R > 5$

presented in Chapter 7 and are reproduced on Figure 8.5 for convenience. It has been possible to identify the key features of the predicted and measured displacement paths followed by soil elements in four separate regions around the penetrometer:

(i) $r_0/R < 1.5$

- In this region the theoretical and experimental vertical movements show similar behaviour before the tip is reached ($z/R < 0$) but following this, the theoretical movements show greater downward drag of the soil resulting in a considerably larger overall $\delta z/R$.
- the magnitude of radial movements are approximately the same for the predicted and measured movements, and show similar reductions in $\delta r/R$ for $z/R > 0$.

(ii) $1.5 < r_0/R < 3$

- The peak vertical movement, ahead of the pile tip ($z/R < 0$) for the predicted solution is greater than that measured experimentally. The final $\delta z/R$ value is similar for both (also illustrated on Figure 8.2), although after the tip has been passed the experimental vertical movements undergo three reversals (compared to two for the theoretical) with the final movement in the upward direction whereas the theoretical movement finishes in the downward direction.
- Predicted peak radial movement is slightly greater than the experimental measurements although both show similar reductions in $\delta r/R$ at $z/R > 0$.

(iii) $3 < r_0/R < 5$

- The peak downward movement of $\delta z/R$ for the experimental results is lower than that predicted theoretically. The experimental vertical movements also show small reversals at $z/R > 0$ (i.e., downward) that are not evident for theoretical $\delta z/R$ values.
- The peak theoretical values of $\delta r/R$ are slightly greater in this region and the predicted reversals in $\delta r/R$ for $z/R > 0$ are less than those measured experimentally.

(iv) $r_0/R > 5$

- The far field theoretical displacement paths generally show close similarities in the most part to the experimental movements for $\delta r/R$ and $\delta z/R$. The final position of predicted $\delta z/R$, however, gives greater upward heave than was measured.

- The theoretical radial displacements in this region show outward movement only (i.e., no reversal occurs for $r_0/R > 4$). However, the experimental results show some reversal in $\delta r/R$ for $r_0/R < 9$.

In summary, many of the key features of the experimental displacement paths are predicted by the theoretical solution. However, the magnitudes of radial and vertical movements tend to be overestimated close to the penetrometer, although closer predictions of the experimental results are given in the far field ($r_0/R > 5$). The modified SPM approach also, in general, shows greater peak downward vertical movement followed by greater upward heave even though the final position (at $z/R = 20$) may be identical to the experimental measurements (i.e., the predicted values show more extreme behaviour).

8.2.3 Strains And Strain Paths

The deviatoric strain paths predicted by the 'best-fit' solution for a flat-ended penetrometer (Flow N) are presented here. Comparisons are alsomade between the predicted strain paths and those established through differentiation of curves fit to the experimental results in Chapter 7. The strain predictions for the near and far field strains are shown in Figures 8.6 and 8.7, respectively.

(i) *Predicted near field strains*

Considerable differences exist between the two near field strains paths, at $r_0/R = 0.5$ & 1 plotted on Figure 8.6, and this serves to highlight the level of predicted strain concentration close to the penetrometer:

- The vertical strain (E_1) of the streamline at $r_0/R = 0.5$ is almost 10 times greater than that shown at $r_0/R = 1$. (Note that both strain paths remain in vertical compression throughout installation).
- The shear strain (E_3) for $r_0/R = 0.5$ shows a reversal after $z/R = 5$ that is not present for $r_0/R = 1$, which continues to increase with increasing z/R.
- The cylindrical expansion strain (E_2) shown by the streamline at $r_0/R = 0.5$ is over twice that experienced at $r_0/R = 1$, although both show reductions in E_2 after peak behaviour close to the tip and then a slight increases in E_2 for $z/R > 5$.

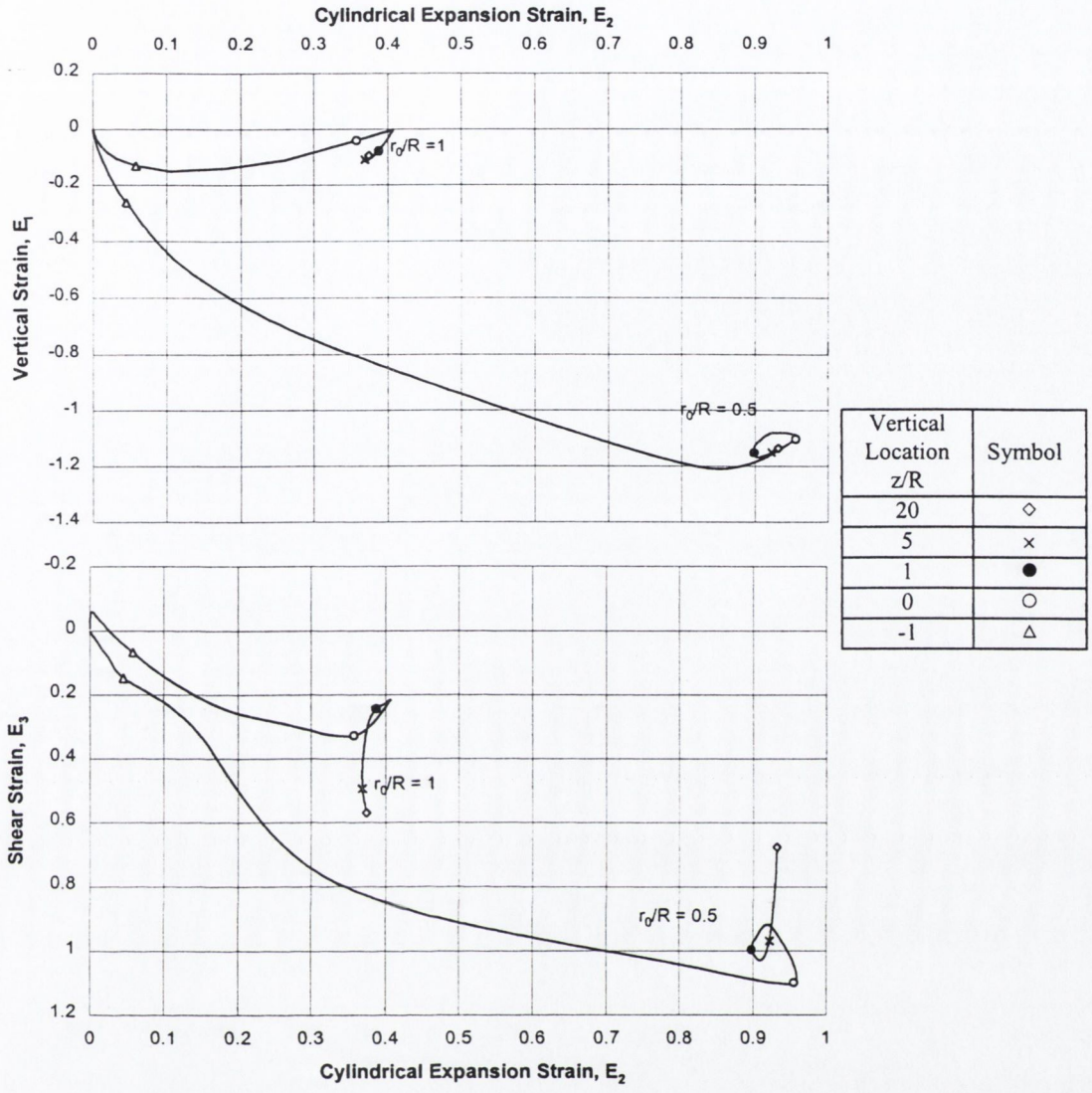

Figure 8.6. Predicted near field deviatoric strain paths at $r_0/R = 0.5$, 1 & 2 during penetration of a flat ended penetrometer for 'best fit' flow

(ii) *Predicted far field strains*

The far field strains predicted for elements with streamlines at $r_0/R = 2$, 4 & 6 are shown in Figure 8.7 and the key features of straining in this region are described here:

- The vertical straining for $r_0/R = 4$ & 6 is similar with E_1 finishing (at $z/R = 20$) in tension for both strain paths. For the streamline with $r_0/R = 2$, E_1 is tensile at $z/R > -1$ but returns to compressive at $z/R = 20$.

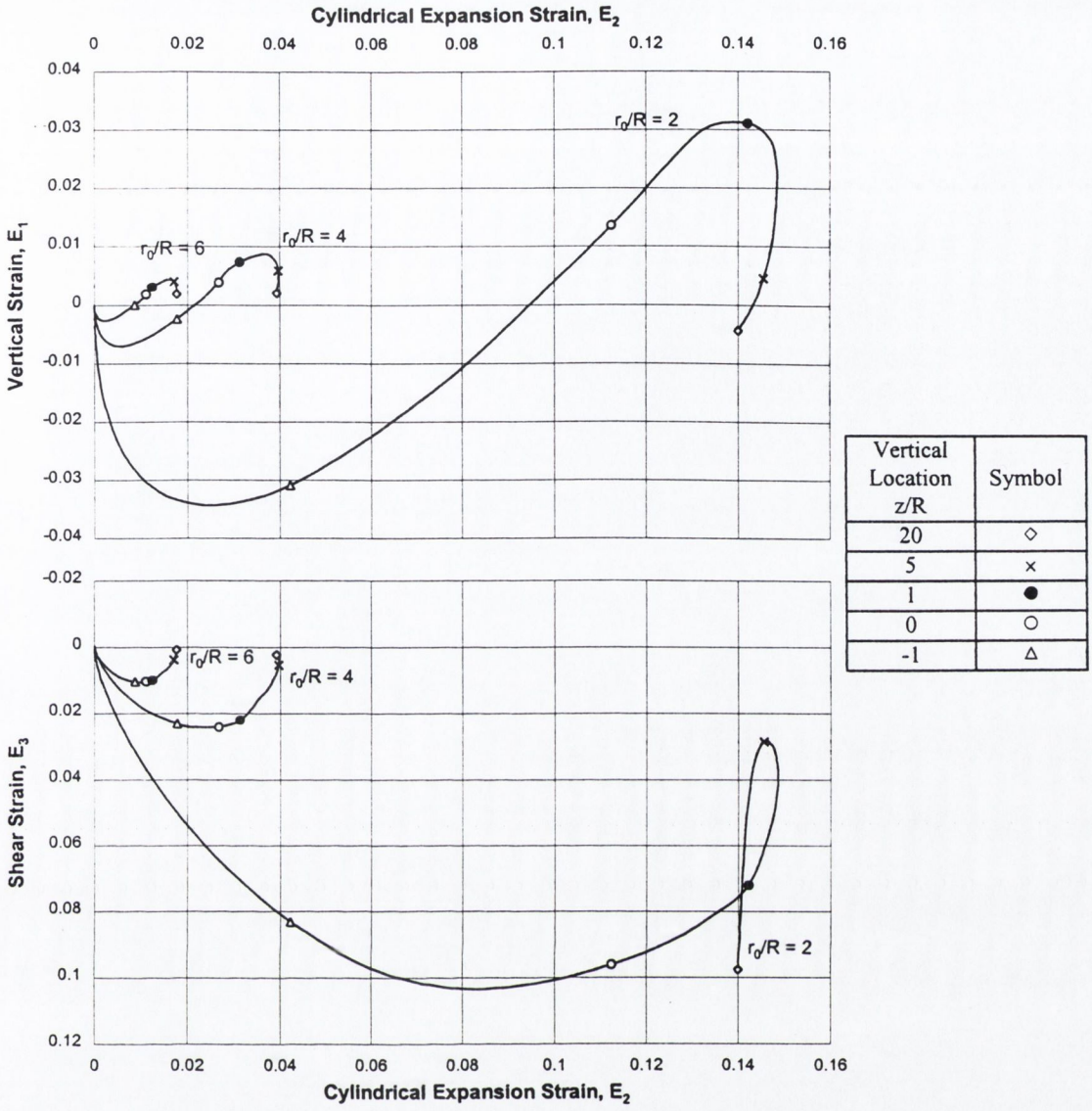

Figure 8.7. Predicted far field deviatoric strain paths at $r_0/R = 2, 4$ & 6 during penetration of a flat ended penetrometer for 'best fit' flow

- E_2 shows post peak reversals for $r_0/R = 2$ & 4 that is not evident for $r_0/R = 6$. The reversals take place for $r_0/R = 2$ at $z/R > 1$ and for $r_0/R = 4$ a slight reversal of E_2 takes place at $z/R > 5$.
- The strain path for $r_0/R = 2$ shows a second reversal present of E_3 at $z/R > 5$ that is not present further away from the penetrometer at $r_0/R = 4$ & 6.

8.2.3.1 Comparison of theoretical and strain paths derived from experimental data

A comparison is made here between the deviatoric strain paths for the 'best-fit' theoretical solution (shown in Figures 8.6 & 8.7) and the experimental strain paths derived in the

previous chapter and reproduced here in Figure 8.8. The different characteristics shown in three regions around the penetrometer (defined by the initial radial distance from the penetrometer), are considered:

(i) $r_0/R < 2.5$

- Compressive values of E_1 from the modified SPM are considerably greater those was measured experimentally, although the peak tensile values of E_1 match the experimental peak values.
- Modified SPM values of E_2 are very similar to the experimental data.
- Peak values of E_3 are also closely predicted by theory, although the final direction of straining is one of increasing values for the modified SPM strain paths whereas inferred strains from the experiment continue to reduce.

(ii) $2.5 < r_0/R < 5$

- The E_1 strain paths are similar for theoretical and experimental results, although peak compressive values predicted for E_1 are greater than those measured experimentally.
- Predictions of E_2 closely match those measured.
- The predicted values of E_3 approximate the experimental values, although a reversal in E_3 is inferred from the experiments at $z/R > 5$.

(iii) $r_0/R > 5$

- Predicted and experimental E_1 values are closely matched.
- Peak E_2 values are similar, although experimental reductions in E_2 after the tip has passed are not predicted by the theoretical strain paths.
- Predicted peak values of E_3 are greater than the experimental values. A reversal also occurs at $z/R > 5$ for the experimental strain paths for, $6 < r_0/R < 9$, which is not predicted by the modified SPM.

It should be noted that the strains derived from the experiments are considered to be approximate and that some localised effects near local maxima/minima may be obscured by the calculation process (the numerical procedure for strain calculation is discussed in Section 7.4).

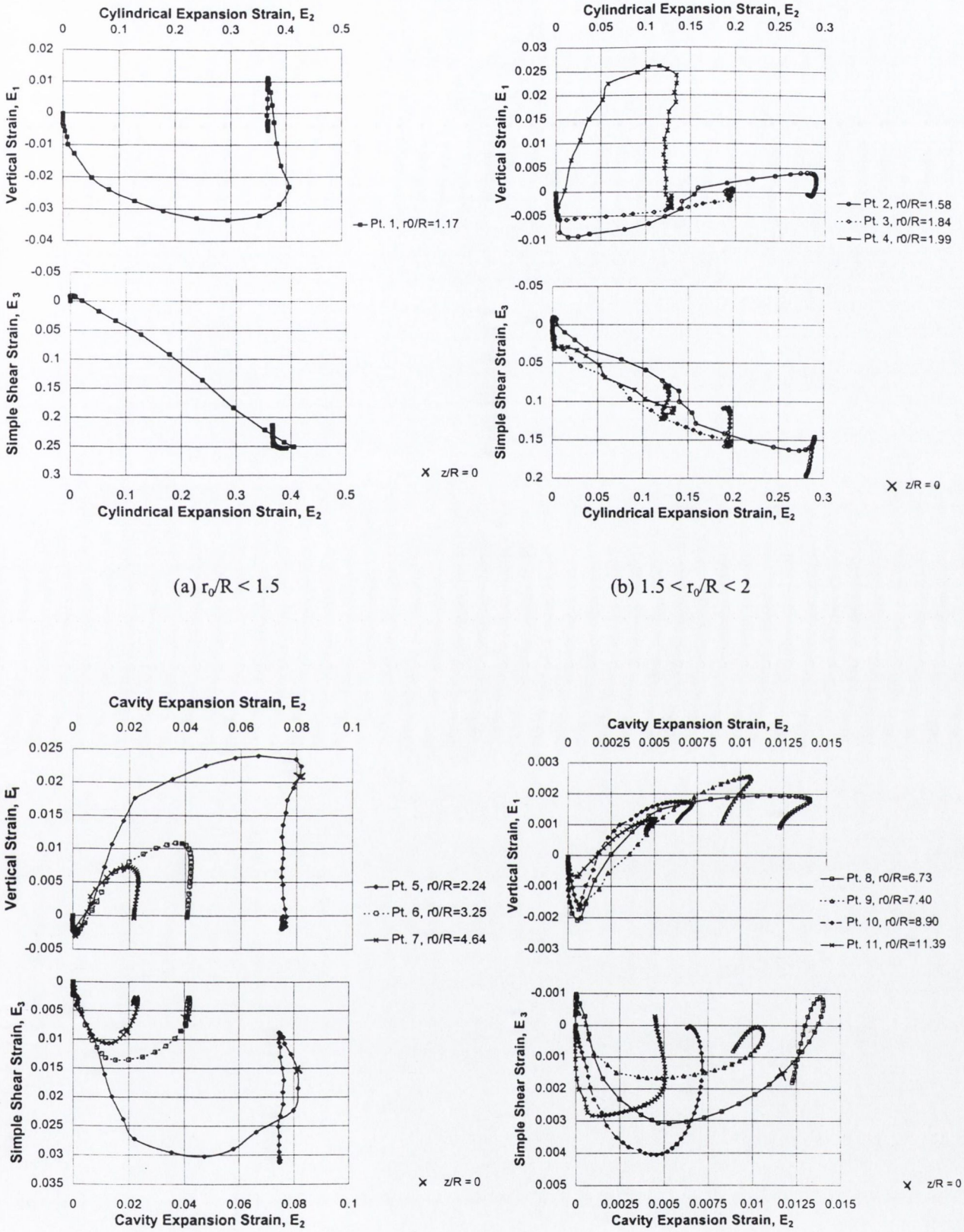

(a) $r_0/R < 1.5$

(b) $1.5 < r_0/R < 2$

(c) $2 < r_0/R < 5$

(d) $r_0/R > 5$

Figure 8.8. Experimental strain paths followed by soil elements during penetrometer installation

In summary, the predicted strain paths reproduce many of the features measured experimentally, but only in an approximate manner. The compressive values of E_1 are over predicted (except in the far field), although tensile E_1 strains are more closely matched. Predictions of E_2 approximate those measured experimentally, including the post peak reversals; the predicted strains tend, however, to be slightly greater than the experimental results. Close to the penetrometer the predicted values of E_3 give good approximations of the experimental measurements, although the final direction of shearing is different in some instances. At greater distances from the penetrometer the peak values of E_3 are twice the experimental values. Note that it has not been possible to make a comparison with alternative flat ended penetrometer SPM solutions since no other published solutions exist.

8.3 BEST FIT SOLUTION FOR 60° CONE

8.3.1 General Flow Description

A SPM prediction of strain and displacement for a penetrometer with a 60° conical tip is presented here and is considered to be more realistic than the standard SPM solutions. The solution applies the 'best-fit' flow properties that were found for the flat-ended penetrometer to the 60° cone tip. This has been done to show that the 'best fit' parameters derived for the flat tipped penetrometer provide more realistic solutions for other penetrometer geometries. The availability of other solutions for the 60° cone by Baligh (1985) and Teh (1987) along with some experimental measurements makes it the most suitable geometry to demonstrate this. The properties of the flow are given in Table 8.1 and are referred to as 'Flow M' in this section in keeping with the terminology of Chapter 4.

The computed soil deformations have been compared with the displacement measurements made in three separate experiments by Cooke & Price (1973), Francescon (1983) and Gue (1984), which are outlined in Table 8.2 (a more complete description of these tests is given in Chapter 2). The observations by Francescon (1983) provide the only comprehensive set of published experimental displacement data for penetrometer tests conducted with a conical tip (albeit with a 45° cone cut off close to the apex); a limited number of data points for radial displacements only are given by Cooke & Price (1973) from field tests for a 60° cone, while the displacements measured by Gue (1984) are for a flat ended penetrometer and, again, only provide a few data points.

Table 8.2. Experimental measurements of displacements around penetrometers

Test series	Experimental details	Penetrometer tip	Displacement resolution
Francescon (1983)	Model piles with R = 9.5 mm in kaolin; Calibration chamber radius = 13R	45° cone cut off at the apex	0.005R (using an X- ray technique)
Gue (1984)	Model piles with R = 8 mm in kaolin; Semi-cylindrical specimen with glass front and radius = 28R.	flat end	0.012R (measured visually)
Cooke & Price (1973)	Field piles with R = 84 mm in London Clay.	60° cone	0.0002R (using inclinometers)

8.3.2 Displacements

The normalised radial and vertical displacement predictions ($\delta r/R$ and $\delta z/R$) for the 'best-fit' flow are shown with the experimental measurements in Figure 8.9 at z/R = 20. The $\delta r/R$ and $\delta z/R$ values are plotted against the normalised radial distance of each measurement point from the penetrometer prior to its installation, i.e. r_0/R. The displacement predictions for a very low viscosity, 'full-slip' flow ('A' in Table 4.1) are also shown on Figure 8.9 and provide a close representation of the existing SPM predictions (by Teh, 1987) for the 60° cone. The z/R value of 20 was selected for comparative purposes on Figure 8.9 as the precise details concerning the final z/R location of the experimental data are not given; however it may be assumed that the data presented corresponds to a final z/R in excess of 10.

The radial and vertical displacements have also been plotted to a log-scale in Figure 8.10 to highlight the relatively small movements which occur at large initial distances from the penetrometer. It should be noted, however, that it is not possible to show the vertical displacements with net upward (negative) movement on Figure 8.10; these occur for Flows A & M at $r_0/R > 3$.

There are only very small differences between the radial displacements computed for the 'best-fit' (Flow M) and 'full-slip' flow predictions (Flow A). Both flows closely approximate the experimental radial data in the near field ($r_0/R < 2$), but over predict the

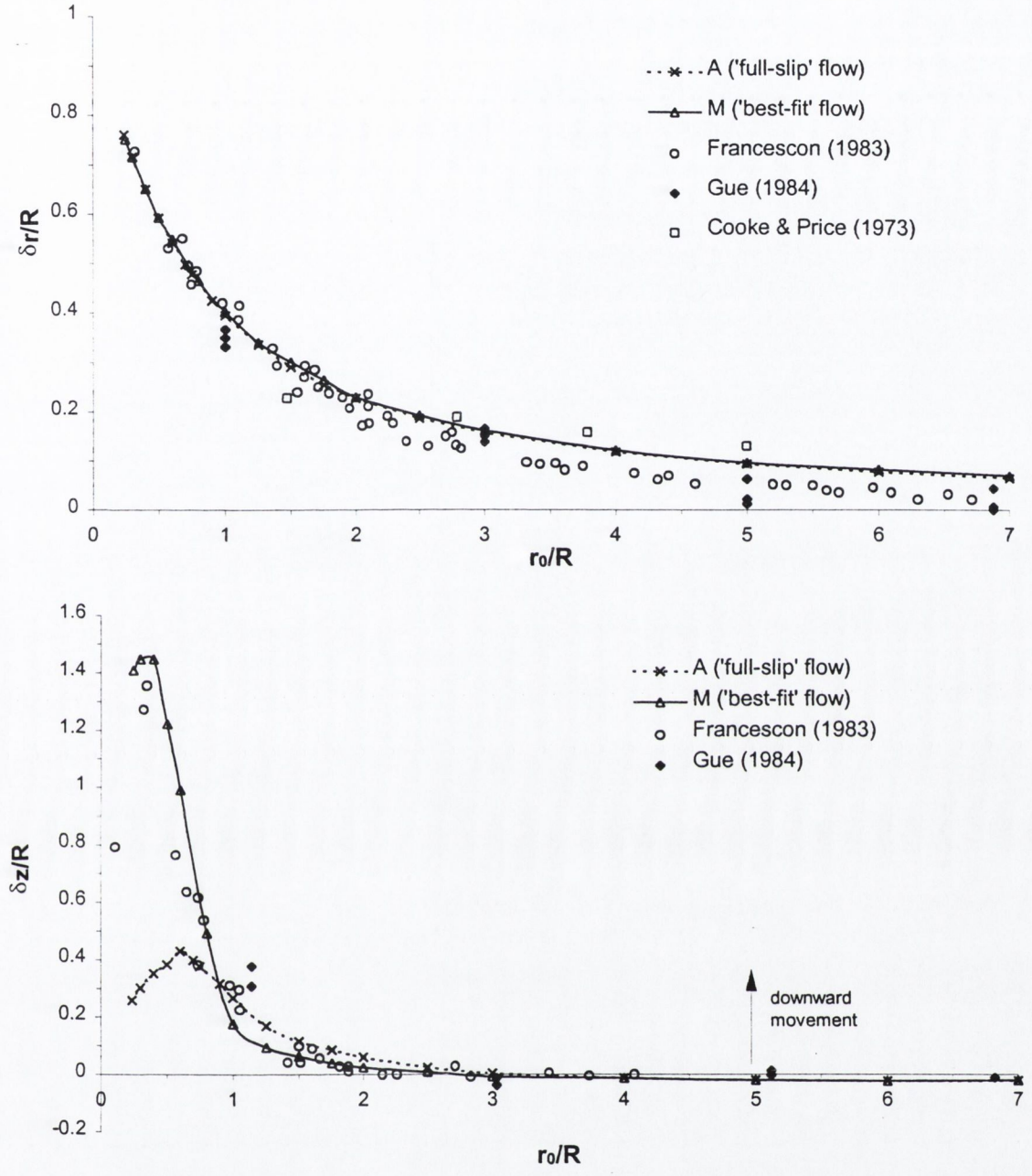

Figure 8.9. Radial and vertical displacement fields at z/R = 20 during penetration of a 60° cone for 'best-fit' and 'full-slip' flows

movements of Francescon (1983) and Gue (1984) in the far field, which is most apparent in the log plot of Figure 8.10. This divergence of the theoretical and experimental results is thought to be partly due to the restricting influence of the far field boundary in the laboratory experiments (which is discussed in Section 7.3.1). The radial displacements measured in field tests by Cooke & Price (1973), which show larger values for $r_0/R > 2$ than the other experimental data or the theoretical predictions, concur with this assumption.

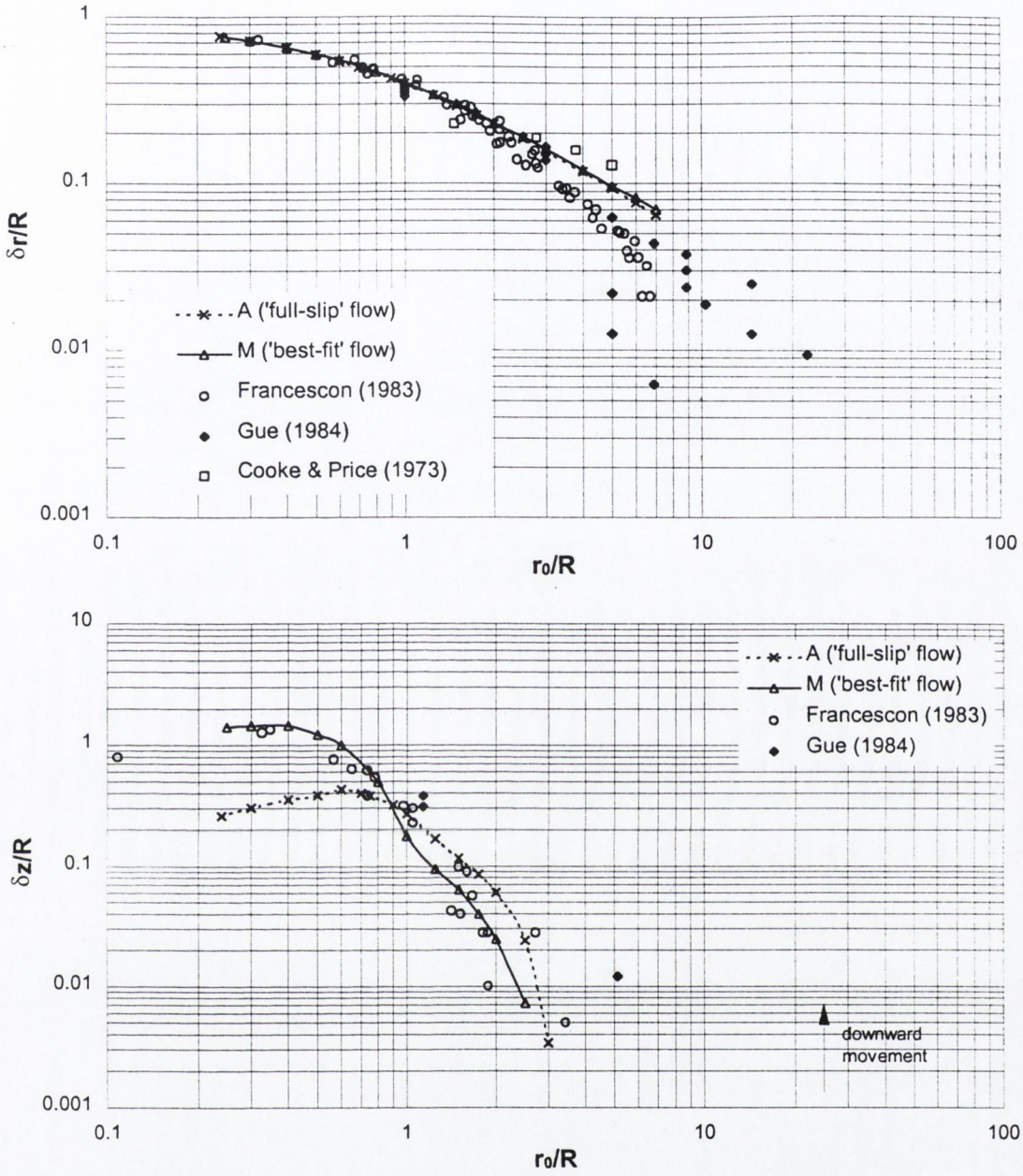

Figure 8.10. Log plot of the radial and vertical displacements at z/R = 20 during penetration of a 60° cone for 'best-fit' and 'full-slip' flows

The vertical displacements in Figures 8.9 & 8.10 show that Flow M gives a significantly closer approximation to the experimental data than Flow A. Close to the penetrometer ($r_0/R < 0.5$), Flow A under predicts the vertical movements by a factor of 3, and although the vertical movements in this region are slightly under predicted by Flow M it is clearly a far better estimate. Flow M also provides a good fit to the vertical displacements further from the penetrometer, in the region $1 < r_0/R < 3$, where Flow A over predicts the downward

movement. At large radial distances from the penetrometer ($r_0/R > 3$) there is little difference between the two flows for $\delta z/R$, and in general they provide a reasonable fit to the experimental data, i.e., small amounts of vertical soil heave are predicted.

The displacement paths predicted during penetrometer installation for elements at r_0/R = 0.5, 1, 2, 4 & 6 for the 'best-fit' solution (Flow M) are shown in Figure 8.11. These paths represent the best estimate of the deformational behaviour of the soil around a 60° cone penetrometer during installation by the predictive method used in this Thesis. The displacement paths predicted for Baligh's 60° cone SPM solution (Baligh 1985) are also presented to highlight the difference in soil behaviour present for the modified SPM solution (Flow M).

Close to the penetrometer, the surface boundary condition of $v_{pent}/U = 0.985$, which simulates the effect of penetrometer friction, results in relatively large downward movement of the soil compared to the movement further out. The displacement paths for soil in the near field of the penetrometer ($r_0/R \leq 1$) which is subjected to this 'drag down' effect, are shown in Figure 8.11(a). A significant proportion of the downward movement for $r_0/R = 0.5$ occurs between $z/R = 5$ and 20. The far field paths ($r_0/R \geq 2$) which show significantly lower movements than those experienced close to the penetrometer (particularly in the vertical direction) are plotted in Figure 8.11(b). The far field displacement paths of $r_0/R = 4$ & 6 show net upward soil movement and are little influenced by friction on the penetrometer shaft.

The predicted paths for Flow M and Baligh's solution show similar trends. However, the displacement paths predicted by Baligh (1985) (shown at r_0/R = 1, 2, 4 & 6) display no evidence of downward drag close to the penetrometer or of net vertical heave further out, but instead tend to return to the initial vertical position. (Note that the displacements are indicated at two vertical positions, $z/R = 0$ & 1, for the paths predicted by Baligh, 1985).

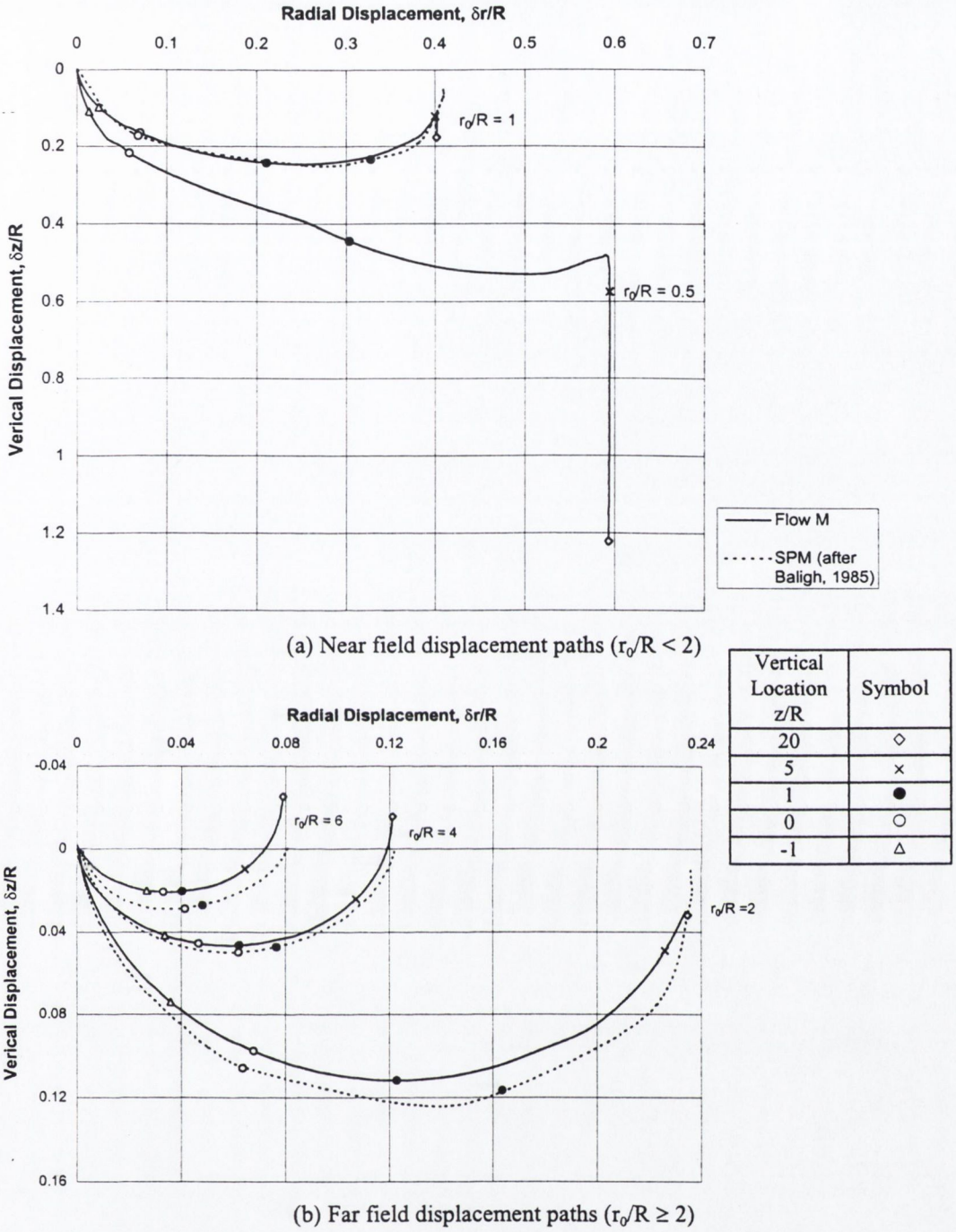

Figure 8.11. Displacement paths during penetration of a 60° cone for the 'best-fit' solution (Flow M)

8.3.3 Strains

The deviatoric strain paths (i.e., E_1, E_2 & E_3) for Flow M are presented in Figure 8.12 & 8.13, and are considered to be more realistic than the standard SPM strain predictions due to the close fit shown by the solution to the experimental displacements on Figure 8.9 & 8.10. The strain paths in the near (Figure 8.12) and far fields (Figure 8.13) have been

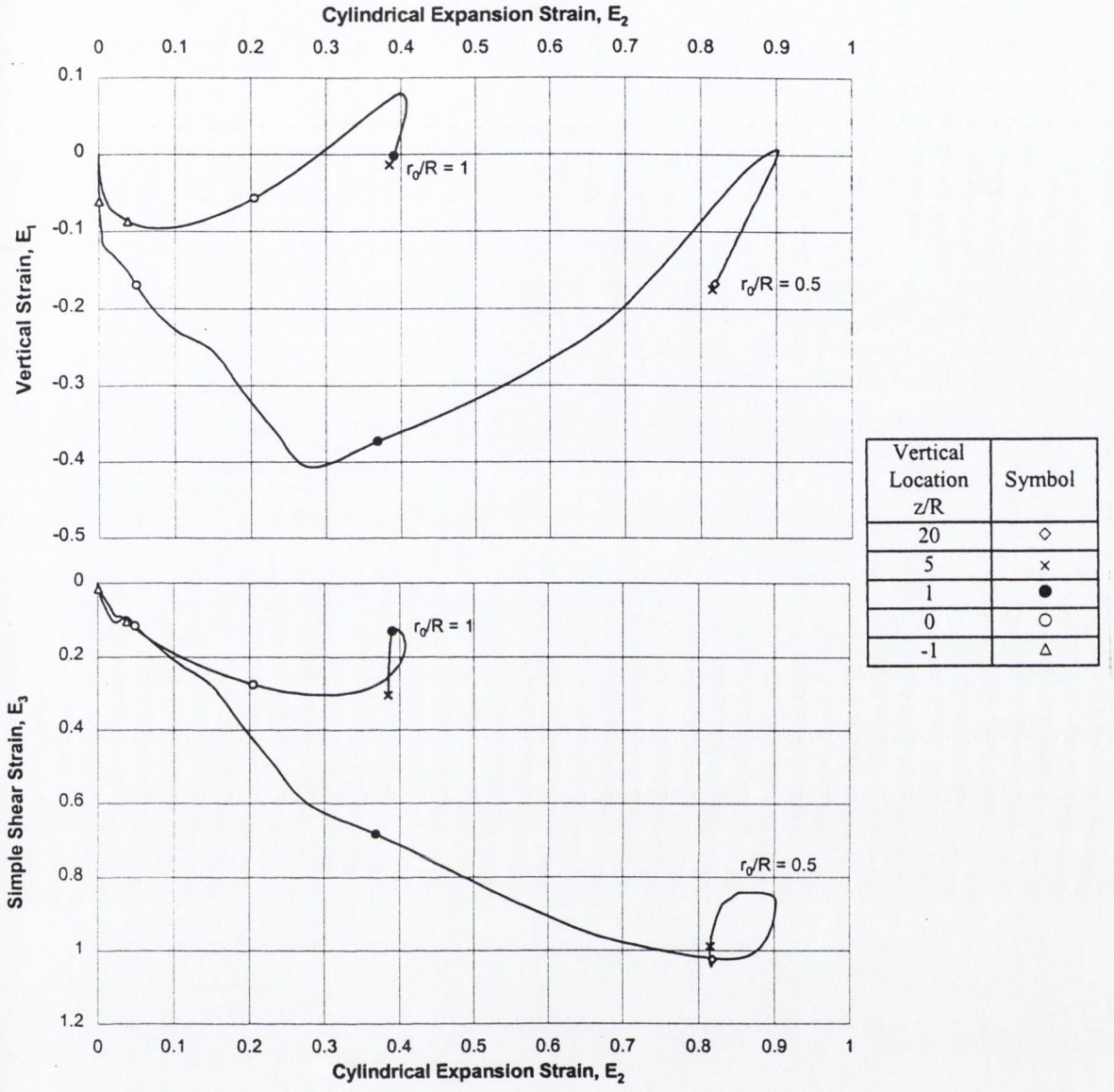

Figure 8.12. Predicted deviatoric strain paths in the near field ($r_0/R \leq 2$) during penetration of a 60° cone for the 'best-fit' solution (Flow M)

plotted separately because of the large difference in the magnitude of straining in these regions.

As expected, the greatest straining occurs close to the penetrometer, although in this near field region the greatest reductions of cylindrical expansion strain (E_2) which occur behind the cone shoulder ($z/R \cong 1.7$) are also evident. Small increases in the initial radial distance of an element from the penetrometer produces a significant reduction in the magnitude of all the deviatoric strains, and this is particularly evident for the strain paths at $r_0/R = 0.5$ &

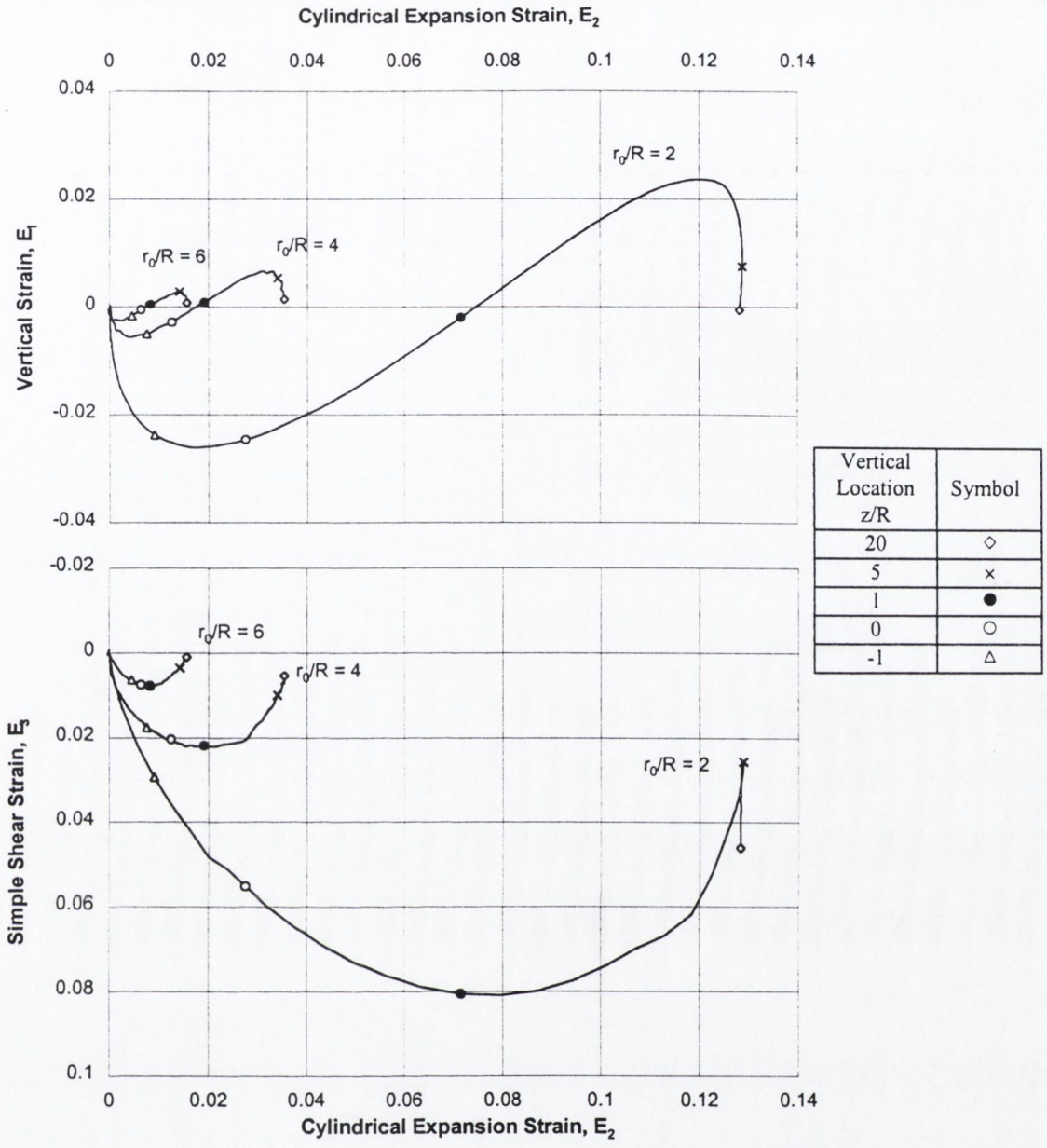

Figure 8.13. Predicted deviatoric strain paths in the far field ($r_0/R \geq 2$) during penetration of a 60° cone for the 'best-fit' solution (Flow M)

1. The characteristics of strain paths also change with increased radial distance from the penetrometer and are summarised here:

- The sharp strain reversals experienced by elements close to the penetrometer, due to rapid strain changes in the vicinity of the tip, are replaced by more gradual strain changes further out.

- Increased radial distance from the penetrometer produces greater tensile strain increments for E_1; for the elements at $r_0/R = 4$ & 6 the final value of E_1 (at $z/R = 20$) is tensile (i.e., positive).
- The reductions in E_2 evident for elements with $r_0/R \leq 2$ are not present further out (at $r_0/R = 4$ & 6) where E_2 is seen to increase with z/R.
- The second reversal in E_3 which causes it to increase with z/R is not present at $r_0/R \geq 2$, i.e., at large radial distances from the penetrometer E_3 decreases with further penetrometer movement when $z/R > 0$.

8.4 DISCUSSION OF THE MODIFIED SPM APPROACH

8.4.1 General

The SPM flow solutions have been shown to allow a large degree of control over the flow velocity field (and hence the inferred strains and displacements) by the adjustment of two parameters; fluid viscosity (μ) and penetrometer boundary velocity (v_{pent}/U). The range of possible flow solutions was, however, constrained by the bounds imposed by Newtonian fluid flow. It has not, therefore, been possible to produce an exact fit to the experimental displacement results at all points but only to provide an approximation to the general trends shown. Most of the flow solutions, which were examined in Chapter 4, showed only small differences in the prediction of radial displacements (except where a high friction value was specified on the penetrometer shaft). This meant that vertical displacements were the controlling factor in selecting the 'best-fit' solutions.

8.4.2 Flat-ended Penetrometer

The 'best-fit' solution for the flat-ended penetrometer gave an approximate prediction of the experimental measurements. Close similarities were found between the predicted and measured data for some features of soil deformation, while for others there were large differences. Some explanation for this is given here.

(i) *Radial predictions*

The 'best-fit' solution for the flat-ended penetrometer, for the most part, was found to over predict the radial displacements by up to 20 %, although the prediction of far field

movements was better. Studies conducted in Chapter 4 indicated that the flat tip caused greater disturbance to the flow than the 60° cone and this resulted in radial displacements that were approximately 10 % higher. The experimental data from different investigations presented in Figure 7.10, however, shows no discernible effect from different tip geometry on the radial displacements. The flow solutions were, therefore, found to be more sensitive to penetrometer tip geometry than has been observed experimentally. This implies that some features introduced by the fluid flow solutions are not compatible with real soil movements.

(ii) *Vertical Prediction*

The vertical displacements predicted for the flat-ended penetrometer gave a reasonable fit to the experimental data, although the values predicted at $z/R = 5$ were found to be closer to the experimental values than those predicted at $z/R = 20$. It was also found that in general the far field predictions were better that those close to the penetrometer.

The displacement paths shown for the 'best-fit' flow in Figure 8.4 and for the experimental data in Figure 8.5 give a more detailed comparison of predicted and measured soil movement around a flat-ended penetrometer. The predominantly downward movement of soil in the model tests close to the penetrometer displayed important differences from the predicted movements:

(a) In the model tests, soil markers which were initially positioned beneath the penetrometer (i.e., $r_0/R < 1$), displayed large downward displacements ahead of the tip ($z/R > 0$), although these movement were difficult to measure (see Section 7.5). The predicted movements in this region show comparable final positions (at $z/R = 20$) with the experimental results but could not replicate the very large movements ahead of the penetrometer tip ($\delta z/R > 4$) that occurred for some soil elements. It is noteworthy that soil markers which came in contact with the shaft of the penetrometer (i.e., $z/R > 0$) were also subjected to large downward movement.

(b) In the region of soil bounded by $1 < r_0/R < 1.5$, a large proportion of the total predicted vertical movement (40-50 %) was from downward 'drag' of the soil after the penetrometer tip has passed ($z/R > 0$). This is typically 3-4 times the level of downward 'drag' that was displayed by the experimental results in this region. The total vertical movements were, however, comparable as the soil in the model tests

showed less influence of further penetrometer movement after the tip had passed than was shown by the flow results.

The features of the model penetrometer tests described in (a) indicate that a cone shaped wedge of soil is pushed ahead of the penetrometer tip, which is not replicated by the flow solution. The differences between the predicted and experimental displacements described in (b) indicate the formation of a shear plane experiencing very high shear strain in close proximity to the penetrometer shaft. This could explain how soil in contact with the penetrometer shaft can experience large downward displacements while the soil only a small distance further away remains relatively unaffected by penetrometer movement after the tip has passed ($z/R > 0$). The transparent nature of the soil used in the model tests meant that the shear planes could not actually be observed in soil around the penetrometer but their presence was indicted by the pattern of movement shown by the soil markers.

It was not possible to reproduce the large soil deformations in the vicinity of the penetrometer, using the flow model, without also over predicting the deformation to soil a short distance further away. This is caused by the more gradual distribution of shear strain throughout the Newtonian fluid, i.e., shear planes with 'sliding' cannot form.

8.4.3 The 60° Cone

The 'best-fit' solution predicted radial displacements for the 60° cone that were practically identical to the existing SPM solutions for this penetrometer geometry (represented by Flow A and Baligh's 60° cone solution). A comparison between final theoretical radial displacements and experimental data at $z/R = 20$ showed that a good fit was achieved close to the penetrometer. A divergence of the predicted radial displacements from the measured movements occurred in the far field, and this was considered to be due to the restricting influence of the far field boundary in the model tests on the experimental displacements.

Some significant differences were found between the displacement paths predicted for Flow M and for the SPM solution for a 60° cone by Baligh (1985);

- the Baligh (1985) solution showed no evidence of downward drag close to the penetrometer, and therefore under predicted the vertical movements for $r_0/R < 2$,

- net vertical heave was also not predicted for $r_0/R > 3$, but instead the soil tended to returned to the initial vertical position.

The vertical displacements from the 'best-fit' solution were consequently seen to give a better estimate of the experimental data than the inviscid, 'full-slip' flow of 'A'. This was particularly true for the vertical displacements close to the penetrometer, where the 'full-slip' flow solution severely under predicted the measured movements (by a factor of 3). This highlights the need for some consideration of frictional effects on the penetrometer boundary if the soil deformation close to the penetrometer is to be replicated. The prediction of small amounts of heave in the far field ($r_0/R > 3$) by both Flows A & M is compatible with the experimental data.

8.4.4 Comparison Of 60° Cone and Flat tip Solutions

A comparison between the 'best-fit' predictions for the two end geometries showed that greater vertical displacements (~1.5-2 times for $r_0/R < 2$) and radial displacements (~10 %) were predicted for the flat tip compared to the 60° cone tip. Predicted displacement paths for the flat-ended and 60° cone penetrometers (in Figures 8.4 and 8.11, respectively) also indicate that the larger displacements will take place with the flat tip. It is notable, however that although the peak radial displacements for the flat tip are greater, they are accompanied by larger post peak reductions in $\delta r/R$ than those predicted for the 60° cone.

Experimental data measured in this Thesis and by Gue (1984) show that greater downward vertical displacements were measured for a flat-ended penetrometer than for a penetrometer with a 45° cone cut off near the apex, used by Francescon (1983), which effectively has geometry between that of a flat tip and 60° cone. The 'best-fit' solution for the 60° cone was found to give a good approximation to the Francescon (1983) data, and the slight under prediction by Flow M of vertical data in the region $0.8 < r_0/R < 1.5$ is consistent with the theoretical effects of geometry on vertical movements. The experimental data, however, display no discernible dependence of radial displacements on penetrometer geometry.

8.4.5 Summary

The modified SPM approach has been shown to provide a good approximation to the soil deformation measured around penetrometers of different geometry. It was not, however, possible to replicate all the features of soil behaviour during penetration, and in particular this was most difficult close to the tip and the shaft of a flat-ended penetrometer. Experimental observations indicate that in reality a cone shaped wedge of soil forms ahead of the tip of a flat penetrometer and that close to the shaft shear planes are formed in the soil which separate regions of high vertical displacement from regions of relatively low vertical displacement a short distance away. These features can only be approximated by Newtonian fluid flow and result in the slight over prediction of the deformation elsewhere in the soil.

The comparison of theoretical and experimental strain paths showed that the modified SPM solutions used in this study were able to approximate the straining regime present in the soil during penetrometer installation. The magnitude of the strains were, however, over predicted in general; this was particularly the case for vertical strains, and to a lesser extent for cylindrical cavity strain and for shear strain.

Experimental results indicate that in reality the radial displacements are relatively insensitive to the tip geometry during penetrometer installation. The vertical displacements, however, were found to have a greater dependence on the shape of the tip. The theoretical solutions were found to have a similar, though perhaps slightly greater dependence of vertical displacements on the tip geometry than was measured experimentally. The radial displacement predictions of the modified SPM were also found to be sensitive to changes the shape of the penetrometer tip, although there is no experimental evidence to suggest this is the case in reality.

8.4.6 Improving The SPM Predictive Method

The modified SPM approach used in this Thesis for the prediction of soil deformation during penetrometer installation, has been shown to be a clear improvement on existing SPM solutions. Further improvements, however, are required if an accurate, rather than approximate, theoretical representation is to be made of the deformational processes that

occur in the soil around a penetrometer, and in particular close to the tip. It is also necessary to check the solution for equilibrium and compatibility with a constitutive soil model.

To aid theoretical prediction, further experimental investigations are required to determine to what extent, if any, the radial and vertical movements are influenced by the penetrometer tip geometry. The visual measuring technique used in this Thesis provides a convenient experimental method for conducting such a study, although the length of time required for the preparation of soil samples has meant it has been beyond the scope of the research presented here.

It is believed that further improvements can be made to the SPM flow predictions which would result in a closer fit to the experimental data. By maintaining the SPM analogy, this allows relatively simple solutions to the penetrometer problem to be produced without the need to develop new sophisticated analytical techniques. Alternative FE analysis of the penetrometer problem (described in Chapter 2) have allowed the introduction of soil properties but suffer from model boundary problems and are largely unverified. The focus of current FE analysis is on the use of an adapted form of the Eulerian approach, which has many similarities to the formulation used in computational fluid dynamics, not least of which is the concept of material 'flowing' through the grid.

This Thesis has introduced two addition flow parameters, fluid viscosity and the penetrometer boundary velocity, to the SPM which have allowed significant control over the resulting soil deformation field. These parameters have allowed behaviour such as drag down and heave to be modelled using Newtonian fluid properties, whereas previous SPM analyses using ideal, inviscid flow have not been able to reproduce these effects. It is quite possible that a more accurate simulation of soil behaviour could be achieved by the introduction of non-Newtonian fluid properties to the SPM analysis.

The ANSYS fluid dynamics package, which was used to produce the flow solutions presented in this Thesis, facilitates non-Newtonian flow analysis, although time constraints have prevented its use here. The Newtonian flows used in this research have a linear relationship between shear stress and the rate of shear (or velocity gradient), with the slope

of the line equal to the viscosity μ as shown in Figure 8.14. Other relationships between shear stress and the rate of shear are shown on Figure 8.14 for non-Newtonian fluids which are not independent of the rate of shear (i.e., they have non-linear relationships). Fluids which have a reduced viscosity when the rate of shear is large are said to be *pseudo-plastic* (such as blood and liquid cement) and fluids which exhibit the converse property of increased viscosity with increasing shear rate are described as *dilatant.* It is possible to model these flow types within ANSYS using a 'power law' relationship between the viscosity and the velocity gradient.

The non-Newtonian flow type that possibly has the greatest potential for modelling soil behaviour is *plastic* flow which is often displayed by fluids such as slurries and pastes. Flow solutions for this type of 'plastic' fluid can be solved with ANSYS using the Bingham model, which requires the specification of a yield stress for the fluid and plastic viscosity (illustrated in Figure 8.15). This effectively would provide a 'bi-viscosity' model which would allow different fluid behaviour to be modelled in the region close to the penetrometer than occurs elsewhere.

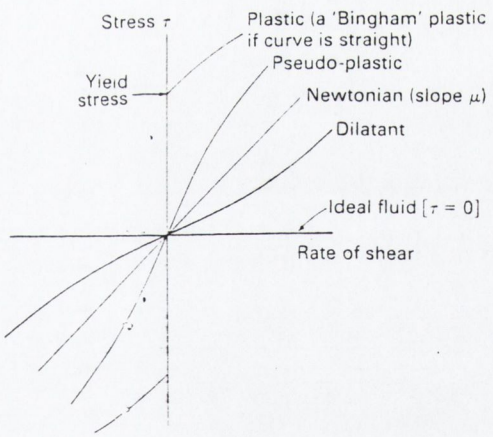

Figure 8.14. Stress-strain rate relationships for different types of fluid (after Massey, 1991)

Another way that improvements could possibly be made to the SPM solution is to vary the relative velocity (slip condition) that is applied to the penetrometer boundary. The SPM solutions in this Thesis specify a uniform velocity boundary condition on this boundary, i.e., a constant value for v_{pent}/U is applied along the complete length of the penetrometer shaft. It is possible that a linear or non-linear relationship between the boundary velocity and distance from the tip (z/R) could be found that would allow frictional effects to be

introduced close to the tip, while also reducing the downward 'drag' effect on the soil further behind the tip that occurs for the current solutions and which experimental results suggest are smaller than were predicted.

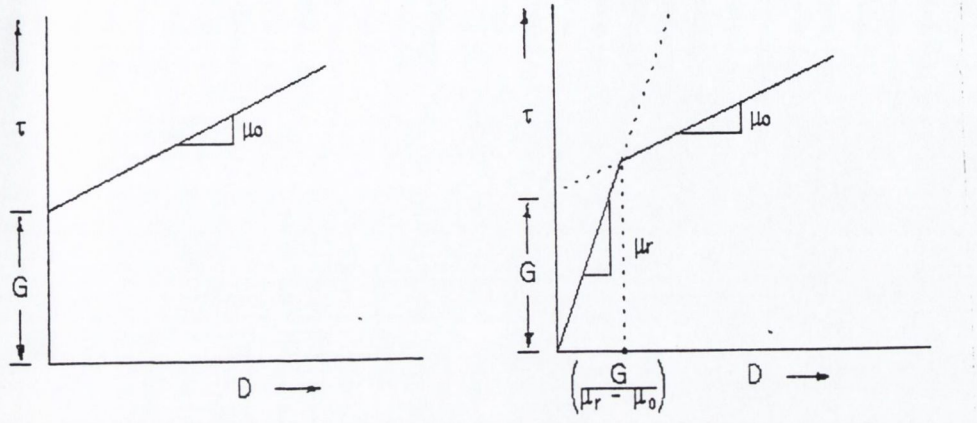

(a) (b)

Figure 8.15. Stress vs. strain relationship for: (a) an 'ideal' Bingham model; (b) a 'bi-viscosity' Bingham model (after ANSYS Users Manual, 1997)

CHAPTER 9
CONCLUSIONS

9.0 CONCLUSIONS

9.1 OUTLINE

A theoretical and experimental investigation of the ground movements and strains that take place during undrained installation of closed-ended penetrometers has been performed. This chapter presents a summary of the main conclusions drawn from this study. The first section presents the main findings from experimental work conducted in this Thesis. The conclusions drawn from investigations using the experimental data and a modified Strain Path Method approach developed in this research are then described. Suggestions for further research are given in the final section.

9.2 EXPERIMENTAL MEASUREMENTS

9.2.1 TCD Model Penetrometer Tests

A series of laboratory tests were conducted to record the soil displacements induced during the installation of a flat-ended penetrometer into a transparent soil using a video camera system. These experimental measurements provide a unique account of the deformational behaviour of the soil surrounding a penetrating penetrometer and give:

- Radial and vertical displacements recorded to a resolution of 0.01 mm (or 0.0016 R).
- Displacements paths showing the movement of soil elements throughout the duration of penetrometer installation.
- Strain paths for soil elements calculated by differentiation of the experimental displacement paths.
- Strain contours showing the distribution of strain around the penetrometer.

Some experimental difficulties were encountered:

- The measurement of soil movements close to the penetrometer centreline ($r_0/R < 1$) was made difficult by the penetrometer which obscured the camera view of the soil markers during penetration,
- Other soil markers were obscured by the infiltration of impurities or air into the transparent soil sample and called their reliability into question. Some averaging of data was also considered necessary to improve accuracy

9.2.2 Observations from Experimental Data

The key features of soil deformation during penetrometer installation in model tests observed are:

- Comparison of the experimental results with those of other studies indicates that the total radial displacement of the soil is relatively insensitive to the tip geometry.
- The dimensions of test chamber relative to the penetrometer radius can have an influence on the far field radial movements, i.e., if the distance to the far field boundary is too small (e.g., $r/R < 30$), it has the effect of reducing the magnitude of the radial displacements.
- Vertical displacements are influenced significantly by the tip geometry and this is particularly the case close to the penetrometer; greater downward vertical displacements occur for penetrometers with blunt or flat tips than with sharper or pointed tips.
- Vertical movements in the high shear zones close to the penetrometer are large and often differ in magnitude by a considerable margin. Results for the flat tip penetrometer used in this research show that soil elements very close to the penetrometer can have vertical displacements varying from 1R to 4R. Similar vertical displacement patterns were measured by Francescon (1983) for a 45° cone cut off near the apex.

9.2.3 Transparent Soil

A transparent material was developed in this research which allows its deformational behaviour to be observed visually and was used successfully in model penetrometer tests. The TCD transparent clay is a two phase media, consisting of fumed silica and a pore fluid blended from two oils to give a refractive index of 1.456 at 20°C.

Advantages

The transparent soil displays a low degradation of transparency with increasing sample thickness and this allows the observation of soil behaviour in three dimensional tests. The material has geotechnical properties that are similar to those of natural soils and it was shown that the TCD transparent soil possesses;

- clay sized aggregate particles (after consolidation to 225 kPa) which are in the order of 0.1-0.4 μm,
- behaviour in compression similar to that of soft clay, although the secondary compression was particularly high and comparable only to highly plastic or organic soils,
- permeability and friction angle consistent with many natural clays.

Disadvantages

- The transparent soil requires that a high percentage of the liquid phase of the soil be removed during consolidation to produce a stiff sample. The initial soil volume must be reduced by over two thirds and it is necessary, therefore, to mix large volumes of slurry. The high formation pressure gives a correspondingly high overconsolidation ratio (this OCR may not be directly applicable to real clay)
- The time taken to consolidate a sample within the test chamber is high due to low permeability of the transparent soil at high consolidation pressures.
- Degradation of transparency occurs if impurities (e.g., dust) or air enters the soil, although air can be removed immediately after the mixing stage if the silica content is not greater than 7 % by weight.

9.3 PREDICTIVE CAPABILITIES OF THE MODIFIED SPM APPROACH

9.3.1 Choice Of Predictive Approach For Penetrometer Installation

- The Strain Path Method (SPM) provides a useful two dimensional analytical solution which attempts to model the complex strain paths experienced by soil elements during penetrometer installation. The SPM postulates that the relative position of soil particles to a penetrometer are the same as the streamlines followed by an inviscid incompressible fluid. Although simplifying the problem significantly, these assumptions ignore both the

material properties of the soil (e.g., shear strength, etc.) and the effects of surface friction on the penetrometer.

- Advances in numerical methods for penetrometer installation, involving large strain and moving boundary finite element analyses are promising but remain largely unverified and require significant further development. It was therefore decided to model penetrometer installation in this Thesis by expanding upon the SPM by introducing additional parameters to the flow model; fluid viscosity (μ) and penetrometer boundary velocity (v_{pent}/U). These parameters induce different soil deformation patterns than currently predicted by the SPM and may be predicted using the ANSYS finite element fluid dynamics package.

9.3.2 Influence Of Flow Properties On SPM Solutions

The introduction of the two parameters, fluid viscosity (μ) and penetrometer boundary velocity (v_{pent}/U), to the fluid flow model facilitated significant control over the flow field, and hence the calculated strains and displacements.

Viscosity, μ

- Increased μ has the effect of increasing the computed disturbance to the soil (in particular the vertical compression and shear strains). The range of influence of the penetrometer and its specified boundary conditions on the surrounding soil elements is also increased.

Relative velocity on the penetrometer boundary, v_{pent}/U

- Reducing the relative velocity (v_{pent}/U) increases the effect of friction on the penetrometer. This results in greater vertical compression strain (E_1) and shear strain (E_3) within the soil. The cylindrical cavity strain (E_2) also shows a greater peak value and subsequent reduction in E_2 with increased distance behind the tip (z/R).
- Greater radial and vertical soil displacements (δr & δz) are calculated for reduced relative velocities. The vertical movements close to the penetrometer ($r_0/R < 2$) are most sensitive to small changes in v_{pent}/U.

The two flow parameters were, however, not found to have any physical significance in relation to real soil properties. This is highlighted by the vast differences in average shear stress calculated on the penetrometer boundary for the 'best fit' flow (N) and the model penetrometer test which were 2×10^{-8} kPa and 15-20 kPa, respectively. Therefore the flow parameters μ and v_{pent}/U are significant only in the influence they show on deformation patterns computed using the SPM. If μ values roughly corresponding to a soil are included in the flow solution the boundary layer formed at the penetrometer results in deformation patterns that bear no relation to observed soil behaviour.

9.3.3 Best-fit Predictions for the Modified SPM

1. Flat-ended penetrometer

A modified SPM solution (μ = 0.01 Ns/m^2 and v_{pent}/U = 0.985) for a penetrometer with a flat tip was selected to provide the 'best fit' to displacement measurements obtained in this research project. A comparison between the displacements predicted by the 'best-fit' solution and the experimental measurements shows:

- The predicted radial displacements, for the most part, are greater than the experimental displacements by up to 20 %, although the prediction of far field movements is good.
- The vertical displacements predicted for the flat-ended penetrometer give a reasonable fit to the experimental data with the far field predictions, in general, giving a better fit than those close to the penetrometer.

A comparison of the predicted and experimental strain paths for a flat ended penetrometer shows that the modified SPM solution reproduces many of the features measured experimentally, but only in an approximate manner: Compressive values of E_1 are generally over predicted (except in the far field), although tensile E_1 strains are more closely matched. Predictions of E_2 and E_3 approximate those measured experimentally in most cases.

Observations of soil behaviour in the model penetrometer tests indicate that:

- In reality, it is likely that a cone shaped wedge of soil forms ahead of the tip of a flat penetrometer,

- Close to the shaft, shear planes are formed in the soil which separate regions of relatively high vertical displacement from regions of low vertical displacement a short distance away.

Although the features close to the penetrometer may be approximated by given flow properties, such a flow would result in over prediction of deformation elsewhere. Such a phenomenon is a consequence of the more gradual distribution of shear strain throughout the Newtonian fluid, i.e., sliding shear planes/discontinuities cannot form.

2. *60° Cone*

The 'best-fit' flow properties derived on the basis of displacement measurements for the flat-ended penetrometer in this Thesis have been applied to a penetrometer with a 60° cone so that comparisons could be made with the standard SPM solution for a 60° cone (Baligh, 1985) and with experimental data in the literature measured by Francescon (1983) (for a 45° cone cut off near the apex). This has allowed the applicabilty of the 'best fit' flow parameters derived for the flat-tip to be assesed for other penetrometer geometries.

- The radial displacements predicted by the 'best-fit' flow and by Baligh's SPM solution are practically identical and both predict radial displacement measurements very well.
- For vertical displacements, significant differences occur between the 'best-fit flow predictions and the SPM predictions by Baligh (1985), which show no evidence of downward drag close to the penetrometer ($r_0/R < 2$) or net vertical heave in the far field ($r_0/R > 3$). Predicted vertical movements for the 'best-fit' flow achieve a close match with the experimental results in both the near and far fields.
- The significant improvement of vertical displacement prediction given by 'best-fit' solution for the 60° cone over the SPM solution by Baligh (1985), highlights the need for some consideration of frictional effects on the penetrometer boundary if the soil deformation close to the penetrometer is to be replicated.

3. *Comparison of 'best-fit' predictions for 60° cone and flat tip*

A comparison between the 'best-fit' predictions for the two end geometries shows that:

- The sharp tip of the 60° cone has a less disturbing effect on the soil than that of the flat ended penetrometer which shows greater E_1, E_2 and E_3 strains, although the flat tip displays greater reversals for these strains.
- Greater vertical displacements (~1.5-2 times for $r_0/R < 2$) and radial displacements (~10 %) are predicted for the flat tip compared to the 60° cone tip, although greater reductions in the radial displacements occur for the flat tip after peak values.
- Overall, the strain and displacement paths indicate a smoother movement of soil around the cone shape, with peak behaviour occurring some way behind the tip ($z/R > 3$). The flat shape causes greater disturbance to the soil and most peak behaviour occurs close to its tip ($z/R \approx 1$).
- It is expected that the application of the 'best-fit' flow properties to penetrometer geometries other than the 60° cone or flat tip, would give predictions of strain and displacement that a real soil would experience. However, a general feature of the method is a greater sensitivity of predicted radial displacements to the penetrometer tip geometry than has been observed experimentally.

4. Concluding observations on predictive approach

The reasonable agreement found between the predicted deformation and experimental measurements gives some confirmation to the assumption of the SPM (first stated by Baligh 1985) that the ground deformation caused by 'deep' penetrometer installation are insensitive to the soil properties. This is also borne out by the general agreement between the experimental displacements from different studies in a range of soil types. The 'best fit' flow parameters give shear stresses that are orders of magnitude less than one would expect in soil, also indicating the strongly kinematic nature of the displacement field.

9.4 FUTURE RESEARCH

9.4.1 Experimental Work

- Further experimental investigations with different penetrometer geometries are required to determine their influence on radial and vertical displacements.
- The visual technique used in the model tests presented in this Thesis provides a useful method for measuring soil deformation. The use of a perspex or glass penetrometer

could allow better observation of the soil deformation close to *closed-ended* penetrometers as well as facilitating the investigation of behaviour during installation of *open-ended* penetrometers such as open-ended piles or samplers.

9.4.2 Improving SPM Prediction

This Thesis introduces two new fluid flow parameters to the Strain Path Method which give a greater control over the predicted deformation field by use of fluid viscosity and the relative velocity on the penetrometer boundary (Newtonian fluid properties). It is possible that further development of the SPM could allow more accurate simulation of soil behaviour to be achieved:

- The introduction of *plastic* non-Newtonian fluid properties to the SPM analysis has potential for modelling real soil behaviour more closely (i.e., the formation of a conical wedge of soil ahead of the tip and shear bands close to the shaft). Flow solutions for this type of 'plastic' fluid can be solved with ANSYS using the Bingham model, which requires the specification of a plastic viscosity yield stress for the fluid. This effectively would provide a 'bi-viscosity' model that could mimic observed differences between the near and far field behaviour.

- Another way that improvements could possibly be made to the SPM solution is to vary the relative velocity (slip condition) that is applied to the penetrometer boundary (v_{pent}/U). The SPM solutions in this Thesis specify a constant velocity along the length of the penetrometer boundary. It is possible that a linear or non-linear relationship between the boundary velocity and distance from the tip (z/R) could be found that would allow frictional effects to be introduced close to the tip, while also reducing the downward 'drag' effect on the soil further behind the tip that occurs for the current solutions and which experimental results suggest are smaller than were predicted.

- The application of stress models (such as the MIT-E3) to the strain fields produced by the modified SPM approach is required to determine their influence on stress distribution along the penetrometer shaft. A preliminary investigation is conducted in Appendix A but further work is required if a 2-D model is to be applied. Studies by others (such as Teh, 1987) have shown that stress calculations in two dimensions gives

rise to inequilibrium problems. It is expected, however, that 'realistic' strain fields would produce less difficulty in achieving stress equilibrium than the standard SPM analyses. However, the compatibility of the deformation solution predicted in this study with a constitutive model needs to be investigated, as does the influence achieving stress equilibrium might have on the strain fields calculated here.

APPENDIX A
APPLICATION OF THE CAVITY EXPANSION METHOD

Appendix A

A. APPLICATION OF THE CAVITY EXPANSION METHOD

A1 GENERAL

This Appendix represents an initial preliminary investigation into the application of stress models to the strain fields produced by both the Strain Path Method (SPM) and the experimental displacement measurements found from model tests. The cavity expansion method (CEM) is one relatively simple and popular (although flawed) technique for estimating the stresses around the shaft of a penetrometer and is used here to illustrate how stresses may be estimated from experimental displacement measurements.

The cavity expansion technique has several major drawbacks with regard to modelling penetrometer installation; the most obvious being the geometrical differences between expanded cavities and real penetrometers. Cavity expansion over simplifies the penetration problem to a one dimensional analysis which does not reproduce the complicated strain paths (involving non-monotonic straining) experienced by the soil during the penetration installation. The method does, however, have the advantage of being relatively simple to apply and has a large number of published solutions, which have been outlined in Section 2.3. In this Appendix, solutions are presented for cylindrical cavity expansion with both an elastic-perfectly plastic material and a version of the Modified Cam-clay soil model. These solutions are presented with stress solutions found by application of the Modified Cam-clay model to experimental data.

A2 CYLINDRICAL CAVITY EXPANSION THEORY

Cylindrical cavity expansion has been used by a number of authors to predict the stresses around the shafts of piles and penetrometers (Carter *et al.*, 1979 and Randolph *et al.*, 1979). The numerical technique for cylindrical cavity expansion used here is the same as that presented by Carter *et al.* (1979). The expansion of a cavity within a finite element mesh, can begin either from an existing cavity with a finite radius or with a initial radius of zero. The latter requires the use of rate equations and large strain theory to avoid infinite

circumferential strain. The analysis presented here is a simple small strain one, and the numerical calculations begin with a finite cavity radius.

A2.1 Derivation Of Expressions For Cylindrical Cavity Expansion

The cavity is first expanded to a radius, ρ for an infinite vertical depth and is then enlarged from ρ to 2ρ, which approximates what happens when a cavity expands from an initial radius of zero to a radius R (see Figure A1). If both types of deformation take place at constant volume then the necessary relation between ρ and R is $\rho = 3^{1/2}R$. No knowledge is gained, however, of strains in the annular region bounded on the inside by the pile (of radius R) and on the outside by the cylindrical surface at $r = 2\rho = \frac{2}{\sqrt{3}}R$.

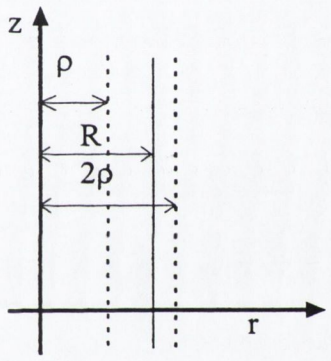

Figure A1. Finite cylindrical cavity expansion as a model for pile installation.

The procedure for calculating displacements, strains and then stresses during cylindrical cavity expansion are presented in steps (i) to (iii) below:

(*i*) *Initial Finite Cavity Expansion*

A cylinder with an initial radius, ρ is expanded into an undisturbed material. The volume of the expansion is given by:

$$V = \pi r^2 h$$

The displacement of the material surrounding the cavity can be calculated by equating the volume change. Therefore, if a cylindrical volume of material, V_0 enclosed by a radius, r_0 within the undisturbed mass, is considered and the change in volume due to cavity expansion is ΔV, then the new volume resulting from cavity expansion is given by;

$$V_1 = \pi r_0^2 h + \pi \rho^2 h$$

and therefore the new radial position of any point in the soil can be found from;

$$\pi r_1^2 h = \pi r_0^2 h + \pi \rho^2 h$$

$$r_1^2 = r_0^2 + \rho^2 \tag{A.1}$$

where,

r_0 = the initial radial distance of a point from the centre of the cavity,

r_1 = the radial distance of the point from the centre of the cavity after expansion,

V_0 = the cylindrical volume associated with r_0.

(*ii*) *Further Cavity Expansion*

The cavity is expanded again by further amount ρ, as has been mentioned above, to simulate the insertion of a pile of radius R, and the new radial position of a point after expansion is found from:

$$r_2 = \sqrt{r_1^2 + \rho^2} \tag{A.2}$$

The change in radial position can be simply calculated from $\Delta r = r_2 - r_1$.

(*iii*) *Axisymmetric Distribution of Stress and Strain*

As the cavity is assumed to have a length much greater than its radius, the surrounding soil is subjected to plane strain with no deformation in the vertical direction. All the displacements are therefore radial in direction. If the outward deformation at radius r is y then the tensile circumferential strain is;

$$\varepsilon_\theta = \frac{2\pi(r + y) - 2\pi r}{2\pi r} = \frac{y}{r} \tag{A.3}$$

and the radial strain is given by;

$$\varepsilon_r = \frac{\partial y}{\partial r} \tag{A.4}$$

The cavity strain is the circumferential strain at the wall of the cavity;

$$\varepsilon_c = \frac{y_c}{\rho} \tag{A.5}$$

For cylindrical cavity expansion into an isotropic elastic material the radial displacements are inversely proportional to the distance from the expansion, and therefore from (A.3) and (A.5) the radial displacement is;

$$y = \frac{y_c \rho}{r} = \frac{\varepsilon_c \rho_0 \rho}{r} \tag{A.6}$$

where ρ_0 is the initial radius of expansion and ρ is the final radius of the cavity. The radial and circumferential strains can now be expressed in terms of the movement at the cavity wall, therefore from (A.3) and (A.6);

$$\varepsilon_\theta = \frac{y}{r} = \frac{y_c \rho}{r^2} \tag{A.7}$$

and from (A4) & (A6),

$$\varepsilon_r = \frac{\partial y}{\partial r} = -\frac{y_c \rho}{r^2} \tag{A.8}$$

It can be seen from (A.7) and (A.8) that ε_r and ε_θ are equal but of opposite sign and vary inversely with the square of the radius.

The cylindrical shape of the expansion gives conditions of overall axial symmetry. This implies that the radial and circumferential stresses on an element of soil are principal stresses as shown in Figure A2. If equilibrium is taken along the centreline of the element then:

$$\left(\sigma_r + \frac{\partial \sigma_r}{\partial r}\delta r\right)(r + \delta r)\delta\theta\delta z - \sigma_r r\delta\theta\delta z - \left(\sigma_\theta + \frac{\partial \sigma_\theta}{\partial r}\delta\theta\right)\delta r\delta z Sin(\delta\theta/2) - \sigma_\theta \delta r\delta z Sin(\delta\theta/2) = 0$$

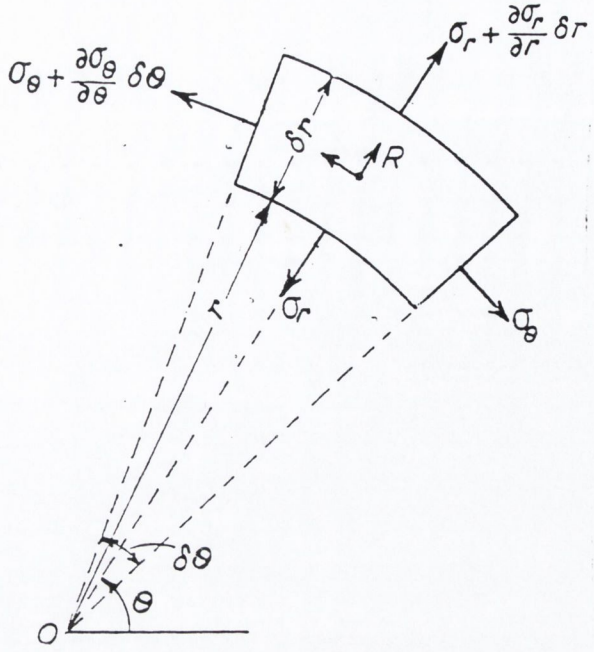

FigureA2. Radial and circumferential stress equilibrium on a soil element (after Benham & Warnock, 1976)

By taking the element to have a unit thickness, $\delta z = 1$, and assuming that as $\delta\theta \rightarrow 0$, $\mathrm{Sin}(\delta\theta/2) \rightarrow \delta\theta/2$, then with second order terms also neglected;

$$\sigma_r \delta r \delta\theta + \frac{\partial \sigma_r}{\partial r} r \delta r \delta\theta - \sigma_\theta \delta r \delta\theta = 0$$

it is possible divide across by $r\delta r\delta\theta$,

$$\frac{\partial \sigma_r}{\partial r} + \frac{\sigma_r - \sigma_\theta}{r} = 0 \qquad \text{(A.9)}$$

This is the equilibrium equation for cylindrical expansion in terms of total stresses. There are two boundary conditions for the cylindrical expansion;

a) at the wall of the cavity the radial stress equals the cavity pressure, p and the radial displacement is y_c.
b) at infinitely large radius, the total radial stress is equal to the in-situ horizontal total stress in the undisturbed soil mass (σ_{ho}) and the radial displacement is zero.

A2.2 Cylindrical Cavity Expansion in Purely Elastic Soil

The expansion of the cavity which appears to be a compressive process is in fact a shearing process. This means no excess pore pressures are generated as a result of the expansion for elastic conditions. For pure elastic shear the proportionality between shear stress and strain is $\tau = G\gamma$, where G is the elastic shear modulus and γ is the shear strain. In a purely elastic material $\delta\sigma_r = \delta\tau$. Therefore;

$$\delta\sigma_r = 2\varepsilon_r G = 2G\varepsilon_c\rho_0\rho/r^2 \tag{A.10}$$

and,

$$\delta\sigma_\theta = -2G\varepsilon_c\rho_0\rho/r^2 \tag{A.11}$$

The radial and circumferential stresses consequently change by equal and opposite amounts from the in-situ horizontal stress, σ_h. Therefore the mean stress level in the elastic material remains constant.

A2.3 Cylindrical Cavity Expansion In Elastic-Perfectly Plastic Soil

In an elastic-perfectly plastic material the shear stress is limited to a maximum value c_U, the undrained shear strength and this shear stress-strain relationship is shown in Figure A3;

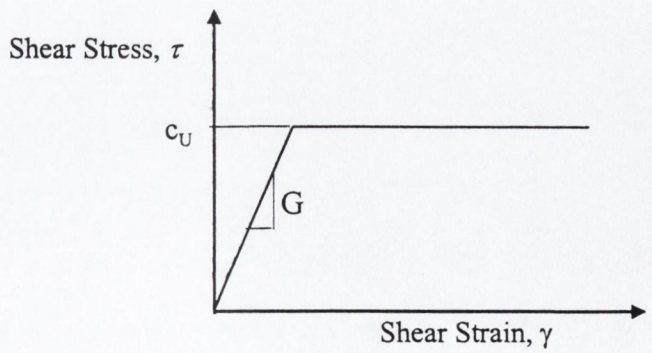

Figure A3. Relationship between shear stress and strain for elastic-perfectly plastic material

In the plastically deformed region since the radial and circumferential stresses are equal and opposite:

$$\sigma_r - \sigma_\theta = 2\tau = 2c_U \tag{A.12}$$

If the forces on an element of soil in the plastic zone around an expanding cylinder are considered, then equilibrium of forces in the radial direction gives,

$$\sigma_{r_2}\left[r_2 d\theta\right] - \sigma_{r_1}\left[r_1 d\theta\right] - 2\sigma_\theta dr \sin\tfrac{\partial\theta}{2} = 0$$

and if $\delta\theta$ is small then $\sin(\delta\theta) \cong \delta\theta$, and this gives;

$$\sigma_{r_2}\left[r_2 d\theta\right] - \sigma_{r_1}\left[r_1 d\theta\right] - \sigma_\theta dr d\theta = 0$$

$$\Rightarrow \sigma_{r_2} r_2 - \sigma_{r_1} r_1 - \sigma_\theta\left(r_2 - r_1\right) = 0 \tag{A.13}$$

For an element of soil in the plastically deformed region the circumferential stress, $\sigma_\theta = \sigma_r - 2c_U$, also $\sigma_\theta = (\sigma_{\theta_1} + \sigma_{\theta_2})/2$. These relationships are combined with (A.13) to give the radial stress within the plastically deformed region, i.e., if $\sigma_r \geq c_U$.

$$\sigma_{r_1} r_1 = \sigma_{r_2} r_2 - \left(\frac{\sigma_{\theta_1} + \sigma_{\theta_2}}{2}\right)\left(r_2 - r_1\right)$$

$$= \sigma_{r_2} r_2 - \left(\frac{\sigma_{r_1} - 2Cu + \sigma_{\theta_2}}{2}\right)\left(r_2 - r_1\right)$$

$$\sigma_{r_1} r_1 + \sigma_{r_1}\left(\frac{r_2 - r_1}{2}\right) = \sigma_{r_2} r_2 - \left(\frac{\sigma_{\theta_2} - 2Cu}{2}\right)\left(r_2 - r_1\right)$$

$$\sigma_{r_1} = \left[\sigma_{r_2} r_2 - \left(\frac{\sigma_{\theta_2} - 2Cu}{2}\right)\left(r_2 - r_1\right)\right]\left(\frac{2}{r_1 + r_2}\right) \tag{A.14}$$

The elastic perfectly-plastic stress model was applied to cavity expansion on an MS Excel spreadsheet and Figure A4 plots the radial and circumferential stresses in a soil of undrained shear strength, c_U = 150 kPa. It can be seen that in the elastic zone the radial and circumferential stresses are equal and opposite. In the plastically deformed region the effect of the limiting condition (the undrained strength) is most apparent in the results for the circumferential stress. In both the elastic and plastic regions the soil is in equilibrium in

terms of total stresses. The results from this model were verified using the expression for cavity pressure from Mair and Wood (1987):

$$\Delta p = c_U\left[1 + \ln\left(G/c_U\right)\right] + c_U\left[\ln\left(\Delta V/V\right)\right] \tag{A.15}$$

The accuracy of the cavity pressure results were dependent on the spacing of grid points in the plastic zone. For the 2% expansion shown here, a spacing of $0.06R_p$, (where R_p is the extent of the plastic zone), gives an error of less than 1%.

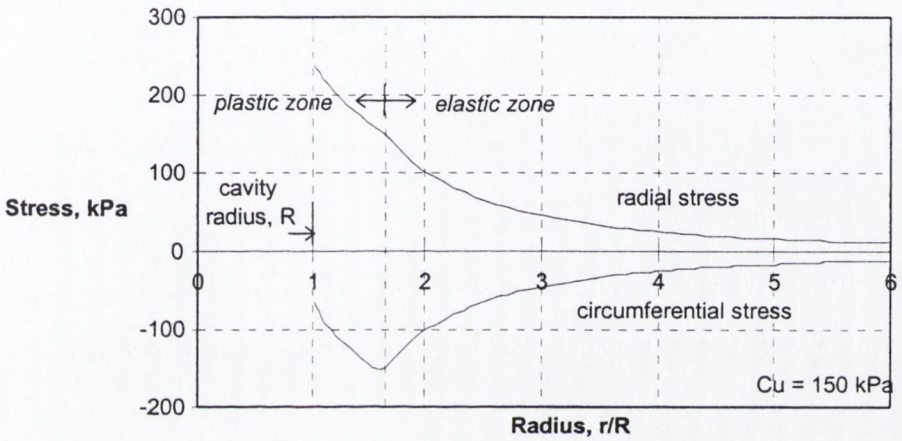

Figure A4. Radial and circumferential stresses around an expanding cylinder (cavity expansion = 2 % R) in an elastic-perfectly plastic soil

A3 THE MODIFIED CAM-CLAY MODEL

A3.1 General

The Modified Cam-clay (MCC) is a theoretical model for clay behaviour which is able to reproduce many of the features of reconstituted clays. It is a volumetric hardening, elastic-plastic material based on the critical state concepts. In particular it contains features common to many elastic-plastic models such as the inclusion of a region of stress space in which the behaviour is elastic and a yield surface which defines the onset of plastic strains. Expansion of the yield surface is a function of not only stresses but also plastic strains. The direction of plastic straining is determined by the flow rule and is assumed to be normal to the yield surface. The magnitudes of these strains is determined by the hardening law.

A3.2 Model Parameters and Stress-Strain Relationships

The parameters used by the model and the relationship between stress-strain that are described here are given in greater detail by Muir Wood (1990). The Modified Cam-Clay model can predict, given any history of stress (or strain), a response for the soil in terms of strain (or stress) and has the advantage of requiring the specification of only five parameters for describing the soil's material properties, which are:

λ, the slope of the normal consolidation line in v-lnp' space (where v is the specific volume and p' is the mean effective stress).

κ, the mean slope of the expansion and re-compression line in v-lnp' space.

Γ, the specific volume at unit p' on the critical state line in v-lnp' space.

M, the value of the shear stress ratio q/p' at the critical state condition.

G, the elastic shear modulus.

The stress conditions within the model are described in terms the mean effective stress, p' and the deviatoric stress, q which in a general form of expression are given by:

$$p' = \frac{1}{3}\left(\sigma'_{xx} + \sigma'_{yy} + \sigma'_{zz}\right) \tag{A.16}$$

$$q = \sqrt{\left[\left\{\frac{\left(\sigma'_{yy} - \sigma'_{zz}\right)^2 + \left(\sigma'_{zz} - \sigma'_{xx}\right)^2 + \left(\sigma'_{xx} - \sigma'_{yy}\right)^2}{2} + 3\left(\tau_{yz}^2 + \tau_{zx}^2 + \tau_{xy}^2\right)\right\}\right]} \tag{A.17}$$

In addition to the listed Cam-clay parameters a knowledge is also required of the *in situ* stresses in the soil. The essential aspects in the elastic-plastic response of the soil can be summarised into five main points:

1. *Consolidation history*

The consolidation history of any element of soil is given by the normal consolidation line and relevant swelling line. This requires the two basic soil parameters λ, κ and a third parameter giving the position of the normal consolidation line (typically Γ).

2. *Critical state line (CSL)*

The position of the CSL requires two soil parameters, M and Γ. The position of the isotropic normal consolidation line is fixed in the model by the position of the critical state line. The spacing between the two lines is controlled by the ratio r, taken as two in the Modified Cam-Clay model as a consequence of the elliptically shaped yield envelope (Figure A5).

3. *Elastic behaviour*

In the elastic stress space it is assumed that recoverable changes in volume accompany any changes in mean effective stress p' according to the expression;

$$\delta\varepsilon_p^e = \kappa \frac{\delta p'}{v p'} \tag{A.18}$$

where $\delta\varepsilon_p$ is the change in volumetric strain. This implies a linear relationship between the specific volume v and log p' for elastic unloading-reloading the of soil. It is also assumed that recoverable shear strains accompany any changes in deviatoric stress q, which is described by:

$$\delta\varepsilon_q^e = \frac{\delta q}{3G} \tag{A.19}$$

4. *Yield envelope*

The yield envelope is a scalar function separating a region of elastic behaviour from plastic behaviour. The size of the envelope is dictated by the isotropic preconsolidation pressure p'_o. The shape of the envelope is an ellipse symmetrical about the p'-axis which passes through the origin and p'_o and is shown in Figure A5(a). Yielding occurs when the stresses obey the following criterion:

$$q^2 - M^2\left\{p'\left(p'_o - p'\right)\right\} = 0 \tag{A.20}$$

5. *Plastic behaviour*

The Modified Cam-clay model obeys the principle of normality, which states that the plastic strain increment vector is perpendicular to the yield envelope at the relevant stress state. This is termed the flow rule which is described by the expression:

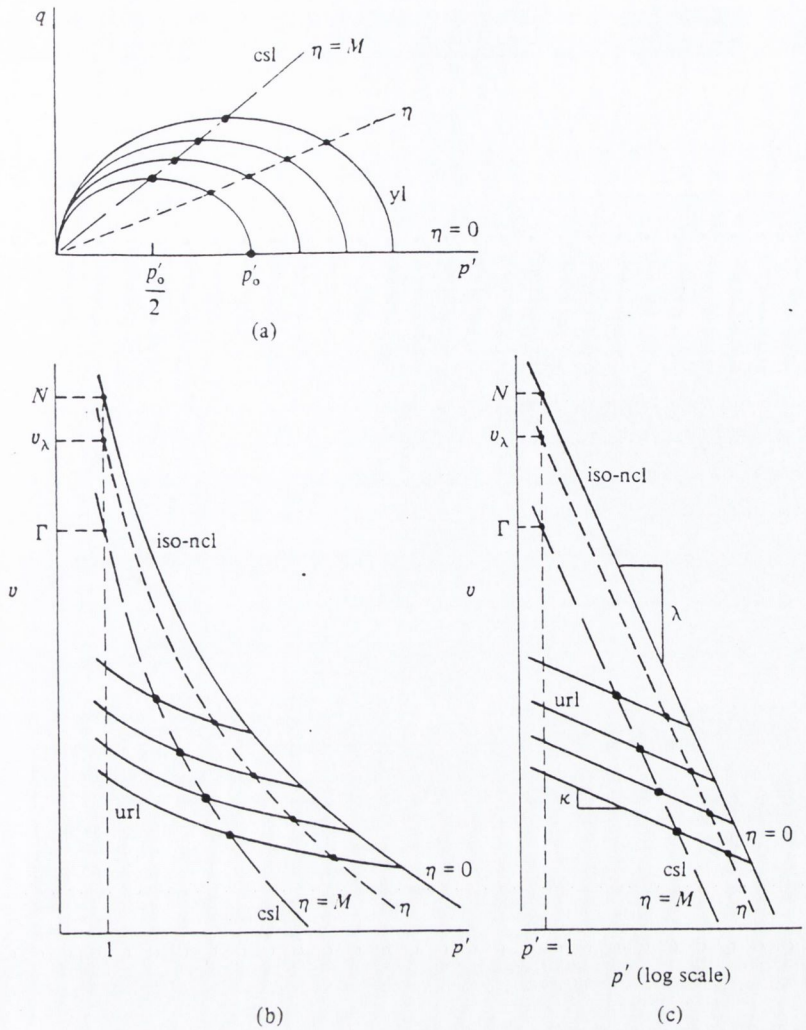

Figure A5. (a) Elliptical yield locus and critical state line (csl) in p':q plane; (b), (c) normal compression line (ncl), unloading-reloading line (url) and csl in compression plane (after Muir Wood (1990).

$$\frac{\delta\varepsilon_p^{\mathrm{p}}}{\delta\varepsilon_q^{\mathrm{p}}} = \frac{M^2\left(2p' - p'_{\mathrm{o}}\right)}{2q} \tag{A.21}$$

The flow rule governs the ratio of the plastic strain increments (i.e., their direction) but does not give their magnitude, which is given by the hardening law. For clay this is obtained from the volumetric strains occurring during consolidation:

$$\delta\varepsilon_p^{\mathrm{p}} = \left[(\lambda - \kappa)/\nu\right]\frac{\delta p'_{\mathrm{o}}}{p'_{\mathrm{o}}} \tag{A.22}$$

Hence the elements of the hardening relationship become;

$$\frac{\partial p'_{\mathrm{o}}}{\partial\varepsilon_p^{\mathrm{p}}} = \frac{\nu p'_{\mathrm{o}}}{\lambda - \kappa} \tag{A.23}$$

and:

$$\frac{\partial p'_0}{\partial \varepsilon_q^p} = 0 \tag{A.24}$$

The description of strain in terms of stress for the model is now complete; the elastic stress/strain response can be summarised in the matrix equation;

$$\begin{bmatrix} \varepsilon_p^e \\ \varepsilon_q^e \end{bmatrix} = \begin{bmatrix} \kappa/vp' & 0 \\ 0 & 1/3G \end{bmatrix} \begin{bmatrix} \delta p' \\ \delta q \end{bmatrix} \tag{A.25}$$

and the plastic stress/strain response can be summarised as,

$$\begin{bmatrix} \delta\varepsilon_p^p \\ \delta\varepsilon_q^p \end{bmatrix} = \frac{(\lambda-\kappa)}{vp'\left(M^2+\eta^2\right)} \begin{bmatrix} \left(M^2-\eta^2\right) & 2\eta \\ 2\eta & 4\eta^2/\left(M^2-\eta^2\right) \end{bmatrix} \begin{bmatrix} \delta p' \\ \delta q \end{bmatrix} \tag{A.26}$$

where $\eta = q/p'$.

Equation A.26 operates only if plastic strains are occurring. It is necessary, therefore, to determine if plastic stresses occur for a given stress path. Consider the soil element at an initial stress state $A(p':q)$, in Figure A6, and a current yield locus defined by a current value of $p'_o = p'_{oA}$. Increments of effective stress $AB(\delta p', \delta q)$ are imposed, giving the new yield locus $p'_o = p'_{oB}$. If the new stress state $B(p':q)$ causes the yield locus to expand (i.e., $p'_{oB} > p'_{oA}$), then plastic strains are occurring. However, if $p'_{oB} < p'_{oA}$, then the new stress state lies inside the current yield locus so only elastic strains occur and the yield locus does not change in size. The procedure can be repeated for a new stress increment using a new current value of p'_o if the yield locus was expanded on the previous increment.

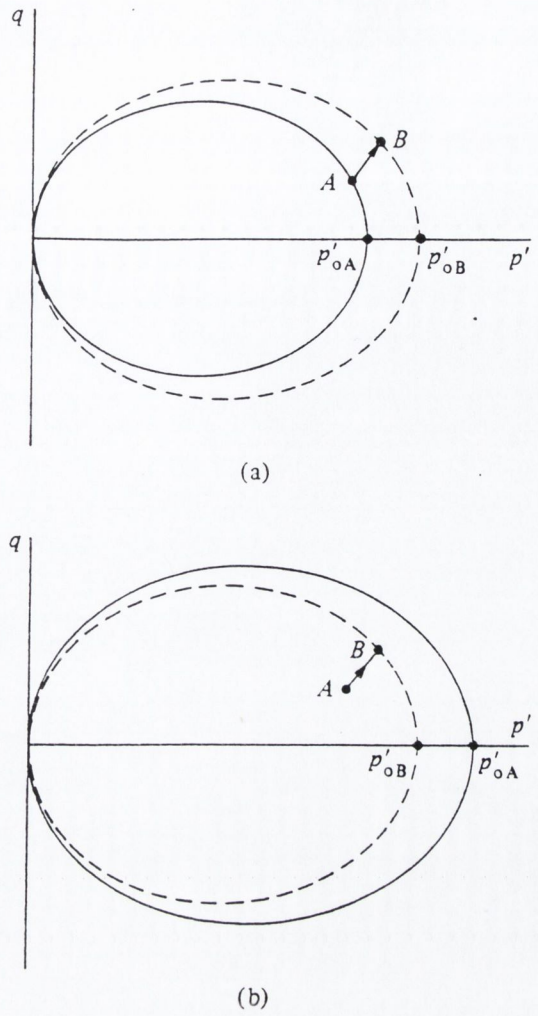

Figure A6. Stress increment expanding current yield locus; (b) stress increment inside current yield locus (after Muir Wood (1990)

A4 APPLICATION OF THE MODIFIED CAM-CLAY MODEL TO STRESS PATH PROBLEMS

A4.1 Outline

The Modified Cam-clay model is typically applied to situations where a stress path is applied to the soil. The application of the model to situations which are dictated by the strains rather than applied stresses, such as in the expansion of a cavity are discussed later in Section A5. In this section the soil model is applied to conventional triaxial conditions, which allows the model results to be verified with published solutions, such as those by Muir Wood (1990), and also served to further the understanding of this author. The MCC model was applied on a spreadsheet program to conditions of conventional drained and undrained triaxial tests, in which stress paths were applied and the resulting strains calculated.

A4.2 Conventional Drained Triaxial Compression

The MCC model was applied first to drained conditions in a conventional triaxial compression test. This type of drained test is constrained by its stress path in the $p':q$ plane, which, if the cell pressure is kept constant, is defined by:

$$\delta q = 3\delta p' = 3\delta p \tag{A.27}$$

A typical increment of loading BC in a drained compression test is shown in Figure A7. The increment starts from a stress state B lying on the current yield locus which has a preconsolidation pressure of p'_{oB}. The stress increment BC then enlarges the yield locus to yl C with preconsolidation pressure p'_{oC}. The change in volume from B to C is made up of a recoverable elastic part, resulting from the change in p', and an irrecoverable plastic part resulting from the expansion of the yield locus. This is represented by the vertical separation δv^p_{BC} of the unloading-reloading lines url B and url C in the compression plane. This irrecoverable change in volume can be expressed as plastic volumetric strain by the expression:

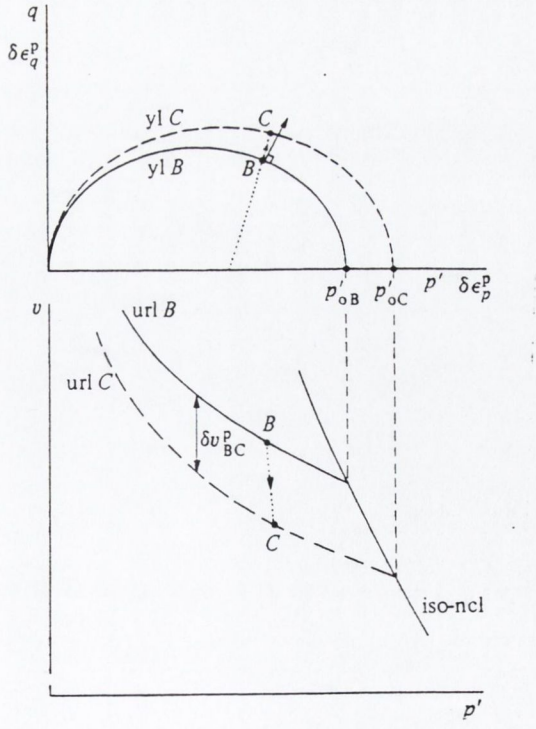

Figure A7. Stress increment in conventional drained triaxial compression test; $\delta q = 3\delta p'$ (after Muir Wood, 1990)

$$\delta\varepsilon^{p}_{pBC} = \frac{v^{p}_{C} - v^{p}_{B}}{v_{B}} \tag{A.28}$$

As further increments of drained compression are applied, *CD*, *DE* and *EF* in Figure A8 the yield locus becomes progressively larger. This continues until the stress state reaches point *F* on the critical state line ($\eta = M$). At this point unlimited plastic shear strains develop with no plastic volumetric strain and the yield locus yl *F* remains of constant size, $\delta p'_{o} = 0$.

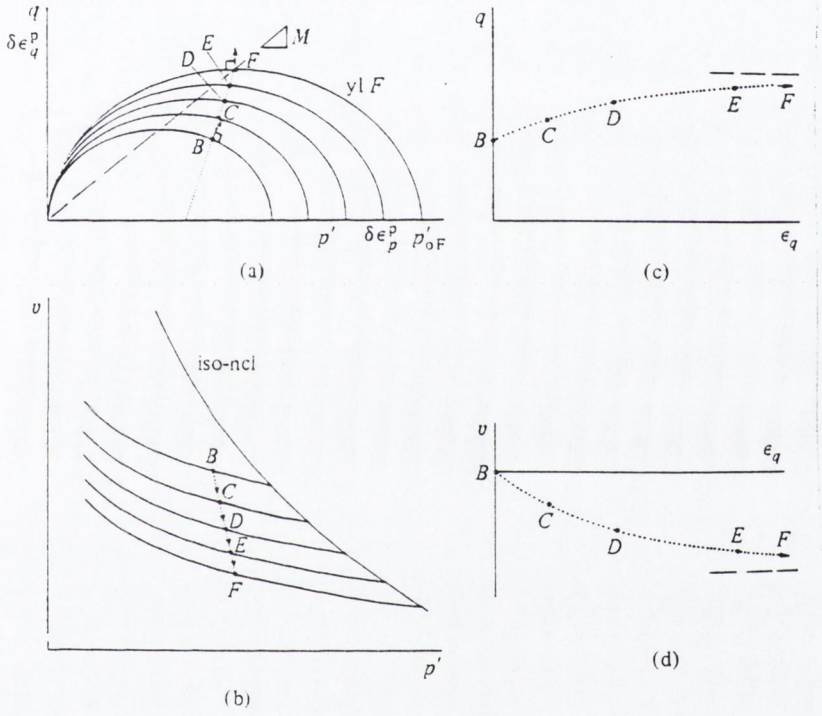

Figure A8. Sequence of stress increments in drained triaxial compression test; (a) p':q effective stress plane; (b) v:p' compression plane; (c) q:ε_q stress:strain plot; (d) v:ε_q volume:strain plot

The conditions imposed by a drained compression test have been applied to a numerical model of the MCC in an MS Excel spreadsheet program. For a given initial stress state p'_i:q_i, the stress path was described by the p':q relationship in (A27) and the yield point was found by combining the equation of the yield curve (A.20), which can be re-written as;

$$p' + q^2 / M^2 - p'_{o}\, p' = 0 \tag{A.29}$$

with the equation of the stress path:

$$3(p'-p'_i)-(q-q_i)=0 \tag{A.30}$$

The combination of equations (A.29) and (A.30) gives a quadratic equation in the form

$$ap'^2+bp'+c=0 \tag{A.31}$$

where

$$a=M^2+9; \qquad b=6q_i-18p'_i-M^2p'_{oi}; \qquad c=(q_i-3p'_i)^2$$

and the solution of the quadratic for the mean effective yield stress is given by:

$$p'_y=\frac{-b+\sqrt{b^2-4ac}}{2a} \tag{A.32}$$

The deviator stress at yield is found by rearranging equation (A.29) to give:

$$q_y=M\sqrt{p'_y\,p'_{oi}-p'^2_y} \tag{A.33}$$

This allows the increment of elastic deviator stress δq^e to be found:

$$\delta q^e=q_y-q_i \tag{A.34}$$

Once the yield point has been reached the stress path is then controlled by incremental changes in deviator stress, δq. The direction of this change (i.e., the sign of δq) depends on where the yield stress state is in relation to the critical state. The MCC model has been applied to two situations for drained conditions, that of lightly overconsolidated and heavily overconsolidated clays.

(a) *Lightly Overconsolidated*

The results from the spreadsheet model for the loading to failure (critical state) of a drained, lightly overconsolidated soil are shown below in Figure A9. The model applied the geotechnical properties of Boston Blue Clay, as described by Bishop and Henkel (1957); $\lambda=0.15$, $\kappa=0.03$ $\Gamma=2.744$, $M=1.2$ and $G=3000$ kPa. The soil was isotropically compressed to 45kPa ($p'=p'_{oB}$) and then isotropically unloaded to 30kPa which became the initial stress state (A) for triaxial loading. Within the yield surface the stresses are elastic only. Therefore, the stress path between A and B (which is on the current yield surface) remains on the unloading-reloading line. Point B lies to the right of the top of the

yield locus, i.e. $p' > p'_{oB}/2$. Further loading expands the yield surface and increases the deviator stress until the critical state at C is reached. Correspondingly, the loading results in increases in the shear strain, ε_q, and the volumetric strain, ε_p, thus reducing the specific volume v as the soil drains.

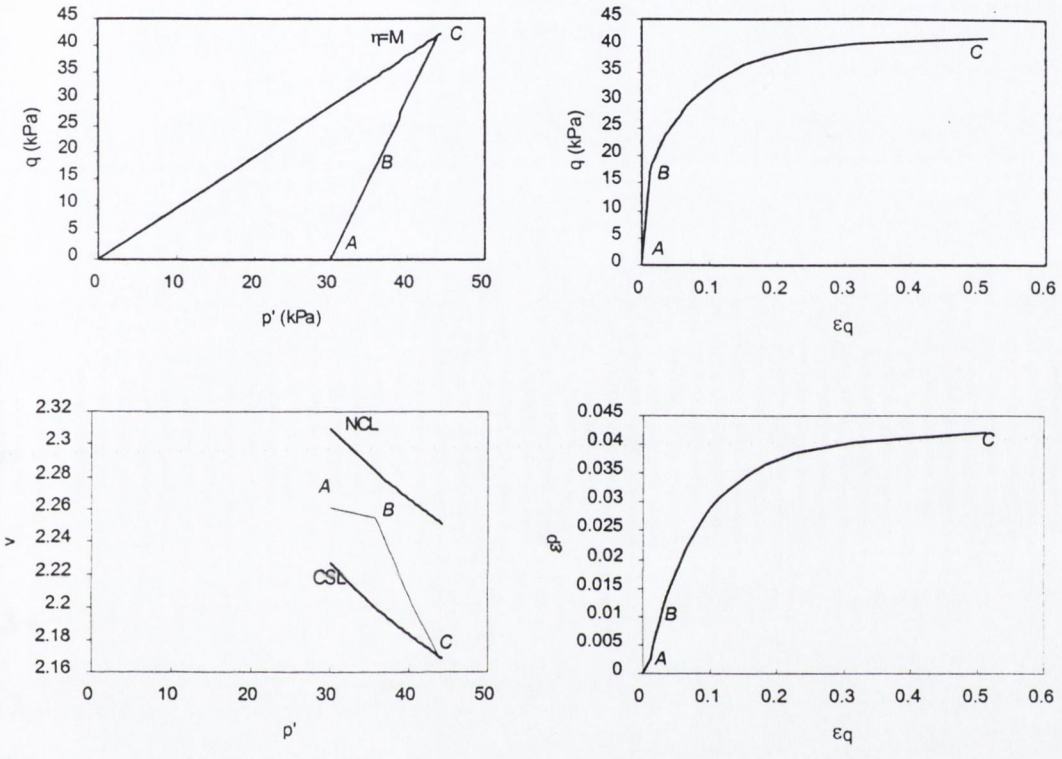

Figure A9. Modified Cam-clay spreadsheet model results for a conventional drained triaxial compression test on a lightly overconsolidated clay (OCR = 1.5)

(b) *Heavily Overconsolidated*

The spreadsheet results for drained heavily overconsolidated compression are shown in Figure A10. In the heavily overconsolidated case the drained compressive response is elastic until point B is reached. This point lies to the left of the top of the yield locus (i.e., $p' < p'_{oB}/2$) and further loading is seen to contract the yield locus and reduce the deviator stress. The increasing shear strain also produces an increase in the specific volume. The q:p' stress state thus moves back down along the stress path until the critical state at C is reached, where there is infinite shear strain.

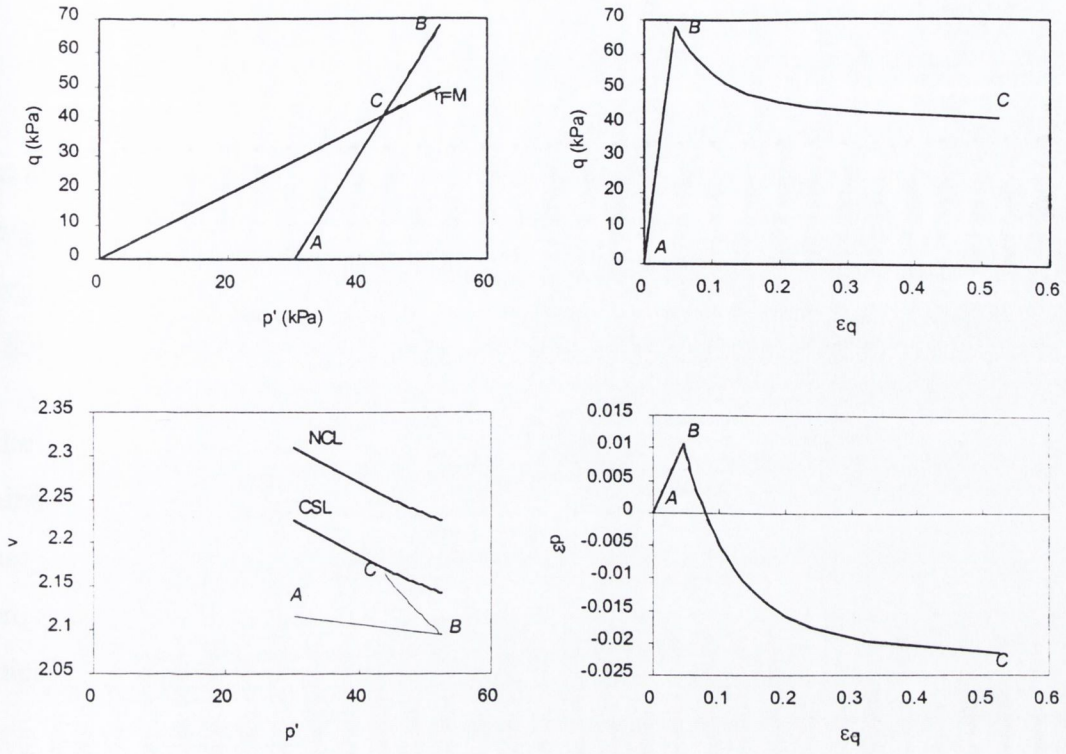

Figure A10. Modified Cam-clay spreadsheet model results for a conventional drained triaxial compression test on a heavily overconsolidated clay (OCR = 5)

A4.3 Conventional Undrained Triaxial Compression

The MCC model is applied here to undrained conditions, and in this case the elastic and plastic volumetric strains must balance each other to give a zero net change in the total volume. The elastic volumetric strain is given by;

$$\delta\varepsilon_p^e = \kappa \frac{\delta p'}{vp'} \tag{A.35}$$

and the plastic volumetric strain increment is:

$$\delta\varepsilon_p^p = (\lambda - \kappa)\frac{\delta p'_o}{vp'_o} \tag{A.36}$$

Since conditions are undrained, there is no change in volume, thus:

$$\delta\varepsilon_p^e + \delta\varepsilon_p^p = 0 \tag{A.37}$$

By combining (A.35) and (A.36) into (A.37) we get:

$$\kappa \frac{\delta p'}{p'} = -(\lambda - \kappa) \frac{\delta p'_o}{\delta p'_o} \tag{A.38}$$

Equation (A.38) gives a link between the change in mean effective stress, $\delta p'$ and the change in the size of the yield locus, $\delta p'_o$. The stress path is controlled by incremental changes in p' and any changes in the deviator stress can then be found from the equation for the yield locus given in (A.29).

If the effective stress state lies inside the current yield surface there can be no plastic strains and, therefore, the only way (A.37) can be satisfied is for the elastic volumetric strain also to be zero. Consequently, from (A.35), in an undrained test there can be no change in the mean effective stress for elastic loading, i.e., the effective stress path rises vertically until the current yield surface is reached (*AB* in Figure A11).

(a) *Lightly Overconsolidated*

The results from the numerical model for undrained compression on a lightly overconsolidated soil are shown in Figure A11. If the soil is in a stress state at yield conditions, where $\eta < M$, (point *B* in Figure A11) as is the case for a lightly overconsolidated soil, the soil wants to harden plastically and the current yield locus must therefore increase in size, $\delta p' > 0$. Thus, the mean effective stress must fall and the effective stress path moves to the left with decreasing p' until critical state is reached at point *C*.

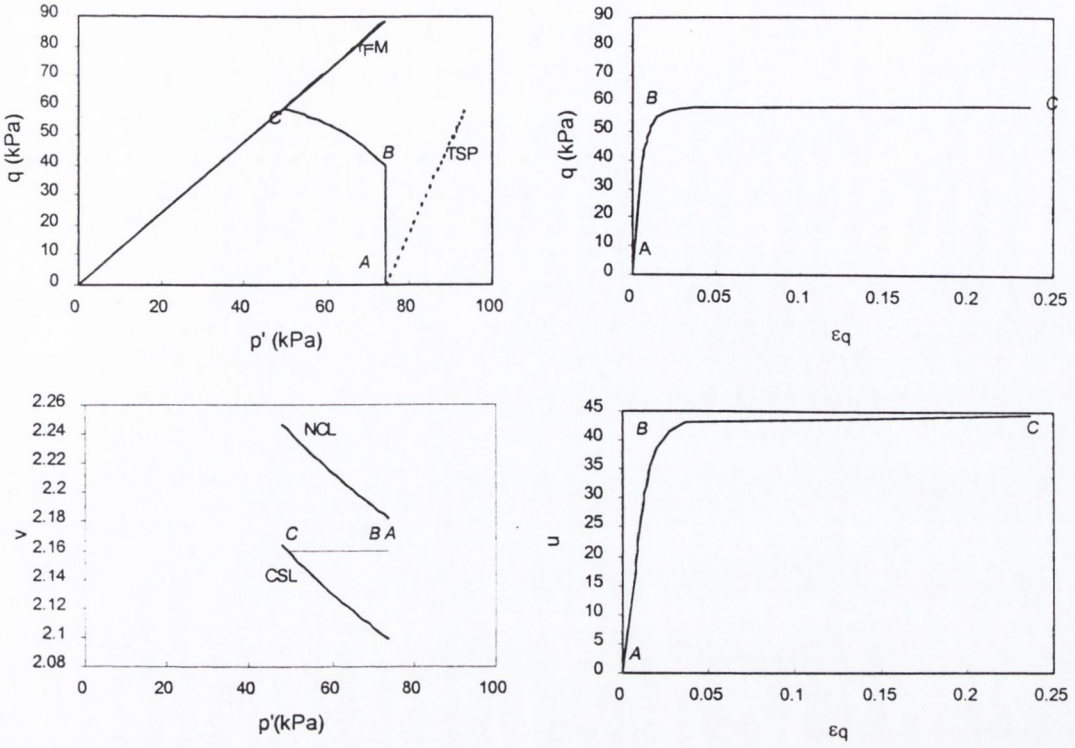

Figure A11. Modified Cam-clay spreadsheet model results for a conventional undrained triaxial compression test on a lightly overconsolidated clay (OCR = 1.2)

(b) *Heavily Overconsolidated*

The results from the numerical model for undrained compression on a heavily overconsolidated soil are shown in Figure A12. If the undrained increment of deformation is being applied at yield conditions with $\eta > M$ as in Figure A12 at point B, the soil wants to soften plastically and therefore the current yield locus must decrease in size, $\delta p' < 0$. Correspondingly the mean effective stress must rise and the stress path moves to the right with increasing p' until critical state at point C is reached.

If the undrained increment of deformation is being applied at the top of the yield locus with $\eta = M$ then the yielding takes place with a plastic strain increment directed parallel to the q-axis, implying zero plastic volumetric strain ($\delta\varepsilon_p^p = 0$). Shearing continues indefinitely without change in the size of the yield locus ($\delta p'_o = 0$), therefore the stress ratio $\eta = M$ acts as a limit to the undrained effective stress path which cannot pass through this particular stress ratio, though can approach it from either direction.

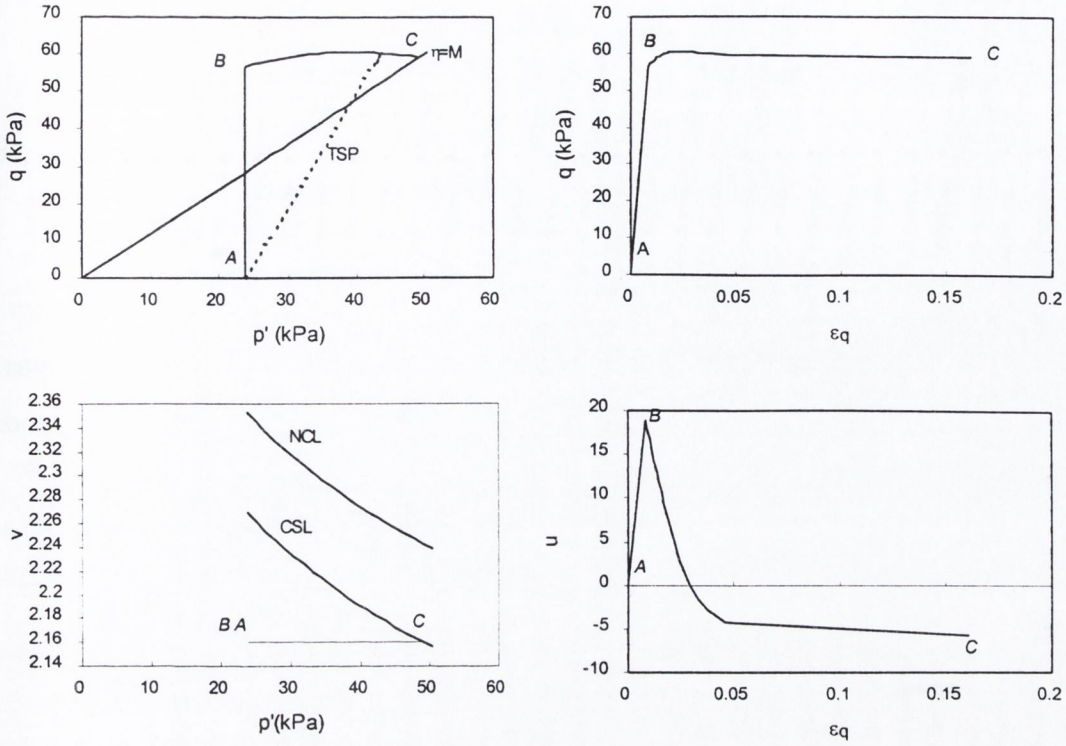

Figure A12. Modified Cam-clay spreadsheet model results for a conventional undrained triaxial compression test on a heavily overconsolidated clay (OCR = 5)

A5 APPLICATION OF THE MODIFIED CAM-CLAY MODEL TO PLANE STRAIN CONDITIONS

A5.1 Outline

The expansion of a cylindrical cavity gives a different set of conditions than the conventional triaxial conditions to which Modified Cam-Clay model is most often applied. The model must therefore be adjusted to plane strain rather than isotropic conditions and, therefore, new forms of expression have been found for the volumetric and distortional stresses and strains. The results from the MCC model applied on a spreadsheet to strain paths defined by cavity expansion are presented here.

A5.2 Expressions For Radial and Circumferential Stress And Strain

The general form of expression for stress (p':q) were given in (A.16) and (A.27) and similarly the volumetric strain, $\delta\varepsilon_p$, and distortional strain, $\delta\varepsilon_q$, increments can be expressed in general form:

$$\delta\varepsilon_p = \delta\varepsilon_{xx} + \delta\varepsilon_{yy} + \delta\varepsilon_{zz} \tag{A.39}$$

$$\delta\varepsilon_q = \frac{1}{3}\left\{2\left[\left(\delta\varepsilon_{yy} + \delta\varepsilon_{zz}\right)^2 + \left(\delta\varepsilon_{zz} + \delta\varepsilon_{xx}\right)^2 + \left(\delta\varepsilon_{xx} + \delta\varepsilon_{yy}\right)^2\right] + 3\left(\delta\gamma_{yz}^2 + \delta\gamma_{zx}^2 + \delta\gamma_{xy}^2\right)\right\}^{\frac{1}{2}} \tag{A.40}$$

For cylindrical cavity expansion the z-axis is considered to be the out of plane direction, the radial stress to be the major principal stress and the circumferential stress to be the minor principal stress. Thus from (A.16) and (A.17) we get:

$$p' = \frac{1}{3}\left(\sigma'_r + \sigma'_\theta + \sigma'_z\right) \tag{A.41}$$

$$q = \sqrt{\left[\frac{1}{2}\left\{\left(\sigma'_r - \sigma'_\theta\right)^2 + \left(\sigma'_\theta - \sigma'_z\right)^2 + \left(\sigma'_z - \sigma'_r\right)^2\right\}\right]} \tag{A.42}$$

The major and minor principal strain directions are the same as for the stresses, although there is no strain in the z-direction, therefore, equations (A.39) and (A.40) become:

$$\delta\varepsilon_p = \delta\varepsilon_r + \delta\varepsilon_\theta \tag{A.43}$$

$$\delta\varepsilon_q = \frac{2}{3}\left(\delta\varepsilon_r - \delta\varepsilon_\theta\right) \tag{A.44}$$

A5.4 Converting Strains To Stresses

It was necessary to adapt the MCC model to allow the stress response of the soil to be found for predefined strain paths, i.e., cavity expansion or SPM strain results. This section presents the expressions required to describe the stress responses to changes in strain.

When the strains are elastic it is a relatively simple operation to reorder equations (A.18) and (A.19) to find the elastic mean effective and deviator stresses. Thus from (A.19) and (A.44);

$$\delta q_e = 3G\delta\varepsilon_q^e = 2G(\delta\varepsilon_r - \delta\varepsilon_\theta) \tag{A.44}$$

For elastic strains there is no change in the mean effective stress, i.e., $\delta p' = 0$.

The plastic stress-strain relationship was summarised in matrix form in (A.26), and this equation only operates if plastic strains are occurring, i.e., when the yield conditions have been met. The yield envelope is described by equation (A.20) and by rearrangement of the expression for deviatoric stress at yield (A.29), q_y can found from;

$$q_y = \left[M^2\left(p'_i\, p'_{oi} - p'^2_i\right)\right]^{\frac{1}{2}} \tag{A.46}$$

where the subscript i denotes initial soil conditions. To find the deviatoric strain at which plastic strains start to occur the range of elastic deviatoric stresses must first be found. This is given by the difference between the deviatoric stress at yield and the initial stress condition:

$$\varepsilon_{q(yield)} = \frac{q_y - q_i}{3G} \tag{A.47}$$

Once the yield conditions have been met the stresses are found using the plastic stress-strain relationship. The plastic stress-strain equations need to be arranged so that the incremental stresses δp and δq can be solved from the changes in strain. The matrix in (A.26) can be simplified to give;

$$\begin{bmatrix} \delta\varepsilon_p^p \\ \delta\varepsilon_q^p \end{bmatrix} = \begin{bmatrix} C_1 & C_2 \\ C_2 & C_3 \end{bmatrix} \begin{bmatrix} \delta p' \\ \delta q \end{bmatrix} \tag{A.48}$$

where:

$$C_1 = \frac{(\lambda-\kappa)\left(M^2-\eta^2\right)}{vp'\left(M^2+\eta^2\right)}; \qquad C_2 = \frac{(\lambda-\kappa)2\eta}{vp'\left(M^2+\eta^2\right)}; \quad C_3 = \frac{(\lambda-\kappa)4\eta^2}{vp'\left(M^2+\eta^2\right)\left(M^2-\eta^2\right)} \tag{A.49}$$

Multiplying out this simplified matrix gives two expressions for volumetric and deviatoric strain:

$$\delta\varepsilon_p^p = C_1\delta p' + C_2\delta q \tag{A.50}$$

$$\delta\varepsilon_q^p = C_2\delta p' + C_3\delta q \tag{A.51}$$

In undrained conditions the overall change in volume is zero since the elastic and plastic volumetric strains are equal and opposite. Therefore, equation (A.50) can be combined with (A.38) to become;

$$(C_1 + C_4)\delta p' + C_2 \delta q = 0 \tag{A.52}$$

where,

$$C_4 = \frac{\kappa}{vp'} \tag{A.53}$$

for elastic strain. By solving (A.51) and (A.52) as a simultaneous equation, the values for mean effective and deviatoric stress increments can be found:

$$\delta p' = \frac{C_2}{C_2^2 - C_3(C_1 + C_4)} \delta \varepsilon_q^p \tag{A.54}$$

$$\delta q = -\frac{C_1 + C_4}{C_2} \delta p' \tag{A.55}$$

The changes in stress given by (A.54) and (A.55) are calculated from the plastic deviatoric strain. However, cavity expansion gives total strains so the elastic component must be separated out in the calculation of plastic stresses. The total deviatoric strain is given by the expressions;

$$\delta \varepsilon_q^T = \delta \varepsilon_q^e + \delta \varepsilon_q^p \tag{A.56}$$

and:

$$\delta \varepsilon_q^T = \frac{2}{3}(\delta \varepsilon_r - \delta \varepsilon_\theta) \tag{A.57}$$

The plastic deviatoric strain can, therefore, be found from:

$$\delta \varepsilon_q^p = \frac{2}{3}(\delta \varepsilon_r - \delta \varepsilon_\theta) - \frac{\delta q}{3G} \tag{A.58}$$

The elastic component of strain is dependant on the incremental change in deviatoric stress as shown in equation (A.18). This means the calculation becomes an iterative procedure as successive 'new' elastic strains are put back into equation (A.58) until a final plastic strain

increment is converged upon. This plastic part of the total strain increment is the permanent strain left should the stress increment be unloaded. When the deviatoric and mean effective stresses have been found the next step is to calculate the radial, circumferential and vertical stresses for each strain increment. This is done by rearranging equations (A.40) and (A.42) to give the following expressions for the radial, circumferential and vertical stress increments:

$$\delta\sigma'_r = \delta p' + \frac{1}{\sqrt{3}}\delta q \tag{A.59}$$

$$\delta\sigma'_\theta = \delta\sigma'_r - \frac{1}{\sqrt{3}}\delta q \tag{A.60}$$

$$\delta\sigma'_z = \frac{1}{2}\left(\delta\sigma'_r + \delta\sigma'_\theta\right) \tag{A.61}$$

The change in pore pressure and hence the total stresses can be found from;

$$\delta u = -\left(\frac{\delta\sigma'_r}{\delta r} + \frac{\sigma'_{r_{avg}} - \sigma'_{\theta_{avg}}}{r_{avg}}\right)\delta r \tag{A.62}$$

If the case of purely elastic cavity expansion is considered, or for soil experiencing elastic straining only, then;

$$\delta\varepsilon_r^e = -\delta\varepsilon_\theta^e \tag{A.63}$$

this gives elastic volumetric strain as:

$$\delta\varepsilon_p^e = 0 \tag{A.64}$$

Therefore, for purely elastic straining in the soil no excess pore pressure is expected to develop.

A5.5 Application Of MCC To A Specific Cavity Expansion Problem

The theory developed in A5.4 has been applied here to the problem of cylindrical cavity expansion in undrained conditions using the Modified Cam-clay soil model.

In this analysis the soil was considered to be initially one dimensionally consolidated, with K_0 = 0.55, and then allowed to swell back after removal of the overburden stress. Two different initial ground conditions were considered prior to cavity expansion. The first case corresponded to a normally consolidated conditions and in the second an overconsolidation ratio of eight was applied (defined as the ratio of the past maximum effective vertical stress σ'_{vmax} to the in situ vertical effective stress σ'_{vi}). In both cases the void ratio, e, before cavity expansion took place was 1.16. A unique value was taken for the voids ratio so that all soils would have the same initial undrained shear strength, making comparison between them easier.

The initial stress states for normally consolidated conditions were found from:

$$p'_i = \frac{1}{3}\sigma'_{vi}\left(1+2K_0\right) \tag{A.65}$$

$$q_i = \sigma'_{vi}\left(1-K_0\right) \tag{A.66}$$

For isotropic conditions the initial preconsolidation pressure can be found from:

$$p'_{oi} = n_p p'_i \tag{A.67}$$

The isotropic overconsolidation ratio is given by;

$$n_p = n\frac{1+2K_{0nc}}{1+2K_0} \tag{A.68}$$

where, n is the conventional overconsolidation ratio given by $\sigma'_{vmax}/\sigma'_{vi}$, and K_{0nc} is the earth pressure coefficient for normally consolidated soil.

Once the soil history and initial stress conditions have been found the MCC model, adapted for cylindrical cavity expansion, can be applied. The results shown on the following pages are normalised in terms of the undrained shear strength c_U. In a conventional triaxial test $\sigma_2' = \sigma_3'$, therefore the undrained shear strength is given by $c_U = ½(\sigma_1' - \sigma_3') = q_f/2$. In undrained plane strain conditions the intermediate principal stress will be equal to the average of the major and minor principal stresses and thus $c_U = ½(\sigma_1' - \sigma_3') = q_f/\sqrt{3}$.

Note that in undrained cylindrical cavity expansion all the elements of the soil mass are subjected to deformations which are similar in mode but only differ in magnitude. This means that all the soil elements have the same stress-strain response, and that elements at different radii have reached different points along an identical stress-strain curve.

The normalised radial and circumferential stress distributions around a cavity expanded to a radius, R, are shown in Figure A13 & A14 for OCRs of 1 & 8, respectively. These stress distributions show a close comparison with those presented by Randolph *et. al.* (1979).

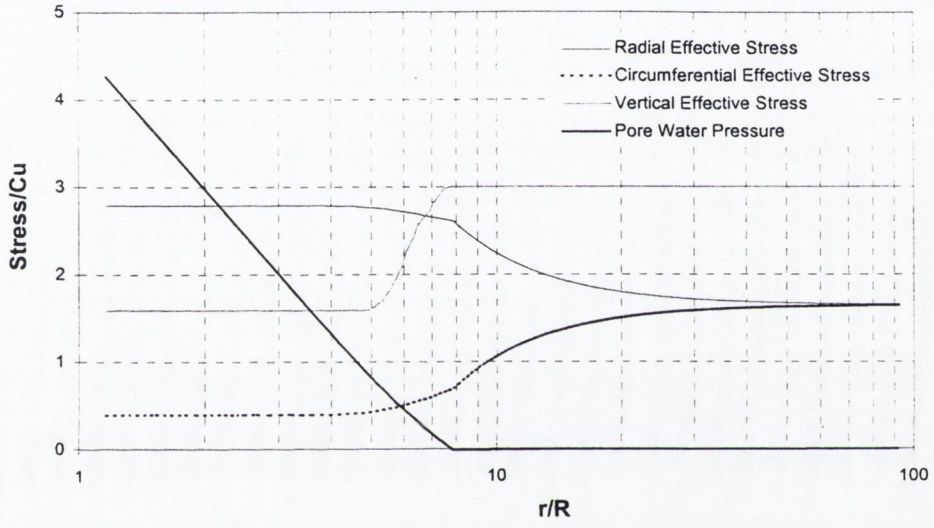

Figure A13. Stress distributions in the soil around a cylindrical cavity expansion, for OCR = 1

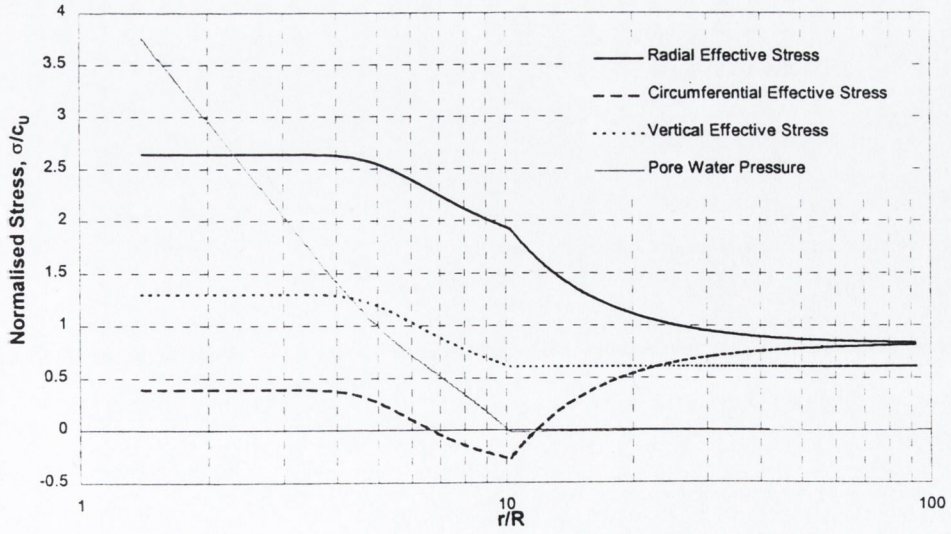

Figure A14. Stress distributions in the soil around a cylindrical cavity expansion, for OCR = 8

The radial displacement data (δr/R) at z/R = 5 & 20 from the model penetrometer tests, presented in Figure 7.10, have been applied to the MCC model. The stress distributions for z/R = 5 shown in Figure A15 use the same soil properties as the cylindrical cavity expansion solution for OCR = 8 shown in Figure A14.

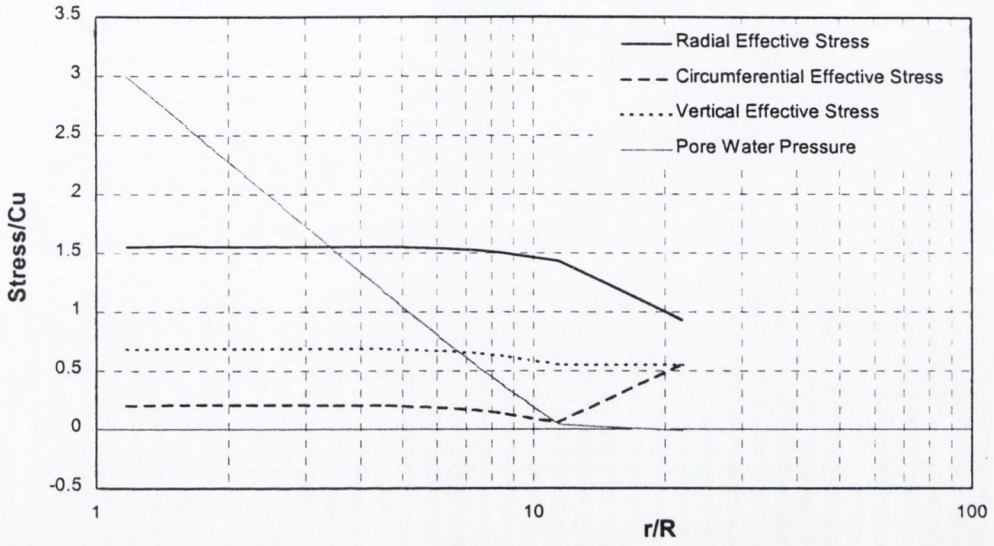

Figure A15. Stress distributions in the soil around the model pile at z/R = 5, for OCR = 8

Further work will be required to apply the MCC or more sophisticated soil models (e.g., MIT-E3) to the measurement displacement paths. In particular this will require (a) extension to two dimensions and (b) correct modelling of stress history (e.g., reversals in strain increment directions).

APPENDIX B
APPLICATION OF SPM TO ANSYS FLOW RESULTS

Appendix B

B. APPLICATION OF SPM TO ANSYS FLOW RESULTS

B1 INTRODUCTION

A description is given here of the complete procedure for finding a SPM solution from the ANSYS flow results. The calculations for strains and displacements were performed in a spreadsheet program (MS Excel), although before this could be done it was necessary to convert the output data from ANSYS into a format compatible with Excel. This was achieved with a simple conversion program (written in FORTRAN) which removed any text and converted the data into a single list of nodal properties. The next step was to calculate interpolation constants for each node in the mesh and this was done in Excel with a macro program. Streamlines could subsequently be interpolated through the grid and the strain rates and strains evaluated along their length. The FORTRAN and Visual Basic macro programs used in all these steps are included here.

It was found that errors existed in some stream function values given in the ANSYS flow solutions. The problem lay in the sequence of meshing which affected the stream function values at some nodes between 'mesh areas'. These errors, although relatively small, affected the streamline interpolation process. The problem and the steps taken to solve it are described in Section B.6.

B2 CONVERSION OF ANSYS RESULTS FILES

The ANSYS results used in this Thesis were the velocity and stream function values at each node in the finite element mesh. The nodal results files from ANSYS are not suitable for direct importation into Microsoft Excel (where the SPM calculations are performed) due to the presence of text separating the numerical data. This is evident in the sample of the results files from ANSYS shown here. They consist of three separate files for the nodal co-ordinates, velocities and stream function values. It is necessary to remove all text from data files and to combine all the data into a single file containing all the output data for a particular flow solution, which was done with a simple FORTRAN program (rspm.for).

Each of the data files must be edited (in the MS DOS editor) so they can be read by the FORTRAN program. The three digits '0 0 0' (with the spaces) have been chosen to identify the end of each block of numbers and must be typed in manually. This allows the program to skip the text before the next block of numbers.

Sample Nodal Co-ordinate File

```
 LIST ALL SELECTED NODES.  DSYS= 0

  NODE      X       Y       Z      THXY   THYZ   THZX
    1   .00000   .00000   .00000     .00    .00    .00
    2   30.000   .00000   .00000     .00    .00    .00
    3   .18126   .00000   .00000     .00    .00    .00
...
   19   7.3712   .00000   .00000     .00    .00    .00
   20   8.2919   .00000   .00000     .00    .00    .00
    0 0 0
  NODE      X       Y       Z      THXY   THYZ   THZX
   21   9.3051   .00000   .00000     .00    .00    .00
   22   10.420   .00000   .00000     .00    .00    .00
```

Sample Velocity File

```
 2D RY   169 ITERATIONS   ISOTHERMAL INCOMPRESSIBLE LAMINAR FLOW   .26950E+01

  ***** POST1 NODAL DEGREE OF FREEDOM LISTING *****

  LOAD STEP=    2  SUBSTEP=   10
  TIME=   2.6950     LOAD CASE=  0

  THE FOLLOWING DEGREE OF FREEDOM RESULTS ARE IN GLOBAL COORDINATES

   NODE     VX       VY       VZ       VSUM
     1   .00000    2.0000   .00000    2.0000
     2   .00000    2.0000   .00000    2.0000
     3   .00000    2.0000   .00000    2.0000
...
    33   .00000    2.0000   .00000    2.0000
    34   .00000    2.0000   .00000    2.0000
 0 0 0

  2D RY   169 ITERATIONS   ISOTHERMAL INCOMPRESSIBLE LAMINAR FLOW   .26950E+01

  ***** POST1 NODAL DEGREE OF FREEDOM LISTING *****

  LOAD STEP=    2  SUBSTEP=   10
```

Sample Stream Function File

```
 2D RY    10 ITERATIONS   ISOTHERMAL INCOMPRESSIBLE LAMINAR FLOW   .14207E+01
```

```
 ***** POST1 NODAL DEGREE OF FREEDOM LISTING *****

 LOAD STEP=    1  SUBSTEP=   10
  TIME=   1.4207     LOAD CASE=  0

   NODE     STRM
     37   900.01
     38   900.01
...
     71   133.30
     72   106.20
0 0 0
```

Sample Converted File

```
    1, .0000000E+00, .0000000E+00, .0000000E+00, .2000000E+01, .0000000E+00
    2, .3000000E+02, .0000000E+00, .0000000E+00, .2000000E+01, .9000000E+03
    3, .1812600E+00, .0000000E+00, .0000000E+00, .2000000E+01, .3285400E-01
...
   23, .1164700E+02, .0000000E+00, .0000000E+00, .2000000E+01, .1356400E+03
   24, .1299600E+02, .0000000E+00, .0000000E+00, .2000000E+01, .1689000E+03
```

FORTRAN File Conversion Program

rspm.for

```
$debug
C
C
     dimension x(6000),y(6000)
     character*8 fnode
     character*20 sent
     CHARACTER*14 FVEL
     CHARACTER*14 FCORD
     CHARACTER*14 FLOUT
     CHARACTER*14 FSFN
c
     WRITE(0,7005)
     READ(0,7010)FCORD
     WRITE(0,7000)
     READ(0,7010)FVEL
     WRITE(0,7015)
     READ(0,7010)FSFN
     WRITE(0,7020)
     READ(0,7010)FLOUT
     WRITE(0,7030)
     READ(0,*)NINIT
C
 7000 FORMAT(1X,'Enter name of velocity data file',/)
 7005 format(1x,'Enter name of co-ordinates file',/)
 7015 FORMAT(1X,'Enter name of stream fn. file',/)
 7010 FORMAT(A14)
 7020 FORMAT(1X,'Enter name of csv file',/)
 7030 FORMAT(1X,'Enter the first node no. in file',/)
c----
c Initialise
```

```
c----
      do 800 i=1,6000
      x(i)=0.0
      y(i)=0.0
 800  continue
c
c-----
C read and store co-ordinate values
C-----
      open(1,file=fcord,status='old')
 10   continue
      read(1,500)fnode
      write(0,500)fnode
 500  format(a8)
      if(fnode.eq.'  NODE ')then
 20    read(1,*)in,x(in-ninit+1),y(in-ninit+1)
       if(IN.lt.1)GOTO 10
       GOTO 20
      end if
      if(fnode.eq.'  ENDF ')goto 25
      goto 10
c
 25   continue
      close (1)

      open(5,file=fsfn,status='old')
 11   continue
      read(5,500)fnode
      write(0,500)fnode
      if(fnode.eq.'  NODE')then
 21    read(5,*)in,sf
       if(IN.lt.1)GOTO 11
       GOTO 21
      end if
      if(fnode.eq.'  ENDF ')goto 26
      goto 11
c
 26   continue
      close (5)
c

      open(3,file=fvel,status='old')
      open(2,file=flout,status='new')
c
 30   continue
      read(3,500)fnode
      write(0,500)fnode
      if(fnode.eq.'  NODE')then
 35    read(3,*)in,vx,vy
       if(IN.lt.1)GOTO 30
       WRITE(2,8000)IN,x(in-ninit+1),y(in-ninit+1),vx,vy,sf
       GOTO 35
      end if
      if(fnode.eq.'  ENDF ')goto 100
      goto 30
c
 8000 format(1x,i6,',',e14.7,',',e14.7,',',e14.7,',',
     *e14.7,',',e14.7)
 100  continue
      close (3)
```

```
close (2)
stop
end
```

B3 FINDING INTERPOLATION CONSTANTS

Once the nodal co-ordinates and stream functions values have been imported into MS Excel, it is then possible to calculate the strain rates and strains. Central to the process is the calculation of a set of interpolation constants $\{\alpha\}$ for each node in the grid. The data are first sorted in order of their vertical (z) and then radial (r) grid positions. To maintain consistency between different flow meshes, all the files are cut down in size to 20 nodal points on each row. This has allowed the same calculation procedure to be used for any of the flow solutions.

The macro program 'Matrix' was used to calculate the interpolation constants by performing the matrix operations in equation (3.25). This is done by first finding the local co-ordinates (ξ, η) for each of the eight nodes surrounding the central node in the local mesh (see Figure 3.10). The set of stream function values $\{\psi\}$and local co-ordinate polynomials [M] are laid out in a single row across the spreadsheet for each node in the grid. The matrix problem in (3.25) can then be solved for $\{\alpha\}$.

The macro 'Matrix' which calculates the interpolation constants is shown here and the calculation steps performed can be summarised:

- The M values (0 to 8) are copied into a 9x9 matrix
- The [M] matrix is inverted and then multiplied by the $\{\psi\}$ vector
- The resulting $\{\alpha\}$ values are copied as a 1x9 matrix to the spreadsheet
- Finally the 9x9 [M] matrix is deleted before moving to the next node.

The number of repetitions of this procedure can be specified in the Matrix macro depending on the number of nodes.

```
' Matrix Macro
' Macro recorded 31/10/96
' Calculates interpolation constants, a 0-8 from stream
' function values and M 0-8.
' Start in column EP
'
Sub Matrix()
```

```
Limit = 1250
For n = 1 To Limit
ActiveCell.Offset(0, -100).Range("A1:I1").Select
Selection.Copy
ActiveCell.Offset(0, 90).Range("A1").Select
Selection.PasteSpecial Paste:=xlValues, Operation:=xlNone, _
    SkipBlanks:=False, Transpose:=False
ActiveCell.Offset(0, -80).Range("A1:I1").Select
Application.CutCopyMode = False
Selection.Copy
ActiveCell.Offset(1, 80).Range("A1").Select
Selection.PasteSpecial Paste:=xlValues, Operation:=xlNone, _
    SkipBlanks:=False, Transpose:=False
ActiveCell.Offset(-1, -70).Range("A1:S1").Select

ActiveCell.Range("A1:I1").Select
Application.CutCopyMode = False
Selection.Copy
ActiveCell.Offset(2, 70).Range("A1").Select
Selection.PasteSpecial Paste:=xlValues, Operation:=xlNone, _
    SkipBlanks:=False, Transpose:=False

ActiveCell.Offset(-2, -60).Range("A1:I1").Select
Application.CutCopyMode = False
Selection.Copy
ActiveCell.Offset(3, 60).Range("A1").Select
Selection.PasteSpecial Paste:=xlValues, Operation:=xlNone, _
    SkipBlanks:=False, Transpose:=False
ActiveCell.Offset(-3, -50).Range("A1:I1").Select
Application.CutCopyMode = False
Selection.Copy
ActiveCell.Offset(4, 50).Range("A1").Select
Selection.PasteSpecial Paste:=xlValues, Operation:=xlNone, _
    SkipBlanks:=False, Transpose:=False
ActiveCell.Offset(-4, -40).Range("A1:I1").Select
Application.CutCopyMode = False
Selection.Copy

ActiveCell.Offset(5, 40).Range("A1").Select
Selection.PasteSpecial Paste:=xlValues, Operation:=xlNone, _
    SkipBlanks:=False, Transpose:=False
ActiveCell.Offset(-5, -30).Range("A1:I1").Select
Application.CutCopyMode = False
Selection.Copy
ActiveCell.Offset(6, 30).Range("A1").Select
Selection.PasteSpecial Paste:=xlValues, Operation:=xlNone, _
    SkipBlanks:=False, Transpose:=False

ActiveCell.Offset(-6, -20).Range("A1:I1").Select
Application.CutCopyMode = False
Selection.Copy
ActiveCell.Offset(7, 20).Range("A1").Select
Selection.PasteSpecial Paste:=xlValues, Operation:=xlNone, _
    SkipBlanks:=False, Transpose:=False

ActiveCell.Offset(-7, -10).Range("A1:I1").Select
Application.CutCopyMode = False
Selection.Copy
ActiveCell.Offset(8, 10).Range("A1").Select
Selection.PasteSpecial Paste:=xlValues, Operation:=xlNone, _
```

```
    SkipBlanks:=False, Transpose:=False

  ActiveCell.Offset(-8, 10).Range("A1:I1").Select
  Application.CutCopyMode = False
  Selection.FormulaArray = _
    "=MMULT(RC[-130]:RC[-122],TRANSPOSE(MINVERSE(RC[-10]:R[8]C[-2])))"

  Selection.Copy
  Selection.PasteSpecial Paste:=xlValues, Operation:=xlNone, _
    SkipBlanks:=False, Transpose:=False
  ActiveCell.Offset(0, -10).Range("A1:I1").Select
  Application.CutCopyMode = False
  Selection.ClearContents
  ActiveCell.Offset(1, 10).Range("A1").Select
  Next n
End Sub
```

B4 INTERPOLATING STREAMLINES THROUGH THE GRID

The interpolation constants allow streamline paths (of constant stream function) to be interpolated through the nodal grid. The nodal co-ordinates, stream function values and interpolation constants are copied into a spreadsheet. In this file the nodes and their properties are listed in ascending grid order, first by vertical (z) position then by radial (r) position. Interpolation can then be conducted to find the path of a chosen streamline through the grid. This has been done using the macro 'Interpolate', which searches though the grid points, starting on the bottom horizontal grid row at r = 0 and when the nodes either side of the streamline are found the interpolation calculation is performed (given by equation 3.26). The macro then continues the search for nodes on the next row until the top of the grid is reached. The velocities and strain rates along the flow path are calculated at the same time for each interpolated point along the streamline given by equations (3.29) to (3.34).

```
' Interpolate Macro
' interpolates a streamline between nodal points
' Start in the stream function (ψ) column
'
Sub interpolate()
  ActiveCell.Range("A1").Select
  streamline = Range("U1")
  value1 = ActiveCell.Value
  value2 = ActiveCell.Offset(1, 0).Value
  Limit = 136
  For n = 1 To Limit
    Do Until value1 < streamline And value2 >= streamline
      ActiveCell.Offset(1, 0).Select
      value1 = ActiveCell.Value
      value2 = ActiveCell.Offset(1, 0).Value
    Loop
```

```
'     ActiveCell.Offset(1, 0).Select
' (use if interpolating from outside points)
    ActiveCell.Offset(0, 12).Range("A1").Select

' 1. Calculates radial position
    ActiveCell.FormulaR1C1 = "=(R1C21-RC[-10])/(RC[-9]+RC*RC[-7])"
    ActiveCell.Offset(0, 1).Range("A1").Select
    ActiveCell.FormulaR1C1 = "=RC[-17]+RC[-1]"
    ActiveCell.Offset(0, 1).Range("A1").Select
    ActiveCell.FormulaR1C1 = "=RC[-17]"

' 2. Calculate velocities
    ActiveCell.Offset(0, 1).Range("A1").Select
    ActiveCell.FormulaR1C1 = _
     "=-(1/RC[-2])*(RC[-11]+RC[-9]*RC[-3]+RC[-7]*RC[-3]^2)"
    ActiveCell.Offset(0, 1).Range("A1").Select
    ActiveCell.FormulaR1C1 = _
     "=(1/RC[-3])*(RC[-13]+2*RC[-11]*RC[-4])"
    ActiveCell.Offset(0, 1).Range("A1").Select
    ActiveCell.FormulaR1C1 = "=(RC[-2]^2+RC[-1]^2)^0.5"
    ActiveCell.Offset(0, 1).Range("A1").Select

' 3. Calculate strain rates
    ActiveCell.FormulaR1C1 = _
     "=-(1/RC[-5]^2)*(RC[-14]+RC[-12]*(RC[-6]-RC[-5])+RC[-10]*RC[-6]*(RC[-6]-2*RC[5]))"
    ActiveCell.Offset(0, 1).Range("A1").Select
    ActiveCell.FormulaR1C1 = "=(1/RC[-6])*(RC[-13]+2*RC[-11]*RC[-7])"
    ActiveCell.Offset(0, 1).Range("A1").Select
    ActiveCell.FormulaR1C1 = _
     "=(1/RC[-7]^2)*(RC[-16]+RC[-14]*RC[-8]+RC[-12]*RC[-8]^2)"
    ActiveCell.Offset(0, 1).Range("A1").Select
    ActiveCell.FormulaR1C1 = _
     "=0.5*(1/RC[-8]^2)*(-RC[-18]+2*RC[-16]*(RC[-8]-RC[-9])-2*RC[-14]*RC[-8]-
2*RC[12]*RC[-8]*RC[-9]-2*RC[-11]*RC[-8]*RC[-9]^2)"

' 4. Moves back to stream function column
    ActiveCell.Offset(1, -21).Range("A1").Select
    ActiveCell.Offset(1, 0).Select
    value1 = ActiveCell.Value
    value2 = ActiveCell.Offset(1, 0).Value

  Next n
End Sub
```

B5 DETERMINING STRAINS AND DISPLACEMENTS

The accumulated strain along a streamline is found by integration of the strain rates at each interpolated point. The data from the 'interpolation' macro, including the streamline position, velocities and strain rates, are first grouped together on the spreadsheet to make further calculations more convenient. The macro 'compaction' achieves this by searching through the spreadsheet and copying the data for the interpolated points to the top of the spreadsheet. The

strains and displacements can then be found with the macro 'displacement' which evaluates equations (3.35) to (3.37).

```
' compacting Macro
' Start in the Z-coordinate column, repeat until last grid row
'
'
Sub comp()
   ActiveCell.Range("A1").Select
   ycell = ""
   value1 = ActiveCell.Value
' Loop1
    Limit = 136
    For n = 1 To Limit
    Do Until value1 <> ycell
    ActiveCell.Offset(1, 0).Select
    value1 = ActiveCell.Value
    Loop
' Copy cells
     ActiveCell.Offset(0, 0).Range("A1:J1").Select
     Selection.Copy
     Range("R23").Select
     ActiveCell.Offset(n - 1, 0).Select
     Selection.PasteSpecial Paste:=xlValues, Operation:=xlNone, _
     SkipBlanks:=False, Transpose:=False
      ActiveCell.Offset(1, 0).Select
      ActiveCell.Range("A1").Select
      y2cell = ""
      value3 = ActiveCell.Value
' Loop2
      Limit = 79
      For k = 1 To Limit
      Do Until value3 <> y2cell
      ActiveCell.Offset(1, 0).Select
      value3 = ActiveCell.Value
      Loop

        ActiveCell.Offset(0, 0).Range("A1:J1").Select
        Selection.ClearContents

      Next k

     value1 = ActiveCell.Value
   Next n

 End Sub


' Displacement Macro
' Calculates velocities, strain rates and strains for displacement calculation
' Start in the ε_rz-coordinate column, repeat until last grid row
'
'
Sub displacement()
  ActiveCell.Range("A1").Select
   ycell = ""
   value1 = ActiveCell.Value
   Limit = 136
    For n = 1 To Limit
```

```
    Do Until value1 <> ycell
      ActiveCell.Offset(1, 0).Select
      value1 = ActiveCell.Value
    Loop


' 3. calculate the distance, s between the two streamline points.
    ActiveCell.Offset(0, 1).Range("A1").Select
    ActiveCell.FormulaR1C1 = "=RC[-8]-R[-1]C[-8]"

' 4. calculate the strains from 1,2&3.
    ActiveCell.Offset(0, 1).Range("A1").Select
    ActiveCell.FormulaR1C1 = _
     "=RC[-5]*RC[-1]/((RC[-7]+R[-1]C[-7])/2)+R[-1]C"
    ActiveCell.Offset(0, 1).Range("A1").Select
    ActiveCell.FormulaR1C1 = _
     "=RC[-5]*RC[-2]/((RC[-8]+R[-1]C[-8])/2)+R[-1]C"
    ActiveCell.Offset(0, 1).Range("A1").Select
    ActiveCell.FormulaR1C1 = _
     "=RC[-5]*RC[-3]/((RC[-9]+R[-1]C[-9])/2)+R[-1]C"
    ActiveCell.Offset(0, 1).Range("A1").Select
    ActiveCell.FormulaR1C1 = _
     "=RC[-5]*RC[-4]/((RC[-10]+R[-1]C[-10])/2)+R[-1]C"
    ActiveCell.Offset(0, 1).Range("A1").Select

' 5. calculate the deviatoric strains
    ActiveCell.FormulaR1C1 = "=RC[-3]"
    ActiveCell.Offset(0, 1).Range("A1").Select
    ActiveCell.FormulaR1C1 = "=(RC[-5]-RC[-3])/3^0.5"
    ActiveCell.Offset(0, 1).Range("A1").Select
    ActiveCell.FormulaR1C1 = "=2*RC[-3]/3^0.5"

' 6. Calculates radial and vertical displacement
    ActiveCell.Offset(0, 1).Range("A1").Select
    ActiveCell.FormulaR1C1 = "=(RC[-14]-R8C22)*RC[-8]/R8C22+R[-1]C"
    ActiveCell.Offset(0, 1).Range("A1").Select
    ActiveCell.FormulaR1C1 = "=RC[-18]-R8C19"
    ActiveCell.Offset(0, 1).Range("A1").Select
    ActiveCell.FormulaR1C1 = _
     "=(RC[-16]-R8C22)*(((R[-1]C[-19]-RC[-19])^2+RC[-10]^2)^0.5)/((R[-1]C[-15]+RC[-
15])/2)+R[-1]C"
    ActiveCell.Offset(1, -11).Range("A1").Select
    value1 = ActiveCell.Value
  Next n

End Sub
```

B6 ANSYS STREAM FUNCTION ERROR

It was found that the flow solutions from ANSYS were prone to error in the calculation of stream function values for nodes along horizontal grid rows a short distance behind the cone shoulder, in the case of the 60° cone, and the tip in the case of the flat-ended geometry. The error only appeared in the stream function values (the ANSYS nodal velocities showed no sign of error) and consistently appeared in the same place in the nodal mesh for different solutions.

Shown below in Figure B.1 is a plot of the interpolated path of a streamline (of constant stream function) through the nodal grid. This path is produced by a nine-node interpolation procedure outlined in Chapter 3. This streamline plot shows a clear 'kink' just behind the cone shoulder.

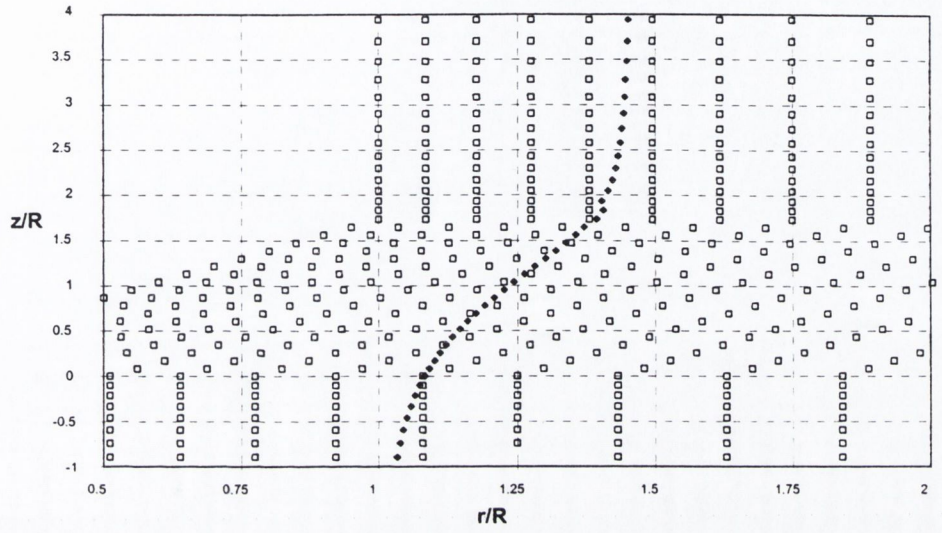

Figure B1 Interpolated streamline through the nodal mesh showing a 'kink' behind cone shoulder

Figure B.2 shows a comparison of the velocities found from the stream function values and those interpolated from the nodal velocities outputted directly from ANSYS. This graph shows that there is no problem with the flow solution in general (and its velocities) but that an error lies in the stream function values produced, which only becomes apparent at the cone shoulder for the calculations of radial velocity .

A consequence of discovering this error was the examination of the nine-node interpolation technique which is used to find streamline paths and also used to find velocities and strains. The investigation, which focused particularly on where the grid was irregular (i.e., not rectilinear), found no problem with the interpolation technique. The focus then turned to the ANSYS stream function results. Correspondence with the ANSYS authors', which led to an investigation by them, found that there was a problem in the calculation of stream function values. In ANSYS the stream function values are derived from the velocities and this calculation is path orientated. It was found that reordering the elements and nodes, which resulted in the stream function integration starting from a different place, provided a

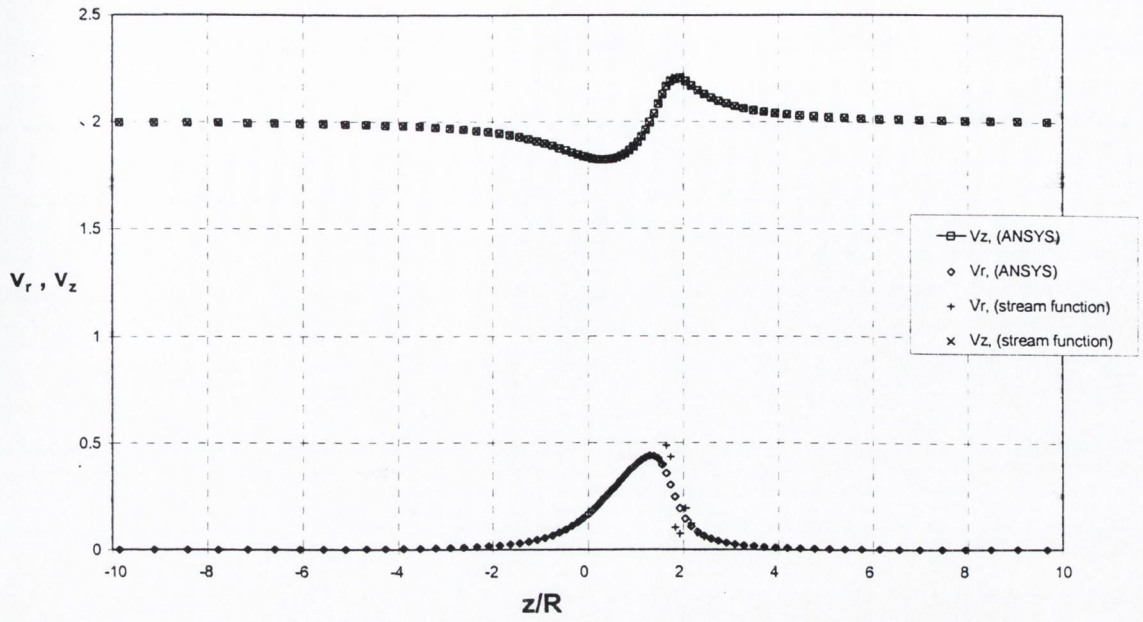

Figure B2. Comparison of radial and vertical velocities; (i) found directly from ANSYS and (ii) derived from the nodal stream function values

solution to the problem. In practical terms this meant the problem did not arise if the flow area was meshed in a particular order. The mesh for the 60° cone is divided by geometry into three areas as shown in Figure B.3 and if the outlet area (1) is meshed first, then the middle section (2) and finally the inlet area (3) there was found to be no significant error in the stream function values.

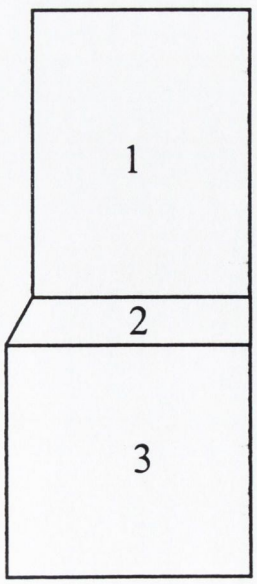

Figure B3. Mesh areas for 60° cone; the 'correct' order of meshing is shown

APPENDIX C
THE VIDEOEXTENSOMETER DOT MEASURING SYSTEM

C. THE VIDEOEXTENSOMETER DOT MEASURING SYSTEM

C1. GENERAL

This Appendix gives a detailed description of the video camera system used in the experiments measuring the soil displacements around model penetrometers (which has been described in Chapter 6). The system components, operation procedures and accuracy capabilities have been described here (note that much of the camera detail has been taken from the Videoextensometer Users Manual, 1997). Two series of tests conducted to determine the resolution of the camera in practice are also presented here.

C2. SYSTEM COMPONENTS

The Videoextensometer system comprises four key components; a video camera, a high precision lens, a 'frame grabber' interface card and a PC. The video camera is monochrome with a high precision CCD (Charged Coupled Device) chip, which comprises photosensitive cells arranged in an accurate grid. A high precision 'zoom' lens allows a wide range of specimen sizes to be covered from any one camera position. The 'frame grabber' interface card is connected into the Videoextensometer controlling PC and linked to the camera via a flexible cable. The card converts the PAL video signal into an 8 bit digital format whilst simultaneously generating a 640×480 pixel image on the colour monitor. The system operates under Windows95 based software.

C3. GENERAL CAMERA OPERATION PROCEDURES

It is important, before any testing is commenced that the recommended set-up procedures are adhered to and the appropriate system configurations, which differ from test to test, are made. These procedures are listed below and ensure that optimum accuracy with the dot measuring system is achieved.

- *Marking the specimen*

  The specimen to be tested is marked with a series of contrasting, approximately round, equal sized targets (up to a maximum of 100) around the area where movement is to be measured. The measurement algorithm used by the Videoextensometer is based on the evaluation of the grey contrast between target and the specimen. In general, the greater this contrast, the more consistent are the results that can be obtained. It is necessary therefore, to have either black targets on a light specimen or white targets on a dark specimen, and they should remain in the view of the camera at all times. Any smudging or distortion of the dot edges will have a detrimental effect on the results.

- *Camera set-up*

  The camera is mounted on a tripod and focused on the specimen. It is important that the distance between the camera and specimen remains constant during testing. Any movement will result in an enlarged or reduced image and an apparent change in the specimen's dimensions. Vibrations which cause small camera or target movement must be reduced to the absolute minimum as they create 'noise' in the results. The camera must be positioned horizontally, since any inclination from the horizontal plane will cause measuring errors; a spirit level is used for this purpose. The camera must also be positioned orthogonal to the target surface, otherwise target movements will be seen at an oblique angle. Finally, correct focusing of the camera is vital to ensure maximum target sharpness.

- *Illumination*

  It is essential for accurate measurement to provide the specimen with illumination that is of adequate, even and constant intensity. It was found that artificial lighting was required to achieve this, masking such effects as changes in sunlight intensity or shadows. The diaphragm of the camera (lens aperture) is adjusted to provide the correct illumination settings, since both over exposure and insufficient illumination are to be avoided. If saturation occurs the discrimination range of the CCD chip is reduced and a reduction in accuracy and increase in signal noise can occur.

- *Calibrating image scale*

  Setting the camera's field of view requires two targets of a known distance apart. All displacement measurements recorded by the camera are scaled to the field of view so it is important this is done as precisely as possible.

- *Data storage*

  The data can be saved onto the hard drive of the PC manually (by clicking on an icon with the mouse) or automatically at a set frequency. If automatic logging is selected but no frequency is set, the data are stored at the maximum possible logging rate (up to 25 Hz), although this depends on the number of targets (dots) the camera is tracking.

- *Smoothing parameter*

  The smoothing parameter is a feature of the system that allows averaging of the measured data, during logging, to reduce the effect of signal 'noise' in the results. The smoothing parameter has two algorithms; a moving average algorithm and regression algorithm. The moving average algorithm produces the average value of the last set of data reads. This setting is recommended for very slow creep or calibration tests. The regression algorithm produces an average value based upon the least-mean-square value of the last set of data reads. The value assigned to the smoothing parameter specifies the number of data reads used to calculate the mean value. The value can be set between 1 and 40 and while setting a high value will result in more stable measurements it may also filter out real non-linear dynamic specimen characteristics.

- *The number of angle divisions*

  When a target (dot) is selected, an active 'box' is placed around it and the dot's position within the box is measured and constantly updated. This is done by a calculation which takes a number of angular divisions across this box and uses them to detect the centre (of area) of the dot. Any integer between 4 and 360 can be entered. The more divisions selected, the greater the accuracy but this also results in a lower sampling frequency due to the increased number of calculations.

C4. ASSESSING VIDEOEXTENSOMETER DOT MEASURING ACCURACY

The theoretical accuracy of the camera is determined from the number of pixels in the image and from grey scale interpolation. The analogue signal from the camera is converted into digital format (8 Bit) giving a 640×480 pixel image. The grey scale level of each pixel is resolved in 256 shades which results in a minimum *theoretical* displacement resolution better than 1:131,073 (17 bit) of the camera field of view.

The digitised camera image and the resulting grey scale values (0-255) of each pixel are stored in a frame buffer. Using the buffer data, it is possible to produce a grey scale (contrast) diagram for every horizontal scan line and for every vertical column of pixels. Due to the vast amounts of data produced by each picture scan (9.2 MB/scan), efficient processing is required to achieve an adequate dynamic response. The Dot Measuring software uses the frame buffer to automatically detect the targets and follow them during testing. This can be done if the targets produce sufficient contrast changes in grey scale. The image data are differentiated to produce distinct peaks and having established the target's differential signature pattern, a zone is defined around these values in the frame buffer so that only data related to these areas are further processed. This value is dynamically adapted throughout the testing process and compensates if the contrast points fade or change shape.

Angular scan lines (up to 360) are selected for each target and the crossover point of each is calculated. A mean value can therefore be obtained and this results in better measurement accuracy, resolution and stability. The manufactures claim that this system allows resolutions far better than the theoretical minimum value of 1:131,073 of the field of view to be achieved.

The resolution of the system, as has been stated previously, is dependent on, amongst other factors, by the number of pixels. The field of view is the image created by the complete 640×480 set of these pixels. The field of view, and how it is set in terms of the specimen being measured, is therefore is a vital consideration as regards accuracy. While the field of view must be large enough to measure the full range target movements, by keeping it to a minimum the accuracy can be improved. This is shown clearly in Table C1 which presents the theoretical minimum resolution for different fields of view.

Table C1. Minimum resolution for different fields of view

Axial Field of View	Minimum Resolution
50 mm	<0.4 μm
250 mm	<2 μm
500mm	<4 μm
1000 mm	<8 μm

C5. DETERMINING CAMERA ACCURACY IN PRACTICE

Two series of simple tests were conducted to determine the accuracy of the Videoextensometer Dot Measuring System in practice, and to find the optimum system set-up, i.e., which settings would give the most accurate results. The first series of tests investigates the influence of the dot measure software options on the measurement results, and the second investigates the accuracy of the camera in test conditions.

Test Series 1.

The objective of the first test series was to find the most accurate camera set up. In these tests, the position of a target (a soil marker as used in the penetrometer tests) was recorded for several hundred readings. This allowed the consistency of the measurements for different set-ups to be assessed. Vibrations and inconsistent illumination are suspected to have resulted in the significant errors that are present in these test results. However, since the objective of this test was to find the best set-up, the magnitudes of the errors are considered of less importance than the relative errors between them. Table C2 shows the standard deviation of error for six tests using different smoothing parameters, angle divisions and camera/target distances. Figure C1 plots the deviation of the camera results about its mean position (0,0) in the x-y plane for the six tests.

The camera-target distance was seen to be of only small significance since the field of view (~100 mm in longest direction) was kept approximately constant using the zoom lens. Since accuracy, and not scanning speed, was of priority in these tests, the lowest number of angle line divisions used was 60 and increasing the number to 360 was seen to have little effect. The choice of smoothing parameter had the greatest effect on the scatter of results, which is evident in Figure C1. The continuous average algorithm is clearly more effective at reducing 'noise' in the results. The optimum set-up found from these tests uses a

continuous average smoothing parameter for the last ten data reads and 360 angle line divisions

Table C2. Comparison of different videoextensometer set-ups

Test No.	Smoothing Parameter (No. of Points Used)	Distance Between Camera And Target (m)	Angle Line Divisions	Camera Error:- Standard Deviation of $\sqrt{\partial x^2 + \partial y^2}$ (mm)
1	Regression (10)	0.3	360	0.03443
2	Regression (5)	1.05	360	0.04563
3	Continuous Average (10)	1.05	360	0.00346
4	Continuous Average (5)	1.05	360	0.00548
5	Continuous Average (10)	0.3	360	0.00320
6	Continuous Average (5)	1.05	60	0.00481

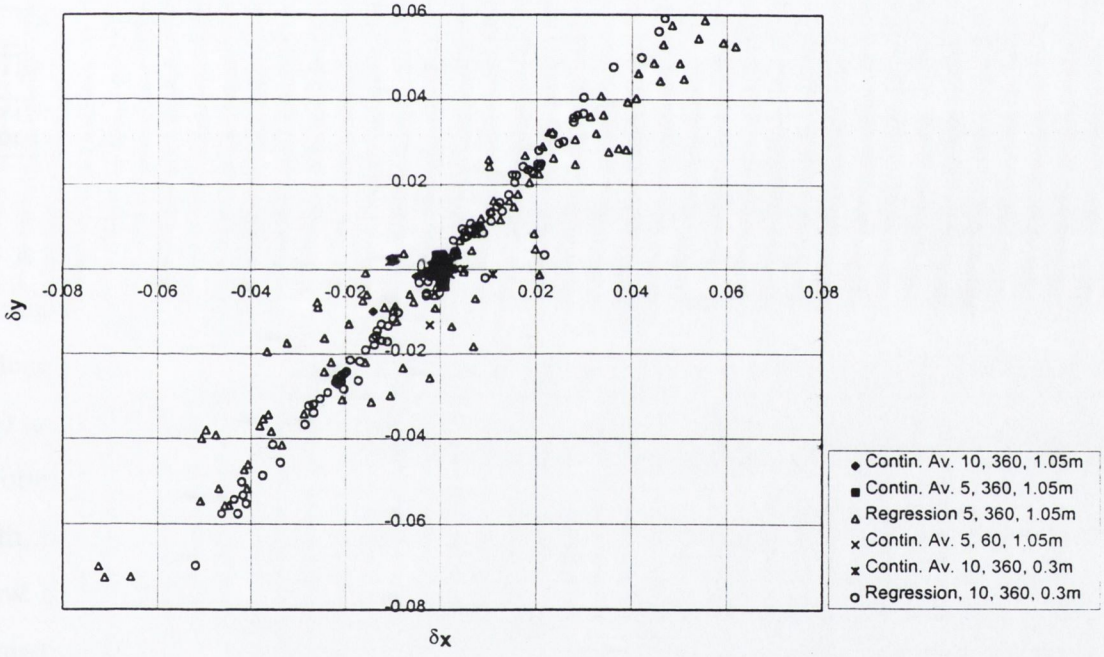

Figure C1. Deviation of camera measurements for different set-ups

Test Series 2

For the second series of tests, the camera accuracy in the measurement of displacements was assessed, using the optimum set-up taken from Test Series 1. The measurements were taken for the relative displacement of two metal plates which could be moved together or apart with a screw system. Dots were painted on the plates (Figure C2) to allow the camera to track any movement. The distance between the plates was measured independently with a micrometer. Table C3 shows results for this series of tests; the camera and micrometer

measurements are presented in terms of percentage difference, difference in millimetres and the maximum scatter of camera readings.

From early investigations, it was found that correct calibration of the field of view was vital if any meaningful comparison could be made between camera and micrometer measurements. All the results presented are for tests which have been carefully calibrated to minimise this error. Other significant sources of difference can arise from micrometer errors, camera or target movement and any inaccuracy inherent in the camera system. Micrometer accuracy is limited to 0.01 mm and is also subject to error. There were a number of possible sources of vibrations which could result in small movements to the camera and target, e.g., traffic vibrations due to the proximity of a road. If the vibrations are severe enough and the camera or target are not securely fixed to a stable surface they can cause large errors. From Table C3 it can be seen the differences between camera and micrometer measurements range from 0.003 to 0.084 mm.

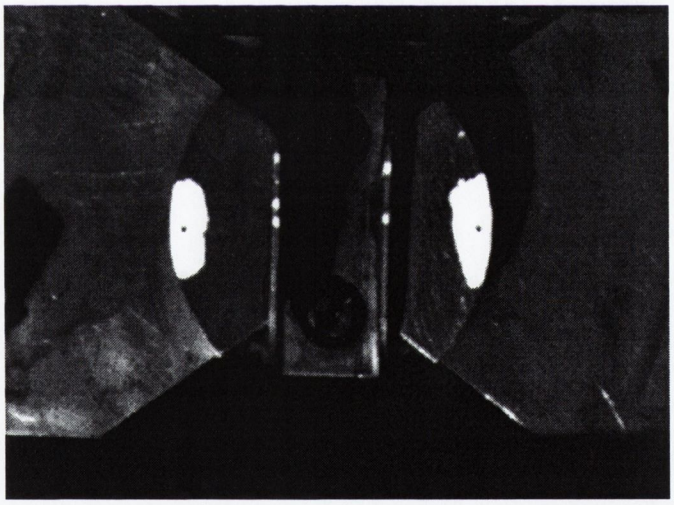

Figure C2. Camera view of 'screw-adjusted' plates painted with dots

A major difficulty in these tests was in providing accurate alternative measurements with which to test the accuracy of the Videoextensometer system. Various different tests were tried involving the use of micrometers and dial gauges, both of which are less accurate than the Videoextensometer system. The micrometer is accurate to 0.01 mm which means that if the field of view of the camera in one direction is 100 mm the micrometer can measure the strain for this range of movement to 0.01 %. Over this range the camera is reputed by the manufacturers to be capable of measuring strain accurately to at least 0.001 % (10

microstrain). The consistency of the error in these tests, therefore, gives a better indication of the degree of accuracy of the system.

Table C3. Comparison of camera and micrometer displacement measurement

Test No.	Data Logging	% Difference Camera/Micrometer	± Difference (mm)	Camera Error Standard Deviation (mm)
1	Automatic (10 Hz)	0.5240	0.01	0.00068
2	Manual	0.0075	0.01	0.00005*
3	Manual	0.0925	0.0076	0.00190*
4	Manual	0.0075	0.003	0.00057*
5	Automatic (10 Hz)	0.3025	0.0037	0.00130
6	Automatic (10 Hz)	0.3875	0.002	0.00039
7	Automatic (10 Hz)	0.5710	0.088	0.00065
8	Automatic (10 Hz)	0.4502	0.084	0.00088
9	Automatic (10 Hz)	0.3760	0.051	0.00066
10	Automatic (10 Hz)	0.2730	0.041	0.00408
11	Automatic (10 Hz)	0.1820	0.027	0.00152
*The manually recorded tests provide only a small sample size for standard deviation calculation (typically 4 or 5 readings) For all tests:- Field of View in the range of 95×72 to 110×83 mm.				

As a result, the standard deviation of the camera results has been used to assess their accuracy. This removes external sources of error and considers only those produced by the videoextensometer system. The deviation of results for a typical test, (Test No. 1 in Table C3) are shown in Figure C3, as is the mean value with error lines, for a standard deviation of one, on either side. Table C3 shows that the standard deviation of error for the camera, with the optimum set-up, is typically less than 0.001 mm (or 0.001 % strain) for a field of view of approximately 100 mm, although a maximum deviation of 0.004 mm (0.004 % strain) was recorded. This finding concurs with the manufacturer's accuracy claims. However, it is concluded from these tests that the best accuracy possible with the camera in normal testing conditions is 0.001 % strain, and this is not as the manufacturers state, the minimum resolution.

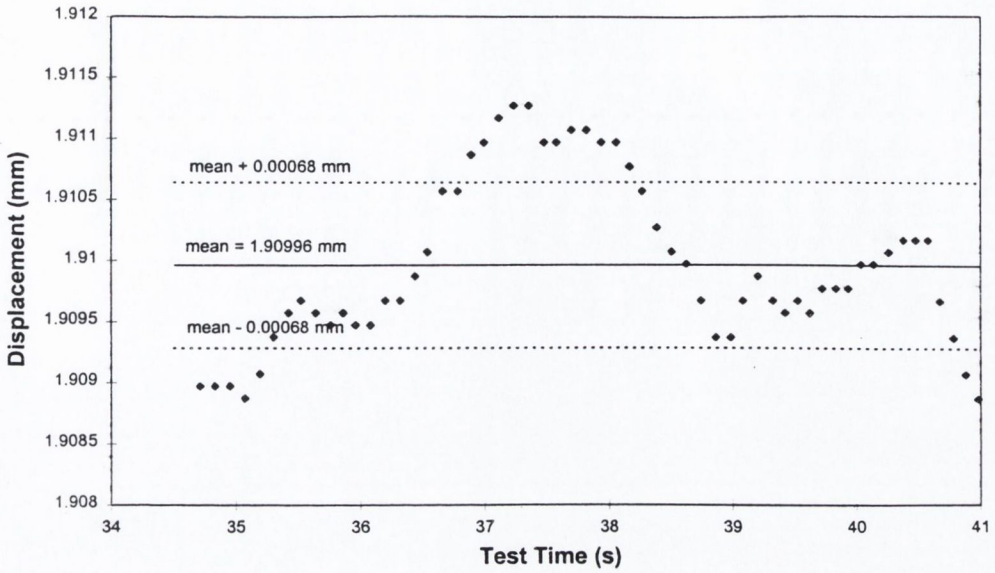

Figure C3. Typical displacement error for camera plotted against test time

REFERENCES

REFERENCES

Abu-Farsakh M. Y., Voyiadjis G. Z. and Tumay M. T. (1998), 'Numerical analysis of the inature piezocone penetration tests (PCPT) in cohesive soils', *Int. J. Numer. Anal. Meth Geomech.*, **22**, 791-818.

Al Tabbaa, A. and Wood, D. M. (1987), 'Some measurements of the permeability of kaolin', *Geotechnique* **37** (4), 499-503.

ANSYS (1997), *Help Manual for Revision 5.3,* SAS IP, Inc.

Baligh, M. M. and Scott, R. F. (1975), 'Quasi-static deep penetration in clays', *J. Geotech. Eng. ASCE*, **101**, 1119-1133.

Baligh, M. M. (1975), 'Theory of deep site static cone penetration resistance', Dept. of Civil Eng., Massachusettes Institute of Technology, Research Report No. R75-56.

Baligh, M. M. (1985), 'Strain Path Method', *Journal of the Geotechnical Engineering Division,* ASCE, Vol. 111, 1108-1136.

Baligh, M. M. (1986), 'Undrained deep penetration, I: shear stresses', *Geotechnique* **36**, No. 4, 471-485.

Baligh, M. M., Azzouz, A. S. and Chin, C. T. (1987), 'Disturbance due to ideal sampling disturbance', *J. Geotech. Eng. Div., ASCE* **113**, No. GT7, 739-757.

Benham, P. P. and Warnock, F. V. (1976), *Mechanics of solids and structures*, Pitman Books Ltd., London.

Bishop R. F., Hill R., & Mott N. F. (1945), 'The theory of indentation and hardness tests', *Proceedings of the Physical Society,* London, England, Vol. 57, No. 3 147-159.

Bond, A. J. (1989), 'Behaviour of displacement piles in overconsolidated clays', *PhD Thesis,* Faculty of Engineering, Imperial College of Science, University of London.

Butterfield R. & Banerjee P. K. (1970), 'The effect of pore water pressures on the ultimate bearing capacity of driven piles', *Proc. Second South East Asian Conf. on Soil Engineering*, Bankok, 385-394.

Carter J. P., Randolf M. F. and Wroth, C. P. (1979), "Stress and Pore Pressure Changes in Clay During and After the Expansion of a Cylindrical Cavity", *Int. J. Num. Analyt. Meth. in Geomech.*, Vol. 3, 305-322.

Cividini A., & Gioda G. (1989), 'Finite Element Modelling of the Driving Process of Piles', *Proc. 12th Int. Conf. on Soil Mech. and Found. Eng.*, Rio de Janeiro.

Collins I. F. & Stimpson J. R. (1994), 'Similarity solutions for drained and undrained cavity expansions in soils', *Geotechnique*, **44**, 21-34.

Collins I. F. & Yu H. S. (1996), 'Undrained cavity expansions in critical state soils', *Int. J. Numer Anal. Methods Geomech.*, **20**, 489-516.

Cooke, R. W. and Price, G. (1973), 'Strains and displacements around friction piles', *Proceedings*, 8th Int. Conf. Soil Mech. Fdn. Eng., Moscow, No. 1 pp 53-60.

Cooke, R. W., Price, G., and Tarr, K. (1979), 'Jacked Piles in London Clay: a study of load transfer and settlement under working conditions', *Geotechnique*, **29**, No. 2 pp 113-147.

Crisfield M. A. (1997), *Non-linear Finite Element Analysis of Solids and Structures*, John Wiley and Sons Ltd.

Davidson, J. L. and Boghrat, A., "Displacements and strains around probes in sand", *Geotchnical Practice in Offshore Engineering,* 181-202 (1983).

Francescon M. (1983), 'Model pile tests in clay. Stresses and displacements due to installation and axial loading', *Ph.D. Thesis,* University of Cambridge, U.K.

Gill, D. R., and Lehane, B. M. (1998), 'Modelling penetrometer installation using a modified Strain Path Method approach', *Proceedings*, 4th European Conference on Numerical Methods in Geotechnical Engineering - NUMGE98, 303-314, Udine.

Gill, D. R., and Lehane, B. M. (1999), 'Extending the strain path method analogy for modelling penetrometer installation', *Int. J. Numer. Anal. Meth. Geomech.*, **23** (in press).

Gue, S. S. (1984), 'Ground heave around driven piles in clay', *Ph.D. Thesis,* Dept. Eng. Sci., University of Oxford, U.K.

Houlsby G. T. and Wroth, C. P. (1982). 'Determination of undrained strengths by cone penetration tests', *Proceedings*, 2nd ESOPT, 585-590, Amsterdam.

Huebener K. H., Thornton E. A. and Byrom T. G. (1995), *The Finite Element Method For Engineers,* John Wiley & Sons, New York.

Iler, R. K. (1979), *The Chemistry of Silica: solubility, polymerization, colloid and surface properties, and biochemistry*, John Wiley & Sons, Inc., New York.

Iskander, M. G. (1997), 'A transparent material to model the geotechnical properties of soils', *Proceedings*, 14th International Conference on Soil Mechanics and Foundation Engineering (Hamburg), 315-318.

Iskander, M. G., Lai, J., Oswald, C. J., and Mannheimer, R. J. (1994), 'Development of a transparent material to model the geotechnical properties of soils', *ASTM Geotechnical Testing Journal*, Vol. 17, No. 4, 425-433.

Jardine R. J. and Chow F. C. (1996), *New design methods for offshore piles*, MTD Publication 96/103, Marine Technology Dept., London.

Kiousis P. D. Voyiadjis G. Z. and Tumay M. T. (1988), 'A large strain theory and its application in the analysis of the cone penetration mechanism', *Int. J. Numer. Anal. Meth Geomech.*, **12**, 45-60.

Lehane, B. M. (1992), 'Experimental investigations of pile behaviour using instrumented field piles', *PhD Thesis,* Faculty of Engineering, Imperial College of Science, University of London.

Lehane B. M. and Jardine R. J.(1994), 'Displacement-pile behaviour in a soft marine clay', *Can. Geotech. J.*, **31**, 181-191.

Levadoux, J. N., and Baligh, M. M. (1980), 'Pore pressure during cone penetration', *Research Report R80-15*, Dept. of Civil Engineering, Massachusetts Institute of Technology, Cambridge, Massachusetts.

Mair R. J. and Wood D. M. (1987) *Pressuremeter testing: methods and interpretation*, Butterworths, London.

Mannheimer, R. and Oswald, C. (1993), 'Development of transparent porous media with permeabilities of soils and reservoir materials', *Ground Water*, Vol 31, No. 5, 781-788.

Massey, B.S. (1991), *Mechanics of Fluids*, Chapman & Hall, London.

McMeeking R. M. and Rice J. R. (1975), 'Finite-element formulations for problems of large elastic-plastic deformation', *Int. J. Solid Struct.*, **11**, 611-616.

Mesri, G. and Ali, S. (1999), 'Undrained shear strength of a glacial clay overconsolidated by desiccation', *Geotechnique* **49** (2) 181-198.

Meyerhof G. G. (1951), 'The ultimate bearing capacity of wedge shaped foundations', *Geotechnique*, Vol. 2, No. 3.

Randolph M. F., Carter J. P. and Wroth C. P. (1979), "Driven Piles in Clay - the effects of Installation and Subsequent Consolidation" *Geotechnique* **29** (4) pp 361-393.

Randolph M. F., Steenfelt, J. S. and Wroth, C. P. (1979), 'The effect of pile type on design parameters for driven piles – design parameters in geotechnical engineering' *Proceedings,* 7th European conference on Soil Mechanics, Brighton, Vol. 2, pp 107-114.

Silvestri V., Dakroub H. & Fahmy Y. (1997), 'Analysis of cone penetration and indentation tests in clayey soils', *Can. Geotech. J.*, Vol. 34, 224-263.

Skempton A. W. (1951), 'The bearing capacity of clays', *Building research Congress*, London, Vol. 1.

Steenfelt, M.F., Randolph M. F. and Wroth, C. P. (1981), 'Instrumented model piles jacked into clay', *Proceedings*, 10th International Conference on Soil Mechanics and Foundation Engineering, Stockholm, pp. 856-864.

Szechy K. (1968), 'Deformation around and below driven and vibrated test tubes', Acta. Technica. Acd. Sci., Hungary, Vol. 62.

Teh C. I. (1987), 'An analytical investigation of the cone penetration test', *Ph.D. Thesis,* Dept. Eng. Sci, University of Oxford, U.K.

Tumay M. T., Acar Y. B. and Cekirge M. H. (1985), 'Flow field around cones in steady penetration', *Journal of Geotechnical Engineering*, Vol. **111**, 193-204.

Van Den Berg P., De Borst R. and Huetink H. (1996), 'An Eulerian finite element model for penetration in layered soil', *Int. J. Numer. Anal. Meth Geomech.,* **20**, 865-886.

Vesic A. S. (1963), 'Bearing capacity of deep foundations on sand', Stresses in Soils and Layered Systems, Can. Highway Research Board, No. 39.

Whittle A. J. (1991), 'Predictions of instrumented pile behaviour at the Bothkennar site', Report submitted to Dept. of Civ. Eng., Univ. of London (Imperial College).

Whittle A. J. and Baligh M. M. (1988), 'The behaviour of piles supporting tension leg platforms: Final Report Phase III', *MIT Sea Grant and Joint Oil Industry Consortium Report,* Dept. Civil Eng., MIT, Cambridge, MA.

Whittle (1999), Written correspondence regarding current developments in SPM at MIT.

Wroth C. P. and Houlsby G. T. (1985). Soil Mechanics - Property characterisation and analysis procedures. Proc. 11th Int. Conf. On Soil Mech. and Foundation Engineering.